



Dipl.-Ing. Christoph Stefan Aigner

# **Magnetic resonance RF pulse design for simultaneous multislice imaging**

**DOCTORAL THESIS**

to achieve the university degree of

Doktor der technischen Wissenschaften

submitted to

Graz University of Technology

Supervisor

Univ.-Prof. Dipl.-Ing. Dr.techn. Rudolf Stollberger  
Institute for Medical Engineering

Graz, 2018

## Statutory Declaration

I declare that I have authored this thesis independently, that I have not used other than the declared sources/resources, and that I have explicitly marked all material which has been quoted either literally or by content from the used sources.

Graz, \_\_\_\_\_  
Date

\_\_\_\_\_  
Signature

## Eidesstattliche Erklärung<sup>1</sup>

Ich erkläre an Eides statt, dass ich die vorliegende Arbeit selbstständig verfasst, andere als die angegebenen Quellen/Hilfsmittel nicht benutzt, und die den benutzten Quellen wörtlich und inhaltlich entnommenen Stellen als solche kenntlich gemacht habe.

Graz, am \_\_\_\_\_  
Datum

\_\_\_\_\_  
Unterschrift

<sup>1</sup>Beschluss der Curricula-Kommission für Bachelor-, Master- und Diplomstudien vom 10.11.2008; Genehmigung des Senates am 1.12.2008

# Acknowledgements

This work was carried out during the years 2012-2018 at the Graz University of Technology, at the Institute of Medical Engineering in strong and tight cooperation with researchers from the Department of Mathematics at the Karl Franzens University of Graz. It is a pleasure to thank those who made this thesis possible.

Firstly, I would like to thank my supervisor **Prof. Rudolf Stollberger** for introducing me to the exciting research field of magnetic resonance imaging (MRI), his continuous support and optimism concerning this work and for giving me the opportunity to work on this topic. RF pulse design for MRI is a highly interdisciplinary research field that requires knowledge from various topics including physics, computer science, engineering, medicine and mathematics. Therefore, I would like to point out that the working environment as a member of the SFB Research Center "Mathematical Optimization and Applications in Biomedical Sciences" turned out to be optimal for the progress of this thesis. Hence, a special thanks goes to **Prof. Karl Kunisch** as the Coordinator of the SFB for his support and cooperation. In addition, I would like to highlight two people, **Prof. Christian Clason** and **Armin Rund**. You have been my two main collaborators and I owe you my deepest gratitude for your endless patience, support and motivating guidance. Moreover, the results presented in this work were only possible thanks to our tight and fruitful cooperation. Thank you! I am looking forward to further joint work in the future.

Further, I want to express my immense gratitude to all present and former colleagues at the Institute of Medical Engineering (TU Graz), the Institute of Mathematics and Scientific Computing (Uni Graz), the Institute of Psychology (Uni Graz), the Department of Neurology (Medical University) and the Ludwig Boltzmann Institute for Clinical Forensic Imaging for numerous interesting and highly productive discussions and the relaxed working atmosphere. Special thanks go to **Deepika Bagga, Christoph Birkl, Markus Bödenler, Prof. Kristian Bredies, Clemens Diwok, Christian Gössweiner, Christina Graf, Kamil Kazimierski, Karl Koschutnig, Markus Kraiger, Christian Langkammer, Andreas Lesch, Oliver Maier, Adrián Martín Fernández, Bernhard Neumayer, Peter Opriessnig, Isabella Radl, Lukas Pirpamer, Prof. Stefan Ropele, Andreas Petrovic, Prof. Veronika Schöpf, Prof. Hermann Scharfetter, Matthias Schlögl, Martin Söllradl, Johannes Strasser, Stefan Spann and Bridgette Webb.**

I am thankful for the great time we had together and I am glad I got to share the last years with you.

I would additionally like to thank my so far not mentioned national and international cooperation partners from the Medical University of Vienna, King's College London and the MGH Harvard-MIT group in Boston, especially, **Samy Abo Seada, Prof. Elmar Laistler, Prof. Shaihan Malik, Lena Nohava, Prof. Gert Pfurtscheller, Daniel Polak** and **Prof. Kawin Setsompop**. The collaboration with you has allowed me to extend and deepen my knowledge of various exciting MR related topics previously unknown to me. Thank you!

Very special thanks go to all proofreaders, especially **A. Lesch** and **B. Webb**, whose comments greatly helped me to polish and to finish this thesis.

I extend my deepest gratitude to my friends and everyone else who is not listed here explicitly. Finally, I would like to thank my girlfriend **Sara**, my brother **Michael** and my parents **Stefan** and **Gertraud Aigner** for their continuous love, help and endless support. This journey would not have been possible without you!

# Abstract

Magnetic Resonance Imaging (MRI) is one of the leading non-invasive medical imaging techniques to image healthy and pathological anatomy and physiological processes of the body and is primarily known for its excellent soft tissue contrast. Contrary to other high resolution imaging techniques, MRI is based on strong magnetic and electric fields and does not require ionizing radiation. Image acquisition, however, is often limited by long acquisition times resulting from the need to repeat the measurement several times to encode multiple k-space data points. In addition to lengthy acquisition times, limited MR hardware performance as well as physical and physiological effects further restrict the MR sequence parameters, which results in lower signal to noise ratio and increased sensitivity to motion or magnetic susceptibility effects. This thesis is dedicated to the development and practical implementation of tailored large tip-angle radio frequency (RF) pulses and slice selective gradient shapes with increased excitation accuracy, lower power requirement and reduced pulse duration. The presented optimal control based RF pulse design methods are formulated for the joint design of RF and slice selective gradient shape for different large tip-angle applications. The focus of this work is on simultaneous multislice (SMS) applications to push acceleration of existing 2D MRI acquisition strategies. The extension to constrained RF pulse optimization allows exploitation of various MR hardware limits and yields accurate low power RF pulses and slice selective gradient shapes with short pulse durations. The optimized waveforms proved to outperform existing RF pulses and can be used to reduce the minimal echo spacing and echo time. Numerous simulation and experimental examples based on phantom and in-vivo measurements demonstrate the increased excitation accuracy and the reduction of both RF power and RF duration.

Keywords: RF pulse design, slice-selective, simultaneous multislice, refocusing, physical constraints, optimal control

# Kurzfassung

Die Magnetresonanztomographie (MRT) ist eines der führenden nicht-invasiven bildgebenden Verfahren zur Abbildung gesunder und pathologischer Gewebstypen und physiologischer Prozesse des Körpers und ist vor allem für seinen hervorragenden Weichteilkontrast bekannt. Im Gegensatz zu anderen hochauflösenden bildgebenden Verfahren basiert die MRT auf starken magnetischen und elektrischen Feldern und benötigt keine schädliche ionisierende Strahlung oder Röntgenstrahlung. Die Bildaufnahme ist jedoch oft durch lange Aufnahmezeiten begrenzt, die sich aus der Notwendigkeit ergeben, die Messung mehrmals zu wiederholen, um mehrere k-space Datenpunkte zu kodieren. Zusätzlich zu den langen Messzeiten, begrenzen die limitierte MR-Hardware und physische und physiologische Beschränkungen die MRT Sequenzparameter, was zu einem geringeren Signal-Rausch-Verhältnis und einer höheren Empfindlichkeit für Bewegungseffekte führt. Diese Arbeit widmet sich der Entwicklung und praktischen Umsetzung maßgeschneiderter Hochfrequenzpulse und schichtselektiver Gradientenformen mit erhöhter Anregungsgenauigkeit, geringem Leistungsbedarf und reduzierter Pulsdauer. Die vorgestellten HF-Impulsentwurfsmethoden basieren auf Methoden der Optimalsteuerung und sind für den gemeinsamen Entwurf von HF Puls und schichtselektiven Gradientenform formuliert. Der Schwerpunkt dieser Arbeit liegt auf der simultanen Mehrschichtanwendungen zur weiteren Beschleunigung von 2D-MRT-Aufnahmestrategien. Die Erweiterung der Designmethode auf die eingeschränkte Optimierung ermöglicht die Ausnutzung verschiedener MR-Hardware-Grenzen, was zu einer geringeren Pulsleistung oder minimalen Dauer von HF-Impulsen und schichtselektiver Gradientenformen führt. Die optimierten Wellenformen übertreffen vorhandene HF-Impulse und können dazu verwendet werden, das minimalen Echo-Spacing zu reduzieren und die kürzeste erreichbare Echozeit zu nutzen. Zahlreiche Simulations- und Experimentallbeispiele auf Basis von Phantom- und In-vivo-Messungen zeigen die Erhöhung der Anregungsgenauigkeit, die Reduzierung der HF-Leistung und die Reduktion der minimalen HF-Dauer.

Schlüsselwörter: Magnetresonanztomographie, HF-Impulsdesign, schichtselektiv, Simultane Multischicht-Anregung, Refokussierung, optimale Steuerung

# Contents

<b>Abstract</b>	<b>v</b>
<b>Acronyms</b>	<b>ix</b>
<b>1 Introduction</b>	<b>1</b>
<b>2 Physical principles of magnetic resonance</b>	<b>3</b>
2.1 Nuclear spin . . . . .	4
2.2 Equation of motion and bulk magnetization . . . . .	6
2.3 RF excitation . . . . .	9
2.4 Relaxation . . . . .	11
2.5 Bloch equations . . . . .	13
<b>3 Bloch simulation</b>	<b>16</b>
3.1 Neglected relaxation . . . . .	17
3.1.1 Small tip angle approximation . . . . .	17
3.1.2 Rotation in the magnetization domain . . . . .	18
3.1.3 Rotation in the spin domain . . . . .	21
3.2 Including relaxation . . . . .	23
<b>4 MR hardware and practical aspects</b>	<b>26</b>
4.1 Experimental design . . . . .	27
4.2 Pulse sequence programming . . . . .	31
4.3 RF pulse and slice selective gradient limitations . . . . .	32
<b>5 RF pulse design</b>	<b>38</b>
5.1 RF pulse categories . . . . .	39
5.2 Spatial non-selective RF pulses . . . . .	41
5.3 Spatial selective RF pulses . . . . .	44
5.4 Variable-rate selective excitation . . . . .	51
5.5 SMS RF pulse design . . . . .	52
5.5.1 Peak RF amplitude reduction . . . . .	53
5.5.2 Peak RF amplitude and RF power reduction . . . . .	56

## Contents

5.6	Slice selective RF pulse design via optimal control . . . . .	59
5.6.1	Single slice selective RF pulse design via OC . . . . .	60
5.6.2	SMS RF pulse design via OC . . . . .	68
<b>6</b>	<b>Discussion</b>	<b>81</b>
<b>7</b>	<b>Outlook</b>	<b>84</b>
<b>8</b>	<b>List of Publications</b>	<b>87</b>
<b>9</b>	<b>Appendix</b>	<b>93</b>
9.1	Efficient high-resolution RF pulse design applied to simultaneous multi-slice excitation . . . . .	93
9.1.1	Introduction . . . . .	94
9.1.2	Theory . . . . .	96
9.1.3	Methods . . . . .	100
9.1.4	Results . . . . .	104
9.1.5	Discussion . . . . .	110
9.1.6	Conclusions . . . . .	113
9.1.7	Trust-region algorithm . . . . .	114
9.1.8	Discretization . . . . .	115
9.2	Magnetic Resonance RF pulse design by optimal control with physical constraints . . . . .	117
9.2.1	Introduction . . . . .	118
9.2.2	Theory . . . . .	119
9.2.3	Methods . . . . .	123
9.2.4	Results . . . . .	125
9.2.5	Discussion . . . . .	134
9.2.6	Conclusions . . . . .	141
9.2.7	Lagrange calculus in the spin domain . . . . .	141
9.3	Simultaneous Multislice Refocusing via Time Optimal Control . . . .	145
9.3.1	Introduction . . . . .	146
9.3.2	Theory . . . . .	147
9.3.3	Methods . . . . .	151
9.3.4	Results . . . . .	155
9.3.5	Discussion . . . . .	161
9.3.6	Conclusions . . . . .	164
	<b>Bibliography</b>	<b>169</b>

# Acronyms

BIR	$B_1$ Insensitive Rotation
CAIPIRINHA	Controlled Aliasing in Parallel Imaging Results in Higher Acceleration
CG	Conjugate Gradient
CPMG	Carr-Purcell-Meiboom-Gill
CPU	Central Processing Unit
CSPAMM	Complementary Spatial Modulation of Magnetization
EPI	Echo-planar imaging
FFT	Fast Fourier Transform
FID	Free Induction Decay
FLASH	Fast Low Angle Single Shot
FOV	Field-of-View
FWHM	Full Width at Half Maximum
GIRF	Gradient Impulse Response Function
GPU	Graphics Processing Unit
GRAPPA	Generalized Autocalibrating Partially Parallel Acquisitions
GRASE	Gradient-and Spin-Echo
GRE	Gradient Recalled Echo
IDEA	Integrated Development Environment for (MR) Applications
ISMRM	International Society for Magnetic Resonance in Medicine
MB	Multiband
MR	Magnetic Resonance
MRI	Magnetic Resonance Imaging
NMR	Nuclear Magnetic Resonance
OC	Optimal Control
PINS	Power Independent Number Of Slices
pTx	Parallel Excitation
RARE	Rapid Acquisition with Refocused Echoes
RF	Radio Frequency
ROI	Region of Interest

## Acronyms

SAR	Specific Absorption Rate
SE	Spin Echo
sG	slice GRAPPA
SINC	Sinus Cardinalis
SLR	Shinnar–Le Roux
SMS	Simultaneous Multi-Slice
SPAMM	Spatial Modulation of Magnetization
SSFP	Steady-State Free Precession
TBWP	Time-Bandwidth Product
TE	Echo Time
THK	Thickness
TR	Repetition Time
TSE	Turbo Spin Echo
VERSE	Variable-Rate Selective Excitation

# 1 Introduction

Most NMR and MR applications need RF pulses to alter magnetization and to create NMR signals, which makes them an essential element in MRI. RF pulses are either used without a slice selective gradient shape for spatial non-selective applications or simultaneously with a slice selective gradient for slice selective excitation, inversion or refocusing and are an essential element of MRI sequences. Contrary to the static main field, RF and slice selective gradient fields are not applied continuously, but in distinct blocks or periods of MRI sequences with a time varying waveform. Yet, achieving well defined spatially selective slice profiles at high field strengths while fulfilling hardware and safety constraints is a challenging task. Consequently, different design approaches were proposed for RF pulse design using different kind of approximations on the Bloch equations for various applications. These assumptions, for instance neglected relaxation terms or the small tip angle approximation, result in analytical expressions with easy solutions and therefore find widespread use. However, the accuracy of conventional RF pulses is limited by the impact of the underlying approximations. An alternative design approach is the minimization of a suitable functional that represents a comprehensive description of the intended RF pulse application. Different optimization methods have been proposed to solve the design task including simulated annealing, evolutionary approaches or optimal control. These design methods often lead to more accurate excitation patterns and allow to consider various other effects, for instance spatially varying slice selective gradients or transmit coil sensitivities. However, the use of numerical optimization techniques are often limited by the computational effort. The main research question that forms the basis of this thesis consists in how numerical optimization can be used to jointly design RF pulse and slice selective gradient shapes for large flip angle applications. Besides single slice selective excitation, the focus of this work lies on SMS applications. Different RF pulse design methods and models based on OC are discussed. These include unconstrained and constrained optimization with fixed and variable pulse duration [1]–[3]. The proposed optimization methods significantly reduce the pulse duration with minimal RF power compared to state of the art RF pulse design methods [4]. Additionally to low RF power and pulse duration requirements, the optimized results fulfil specific hardware and safety limitations. The system limitations can be defined before the optimization and include RF, slice selective gradient and slew rate amplitude and RF power constraints and constraints

## 1 Introduction

on the slice profile accuracy. The optimized RF pulses are experimentally validated and the applicability of the proposed design methods is proved.

The structure of this thesis is as follows. Chapter 2 revises the physical principles of NMR and MR necessary to understand the specifications regarding the RF pulse design process and its substantial consequences. It contains a brief derivation of the Bloch equations and description of MRI strategies for signal generation. Further, it discusses why the Bloch equations can be solved analytically only for special cases. The general simulation and solution of the Bloch equations is covered by Chapter 3. Different numerical and analytical Bloch integration methods, including rotation matrices for piecewise constant fields, small tip angle approximation and analytical eigenvalue approach are discussed and introduced. Chapter 4 summarizes specific aspects on the practical MR sequence implementation and hardware limitations. The focus of this chapter lies in the practical validation of the optimized RF pulse and slice selective gradient waveforms and the impact of hardware limits and imperfections. The design of RF pulses is covered by Chapter 5. This chapter discusses the most prominent RF pulse design methods for single non- and slice selective and SMS selective excitation and refocusing. The main results of the three main publications of this thesis [1]–[3] are summarized at the end of Chapter 5 and are listed in the Appendix. The final discussion and outlook for further applications on the design of parallel transmission and the inclusion of gradient imperfections in the optimization are given in Chapters 6 and 7.

## 2 Physical principles of magnetic resonance

### Contents

---

2.1 Nuclear spin . . . . .	4
2.2 Equation of motion and bulk magnetization . . . . .	6
2.3 RF excitation . . . . .	9
2.4 Relaxation . . . . .	11
2.5 Bloch equations . . . . .	13

---

Nuclear magnetic resonance (NMR) or more general, magnetic resonance (MR) is based on the quantum mechanical interaction of atomic nuclei with a nonzero nuclear magnetic moment and an external magnetic field  $B_0$  [5]–[8]. Besides NMR applications in the field of material research or chemical analysis, the NMR effect can further be used to perform magnetic resonance imaging (MRI) to acquire non-invasive images with excellent soft-tissue contrast. The quantum mechanical effects of individual spins can be summarized for a sample with a large number of spins by a classical description of the macroscopic bulk magnetization [7], [8] whose interactions with the external magnetic field can be modeled by the classical phenomenological Bloch equations [9]. Although this macroscopic description does not include nuclear spin-spin interactions such as j-, dipole-, or quadrupole-coupling, it is sufficient to model the most effects for the intended clinical in vivo MRI applications to image the hydrogen proton. Therefore, the quantum mechanical content in this section is reduced to an absolute minimum. For a quantum mechanical description of NMR the reader is referred to [8], [10] and for an analysis of different MRI myths caused by an incorrect interpretation of quantum mechanics to [11].

In the following section, the emphasis will be on the classical description of the magnetization regarding the effects of an external field on non-zero spins. Furthermore, all discussion is limited to hydrogen protons.

## 2.1 Nuclear spin

The observations of Zeeman [12], Stern and Gerlach [13], Uhlenbeck and Goudsmith [14] and Dirac [15] led to the introduction of the electron spin and the observation, that the quantum mechanical states of atoms in a constant external magnetic field split into discrete energy levels. Figure 2.1 shows such a schematic energy splitting of the proton in an external magnetic field. The energy difference  $E_\Delta$  is generally defined by the Zeeman Hamiltonian

$$\hat{H}_z = -\gamma\hbar B_0 \hat{I}_z, \quad (2.1)$$

using the quantum mechanical spin operator  $\hat{I}_z$ , the reduced Planck constant  $\hbar = 1.0545718 \cdot 10^{-34}$  J s [16], the gyromagnetic ratio  $\gamma$  in  $\text{rad s}^{-1} \text{T}^{-1}$  and the main field  $B_0$  in T. For the hydrogen proton with a nuclear spin  $I = 1/2$  the magnetic spin quantum number

$$m_s = -I, (-I + 1), (-I + 2), \dots, I \quad (2.2)$$

results in  $m_s = \pm 1/2$ . The two energy levels of the eigenstates can be found using the Schrödinger equation

$$\hat{H}_z |I, m_s\rangle = E |I, m_s\rangle, \quad (2.3)$$

with the energy  $E$  and eigenfunction of the proton  $|I, m_s\rangle$ . Using Eq. 2.1 and 2.2 the energy difference  $E_\Delta$  or transition between the two states can be computed with

$$E_\Delta = 1/2\gamma\hbar B_0 - (-1/2\gamma\hbar B_0) = \hbar\omega_0, \quad (2.4)$$

describing the static interaction with the external magnetic field  $B_0$ .

This expression directly leads to the Lamor equation

$$\omega_0 = -\gamma B_0, \quad (2.5)$$

with the nuclei dependent proportionality factor or gyromagnetic ratio  $\gamma$  given by

$$\gamma = \frac{g_p \mu_n}{\hbar}, \quad (2.6)$$

with the experimentally determined proton Landé-factor  $g_p = 5.58$  [17] and the nuclear magnetic moment  $\mu_n$ . The nuclear magnetic moment is defined as

$$\mu_n = \frac{e\hbar}{2m_p}, \quad (2.7)$$

## 2 Physical principles of magnetic resonance

with the magnitude of the particle charge  $e = 1.60 \times 10^{-19}$  C and the proton mass  $m_p = 1.67 \times 10^{-27}$  kg, see [8]. For protons,  $\gamma$  is  $2.6731 \times 10^8 \text{ rad s}^{-1} \text{ T}^{-1}$  or  $\gamma/2\pi = 42.58 \text{ MHz/T}$  [8]. The proton's energy difference  $E_\Delta$  for the two stable energy levels then mainly depends on the field strength, see Eq. 2.1. For a static field of  $B_0 = 3 \text{ T}$  this energy difference is  $E_\Delta = 8.457 \times 10^{-26} \text{ J}$ .

The population ratio of the atoms occupying the two different states is described by the Boltzmann distribution

$$\frac{E[N_1]}{E[N_2]} = e^{\frac{E_\Delta}{kT}}, \quad (2.8)$$

using the reduced Boltzmann constant  $k = 1.381 \times 10^{-23} \text{ J K}^{-1}$ , the temperature  $T$  in K and the energy difference  $E_\Delta$  to predict the different spin populations  $E[N_1]$  and  $E[N_2]$ . From that, one can calculate the macroscopic net magnetization that is proportional to the occupancy difference

$$E[N_1 - N_2] = N \frac{e^{\frac{E_\Delta}{kT}} - 1}{e^{\frac{E_\Delta}{kT}} + 1} \approx N \frac{E_\Delta}{2kT}, \quad (2.9)$$

with  $N$  being the total number of spins [18]. At a field strength of 3 T and at room temperature  $T = 293.15 \text{ K}$  the occupation difference is approximately 10 ppm.

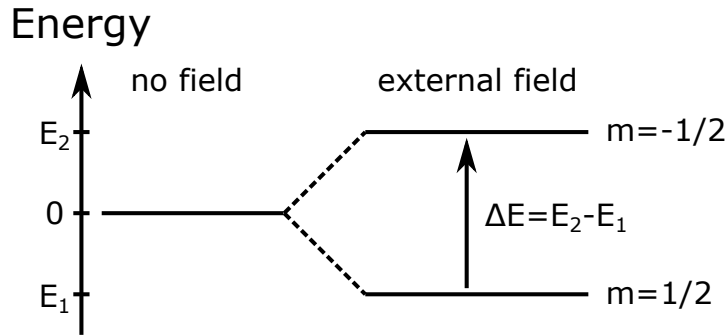


Figure 2.1: Schematic Zeeman splitting of the proton energy levels in an external field. The Energy difference  $E_\Delta$  depends mainly on the external field, see Eq. 2.4.

Due to its high natural abundance in biological tissue and its large gyromagnetic ratio, hydrogen protons are the nuclei primarily used for in vivo MRI. Nevertheless, other nuclei with a non-zero spin, for instance  $^{13}\text{C}$ ,  $^{19}\text{F}$  or  $^{31}\text{P}$ , also have a nuclear magnetic moment  $\mu_n$  that can be used to generate NMR signals. The nuclear magnetic moment  $\mu_n$  can be related to the angular momentum  $\hat{J}$  (the hats above the symbol indicate that they are quantum mechanical operators, refer to Chapter 7 of [10])

$$\mu_n = \gamma \hat{J}, \quad (2.10)$$

## 2 Physical principles of magnetic resonance

with  $\hat{j} = (\hat{j}_x, \hat{j}_y, \hat{j}_z)^T$  in the Cartesian coordinates. For a quantum mechanical description of the spin precession refer to Chapter 10 of [10].

The placement of a spin in an external magnetic field  $B$  results in a torque  $N = (N_x, N_y, N_z)^T$ , given by the cross product of the magnetic spin moment  $\mu_n$  and the external field  $B$

$$N = \mu_n \times B. \quad (2.11)$$

For a non-zero net torque this implies that the angular momentum  $\hat{j}$  changes according to

$$\frac{d\hat{j}}{dt} = N, \quad (2.12)$$

establishing the fundamentals of the equation of motion. For a more rigorous derivation of the magnetic moment and net force, referred to Chapter 2 of [8] and Chapters 2 and 5 of [10].

## 2.2 Equation of motion and bulk magnetization

Combining Eq. 2.10 and Eq. 2.11 allows rewriting of Eq. 2.12 to get the fundamental equation of motion:

$$\frac{d\mu_n}{dt} = \gamma\mu_n \times B. \quad (2.13)$$

This differential equation describes the macroscopic movement of the spin moment in an external field  $B$  and relates the resulting motion to the gyromagnetic ratio  $\gamma$  [8]. For a static and time invariant external field, for instance  $B = (0, 0, B_0)^T$ , Eq. 2.13 reduces to the important Lamor equation, see also Eq. 2.5, with  $\omega_0$  describing the precessional frequency of the spin system, better known as Lamor or precession frequency [8], [10]. The negative sign of Eq. 2.5 results from the main field  $B_0$  pointing along the positive z-axis.

Pure water has a proton concentration of  $110.4 \text{ mol L}^{-1}$  [19], thus resulting in an extremely large number of protons for typical NMR or MRI sample sizes. This holds for most biological tissues, for instance grey matter of the brain has a proton concentration of approximately 70 % of pure water [19]. For such a large number of individual protons, the macroscopic bulk magnetization  $M$  can be defined as the sum of all nuclear spins  $\mu_n$  in the observed sample

$$M = \frac{1}{V} \sum_{\text{protons in } V} \mu_n. \quad (2.14)$$

## 2 Physical principles of magnetic resonance

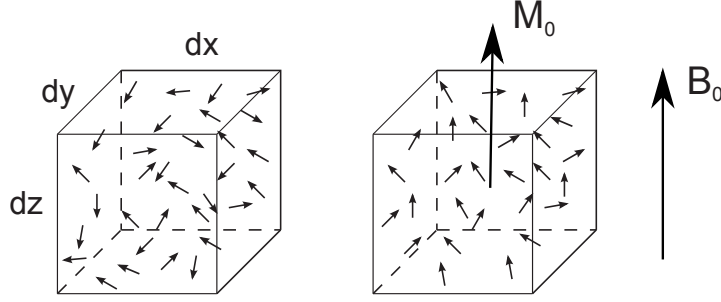


Figure 2.2: Random spin orientation and schematic build up of the macroscopic bulk magnetization in an external field  $B_0$ .

with the volume  $V$ . In the absence of an external field, the direction of the individual spins is purely random due to random thermal motion [8], [10], thus resulting in no observable bulk magnetization  $M = (0, 0, 0)^T$ . However, immediately after applying a strong external magnetic field, a precession around the external magnetic field is triggered. The random spin orientation (spherical) is slightly skewed towards the field direction due to relaxation [11] and a macroscopic observable bulk magnetization accumulates. The macroscopic bulk magnetization  $M$  now describes the macroscopic behaviour in the external field and enables the use of classical descriptions rather than requiring quantum mechanics. Figure 2.2 shows the schematic build up of the classical bulk magnetization  $M_0$  parallel to an external field.

Further, the assumption of non-interacting spins (for coupled spins, refer to Chapter 6 of [10]) and the previously defined bulk magnetization (Eq. 2.14) allow substitution of the magnetic moment  $\mu_n$  in the equation of motion (Eq. 2.13) leading to a predecessor of the Bloch equations without relaxation effects

$$\begin{cases} \frac{dM(t)}{dt} = \gamma M(t) \times B(t), \\ M(0) = M^0, \end{cases} \quad (2.15)$$

with the initial magnetization

$$M^0 = [M_x^0, M_y^0, M_z^0]^T. \quad (2.16)$$

Now, the change of magnetization  $M$  over time can be formulated as a result of the external magnetic field  $B$  on the magnetization  $M$ . The magnitude of the macroscopic bulk magnetization  $M_0$  scales for a hydrogen proton in the equilibrium ( $t \rightarrow \infty$ )

$$M_0 \simeq \frac{\gamma^2 \hbar^2 B_0}{4kT_{\text{sample}}} \rho_0, \quad (2.17)$$

## 2 Physical principles of magnetic resonance

with the magnitude of the applied field  $B_0$ , Boltzmann's constant  $k$ , reduced Plank's constant  $\hbar$ , the sample temperature  $T_{sample}$  in K, the proton density  $\rho_0$  and the protons gyromagnetic ratio  $\gamma$  according to [8].

This implies that in general, a stronger constant magnetic field results in a larger bulk magnetization and thus, a larger MR signal. However, increasing the main field strength causes several other effects which counteract this increase to some extent, for instance elevated  $B_0$  field inhomogeneities and an increased dielectric effect. Furthermore, larger relaxation times and power deposition in combination with peripheral nerve stimulation, limit the optimal field strength for in vivo MR. Therefore, most clinical MR scanners nowadays still use 1.5 to 3 T [20], while human in vivo MR research is done up to 10.5 T [21]. The constant improvement of MR hardware and the use of sophisticated MR techniques, recently resulted in the regulatory approval of 7 T systems to be used for clinical routine applications [22]. For more information on the impact of the hardware the reader is referred to Chapter 4.

The equation of motion Eq. 2.15 is defined with respect to a stationary coordinate system, better known in NMR as the laboratory frame of reference [8]. Typically, the constant main magnetic field ( $B_0$ ) is much larger than the radio frequency (RF) and gradient fields essential for MR signal generation and spatial MRI encoding. This results in a clouding of the much smaller non-static field interactions by the constant Lamor precession, see Figure 2.3 and requires a high temporal and spatial resolution for an accurate description of the magnetization. Furthermore, the bandwidth of RF and slice selective gradient waveforms are much lower than the Lamor frequency, see Section 4.3. This would result in an unjustifiably computational effort and the static field interaction is therefore typically removed by a coordinate transformation similar to a frequency demodulation in signal processing. The transformation of the Cartesian coordinates  $(x, y, z)$  to the rotating frame of reference  $(x', y', z')$  with  $\omega$  by

$$\begin{aligned}x' &= x \cos(\omega t) - y \sin(\omega t), \\y' &= x \sin(\omega t) + y \cos(\omega t), \\z' &= z.\end{aligned}\tag{2.18}$$

In the following, the prime character is used to define variables in the rotating frame of reference. The use of a rotating frame of reference rotating with the Lamor frequency allows for an easier handling of the equations (see Section 2.3) and a better understanding of the non-static field interactions [8], [10], [23]. Figure 5.1 summarizes the differences between the laboratory frame of reference and the rotating frame of reference. Instead of modulation of the RF pulse with the Lamor frequency  $\omega_0$ , the rotation of the coordinate system with  $\omega_0$  results in a stationary and on-resonant  $B_1$  field for the rectangular envelope, while the magnitude varies to achieve a SINC

envelope. The use of the rotating frame of reference simplifies the modelling of RF excitation and signal encoding.

## 2.3 RF excitation

The equilibrium bulk magnetization  $M$ , see Eq. 2.14, does not result in a measurable MR signal [8], [10], [23]. To induce a NMR signal in nearby receiver coils, time varying RF fields  $B_1(t)$ , for instance perpendicular to the much larger but constant field  $B_0$  [8], are applied by setting

$$B(t, r) = [B_{1,x}(t), B_{1,y}(t), B_0 + G_s(t) \cdot r]^T, \quad (2.19)$$

with the slice selective gradient for each axis

$$G_s(t) = [G_{s,x}(t), G_{s,y}(t), G_{s,z}(t)]^T, \quad (2.20)$$

at spatial position  $r = (x, y, z)^T$  being assumed to be zero for the discussion of pure RF excitation. RF fields close to or at the Larmor frequency tip the magnetization away from the initial state  $M^0$ , see Eq. 2.16. After the RF field is turned off, the transversal components of the tipped magnetization precess around the  $B_0$  field with the Larmor frequency  $M_{xy}(t) = (M_x(t), M_y(t))^T$  and result in an electromagnetic induction in the receiver coil [8], [10], see Figure 2.3 The time course of the magnetization  $M$  can be modeled with Eq. 2.15.

While the general solution is hard to solve, see Section 3, the use of a left-circular polarized RF field

$$B_1^+(t) = B_1 \begin{pmatrix} \cos \omega t \\ -\sin \omega t \end{pmatrix}, \quad (2.21)$$

with  $B_1$  being the RF magnitude,  $\omega$  the frequency and  $t$  the time vector allows finding of easy analytical solutions [8]. The further use of a rotating frame of reference [8], [24] rotating with the frequency  $\omega$  instead of the laboratory frame of reference, results in a stationary RF field

$$B_1^+(t)' = \begin{pmatrix} B_1 \\ 0 \end{pmatrix}. \quad (2.22)$$

## 2 Physical principles of magnetic resonance

The combination of  $B_1^+(t)'$  of Eq. 2.22 and Eq. 2.15, with a constant main field  $B_0$  according to [8], results in

$$\left(\frac{dM(t)}{dt}\right)' = \gamma M(t)' \times \begin{pmatrix} B_1 \\ 0 \\ B_0 - \omega/\gamma \end{pmatrix} = \gamma M(t)' \times B_{eff}, \quad (2.23)$$

with  $B_{eff}$  being the effective magnetic field and  $\omega$  the frequency of the RF field. This results in a counter clockwise precession around the axis of  $B_{eff}$ , see Figure 2.3. For the on-resonant case ( $\omega = \omega_0$ ) the  $B_1$  field is synchronized to tip the spin around the  $x'$ -axis and Eq. 2.23 is reduced to the cornerstone equation of motion

$$\left(\frac{dM(t)}{dt}\right)' = \gamma M(t)' \times \begin{pmatrix} B_1 \\ 0 \\ 0 \end{pmatrix}. \quad (2.24)$$

Using Eq. 2.24 the overall rotation of the bulk magnetization can be described by the flip angle  $\phi$

$$\phi = \gamma \int_{t=0}^T B_1(t) dt, \quad (2.25)$$

where  $T$  is the pulse duration and  $B_1(t)$  is the time dependent RF modulation envelope. For this easy example with an constant RF field  $B_1$ , the flip angle  $\phi$  can be further analytically described by

$$\phi = \gamma B_1 T. \quad (2.26)$$

However, it should be noted that Eq. 2.25 and 2.26 are valid only for the on-resonance condition. A more comprehensive discussion of all factors influencing the flip angle and its measurement in MRI is given in [25].

So far, all considerations are mainly based on geometrical solutions resulting from the equation of motion (Eq. 2.15). An alternative solution to the RF excitation (Eq. 2.24) based on rotation matrices is described in Section 3. At this point it is important to state again, that the simplified macroscopic view of the underlying quantum mechanical spin properties is justified only for a large sample of non-interacting spins. For the quantum mechanical modelling of spins in external magnetic fields refer to [10].

## 2 Physical principles of magnetic resonance

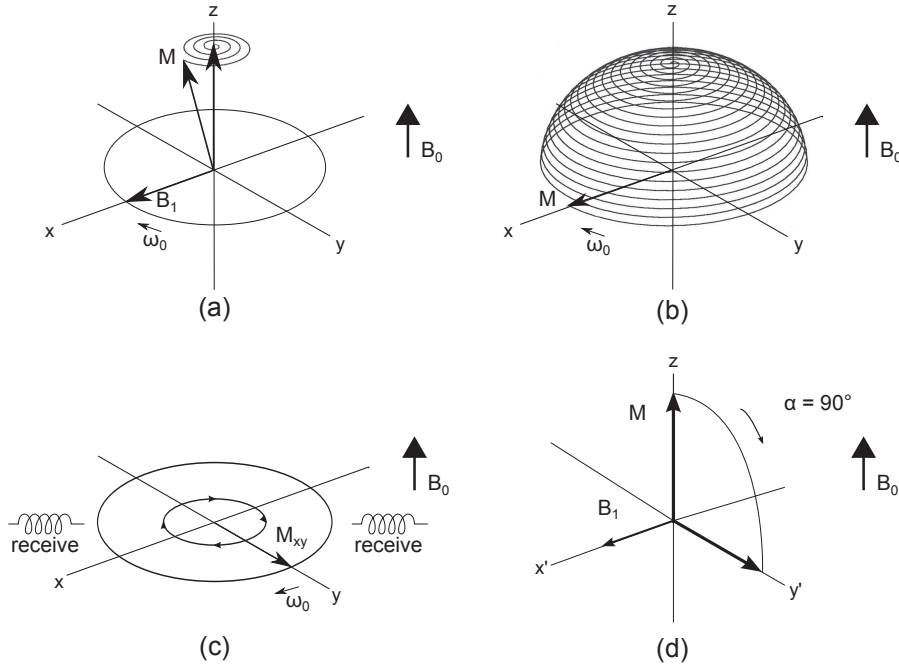


Figure 2.3: Schematic deflection of magnetization by a circular polarized RF field  $B_1$  in the laboratory frame (a) + (b) and rotating frame of reference (d). After turning off  $B_1$ ,  $M$  precesses in the  $xy$  plane and induces a signal in the receive coil (c). Modified from [26].

## 2.4 Relaxation

Besides the interaction with external magnetic fields, there occur further spin interactions with each other and also with the surrounding. Since the exact quantum mechanical mechanisms, which are responsible for these effects, are beyond the scope of this work, only the phenomenological observation of relaxation effects is described here. For an extensive quantum mechanical explanation refer to [8], [10], [27], [28]. After tilting the bulk magnetization vector  $M$  by a RF pulse, it returns back to its equilibrium state  $M = (0, 0, M_0)^T$  after sufficient time. The macroscopic effects behind this behaviour were modeled by Felix Bloch [9] as longitudinal ( $T_1$ ) and transversal relaxation ( $T_2$ ) describing the time constants of a first order exponential kinetics.

The longitudinal relaxation time  $T_1$  is defined as the proportionality factor that connects the recovery rate of the longitudinal magnetization ( $dM_z/dt$ ) and the difference  $M_0 - M_z$

$$\begin{cases} \frac{dM_z(t)}{dt} = \frac{1}{T_1}[M_0 - M_z(t)], \\ M_z(0) = M_z^0. \end{cases} \quad (2.27)$$

## 2 Physical principles of magnetic resonance

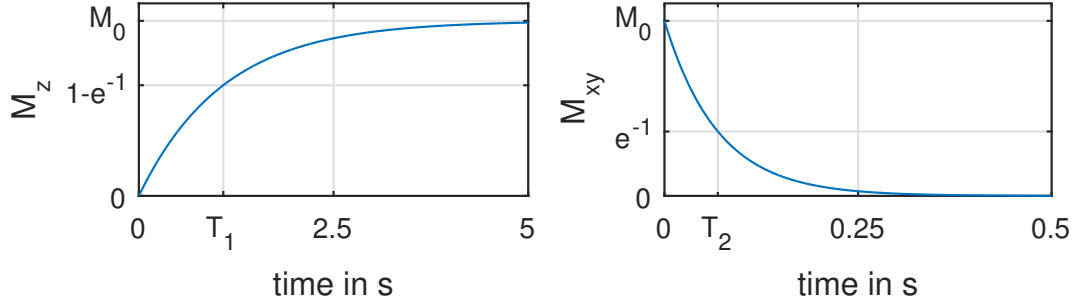


Figure 2.4: Simulated recovery of the longitudinal ( $M_z$ ) and transversal ( $M_{xy}$ ) magnetization based on  $T_1$  and  $T_2$  relaxation for white matter at 3 T ( $T_1 = 1084$  ms,  $T_2 = 69$  ms, [29]).

This differential equation can be solved analytically yielding

$$M_z(t) = M_z^0 e^{-t/T_1} + M_0(1 - e^{-t/T_1}), \quad (2.28)$$

with the initial condition  $M_z^0$  which describes the exponential recovery of the longitudinal magnetization. Please note that the solution assumes that the external field  $B_0$  is along the  $z$ -axis.

The transversal relaxation time  $T_2$  on the other hand is defined as the proportionality factor that connects the decay of the transversal magnetization  $(dM_{xy}/dt)'$  with the initial condition  $M_{xy}^0$

$$\begin{cases} \left( \frac{dM_{xy}(t)}{dt} \right)' = -\frac{1}{T_2} M_{xy}(t)', \\ M_{xy}(0)' = M_{xy}^0, \end{cases} \quad (2.29)$$

Eq. 2.29 has the following analytical solution in the rotating frame of reference

$$M'_{xy}(t) = M_{xy}^0 e^{-t/T_2}. \quad (2.30)$$

Relaxation times depend on proton surroundings and the main field [29]. In soft tissues at 3 T typical relaxation times range from  $T_1 = 100 - 2000$  ms (excluding cerebro spinal fluid) and  $T_2 = 28 - 300$  ms with a large spread in absolute numbers [30]. Figure 2.4 shows the time course of a pure mono-exponential  $T_1$  and  $T_2$  relaxation after a  $90^\circ$  tip. There is an additional decay of the transversal magnetization due to static field inhomogeneities. This additional dephasing can be characterized by the time constant  $T_2'$  with the assumption of a Lorentzian distribution of the inhomogeneities, see [8]. This results in the effective transversal relaxation time  $T_2^*$  given by

$$\frac{1}{T_2^*} = \frac{1}{T_2} + \frac{1}{T_2'}. \quad (2.31)$$

## 2 Physical principles of magnetic resonance

Contrary to the irreversible  $T_2$  decay, the  $T_2'$  decay can be recovered by forming a spin-echo. However, for specific applications, for instance functional imaging of the brain, the  $T_2^*$  decay founds the basis of signal differences [31]. In typical biological tissues relaxation times follow  $T_2^* < T_2 < T_1$ , however it was previously experimentally shown that for extremely low temperatures this relation may change and  $T_2$  actually becomes larger than  $T_1$  [32]–[34].

### 2.5 Bloch equations

The inclusion of the longitudinal and transversal relaxation (Eq. 2.27 and Eq. 2.29) into the equation of motion (Eq. 2.15) leads to the famous Bloch equations

$$\begin{cases} \frac{dM(t)}{dt} = \gamma M(t) \times B(t) + \frac{1}{T_1} \begin{pmatrix} 0 \\ 0 \\ M_0 - M_z(t) \end{pmatrix} - \frac{1}{T_2} \begin{pmatrix} M_x(t) \\ M_y(t) \\ 0 \end{pmatrix}, \\ M(0) = M^0, \end{cases} \quad (2.32)$$

describing the macroscopic change of magnetization in an external magnetic field for a given initial magnetization  $M^0$  [9]. The Bloch equations (Eq. 2.32) are a system of coupled linear differential equations and can be rewritten using a system matrix  $A$  acting on the magnetization  $M$  and a vector  $b$

$$\begin{cases} \frac{dM(t, r)}{dt} = A(B(t, r))M(t, r) + b(t), & t > 0, \\ M(0) = M^0, \end{cases} \quad (2.33)$$

summarizing the cross product of the magnetization  $M$  and the external magnetic field  $B$  for each spatial position  $r = (x, y, z)^T$  and the relaxation effects for a given initial magnetization  $M^0$ , see Eq. 2.16. Using the time varying external field  $B(t)$ , see Eq. 2.19, the system matrix  $A$  and the vector  $b$  result in

$$A = \begin{pmatrix} -\frac{1}{T_2} & \gamma[B_0 + G_s(t) \cdot r] & -\gamma B_{1,y}(t) \\ -\gamma[B_0 + G_s(t) \cdot r] & -\frac{1}{T_2} & \gamma B_{1,x}(t) \\ \gamma B_{1,y}(t) & -\gamma B_{1,x}(t) & -\frac{1}{T_1} \end{pmatrix}, \quad (2.34)$$

$$b = \begin{pmatrix} 0 \\ 0 \\ \frac{M_0(r)}{T_1} \end{pmatrix}. \quad (2.35)$$

## 2 Physical principles of magnetic resonance

It should be noted that Eq. 2.33 is defined to act the system matrix on the magnetization  $AM$  instead of  $MA$ .

There is no analytic solution for the full Bloch equations for a spatially and time varying magnetic field  $B(t, r)$ . Only for special cases, including neglected relaxation effects, left-circular polarized and constant RF field (Section 2.3), or for a zero  $B_1$  field, straight forward analytical solutions exist.

For a static and uniform magnetic field  $B_0$  with no active RF components, for instance  $B = (0, 0, B_0)^T$ , the Bloch equations reduce to

$$\begin{cases} \frac{dM(t, z)}{dt} = \begin{pmatrix} -\frac{1}{T_2} & \gamma B_0 & 0 \\ -\gamma B_0 & -\frac{1}{T_2} & 0 \\ 0 & 0 & -\frac{1}{T_1} \end{pmatrix} M(t, z) + \begin{pmatrix} 0 \\ 0 \\ \frac{M_0}{T_1} \end{pmatrix}, \\ M(0) = M^0. \end{cases} \quad (2.36)$$

with the Larmor frequency  $\omega_0 = -\gamma B_0$  according to Eq. 2.5. This allows an elegant analytical solution of pure relaxation, see Section 2.4, by decoupling the relaxation effects  $T_1$  and  $T_2$

$$\begin{aligned} M_x(t) &= e^{-t/T_2} (M_x^0 \cos \omega_0 t + M_y^0 \sin \omega_0 t), \\ M_y(t) &= e^{-t/T_2} (M_y^0 \cos \omega_0 t - M_x^0 \sin \omega_0 t), \\ M_z(t) &= M_z^0 e^{-t/T_1} + M_0 (1 - e^{-t/T_1}), \end{aligned} \quad (2.37)$$

with the initial magnetization  $M^0$ , see Eq. 2.16. Now, the Bloch equations are decoupled and longitudinal and transversal components can be handled separately. Together with the complex magnetization

$$M_{xy}(t) = M_x(t) + iM_y(t) \quad (2.38)$$

that defines the measurable NMR signal, the transversal solution is given by

$$M_{xy}(t) = M_{xy}^0 e^{-i\omega_0 t} e^{-t/T_2} \quad (2.39)$$

in the stationary field. The solution in the rotating frame of reference is given in Section 2.4, Eq. 2.30.

Non-interacting spins in a perfectly homogeneous proton sample and magnetic field  $B_0$  possess one distinct Larmor frequency  $\omega_0$ , see Eq. 2.5. However, realistic MR systems do not create perfectly homogeneous magnetic fields. Especially MR systems with a large bore have  $B_0$  field variations in the order of a few ppm in the specified field of view [35]. Besides inhomogeneities created by non-perfect coils, there are

## 2 Physical principles of magnetic resonance

additional field inhomogeneities arising from atomic or molecular spin interactions and variations due to magnetic susceptibility [36]–[38]. Contrary to a static resonance shift, or chemical shift, local field inhomogeneities create an additional de-phasing of the transversal magnetization that can be summarized by  $T_2'$  assuming a Lorentzian lineshape by setting  $T_2' = 1/(\gamma\Delta B_0)$  with the field inhomogeneity  $\Delta B_0$  across the voxel [8], [31].

Static field inhomogeneities reduce the transversal relaxation time  $T_2$  according to Eq. 2.31 which results in a faster de-phasing of the magnetization. Contrary to the inevitably lost  $T_2$  dephasing, the static  $T_2'$  dephasing can be recovered with refocusing pulses in a spin echo setting.

The Larmor frequency can be intentionally changed by field gradients to perform spatial encoding. Such field gradients depend on the spatial position, for instance along the  $z$ -axis, and are created by orthogonal gradient coils [39]–[41]. Gradients can be controlled independently for the three Cartesian components  $x$ ,  $y$  and  $z$ . This enables selection of two or three dimensional objects with single or parallel transmission [42]–[49]. It is important to mention here, that all field gradients are added to the  $z$  component of  $B$ , see Eq. 2.19, and thus only change the resonance frequency at a specific location  $r = (x, y, z)^T$

$$B(t, r) = [0, 0, B_0 + G_{s,x}(t)x + G_{s,y}(t)y + G_{s,z}(t)z]^T. \quad (2.40)$$

Besides RF encoding, the gradient coils are further used for encoding of the acquisition  $k$ -space and to establish the  $k$ -space acquisition trajectory [8], [23], [50]–[52].

So far, the discussion has been restricted to situations in which there was no arbitrary time dependent RF pulse involved. Using a time varying RF field  $B_1(t) = [B_{1,x}(t), B_{1,y}(t)]^T$  perpendicular to the external magnetic field  $B_0$  and a spatially dependent slice selective gradient results in the full Bloch equations

$$\begin{cases} \frac{dM(t, z)}{dt} = \begin{pmatrix} -\frac{1}{T_2} & \gamma[B_0 + G_s(t) \cdot r] & -\gamma B_{1,y}(t) \\ -\gamma[B_0 + G_s(t) \cdot r] & -\frac{1}{T_2} & \gamma B_{1,x}(t) \\ \gamma B_{1,y}(t) & -\gamma B_{1,x}(t) & -\frac{1}{T_1} \end{pmatrix} M(t, z) + \begin{pmatrix} 0 \\ 0 \\ \frac{M_0}{T_1} \end{pmatrix}, \\ M(0) = M^0. \end{cases} \quad (2.41)$$

Now, the linear differential equations are coupled and cannot be solved analytically to find the RF or slice selective gradient shape [1]–[3], [53]. Besides numerical approaches, approximative steady state solutions for very short or very long RF applications exist [8]. However for the general case, the Bloch equations have to be discretized and solved numerically.

# 3 Bloch simulation

## Contents

---

<b>3.1 Neglected relaxation</b>	<b>17</b>
3.1.1 Small tip angle approximation	17
3.1.2 Rotation in the magnetization domain	18
3.1.3 Rotation in the spin domain	21
<b>3.2 Including relaxation</b>	<b>23</b>

---

This section presents different strategies to solve the Bloch equations introduced in Section 2.5 and gives a brief overview of the most basic physical concepts behind them.

The Bloch equations, see Eq. 2.32, are a system of coupled bilinear differential equations for which in general it is impossible to find closed form solutions [53]–[55]. Analytical solutions therefore exist only under special assumptions, for instance no external  $B_1$  field [56], a constant  $B_1$  field [57], steady-state solutions or weak RF fields [8], [53]. Since solving the Bloch equations with arbitrary time varying external fields is important for simulations and the design of slice selective MR experiments, the Bloch equations are therefore typically solved numerically [55]. For this, both, the time and  $B$  fields are discretized and the magnetization is computed iteratively for each time-point solving an initial value problem by numerical integration [58]. Numerical integration can be done in different ways, for instance using implicate or explicite single step methods like a higher order Runge-Kutta or multi-step methods [59]. Alternatively, the Bloch integration can be approximated by means of rotation matrices and an exponential scaling to incorporate relaxation effects [60]–[63]. It should be noted, that for neglected relaxation terms, a series of piecewise constant fields can be exactly solved numerically by rotation matrices. The effects of gradients, RF pulses and relaxation with respect to MR echo generation can be further simulated using extended phase graphs [64].

### 3.1 Neglected relaxation

The Bloch equations without relaxation effects are defined by a crossproduct of the magnetization  $M$  and the external field  $B$ , see Eq. 2.15. In matrix vector notation the Bloch equations with neglected relaxation effects in the rotating frame are given by

$$\begin{cases} \frac{dM(t,r)}{dt} = \begin{pmatrix} 0 & \gamma[G_s(t) \cdot r] & -\gamma B_{1,y}(t) \\ -\gamma[G_s(t) \cdot r] & 0 & \gamma B_{1,x}(t) \\ \gamma B_{1,y}(t) & -\gamma B_{1,x}(t) & 0 \end{pmatrix} M(t,r), \\ M(0) = M^0, \end{cases} \quad (3.1)$$

with the main field  $B_0$ , the time dependent complex RF pulse components  $B_{1,x}(t)$  and  $B_{1,y}(t)$ , the time dependent and spatial varying slice selective gradient  $G_s(t) \cdot r$  for the spatial location  $r = (x, y, z)^T$  and the gyromagnetic ratio  $\gamma$ . Eq. 3.1 can be solved by further assumption of the small tip angle approximation or by means of rotation matrices for piecewise constant external fields.

#### 3.1.1 Small tip angle approximation

The approximative solution of  $\sin\phi \approx \phi$  for small angles  $\phi$  allows the assumption that a small tip of the magnetization has only a minor effect on the  $z$  component of the magnetization  $M(t)$  [23], [43]. This means that  $M_z(t)$  is approximately equal to the bulk magnetization  $M_0$  and that it does not change over time [18]

$$\frac{dM_z(t)}{dt} = 0. \quad (3.2)$$

Using the complex notation of the transverse magnetization  $M_{xy}$ , see Eq. 2.38, the Bloch equations reduce to a single differential equation

$$\frac{dM_{xy}(t,r)}{dt} = -i\gamma[G_s(t) \cdot r]M_{xy}(t,r) + i\gamma B_1(t)M_z^0(r), \quad (3.3)$$

with  $B_1(t) = B_{1,x}(t) + iB_{1,y}(t)$  and the time constant longitudinal magnetization  $M_z(t,r) = M_0(r)$ . Using the initial condition  $M_{xy}(0,r) = 0$  the general solution of Eq. 3.3 at the end of the RF pulse  $T$  is given by

$$M_{xy}(T,r) = iM_0(r) \int_0^T \gamma B_1(t) e^{-i\gamma r \cdot \int_t^s G_s(s) ds} dt. \quad (3.4)$$

### 3 Bloch simulation

with time dependent RF and slice selective gradient fields. The excitation k-space formulation [43] with  $k(t)$  being the spatial frequency variable

$$k(t) = -\gamma \int_t^T G_s(s) ds. \quad (3.5)$$

allows further reduction of Eq. 3.4 to

$$M_{xy}(T, r) = iM_0(r) \int_0^T \gamma B_1(t) e^{ir \cdot k(t)} dt, \quad (3.6)$$

that can be solved with the Fourier transform. For a more extensive discussion refer to [43]. This further implies that for small flip angles the RF shape of the can be designed with the Fourier transform for a prescribed desired slice profile, see Section 5.

#### 3.1.2 Rotation in the magnetization domain

An on-resonant and constant RF pulse with a nominal flip angle  $\phi$  and a pulse duration  $T = \tau$ , see Section 2.3 and Eq. 2.26, results in a rotation of the magnetization. A rotation of a vector can be expressed by simple rotation matrices

$$\begin{aligned} R_x(\phi) &= \begin{pmatrix} 1 & 0 & 0 \\ 0 & \cos \phi & \sin \phi \\ 0 & -\sin \phi & \cos \phi \end{pmatrix}, \\ R_y(\phi) &= \begin{pmatrix} \cos \phi & 0 & -\sin \phi \\ 0 & 1 & 0 \\ \sin \phi & 0 & \cos \phi \end{pmatrix}, \\ R_z(\phi) &= \begin{pmatrix} \cos \phi & \sin \phi & 0 \\ -\sin \phi & \cos \phi & 0 \\ 0 & 0 & 1 \end{pmatrix}, \end{aligned} \quad (3.7)$$

describing the rotation around the  $x$ -,  $y$ - or  $z$ -axis with an angle  $\phi$ . An equidistant discretization of the pulse duration interval  $[0, T]$  results in piecewise constant external fields  $B$  that can be solved in each time step analogous to rectangular block pulses. The temporal discretization is defined as

$$0 = t_0 < \dots < t_{N-1} = T. \quad (3.8)$$

### 3 Bloch simulation

with the equidistant temporal step size  $\tau = t_{m+1} - t_m$  and  $N$  being the number of time steps. The impact on the magnetization for a pure rotation with a flip angle  $\phi$  around the  $x$ -axis can be easily computed with

$$M_{m+1} = R_x(\phi)M_m(t). \quad (3.9)$$

The effect of a complex RF pulse in the  $xy$  plane with a flip angle  $\phi$  and a phase angle  $\theta$  can be described by a cascade of three spin rotations [53], [60], [62]

$$M_{m+1} = R_z(\theta)R_x(\phi)R_z(-\theta)M_m(t). \quad (3.10)$$

This can be generalized for the inclusion of local field differences and the rotation around an arbitrary axis. For this purpose, the magnetization is transformed to the new coordinate system followed by the rotation and a transformation back to the original coordinate system

$$M_{m+1} = R_z(\theta)R_y(\phi_y)R_x(\phi_x)R_y(-\phi_y)R_z(-\theta)M_m(t), \quad (3.11)$$

with the effective flip angle

$$\begin{aligned} \phi_x &= -\tau \sqrt{(\Delta\omega)^2 + (\phi/\tau)^2}, \\ \phi_y &= \tan^{-1} \Delta\omega\tau/\phi, \end{aligned} \quad (3.12)$$

using the desired flip angle  $\phi$ , the duration  $\tau$  and the local frequency offset

$$\Delta\omega(x, y, z, t) = 2\pi\gamma[B_0 - B(x, y, z, t)]. \quad (3.13)$$

Alternatively, the field contributions  $B$  for one time step can be summarized and expressed by a single rotation matrix  $R$ . The rotation by an angle  $\phi$  about any arbitrary unit vector  $n = (n_x, n_y, n_z)^T$  is represented by

$$R(\phi) = \begin{pmatrix} \cos\phi + n_x^2(1 - \cos\phi) & n_x n_y(1 - \cos\phi) - n_z \sin\phi & n_x n_z(1 - \cos\phi) + n_y \sin\phi \\ n_y n_x(1 - \cos\phi) + n_z \sin\phi & \cos\phi + n_y^2(1 - \cos\phi) & n_y n_z(1 - \cos\phi) + n_x \sin\phi \\ n_z n_x(1 - \cos\phi) - n_y \sin\phi & n_z n_y(1 - \cos\phi) + n_x \sin\phi & \cos\phi + n_z^2(1 - \cos\phi) \end{pmatrix} \quad (3.14)$$

where  $n_x^2 + n_y^2 + n_z^2 = 1$  has to be satisfied [65]. For each time point  $m$  the angle  $\phi_m$  and the vector  $n_m$  are defined by

$$\begin{aligned} \phi_m &= -\gamma\tau \sqrt{|B_{1,m}|^2 + G_m \cdot r} \\ n_m &= \frac{\gamma\tau}{|\phi_m|} (B_{1,x,m}, B_{1,y,m}, G_m \cdot r)^T, \end{aligned} \quad (3.15)$$

### 3 Bloch simulation

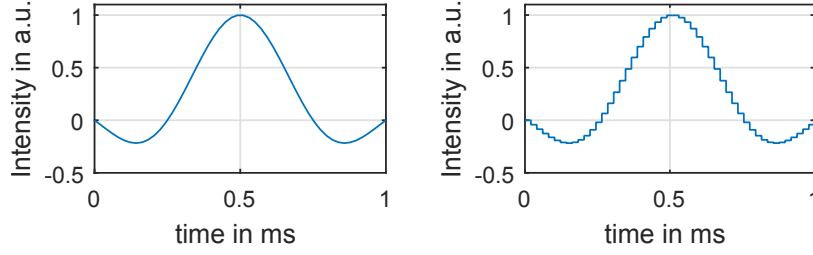


Figure 3.1: Graphical depiction of a SINC based RF waveform with continuous (left) and discretized and piecewise constant (right) representation.

with the time step  $\tau$  and the piecewise constant RF and gradient amplitudes  $B_{1,m}$  and  $G_m$  at spatial position  $r$ .

To simulate a series of piecewise constant  $B$  fields, for instance discrete RF and slice selective gradient waveforms, a consecutive application of rotation matrices can be used. The temporal evolution of the magnetization is then a series of rotation matrices acting on the initial magnetization  $M^0$ , see Eq. 2.16,

$$M(T) = R_N R_{N-1} \dots R_1 M^0. \quad (3.16)$$

The assumption of piecewise constant fields is a good approximation of how RF and slice selective gradient waveforms are implemented on MR scanners, see Section 4 and [66]. This results in a series of block functions as visualized in Figure 3.1.

In contrast to computing the effective external field for each time point, a sequential application of instant RF rotations and gradient precession yields a straightforward solution. This is also known as hard pulse approximation. Pure precession as an effect of spatially selective gradients can be modeled with rotation matrices as well. The phase angle  $\theta_{G_s}$  of the slice selective gradient  $G_s(t)$ , see Eq. 2.20, can be computed with

$$\theta_{G_s}(r) = \gamma r \int_t^{t+\tau} G_s(\tau) d\tau, \quad (3.17)$$

and plugged into the rotation matrix around the  $z$ -axis. The effect of the rectangular external fields is then split into gradient rotation around the  $z$ -axis and RF rotation around an axis in the  $xy$ -plane. The full cascade is now given by

$$M_{m+1} = R_z(\theta_{G_s}) R_z(\theta) R_y(\phi_y) R_x(\phi_x) R_y(-\phi_y) R_z(-\theta) M_m(t). \quad (3.18)$$

If there are more than one gradient dimensions active, Eq. 3.17, has to be computed for each axis, see Eq. 2.40. Field inhomogeneities can be treated accordingly. The concept

### 3 Bloch simulation

of orthogonal rotation matrices for a three dimensional rotation in the magnetization domain can be equivalently described by rotations in other domains.

#### 3.1.3 Rotation in the spin domain

In contrast to a rotation of an orthonormal magnetization vector ( $SO_3$ ), the same rotation can be described by a unitary rotation ( $SU_2$ ) in the spin domain [66], [67]. Equivalent to a rotation of a  $3 \times 1$  vector  $M$  by a  $3 \times 3$  rotation matrix  $R$

$$M_{m+1} = RM_m \quad (3.19)$$

there exists a unitary rotation of a spinor  $\Psi = (\alpha, \beta)^T$

$$\Psi_{m+1} = Q\Psi_m \quad (3.20)$$

with the complex Cayley-Klein parameters  $\alpha$ ,  $\beta$  and the unitary rotation matrix  $Q$ . The spin domain description of  $Q$  is connected with the Pauli spin matrices

$$\sigma_x = \begin{pmatrix} 0 & 1 \\ 1 & 0 \end{pmatrix}, \quad \sigma_y = \begin{pmatrix} 0 & -i \\ i & 0 \end{pmatrix}, \quad \sigma_z = \begin{pmatrix} 1 & 0 \\ 0 & -1 \end{pmatrix}, \quad (3.21)$$

to axis and magnitude of the corresponding rotation. The rotation by an angle  $\phi$  about a vector  $n = (n_x, n_y, n_z)^T$  is represented by

$$\begin{aligned} Q &= \begin{pmatrix} \cos\phi/2 - in_z \sin\phi/2 & -i(n_x - in_y) \sin\phi/2 \\ -i(n_x + in_y) \sin\phi/2 & \cos\phi/2 + in_z \sin\phi/2 \end{pmatrix} \\ &= \begin{pmatrix} \alpha & -\beta^* \\ \beta & \alpha^* \end{pmatrix}, \end{aligned} \quad (3.22)$$

with the complex valued Cayley-Klein parameters

$$\begin{aligned} \alpha &= \cos(\phi/2) - in_z \sin(\phi/2), \\ \beta &= -i(n_x + in_y) \sin(\phi/2), \end{aligned} \quad (3.23)$$

satisfying the constraint  $\alpha\alpha^* + \beta\beta^* = 1$ .

The Cayley-Klein parameters for each time step  $m$  are  $a_m$  and  $b_m$  and can be computed by

$$\begin{aligned} a_m &= \cos(\phi_m/2) - in_{z,m} \sin(\phi_m/2), \\ b_m &= -i(n_{x,m} + in_{y,m}) \sin(\phi_m/2). \end{aligned} \quad (3.24)$$

### 3 Bloch simulation

with the unitary rotation matrix

$$Q_m = \begin{pmatrix} a_m & -b_m^* \\ b_m & a_m^* \end{pmatrix} \quad (3.25)$$

by means of Cayley-Klein parameters. The total rotation is then given by

$$Q = Q_N Q_{N-1} \dots Q_1. \quad (3.26)$$

The redundancy in Eq 3.25 allows to replace the matrix product in Eq. 3.26 by a matrix vector product

$$\begin{pmatrix} \alpha_m \\ \beta_m \end{pmatrix} = Q_m \begin{pmatrix} \alpha_{m-1} \\ \beta_{m-1} \end{pmatrix} \quad (3.27)$$

to compute the accumulated rotation for each time step with the general initial spinor  $\Psi_0$ . The initial  $\Psi_0$  can be found assuming no rotation  $\phi = 0$  and an initial magnetization along the z-axis  $n = (0, 0, 1)^T$  resulting in

$$\Psi_0 = \begin{pmatrix} a_0 \\ b_0 \end{pmatrix} = \begin{pmatrix} 1 \\ 0 \end{pmatrix}. \quad (3.28)$$

The Pauli matrices can be further used to compute the magnetization components for a given spinor  $\Psi$  with

$$M_x = \Psi^* \sigma_x \Psi, \quad M_y = \Psi^* \sigma_y \Psi, \quad M_z = \Psi^* \sigma_z \Psi. \quad (3.29)$$

Alternatively, this can be done for the transversal magnetization defining

$$M_{xy} = \Psi^* (\sigma_x + i\sigma_y) \Psi. \quad (3.30)$$

The final Cayley-Klein parameters  $\alpha$  and  $\beta$  can be then used to describe the overall impact on an arbitrary initial magnetization in the axial representation by

$$\begin{pmatrix} M_{xy}(+) \\ M_{xy}^*(+) \\ M_z(+) \end{pmatrix} = \begin{pmatrix} (\alpha^*)^2 & -\beta^2 & 2\alpha^*\beta \\ -(\beta^*)^2 & \alpha^2 & 2\alpha\beta^* \\ -(\alpha\beta)^* & -(\alpha\beta) & \alpha\alpha^* - \beta\beta^* \end{pmatrix} \begin{pmatrix} M_{xy}(-) \\ M_{xy}^*(-) \\ M_z(-) \end{pmatrix}, \quad (3.31)$$

with  $M_{xy}$  being the transversal magnetization and  $M_{xy}^*$  being the complex conjugate transversal magnetization before  $(-)$  and after  $(+)$  the rotation. Besides mathematical simplifications (only 1 constraint in SU2 compared to 6 constraints in SO3) [23] the rotation in the spin domain allows an elegant description of important RF cases such as excitation, inversion and refocusing by means of  $\alpha$  and  $\beta$ . For instance, the refocusing profile for an initial magnetization  $M = (0, M_0, 0)^T$  can be described by  $M_{xy} = iM_0[(\alpha^*)^2 + \beta^2]$  (without crushers) or  $M_{xy} = iM_0\beta^2$  (assuming perfect

### 3 Bloch simulation

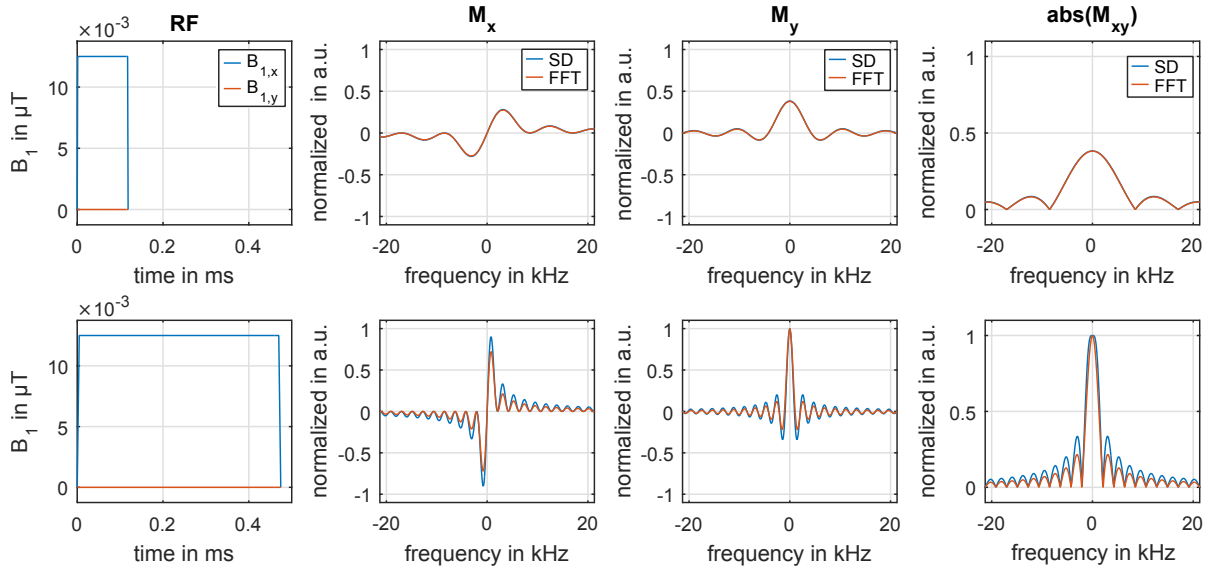


Figure 3.2: Block RF pulses (Row 1:  $\pi/8$  and Row 2:  $\pi/2$  with the Fourier transform (FFT) and spin domain (SD) solution using rotation matrices. For neglected relaxation the solution of the SD rotation matrices is numerical exact.

crushers). See Chapter 5.1 and Table 5.1 for more parameter relations and [23], [66] for a more rigorous derivation.

Figure 3.2 compares the results of the Fourier transform with the results of the rotation matrices in the spin domain for two rectangular RF pulses ( $\pi/8$  and  $\pi/2$ ). While both results of the low flip angle pulse are valid, the Fourier relation fails for larger tip angles where the magnetization clearly changes. Then, an error between the Fourier transform approximation and the Bloch equations occurs. Nevertheless, the RF design up to roughly  $60^\circ$  works surprisingly good.

## 3.2 Including relaxation

The fully time dependent Bloch equations (Eq. 2.41) including relaxation effects are a coupled system of linear differential equations with non-constant coefficients. Again, an analytical solution only exists for special cases, see Section 2.5 and [8], [10]. Assuming piecewise constant RF and gradient fields, the Bloch equations, see Eq. 2.41, reduce to a coupled system of linear differential equations with constant coefficients at each temporal point. For such differential systems exact analytical and approximative numerical solutions can be found.

### 3 Bloch simulation

The Bloch equations in the rotating frame are given by Eq. 2.33. For piecewise constant external fields the Bloch equations are now a set of differential equations with constant coefficients in each time point. If the system matrix  $A$  further becomes a diagonalizable matrix, a calculation of the analytical solution in each time step  $\tau$  would result in

$$M(t) = (M^{m-1} + A_m^{-1}b)e^{A_m t} - A_m^{-1}b, \quad (3.32)$$

with  $M^{m-1}$  being the solution of the previous time step or the initial condition  $M^0$  and  $A_m$  being the piecewise constant system matrices for the uniformly discretized time interval [68], [69]. There are numerous ways to calculate the matrix exponential  $e^{A_m t}$ , refer to [70]. However, if  $A$  is not diagonalizable, the matrix exponential can not be computed analytically. To overcome this hurdle, the piecewise constant Bloch equations can be solved using a case analysis to find an exact analytical solution by computing the eigenvalues and eigenvectors for each time step. Different cases arise from the calculation of the eigenvalues using Cardano's formula. The homogeneous solutions are solved analytically for the different cases adding the constant, and in all cases the same, particular solution yielding the full solution of the differential equations. This analytical approach results in an exact solution of the Bloch equations for piecewise constant  $B$  fields. For more details the reader is refer to [68].

Another approach to solve ordinary differential equations is to compute a numerical solution. Besides potential numerical stability problems, the use of numerical single and multi-step methods is associated with numerical errors. The ordinary Bloch equations  $dM/dt = f(t, M)$  can be solved with a direct application of the backward Euler method to update the magnetization for each discrete time point  $\tau$  with an approximated integration of the differential equations by the rectangle method. In combination with the Bloch equations however, the backward Euler was shown to be not energy conserving thus resulting in loss of magnetization over time. Therefore it should not be used for simulation purposes [68].

A higher order approximation of the integration can be achieved by a combination of implicit and explicit Euler schemes which results in the Crank-Nicolson method. Its approximation is based on the trapezoidal rule and has a second order convergence in time. Compared to backward Euler, the Crank-Nicolson method is energy conserving and can be used for an efficient numerical Bloch simulation. In the context of high off-resonance terms it should be noted that this method leads to numerical phase errors of the transversal magnetization [68], [71]. A higher order numerical solution can be computed using different Runge-Kutta integration methods that reduce the numerical error, but lead to significantly higher computation times.

Alternatively, the full Bloch equations can be approximated by an alternating series of rotation matrices followed by exponential scaling to model relaxation effects according

### 3 Bloch simulation

to [53], [60], [62], [72]. The relaxation effects are typically incorporated by a diagonal matrix with exponential dampening factors resulting in

$$R_{relax}(T_1, T_2) = \begin{pmatrix} e^{-\tau/T_2} & 0 & 0 \\ 0 & e^{-\tau/T_2} & 0 \\ 0 & 0 & 1 - e^{-\tau/T_1} \end{pmatrix}, \quad (3.33)$$

describing the pure relaxation due to  $T_1$  and  $T_2$  for the duration  $\tau$ . Together with the rotation matrices, introduced in Section 3.1, the evolution of the magnetization vector for a short time period  $\tau$  with constant external fields can be described by

$$M_{m+1} = R_{relax}(T_1, T_2)R(B)M_m. \quad (3.34)$$

A more extensive derivation of the different matrices is given in [53]. It should be noted, that in contrast to the above introduced model that splits relaxation and rotation, relaxations happens simultaneously with the rotation on the magnetization. Therefore, the use of separate rotation matrices is always associated with a splitting error. This error can be reduced by finer temporal discretisation or a more sophisticated splitting scheme, for instance a symmetric or higher order splitting compared to the asymmetric splitting scheme presented in [53], [60], [62]. The analysis of different numerical and analytical Bloch solvers was investigated in [68].

## 4 MR hardware and practical aspects

### Contents

---

4.1	Experimental design . . . . .	27
4.2	Pulse sequence programming . . . . .	31
4.3	RF pulse and slice selective gradient limitations . . . . .	32

---

Although there is a wide range of NMR and MRI applications such as material research [73]–[75], pre-clinical animal [76]–[80] or in vivo human imaging [81]–[84], the fundamental hardware systems are very similar. A typical MR setting consists of a very strong static magnetic field, shim coils to increase the spatial field homogeneity, field gradient coils (optional for NMR) to perform spatial encoding, transmit/receive RF coils and transmit/receive electronics [41].

Despite similar principles, a huge range of system relevant parameters require highly specialized MR hardware [41], [85]. For instance, the field strength of the main magnet ranges from 0 T [86] up to 10.5 T (in vivo MRI [21]), 45 T (DC NMR) or even 100 T (pulsed NMR) [87]–[89]). Further, different bore diameters range from several mm (NMR) up to 700 mm (in vivo MRI) for closed-bore systems or alternatively short-bore or open-bore scanners [90], [91] impact the homogeneity and system performance. Typical hardware parameters for each of the three MR modalities are summarized in Table 4.1 [41]. In the following section, the focus is placed on human in vivo MR systems whose system specifications are mainly limited by the larger volume and field of view required to image whole body parts [41]. Specifically, the experimental results shown in Section 5 are designed for 3 T human MR systems with the hardware specifications listed in Table 4.2. The RF pulse design methods presented in Section 5, can be easily adapted for other hardware specifications by changing the specific hardware constraints to the desired system properties.

In addition to the hardware constraints listed in Tables 4.1 and 4.2 there are further and less obvious hardware limitations that impact digitally sampled RF and gradient waveforms. The digital waveforms have to be converted to analogue signals and be

## 4 MR hardware and practical aspects

Table 4.1: Characteristics of the magnet, gradients, and RF coils in commercial systems, adapted and modified from [41].

	NMR	MRI animal	MRI human
$B_0$ in T	4.7 – 23.5	4.7 – 45	1.5 – 10.5
$\omega_0$ in MHz	200 – 1900	200–900	63.8–450
$G_{max}$ in $\text{mT m}^{-1}$	25000	1000	25 – 300
RF coil diameter in mm	1.3 – 20	10 – 60	100 – 700
RF amplifier power in kW	1	4	0.5 – 35
minimal RF duration in $\mu\text{s}$	1	5 – 10	10 – 50

Table 4.2: Hardware specifications of two 3 T human in vivo Siemens Magnetom MR scanners used for the experimental implemetations presented in [1]–[3] and in the Appendix.

	Skyra-XQ	Prisma-XR
$B_0$ in T	2.89	2.89
$G_{max}$ in $\text{mT m}^{-1}$	43	80
$\dot{G}_{max}$ in $\text{mT m}^{-1} \text{s}^{-1}$	200	200
bore diameter in mm	700	600
RF amplifier power (BC) in kW	29.7	16.2

amplified resulting in non-piecewise constant waveforms. More information on RF and slice selective gradient amplifier imperfections is discussed in Section 4.3.

### 4.1 Experimental design

This chapter describes some typical experiments for the excitation and refocusing of the magnetization in MRI. For the practical assessment of designed RF pulses the interaction with the involved hardware components are of great importance and should be also considered. Proton signals proportional to the net magnetization and the relaxation times can be acquired after tilting the net magnetization from its equilibrium state by an RF pulse close to the Larmor frequency. The precession of the tilted magnetization around the main magnetic field emits a measurable RF pulse with the Larmor frequency. Based on first insights by Bloch [9], Purcell [92] and Bloembergen [93] with continuous wave NMR experiments this phenomenon was investigated in Hahn’s experiment with pulsed NMR techniques [94] resulting in the first FID sequence. For MR imaging, we are additionally interested in the

## 4 MR hardware and practical aspects

spatial origin of the NMR signal, which requires a spatial encoding. This encoding can be separated into slice selection and an additional in-plane encoding [8], [23], [50], [51].

In general, tipping the magnetization out of equilibrium results in an electromagnetic induction of a signal in the receiver coil. Receiver coils have to be placed perpendicular to the main magnetic field along the  $z$ -axis and the induced signal is recorded as the sum of the transversal magnetization of all spins in the range of the receiver coil. The easiest MR sequence is therefore the generation of a FID. After the excitation RF pulse is turned off, the induced time-domain signal is digitalized and a Fourier transform can be applied to compute the NMR spectrum. Assuming an ideal RF receiver with no noise and uniform receive sensitivity, the received and with the Lamor frequency  $\omega_0$  demodulated signal and neglected relaxation terms is given by

$$s(t) = \iiint M_{xy}(r, 0) e^{-\theta(r,t)} dr, \quad (4.1)$$

with  $\theta(r, t) = -\int_0^t \Delta\omega(r, t') dt'$  being the accumulated phase of the intended or unwanted inhomogeneous  $B_0$  field. The spatial location is summarized by  $r = (x, y, z)^T$ . For the non-selective case where no gradient is present, the static field is assumed to be homogeneous, thus resulting in no spatial phase differences. In reality, the FID signal decays with  $T_2^*$  since field inhomogeneities increase the dephasing of the transversal magnetization [31]. The static field inhomogeneities summarized by  $T_2'$  can be corrected by a second RF pulse applied to form a SE [94].

Spatial selection is achieved by a combination of frequency selective RF pulses and slice selective gradient shapes. This has the advantage, that only spins in a certain slice or multi-dimensional object are tipped and therefore contribute to the overall signal, while other spins remain unchanged due to spatial off resonance. This enables sequential multiplexing of the slice selective acquisition to increase temporal efficiency and to design sequential multi-slice sequences. This should however not be confused with the SMS approach [95]. The frequency selectivity or bandwidth of RF pulses is used in combination with spatially dependent slice selective gradients to map the frequency to distinct spatial positions by a variation of the magnetic field and the Lamor frequency, see Eq. 2.5. This relation can be easily described by

$$G_s = \frac{2\pi\Delta f}{\gamma\Delta z}, \quad (4.2)$$

to find the required amplitude of a constant slice selective gradient  $G_s$  in  $\text{mT m}^{-1}$  to map the bandwidth  $\Delta f$  to the spatial thickness  $\Delta z$ . The design of the slice selective gradient therefore would ideally result in rectangular waveforms. Besides the maximal

## 4 MR hardware and practical aspects

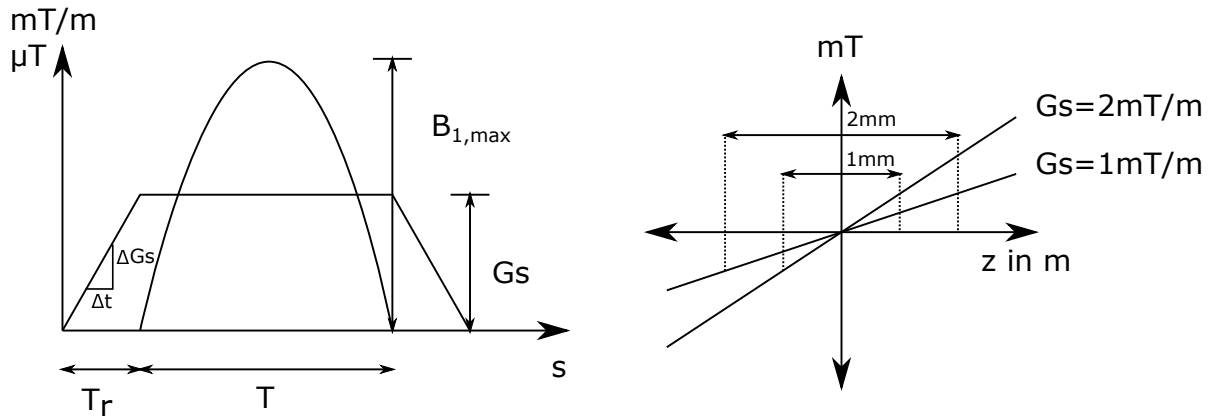


Figure 4.1: Schematic RF and slice selective gradient shapes with ramp-up and ramp-down periods ( $T_r$ ) together with amplitude constraints  $B_{1,max}$  and  $G_s$  (left) and the relation of the ideal spatial extension of the slice selective gradient amplitude  $G_s$ .

gradient strength  $G_{s,max}$  the slew rate of the slice selective gradient  $\dot{G}_s = \Delta G_s / \tau$  limits the minimal achievable rise time  $T_r$ , see Tables 4.2, 4.1. The additional ramp up and ramp down segments result in trapezoidal gradient shapes and extend the minimal echo time (TE). Figure 4.1 visualizes a typical trapezoidal slice selective gradient and the scaling of the frequency selectivity. It should be noted, that a scaling of the slice selective gradient may violate the slew rate constraint and the rise time may have to be increased. Figure 4.1 assumes that there is a linear slice selective gradient over the whole spatial domain. In reality the linearity is violated which results in a mismatch of the spatial encoding during RF application in the context of off-isocenter or SMS imaging and in k-space encoding [39].

The spatial in-plane encoding is typically done after the RF pulse application and can be assumed to be independent of the RF excitation. Similar to slice selection, spatially dependent gradients change the phase of the spins as a function of their location with respect to the isocenter. This phase difference efficiently encodes a multidimensional dataset which can be transformed back to the spatial domain by using the Fourier transform according to the k-space formalism. There are numerous different strategies to acquire k-space data [52], [96], [97] realized by MRI sequences. These MRI sequences can be adapted for different sequence parameters, including TE and TR, THK, k-space and image matrix size, or read-out bandwidth and typically consist of a sequence kernel that is repeated with different spatial encoding. Figure 4.2 shows a schematic sequence diagram of the two most basic MR sequence kernels to acquire a simple GRE and SE images. Based on the fundamental ideas of GRE and SE there are numerous multi-shot sequence variants to increase the acquisition efficiency, for instance FLASH [98], SSFP [99] or TSE/RARE [100]. Additionally there are single shot techniques such as EPI [101], [102] or HASTE [103] to acquire the

## 4 MR hardware and practical aspects

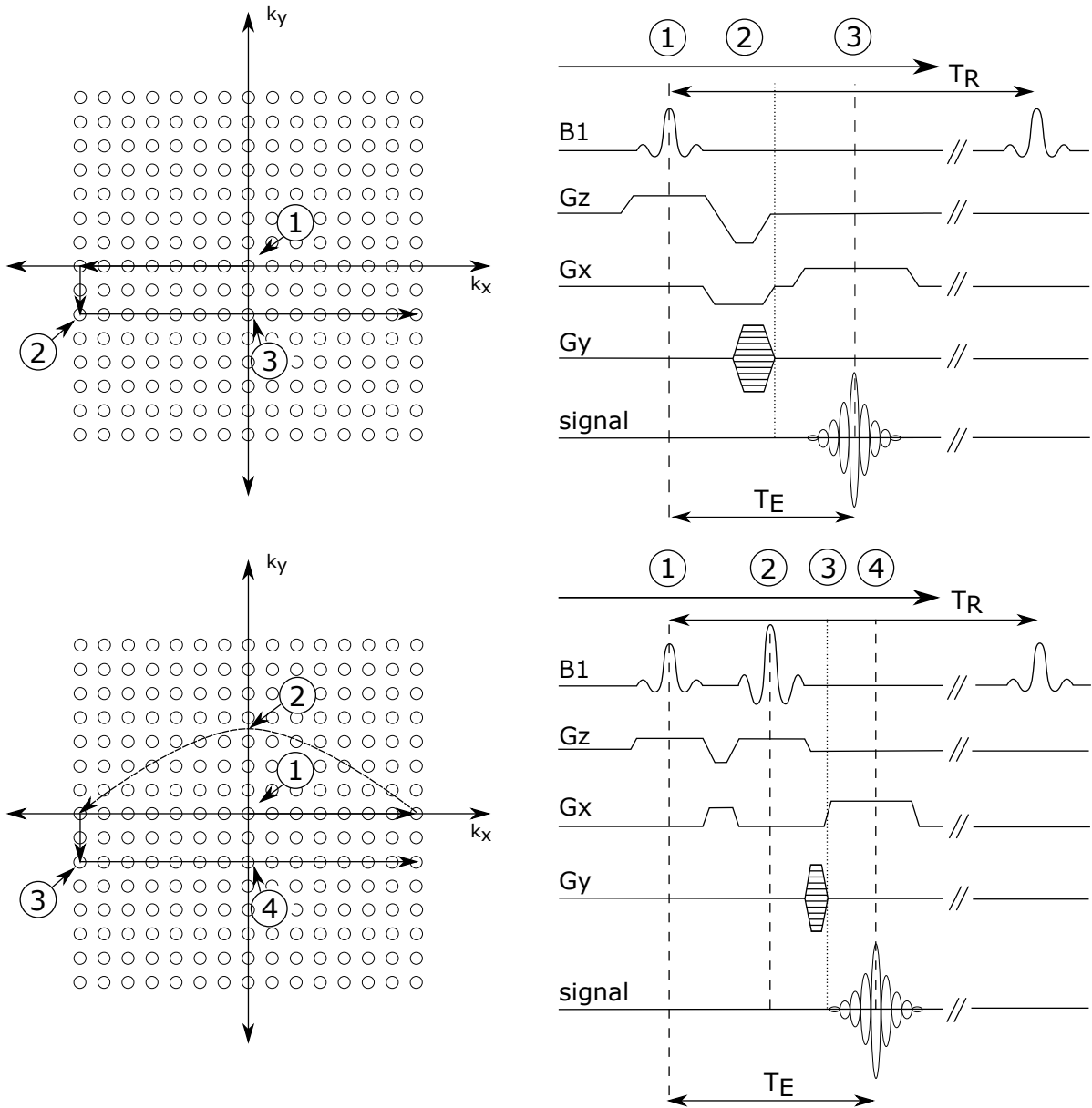


Figure 4.2: Schematic GRE (first row) and SE generation (second row) with the corresponding k-space acquisition scheme. Figure idea from [85].

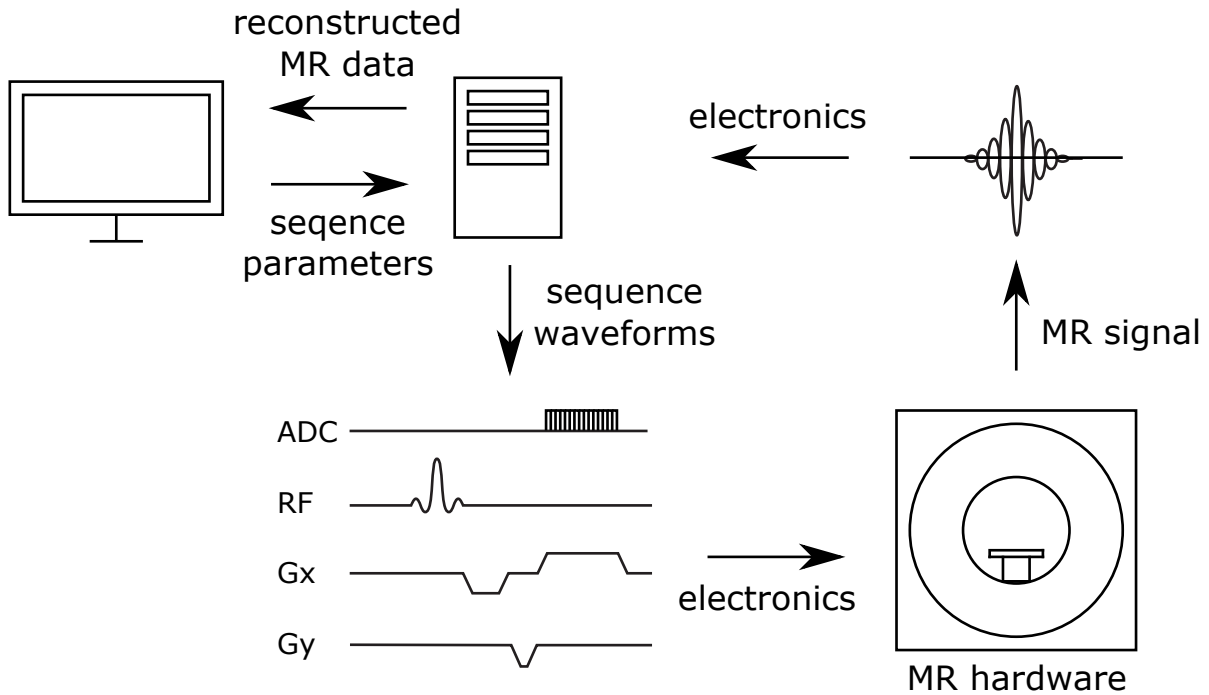


Figure 4.3: Schematic block diagram of the MR experiment.

whole k-space and intermediate techniques, for instance segmented EPI [104] or TSE and GRE combinations such as GRASE [105] to acquire large k-space parts. For a more comprehensive discussion the reader is refer to [23].

## 4.2 Pulse sequence programming

To perform MR experiments, different hardware parts have to be controlled in a highly synchronized and exact manner over a large range of signal frequencies and signal intensities. Commercial MR systems therefore have pre-compiled MR sequences based on C or C++ source code that can be set and modified via a graphical user interface. The sequence parameters are translated to create time courses or waveforms for the different MR hardware parts and are checked for validity prior to the experiment. These discrete waveforms are converted and amplified by electronic circuits and connected to the transmit/receive RF and gradient coils respectively. A schematic overview of MR experiments is depicted in Figure 4.3 showing the interaction of the sequence waveforms, MR hardware, signal acquisition and reconstruction to visualize the acquired MR data. Besides software checks that may be circumvented by exploitive programming, there are further experimental checks during runtime (SAR

## 4 MR hardware and practical aspects

and gradient watchdog) to prevent a possible violation of safety or hardware limits. The most common and relevant ones are listed in Table 4.3 for two MR systems.

MR vendors give researchers the opportunity to set up and test their own source code which in general allows design of custom sequences and acquisition of preliminary data, or to check simulations with different timings using custom RF pulse or slice selective gradient shapes. The sequence programming environments and available source codes differ a lot between the different vendors and although most vendors argue that they offer an open source software environment, in practice their source code is only available after signing specific research agreements which limits the ability for rapid prototyping. Even with access to the source codes, the complexity of the code and the sensitive software environments in combination with very limited documentation and debugging capabilities often results in large time delays. Recently, an open source framework for the development and execution of MR pulse sequences (<https://pulseseq.github.io/>) was proposed to overcome these hurdles. This tool reads an open source file format and allows interpretation of MR sequences created in MATLAB (The MathWorks, Inc., Natick, Massachusetts, United States) with the open source MRI simulation (JEMRIS, <http://www.jemris.org/>, [58]).

The later presented numerically designed RF and slice selective gradient shapes are experimentally validated with GRE and SE MR sequences on two 3 T MR scanners (Magnetom Skyra-XQ and Magnetom Prisma-XR, Siemens Healthcare, Erlangen, Germany). For this purpose, the C++ source codes (software versions IDEA VD13A and VE11C) were modified to read external RF pulses and slice selective gradient shapes and the encoding was changed to measure the slice selection direction. The following paragraph therefore focuses only on the vendor and scanner specific limitations.

### 4.3 RF pulse and slice selective gradient limitations

The layout of the RF and selective gradient shapes is relatively simple and excellently fit to the assumption of piecewise constant  $B$ -fields, see Section 5. The discrete waveforms, including RF and gradient shapes, are evaluated and matched to a common time grid defined by the minimal raster time (10  $\mu$ s for the used MR system, see Table 4.3). For single transmit systems, the RF pulse shape can be defined by a sequence of complex piecewise constant blocks with a distinct magnitude and phase. Figure 4.4 shows an optimal SMS RF pulse and slice selective gradient shape [3] normalized to additionally fulfill the software constraints shown in Table 4.3.

#### 4 MR hardware and practical aspects

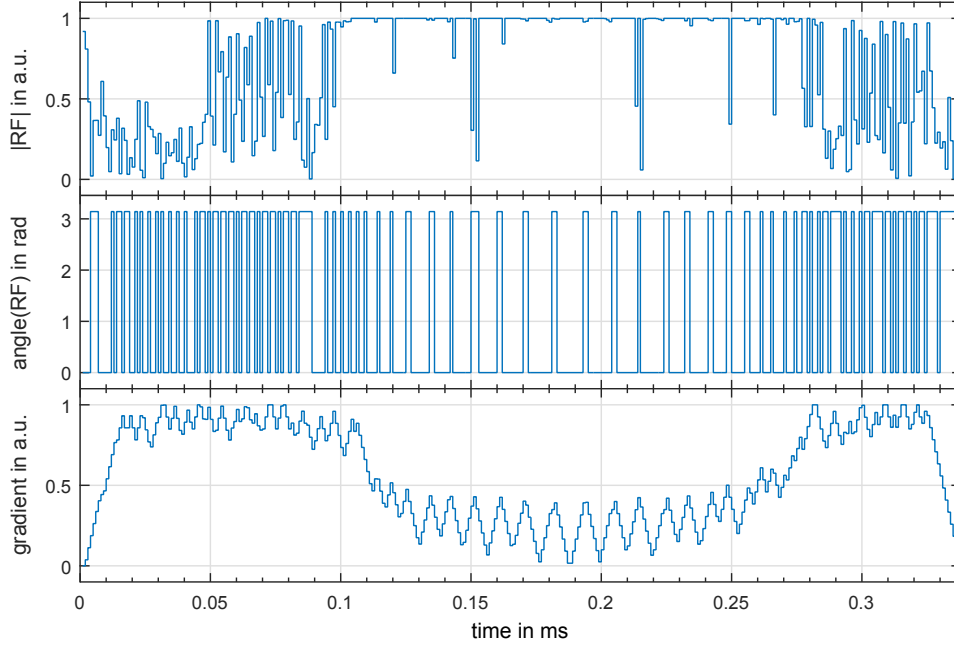


Figure 4.4: Optimal SMS RF pulse (Row 1 shows the magnitude and Row 2 the phase) and slice selective gradient shape used for the experimental validation in [3].

Conventional RF pulses are typically computed at runtime by evaluation of analytical functions, for instance Hamming filtered SINC or Gauss functions, see Section 5, for a desired pulse duration, number of sample points and RF bandwidth.

The discrete RF pulse shapes are scaled at runtime depending on the normalized RF pulse amplitude integral  $A_{RF}$ , pulse duration  $T$ , desired flip angle  $\phi$  and temporal discretization to compensate coil loading effects. The amplitude integral  $A_{RF}$  is defined as

$$A_{RF} = \sqrt{\left(\sum_{m=1}^N r_m \cos \theta_m\right)^2 + \left(\sum_{m=1}^N r_m \sin \theta_m\right)^2}, \quad (4.3)$$

where  $N$  is the number of sample points,  $r_m$  is the normalized RF pulse magnitude and  $\theta_m$  is the phase of each time point  $m$ . It should be noted that the Eq. 4.3 is independent of the temporal discretization. The temporal settings are defined together with the desired flip angle by the MR sequence.

The actual RF pulse waveform is amplified at runtime with respect to a reference scan performed at the beginning of each MR experiments. This reference scan calibrates the RF transmitter to achieve a  $180^\circ$  flip angle with a rectangular RF pulse with a duration of  $T = 1$  ms. This calibration step compensates field fluctuations caused by coil loading which depends on the coil, but also on the geometry and material of the

## 4 MR hardware and practical aspects

used phantom or body part [106], [107]. Therefore, numerically designed RF pulses are normalized to 1 and scaled with the experimentally determined reference scan. Special care has to be taken to define consistent discretisation, flip angle and pulse duration in the MR sequence.

For real valued RF pulses the scaling is straight forward and can be done analogous to conventional RF pulses via the RF pulse amplitude integral given in Eq. 4.3. For phase modulated RF pulses, however, for instance SMS pulses with an even number of symmetric slices, the amplitude integral computation, see Eq. 4.3 would become close to zero. This is a result of RF symmetry and would result in a wrong and far too large transmit voltage factor, hence producing a wrong field in coil. This can be compensated by relating  $B_{1,max}$  directly to the reference scan by a manual calculation of the amplitude integral

$$A_{RF,V} = \frac{N\phi}{360T\gamma B_{1,max}}, \quad (4.4)$$

with the number of discrete samples  $N$ , the flip angle  $\phi$  in  $^\circ$ , the pulse duration  $T$ , the gyromagnetic ration  $\gamma$  and the maximal  $B_1$  magnitude  $B_{1,max}$ . Based on the linearity assumptions of the RF amplifier and the reference scan performed in the calibration step before MR data acquisition.

Arbitrary RF pulse shapes (normalized magnitude and phase vector) can be imported to MR sequences in different ways. The most straight forward and safest with respect to reproducibility and validity is a direct numerical import into the sequence source code. This comes with the hurdle that a change of the RF pulse requires a sequence compilation, a lengthy and error-prone step. Higher flexibility can be achieved by storing the RF pulses in external RF pulse containers or supply them in exchangeable external text or binary files that allows to change RF pulses independently to the MR sequence. It should be kept in mind that for Siemens systems RF pulse containers and their shapes are loaded and set up during the booting of the MR scanner. Changing an existing RF pulse during runtime therefore does not change the RF pulse and requires a scanner reboot. The most flexible form for rapid prototyping is the inclusion of external files containing the RF and slice selective gradient vectors. These files can be automatically created with an appropriate header containing additional information such as the amplitude integral, number of sample points or on the timing.

In order to align the RF pulse with other sequence objects, for instance the slice selective gradient or additional phase objects to perform RF spoiling or off-resonant frequency shifts, the start and end-time of the RF pulses have to match the gradient raster time of the MR system (for Siemens: 10  $\mu$ s). The minimal raster time of RF pulses of 25 ns however is much smaller, which would allow to use much finer resolved RF pulses. The piecewise constant normalized slice selective gradient shape

## 4 MR hardware and practical aspects

can be included to the source code analogous to the RF pulse. Figure 4.5 exemplary

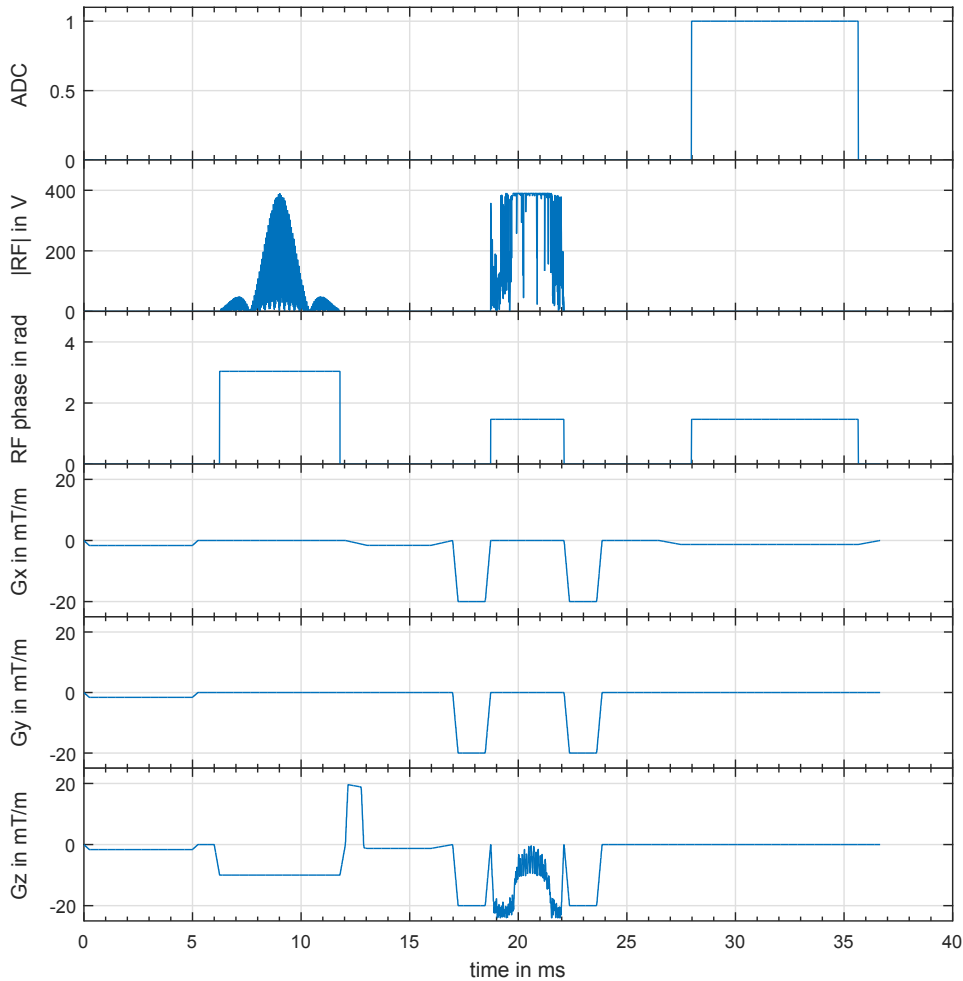


Figure 4.5: Modified SE sequence with the phase encoding in slice direction to directly encode and measure the refocused slices. The diagram shows one k-space line and the optimizedSMS refocusing pulse shown in [3].

shows a modified SMS SE sequence with spoiler gradients before the excitation and crusher gradients before and right after refocusing with a time optimal MB3 RF refocusing pulse, for details see [3]. For displaying purposes only one of the 128 encoding lines is shown. The whole sequence duration is roughly 15.5 s with a readout bandwidth of 130 Hz per pixel and a matrix of  $128 \times 128$  for a FOV of  $300 \times 300$ . It should be noted that the RF pulse is scaled to a virtual reference voltage of 340 V. The actual value in the experiment depends on the used coil and the coil loading.

In contrast to the RF pulse, the normalized slice selective gradient waveform can be directly scaled using the maximal gradient strength. Special care should be given

## 4 MR hardware and practical aspects

not to violate the minimal raster time and the maximal amplitude and slew rate constraints of the slice selective gradient amplifier. These parameters are evaluated before and during the actual MR scan, thus presenting a potential pitfall. The used RF pulse and slice selective gradient shapes have a strong influence on the sequence timing and the validity of the sequence. Therefore, validity should be checked to prevent hardware errors that may result in scanner reboots. There are different limitations that are specific for the software and hardware version and these influence the RF pulse design. Table 4.3 summarizes the most important software and hardware limitations for Siemens IDEA VD13A/VE11C and the Siemens Skyra-XQ 3 T MR scanner used later on. The change of the read-out gradient from the phase encoding

Table 4.3: Overview of the important software and hardware (Skyra-XQ) constraints for MR sequence programming.  $N_s$  denotes the maximal number of discrete sample points,  $r_m$  the normalized RF magnitude,  $\theta_m$  the RF phase,  $G_{s,m}$  the normalized slice selective gradient amplitude,  $\tau_{RF}$  the RF raster time and  $\tau_{G_s}$  the gradient raster time.

software constraints		hardware constraints	
$N_s$	8192	min $\tau_{RF}$	25 ns
$r_m$	0 – 1	min $\tau_{G_s}$	10 $\mu$ s
$\theta_m$	0 – $2\pi$	min RF hold duration	8 $\mu$ s
$G_{s,m}$	-1 – 1	min $G_s$ rise time	5.55 $\mu$ s mT <sup>-1</sup> m <sup>-1</sup>
max $G_s$	24 mT m <sup>-1</sup>	max $G_s$	43 mT m <sup>-1</sup>
max $\dot{G}_s$	180.18 T m <sup>-1</sup> s <sup>-1</sup>	max $\dot{G}_s$	200 T m <sup>-1</sup> s <sup>-1</sup>
min $\tau_{RF}$	25 ns	max RF power	29.7 kW
min $\tau_{G_s}$	10 $\mu$ s	max RF bandwidth	800 kHz

to the slice direction allows measurement and visualization of the excited slices [3]. The result is a phase encoding along the slice direction, thus obtaining the spatial dependent signal.

Besides obvious imperfections such as  $B_0$  and  $B_1$  variations or non-linear gradients across the field of view [23], [25], [108], the time varying RF and slice selective gradient shapes may further deviate from the theoretical waveforms. The slope of the RF and slice selective gradient shapes are implemented as piecewise constant functions, see Section 4.2, which cannot be exactly realized by the amplifiers and coils due to an inherent low pass characteristics. Furthermore, the RF and gradient amplification have different frequency content and power which makes them not directly comparable. For an extensive review the reader is referred to [109] for RF and [39] for gradient amplification.

The discrete RF signals are converted into analogue signals and modulate the amplified RF-transmitter signal in order to create RF fields in the  $\mu$ T range. For human in

vivo MR systems the RF power lies in the range of 0.5 – 35 kW [109]. RF amplifier imperfections may alter the discrete pulse amplitude and phase slopes, thus resulting in potential slice profile degradation and alterations. Most of these RF amplifier non-linearities can be corrected by a pre-distortion of the RF shape [110]. The use of highly modulated complex RF pulses however can result in unwanted slice profile artifacts, whereas real valued RF pulses create less artifacts [111]. In general, the effective RF bandwidth outperforms the bandwidth achievable by the gradient system and alterations on the RF shape should be minimal [3].

The gradient system on the other hand typically has much more restricted bandwidth limitations in the range of several tenths of kHz thus potentially impacting rapidly varying slice selective gradient slopes. These limitations results from the need for higher currents to produce the gradient waveforms [112] and eddy current effects [113], [114]. The overall alterations can be measured and modeled by the gradient impulse response function (GIRF) [115]–[117]. It should be further kept in mind that the gradient bandwidth is highly vendor specific and time varying gradient forms result in different alterations on different systems [3], [111], [115]. The actually produced slice selective gradient waveform  $G_{s,GIRF}(t)$  can be computed by a convolution

$$G_{s,GIRF}(t) = G_s(t) * GIRF(t), \quad (4.5)$$

of the ideal slice selective gradient shape  $G_s(t)$  and the measured or modelled GIRF. The impact of the GIRF is comparable to a low-pass effect with a runtime delay resulting in a smoothed and time shifted slice selective gradient shape which alters the slice profile accuracy. However, knowledge of the GIRF allows iterative correction of the RF pulse [118] for non-ideal gradient distortions. The GIRF can be also incorporated directly in the OC pulse design [119], see Section 7. This allows to use the OC based constrained joint design of RF and slice selective shape for systems with a limiting gradient amplifier bandwidth [119].

# 5 RF pulse design

## Contents

---

<b>5.1</b>	<b>RF pulse categories</b>	<b>39</b>
<b>5.2</b>	<b>Spatial non-selective RF pulses</b>	<b>41</b>
<b>5.3</b>	<b>Spatial selective RF pulses</b>	<b>44</b>
<b>5.4</b>	<b>Variable-rate selective excitation</b>	<b>51</b>
<b>5.5</b>	<b>SMS RF pulse design</b>	<b>52</b>
5.5.1	Peak RF amplitude reduction	53
5.5.2	Peak RF amplitude and RF power reduction	56
<b>5.6</b>	<b>Slice selective RF pulse design via optimal control</b>	<b>59</b>
5.6.1	Single slice selective RF pulse design via OC	60
5.6.2	SMS RF pulse design via OC	68

---

RF pulses and gradients are key factors and essential for most MR experiments. RF pulse design summarizes how to compute waveforms for the RF and gradient system that change the magnetization from a given initial state to a desired state with respect to different parameters, including profile accuracy, amplitude restrictions and safety constraints. This work mainly focusses on one dimensional slice selective RF pulses for single transmit to excite or refocus one dimensional slice profiles.

This section discusses different approaches to design RF pulse and slice selective gradient shapes for single- and SMS applications. For simplicity reasons, the following sections use the rotating frame of reference. This implies, that for experimental application, the RF pulses have to be modulated with the Larmor frequency with respect to the main field, see Eq. 2.5. Figure 5.1 shows this relationship for a rectangular RF pulse.

The focus of this thesis lies on the design of RF and slice selective gradient waveforms via optimal control theory, it's application to SMS imaging and the experimental validation. The first part of this section introduces and compares different RF pulse

## 5 RF pulse design

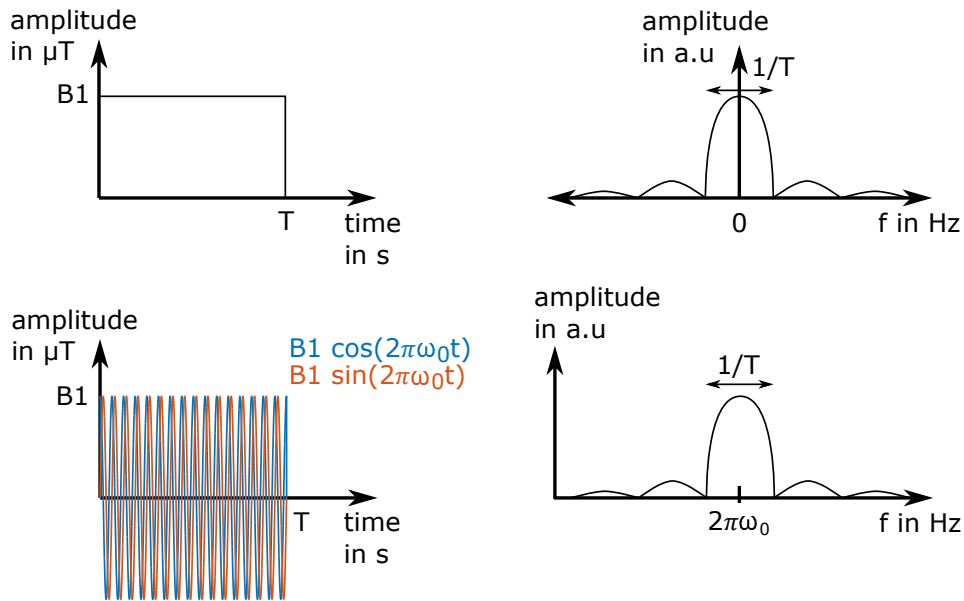


Figure 5.1: RF pulse in the rotating frame of reference (Row 1) and in the laboratory frame of reference. Please note, that the magnitude remains unchanged.

design methods that were used to initialize and benchmark the optimized results presented in [1]–[3] and the Appendix. The main results of these works are introduced and summarized at the end of this section.

### 5.1 RF pulse categories

The most basic RF pulses can be summarized in four main categories: excitation, inversion, saturation and refocusing [23]. The description and visualization of RF pulse categories is straight forward and can be formulated in the magnetization [120] or spin domain [66]. Although the spin domain description with the Cayley-Klein parameters appears to be more complicated, elegant transformations exist to assess the main RF classes and transform their result to the other domain respectively [66]. These relations and transformations are summarized in Table 5.1. It should be noted, that the perfectly crushed refocusing scenario, where the FID of refocusing pulse is assumed to be perfectly de-phased, can be easily described in the spin domain by setting  $\alpha$  to zero such that it does not contribute to the transverse magnetization. The later described optimal control (OC) approaches use the magnetization domain formulation for excitation [1] and the spin domain formulation for perfectly crushed refocusing [2], [3], see also the Appendix. Figure 5.2 gives a graphical overview of

## 5 RF pulse design

Table 5.1: Response of the Magnetization to commonly used RF Pulse Types in Terms of the Cayley-Klein Parameters, adopted from [23]

Pulse Type	Initial Condition $(M_x, M_y, M_z)^T$	Final state
Excitation or saturation	$(0, 0, M_0)^T$	$M_x = 2M_0 \text{Re}(\alpha\beta^*)$ $M_y = 2M_0 \text{Im}(\alpha\beta^*)$ $M_t = 2\alpha\beta^*$
Inversion	$(0, 0, M_0)^T$	$M_z = M_0(1 - 2 \beta ^2)$
Refocus	$(M_0, 0, 0)^T$	$M_t = M_0((\alpha^*)^2 + \beta^2)$
Refocus (perfect crusher)	$(M_0, 0, 0)^T$	$M_t = M_0\beta^2$

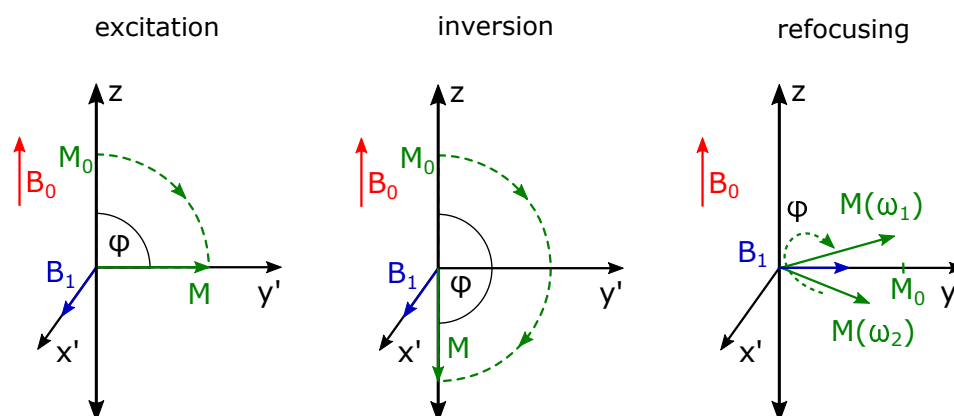


Figure 5.2: Most common RF pulse categories (excitation, inversion and refocusing) and their desired trajectory of the isocenter magnetization.

three RF pulse categories. For simplicity reasons, this is shown only for one perfectly on-resonant spin in the isocenter.

The concept of one dimensional slice selective RF pulse design can be easily extended to multiple dimensions, see [23], for instance to design RF pulses that excite, refocus or saturate two or three dimensional shapes [42]–[49]. Analogous, this idea can be further extended to compute spatially spectral RF pulses [121]–[123]. A relatively simple and direct extension to the basic pulse categories introduced above are composite RF pulses [23], [38], [110], a series of non-selective RF pulses with or without varying phase that are commonly used in NMR applications, for instance broadband excitation [124], WALTZ-16 [125] decoupling, or saturation at distinct frequencies [38], [126]. Moreover, special RF classes developed over time, such as velocity compensating excitation [127], velocity selective excitation [128] or myocardial tagging (SPAMM [129] and CSPAMM [130]) by an application of alternating non-selective RF blocks and slice selective gradient blips. This alternating application scheme and the

## 5 RF pulse design

corresponding replicating excitation pattern form the fundamentals of the PINS [131] method developed for SMS imaging. A completely different RF pulse category are adiabatic RF pulses [23], [38], [110]. Their main advantage is an inherent  $B_1$  robustness with the hurdle of large RF power requirements. Since adiabatic pulses are not the main focus of this work, the reader is referred to [23], [110] for additional information on this topic. Besides the RF pulse type, parallel transmit (pTx) [132]–[135] allows the use of independent RF channels to directly address  $B_1$  and local SAR issues [136]–[139].

RF pulses alter the magnetization from a given initial magnetization as close as possible to a desired magnetization (for instance from  $M^0 = (0, 0, M_0)^T$  to  $M_{des} = (0, M_0, 0)^T$  for an ideal  $90^\circ$  excitation RF pulse). This process can be defined in the frequency or spatial domain for non-selective and slice selective applications respectively. Conventional RF pulse design based on analytical RF waveforms typically enables choice of only a limited number of parameters, for instance the pulse duration  $T$ , nominal time bandwidth product (TBWP), slice thickness (THK) defined on the full width at half maximum (FWHM), or maximal error deviations ( $e_1$  and  $e_2$ ). The TBWP of SINC based pulses can be approximated

$$TBWP = T\Delta f \quad (5.1)$$

with the pulse duration  $T$  and the bandwidth of the main lobe  $\Delta f$ . Alternatively, the TBWP is directly given by the number of zero crossings [23].

RF pulse design based on optimization methods further allows assessment and predefinition of more parameters. For instance, the spatial domain can be treated point-wise in space to define a desired magnetization for all spatial points. Figure 5.3 summarizes four different design approaches for rectangular, SINC, SLR and optimization based RF pulse design. Additionally to these state constraints, optimization based methods typically allow to further define limitations on the RF pulse and slice selective gradient shape, for instance the maximal amplitudes or time derivatives [2], [3]. It should be noted, that most RF pulse methods typically assume a constant slice selective gradient while OC based methods, presented in Section 5.6, enable simultaneous design of the RF and slice selective gradient.

### 5.2 Spatial non-selective RF pulses

Even in the most basic NMR experiment, the creation of a FID signal without a spatial varying gradient, RF pulses typically can not be analytically designed. There are

## 5 RF pulse design

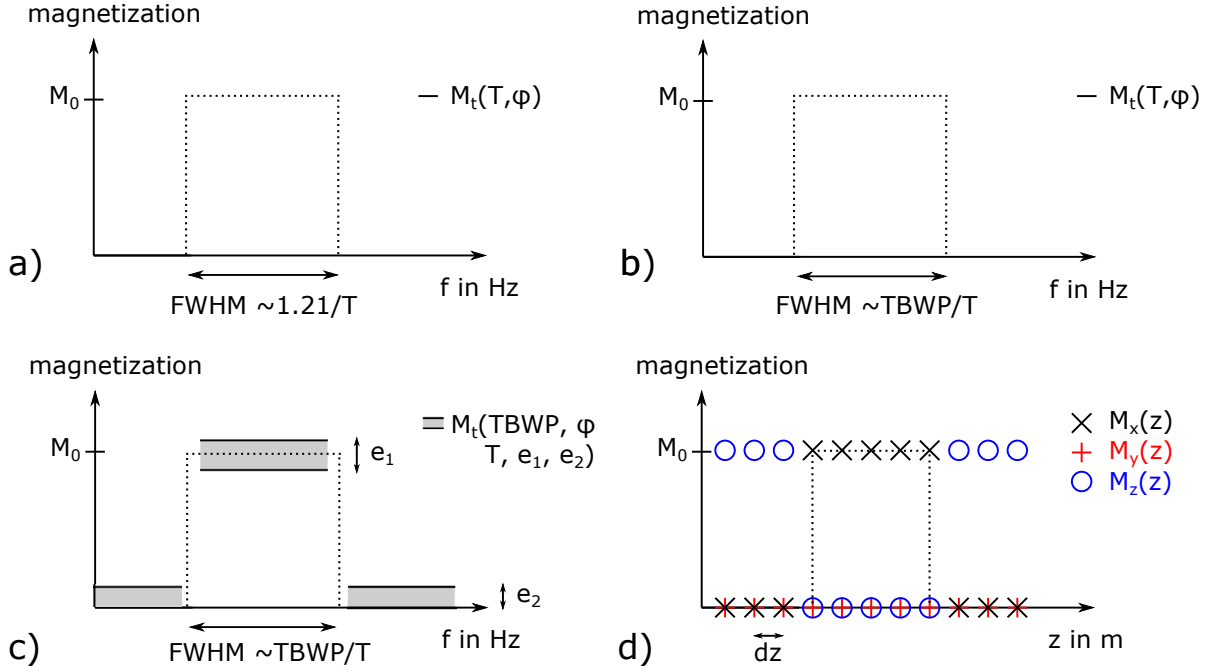


Figure 5.3: Parametrized and pointwise description of the desired magnetization in slice selection direction for a rectangular (a), SINC (b), SLR (c) and optimization (d) based RF pulse design method.

two problems which prevent an analytical solution, a coupling of the transversal and longitudinal component and inherent relaxation effects. However, neglecting the relaxation terms decouples the Bloch equations. The additional assumptions of a perfectly homogeneous  $B_0$  field and an absent slice selective gradient, allows for a geometric description of the rotating magnetization vector, see Section 2.3. To visualize the off-resonance behaviour of spatial non-selective RF pulses, the assumption of a constant slice selective gradient amplitude maps the spatial variable  $z$  to the corresponding frequency  $f(z)$ . The frequency can be computed as

$$f(z) = \frac{\gamma}{2\pi} G_s z, \quad (5.2)$$

with the gyromagnetic ratio  $\gamma/(2\pi)$  of the used nuclei in  $\text{MHz T}^{-1}$ , the time constant amplitude of the slice selective gradient  $G_s$  in  $\text{mT m}^{-1}$  and the spatial position  $z$  in m. It should be noted, that this relies on the assumption of a spin ensemble with a uniform frequency distribution, according to Eq. 5.2. In the following section only rectangular pulses are discussed. For a more extensive comparison of non-selective RF pulses, including composite pulses, adiabatic pulses (for instance half-, full-passage or BIR pulses) or optimized block pulses, the interested reader is referred to [140].

## 5 RF pulse design

Rectangular RF pulses are fully described by the  $B_1$  amplitude, the Lamor frequency and the pulse duration  $T$  resulting in the flip angle, see Eq. 2.26 and Section 2.3. A simple example can be found using the gyromagnetic ratio of hydrogen protons  $\gamma = 2.6731 \times 10^8 \text{ rad s}^{-1} \text{ T}^{-1}$ , a pulse duration  $T = 1 \text{ ms}$  and a desired flip angle of  $\pi/2$  to compute the required  $B_1$  amplitude according to

$$B_1 = \frac{\phi}{\gamma T} = 5.876 \mu\text{T}. \quad (5.3)$$

In order to minimize relaxation effects and the minimal achievable echo time, the RF pulse duration should be typically as short as possible.

Although an infinitely high and short rectangular RF pulse would be desirable, the RF power amplifier constraints limit the achievable maximal field strength and therefore limit the minimal RF duration. See Section 4 for the description of how the  $B_1$  field is connected to the voltage of the RF amplifier.

Two rectangular RF pulses ( $\pi/8$  and  $\pi/2$ ) are shown together with a two-sided FFT and Bloch simulations in Row 1 of Figure 3.2. It can be seen, that for this small tip angle RF pulse both simulations result in comparable slice profiles. However, it should be noted that although there is no clear visual difference between these results, they are not numerically identical. Using the small tip angle approximation, rectangular RF pulses result in SINC-shaped excitation profiles whose full half width maximum and zero crossings are defined by the pulse duration and the FWHM can be approximated by  $1.21/T$  [23]. For the shown  $\pi/8$  pulse this results in a FWHM of 10.37 kHz which fits nicely to the simulations given in Figure 3.2. The frequency selectivity of non-selective pulses is mainly determined by the pulse duration, the main parameter for the desired magnetization, see Figure 5.3, and the RF waveform. The prominent side-lobes of rectangular pulses can be suppressed using Gaussian pulses, see Section 5.3 with the drawback of lower frequency selectivity.

Increasing the flip angle to  $\pi/2$  for the same maximal  $B_1$  amplitude ( $B_{1,max} = 12.5 \mu\text{T}$ ) requires to increase the pulse duration  $T = 0.47 \text{ ms}$  to be 4 times longer. The  $\pi/2$  RF pulse and the corresponding forward FFT simulations are shown in Row 2 of Figure 3.2. Now, the small tip angle approximation is violated and a significant difference between FFT and Bloch simulations is the result. Compared to the  $\pi/8$  example, the longer pulse duration additionally leads to a more selective excitation profile. The small tip angle approximation results in a FWHM of 1.3 kHz, while the Bloch simulation shows a merely smaller FWHM of roughly 1.1 kHz. Although rectangular RF pulses could be also used for slice selective applications, their poor slice profile limits the practical value for slice selective applications. Nevertheless, they are commonly used for spatial non-selective NMR and MRI applications.

### 5.3 Spatial selective RF pulses

To achieve a spatially selective RF pulse, a slice selective gradient is applied simultaneously with the RF field.

All spins in the object of interest are acquired simultaneously during signal acquisition and a de-phasing across the slice selection direction would result in a reduced FID signal. Therefore, the phase across the slice is an important parameter to characterize slice profiles. Slice selective RF pulses for conventional GRE or SE imaging preferably tilt the magnetization uniformly across the slice selection axis. However, specialized applications such as peak power reduction [141], [142] may benefit from a de-phased slice profile. Using the complex description of the magnetization the phase  $\theta$  can be computed with

$$\theta(z) = \tan^{-1} \frac{\text{Im}(M_{xy}(z))}{\text{Re}(M_{xy}(z))}, \quad (5.4)$$

for the spatial position  $z$ . In the context of slice selective RF pulses, the use of a slice selective gradient inherently results in a de-phasing of the magnetization in the transversal plane. For linear-phase RF pulses, for instance SINC (Section 5.3), Gauss (Section 5.3) or SLR (Section 5.3) based RF pulses, the accumulated phase dispersion can be corrected with a re-phasing gradient. The required gradient area depends on the isodelay [23] of the RF pulse. For symmetric pulses the isodelay is typically half the RF duration, for SLR or optimized RF pulses the iso-delay may further depend on the flip angle. Besides linear-phase RF pulses, the SLR design method allows computation of maximal-phase with a larger iso-delay or minimal-phase pulses with a smaller iso-delay [43]. Although these pulses typically suffer from a worse slice profile, their phase properties allow for a direct use in saturation or in the context of minimal TE since less refocusing area is required. Figure 5.4 summarizes a linear-phase SLR pulse without (Column 1) and with (Column 4) a matched slice selective re-phasing gradient. Column 2 shows a maximal-phase SLR pulse, intended for the use of saturation with an even higher de-phasing, compared to Column 1. Column 3 shows a minimal-phase SLR pulse where a reduced refocusing area is required, thus enables reduction of the TE. The minimal- or maximal-phase pulses should not be confused with non-linear-phase pulses such as quadratic [142] or quasi random phase RF pulses. In contrast to the residual linear-phase, a non-linear-phase cannot be corrected by a slice selective gradient. However, the use of two consecutive RF pulses with the same non-linear-phase results in a phase cancellation and allows the use of non-linear pulses, for instance in double refocused diffusion or matched spin echo sequences [143], [144].

## 5 RF pulse design

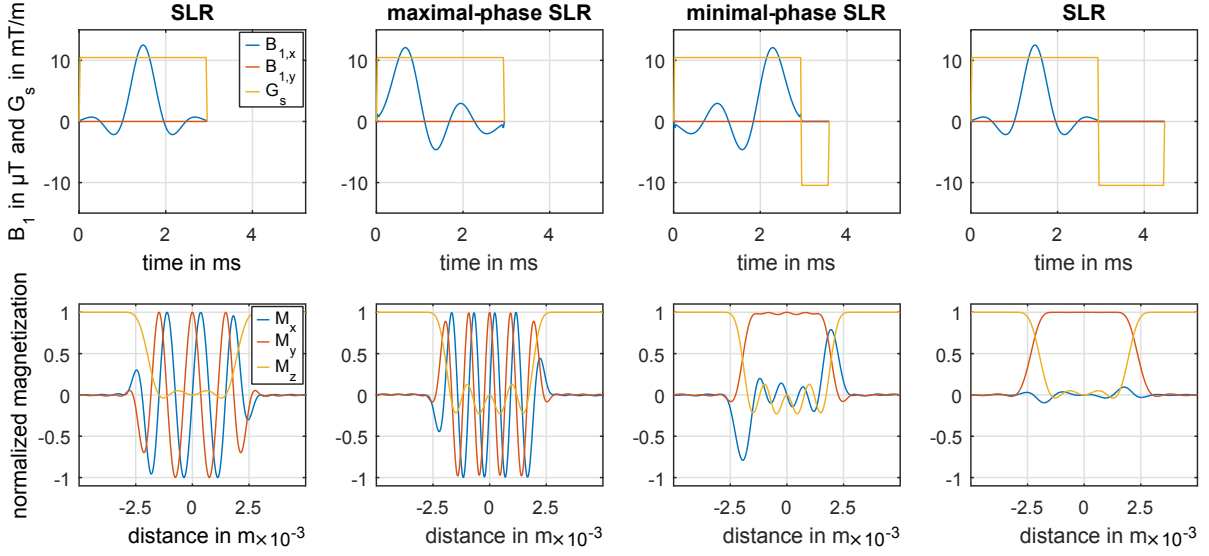


Figure 5.4: Overview of slice selective SLR based RF pulses with constant slice selective gradient shapes and the Bloch simulations. Column 1 shows the linear de-phasing that is corrected in Column 4 with a slice selective re-phasing gradient. Column 2 shows a maximal-phase RF pulse for saturation and Column 3 shows a minimal RF pulse with decreased gradient refocusing lobe for minimal TE purposes.

### SINC pulses

The Fourier transform of a rectangular function in one domain results in an infinite SINC-function in the transformed domain. Assuming the small tip angle approximation, SINC-shaped RF pulses therefore excite rectangular slice profiles. The RF pulse shape  $B_1(t)$  can be easily defined using the SINC function:

$$B_1(t) = \begin{cases} \frac{\sin \pi t}{\pi t} & \text{if } t \neq 0, \\ 1 & \text{if } t = 0, \end{cases} \quad (5.5)$$

using  $t = -\text{TBWP} \cdot \tau$  to compute a  $B_1(t)$  with the intended frequency selectivity based on the TBWP and the discretization step  $\tau$ . However, there are two problems associated with the use of SINC pulses. First, the aforementioned assumption only holds for small flip angles. Second, the SINC function is defined for an infinite temporal duration which is not feasible due to limited TE and RF amplifier requirements. Since the RF area defines the flip angle in the iso-center, the limited  $B_1$  amplitude results in longer RF durations. This results in an inherent trade-off between frequency selectivity and pulse duration.

## 5 RF pulse design

The selectivity of a SINC pulse is defined by the dimensionless TBWP, see Eq. 5.1. Together with a limited  $B_{1,max}$ , the choice of the TBWP is a crucial decision that strikes a balance between RF pulse duration and slice profile fidelity. Similar to rectangular block pulses, see Section 5.2, there are useful approximations to define the bandwidth or slice profile thickness with respect to the FWHM of SINC based RF pulses [23]. As an example, Figure 5.5 shows a SINC based RF pulse with 3 zero crossings, that correspond to  $TBWP = 3$ . The pulse duration is scaled to  $T = 2.644$  ms to perform a  $90^\circ$  excitation with  $B_{1,max} = 12.5$   $\mu$ T, see Eq. 2.25. For a time-constant slice selective gradient, the slice thickness THK can be chosen by scaling the amplitude of the slice selective gradient. According to Eq. 4.2 a THK of 5 mm results in  $G_s = 10.461$  mT m<sup>-1</sup>, which is confirmed by the Bloch simulations in Figure 5.5. Jump discontinuities at the beginning and end of the RF pulse result in clearly visible and severe ripples in both the slice profile and the out-of-slice profile. This effect is similar to leakage in digital signal processing and can be reduced by filtering the RF waveform with proper window functions such as Hamming or Hann windows. Column 2 of Figure 5.5 summarizes the effect of an Hamming window (shown dotted) on the SINC based RF pulses shown in Column 1. It can be clearly seen, that the unwanted ripples are reduced with the drawback of a simultaneous reduction of the slice profile transition steepness or TBWP. This is strongly connected to digital signal processing and results in a trade-off between frequency selectivity and leakage suppression. Nevertheless, and mainly due to their simplicity and analytical description, windowed SINC functions are still the most used RF pulse shapes for small flip angles in slice selective MR experiments.

### Gaussian pulses

Comparable to SINC pulses, Gaussian pulses are another special case of analytical RF pulse types that originate from the small tip angle approximation. Gaussian RF pulses can be designed analytically by

$$B_1(t) = B_{1,max} e^{-t^2/(2\sigma^2)}, \quad (5.6)$$

with the time-vector  $t$  running from  $-T/2$  to  $T/2$  with  $T$  being the pulse duration [23]. The variance  $\sigma^2$  is used to adjust the desired frequency selectivity. The Fourier transform of a Gauss function is another Gauss function with a favourable smooth decline of the slice profile.

## 5 RF pulse design

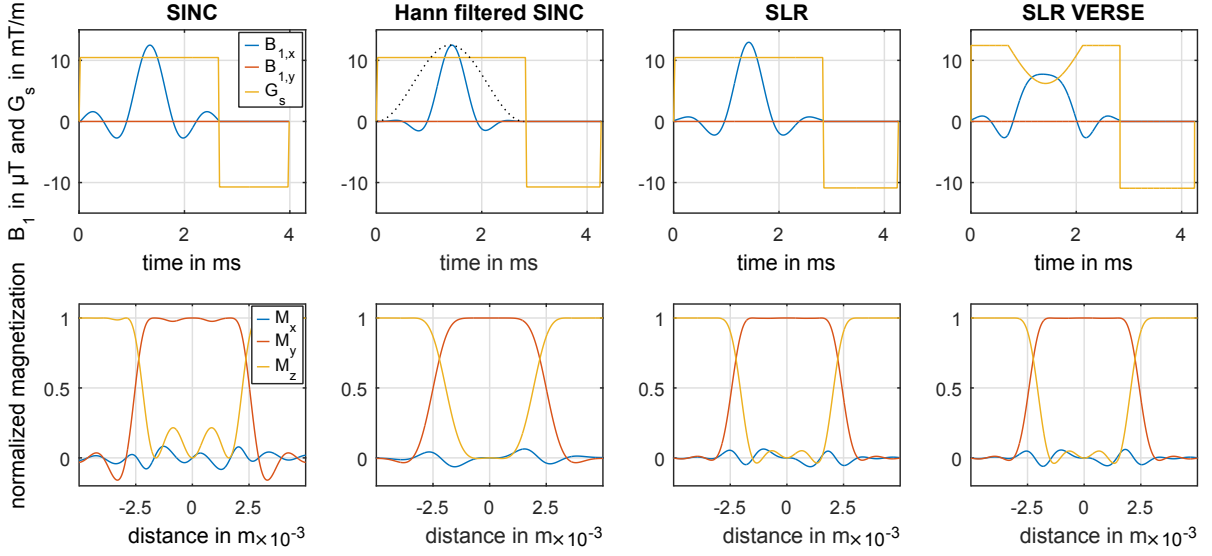


Figure 5.5: Overview of slice selective RF pulses designed with the Fourier approximation (Column 1 and 2) and SLR (Column 3 and 4). Column 2 shows a Hamming windowed version (dotted line) of the pulse shown in Column 1 and Column 4 shows a VERSE'd version (with prescribed gradient shape) of Column 3 respectively.

### Shinnar–Le Roux algorithm

The SLR algorithm does not rely on the small tip angle approximation and can be used for accurate large flip angle RF pulse design. It is formulated in the spin domain with neglected relaxation terms and makes use of the hard pulse approximation, see Section 3.1.3. Then, the rotation for each time point can be separated for RF and slice selective gradient as

$$Q_m = \begin{pmatrix} C_m & -S_m^* \\ S_m & C_m \end{pmatrix} \begin{pmatrix} z^{1/2} & 0 \\ 0 & z^{-1/2} \end{pmatrix}, \quad (5.7)$$

with  $C_m = \cos(\gamma|B_{1,m}|\tau/2)$ ,  $S_m = ie^{i\angle B_{1,m}}\sin(\gamma|B_{1,m}|\tau/2)$  describing the effect of the RF pulse and  $z = e^{i\gamma Gx\tau}$  describing the effect of the slice selective gradient  $G$  at the spatial position  $x$ . Using Eq. 5.7, the recursion to compute the accumulated rotation, see Eq. 3.27, becomes

$$\begin{pmatrix} \alpha_m \\ \beta_m \end{pmatrix} = z^{1/2} \begin{pmatrix} C_m & -S_m^* \\ S_m & C_m \end{pmatrix} \begin{pmatrix} 1 & 0 \\ 0 & z^{-1} \end{pmatrix} \begin{pmatrix} \alpha_{m-1} \\ \beta_{m-1} \end{pmatrix}, \quad (5.8)$$

## 5 RF pulse design

with the Cayley-Klein parameters  $\alpha_m$  and  $\beta_m$  for each time step  $m$ . The definition of two complex polynomials  $A_m = z^{j/2}\alpha_m$  and  $B_m = z^{j/2}\beta_m$  defines the forward SLR transform

$$\begin{pmatrix} A_m \\ B_m \end{pmatrix} = \begin{pmatrix} C_m & -S_m^* z^{-1} \\ S_m & C_m z^{-1} \end{pmatrix} \begin{pmatrix} A_{m-1} \\ B_{m-1} \end{pmatrix}. \quad (5.9)$$

Starting with  $(A_0, B_0)^T = (1, 0)^T$ , see Eq. 3.28, the polynomials for the  $n$ th step  $A_n$  and  $B_n$  are complex polynomials in  $z^{-1}$

$$\begin{aligned} A_n(z) &= \sum_{m=0}^{n-1} a_m z^{-m}, \\ B_n(z) &= \sum_{m=0}^{n-1} b_m z^{-m}, \end{aligned} \quad (5.10)$$

of order  $n - 1$ . The forward SLR transformation (Eq. 5.9) computes  $A_n(z)$  and  $B_n(z)$  of an arbitrary piecewise constant RF pulse. For small tip angles the SLR transformation can be reduced to the z-transform [66].

The idea leading to SLR based RF pulse design is to invert the forward SLR transform and use two complex polynomials  $A_n(z)$  and  $B_n(z)$  to calculate the RF pulse that creates these polynomials. The inversion of Eq. 5.9, or inverse SLR transform, is given by

$$\begin{pmatrix} A_{m-1} \\ B_{m-1} \end{pmatrix} = \begin{pmatrix} C_m & S_m^* \\ -S_m z & C_m z \end{pmatrix} \begin{pmatrix} A_m \\ B_m \end{pmatrix} = \begin{pmatrix} C_m A_m + S_m^* B_m \\ z(-S_m A_m + C_m B_m) \end{pmatrix}. \quad (5.11)$$

It can be proven [66] that the relation

$$\frac{B_{m,0}}{A_{m,0}} = \frac{S_m}{C_m} = \frac{ie^{i\theta_m} \sin\phi_m / 2}{\cos\phi_m / 2}, \quad (5.12)$$

can be used to compute the RF waveform for each time point

$$B_{1,m} = \frac{1}{\gamma\tau} \phi_m e^{i\theta_m}, \quad (5.13)$$

with the rotation angle  $\phi_m$  and the RF phase  $\theta_m$

$$\begin{aligned} \phi_m &= 2 \tan^{-1} |B_{m,0} / A_{m,0}|, \\ \theta_m &= \angle(-iB_{m,0} / A_{m,0}), \end{aligned} \quad (5.14)$$

where  $A_{m,0}$  and  $B_{m,0}$  are the lowest order of the polynomials.

The SLR based RF pulse design consists of two main steps. After the design of the filter polynomials  $B_n(z)$  and  $A_n(z)$ , the inverse SLR transform computes the corresponding RF pulse.

## 5 RF pulse design

To design a  $90^\circ$  excitation pulse, the polynomial  $B_n(z)$  should be as close as possible to an ideal rectangular slice profile with the in-slice amplitude for  $\phi = 90^\circ$

$$B_d(z = e^{i\gamma Gx\tau}) = i(n_x + in_y)\sin\phi/2 = i\sin\phi/2 = i\sqrt{2}/2 \quad (5.15)$$

and the out-of-slice amplitude for  $\phi = 0^\circ$

$$B_d(z = e^{i\gamma Gx\tau}) = i\sin\phi/2 = 0. \quad (5.16)$$

However, rectangular functions cannot be described exactly by the  $B_n(z)$  polynomial. The goal is to find a polynomial approximation  $B_n(z)$  close to the ideal slice profile which can be computed with different filter design methods including the Parks-McClellan algorithm (equi-ripple error) or by a least squares approach [66]. It can be shown that the FIR filter design parameters  $d_1$ ,  $d_2$ , and the two cut-off frequencies for pass- and stop-band directly relate to slice profile accuracy, frequency selectivity and intended RF pulse category [66]. After  $B_n(z)$  has been designed, the magnitude of the polynomial  $A_n(z)$  can be computed by

$$|A_n(z)| = \sqrt{1 - B_n(z)B_n^*(z)} \quad (5.17)$$

using the magnitude constraint  $|A_n(z)|^2 + |B_n(z)|^2 = 1$ . In order to get low RF energy requirements [23] the phase of the polynomial  $A_n(z)$  is typically set to fulfil a minimum-phase solution. Finally, the corresponding RF pulse can be computed by the inverse SLR transform of the polynomials  $A_n(z)$ ,  $B_n(z)$ . Figure 5.6 gives an overview of the different SLR design steps and shows the two polynomials  $A_n(z)$ ,  $B_n(z)$  and the resulting RF pulse together with the corresponding profiles. The symmetric SLR RF pulse results in a linear de-phasing across the slice direction that can be recovered with a slice selective refocusing gradient. Other phase patterns can be achieved choosing a non-symmetric (minimum and maximum phase) or complex  $B_n$  polynomial. Column 3 of Figure 5.5 shows a representative SLR excitation pulse ( $\phi = 90^\circ$ ,  $N = 256$ ,  $T = 2.894$  ms,  $TBWP = 3$ ,  $d_1 = 0.01/4$ ,  $d_2 = 0.01/\sqrt{2}$ ), linear-phase, least squares filter design method) together with a constant slice selective gradient and the forward Bloch simulation.

Although the overall RF pulse slope is similar to the SINC based RF pulses, the slice profile is closer to the desired rectangular shape. Efficient digital filter design methods allows rapid design of RF pulses and makes the SLR the gold standard for large tip angle design with constant slice selective gradient and neglected relaxation terms [66].

## 5 RF pulse design

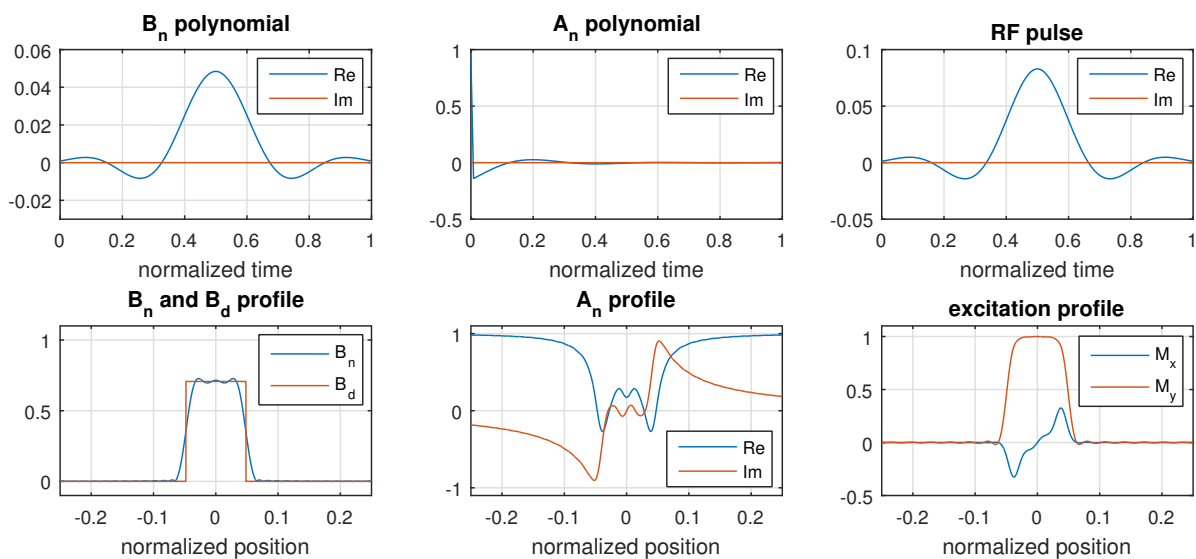


Figure 5.6: Overview of the different stages of the SLR Pulse design for a  $90^\circ$  excitation pulse. The  $B_n$  polynomial is designed with a least squares approach to fit to the desired slice profile  $B_d$ .  $A_n$  is computed based on  $B_n$  with a minimal phase constraint. Both polynomials result in the complex RF pulse using the inverse SLR transform. The results of the Bloch simulations with corrected linear phase dispersion shows the final  $M_x$  and  $M_y$  components.

### Additional RF design methods

In addition to the above described RF design methods further methods have been proposed. These include RF pulse design with the continuous or discrete inverse scattering transform [145], [146] or the design of adiabatic RF pulses [23], [110], [140] together with most of the design methods listed in Section 5.1.

Alternatively, RF pulse design problems can be formulated using optimization techniques such as simulated annealing [147], [148], evolutionary approaches [149], [150], neuronal networks [151] or optimal control theory [1]–[3], [47], [49], [120], [152]–[158]. For the ease of readability the description of the proposed OC methods are given in Section 5.6. The underlying idea is to formulate a suitable functional and minimize it by finding the external magnetic field, for instance the RF pulse or the slice selective gradient waveform, based on the Bloch equations measured in different norms. The main advantage of numerical optimization methods lies in its flexible formulation that can be extended and adapted to many different applications with problem specific functionals, for instance parallel transmit, SMS or multidimensional modelling, as well as  $B_1$  and  $B_0$  robustness. Due to the accurate design model, these numerical design methods typically lead to better magnetization profiles with the hurdle of increased computational costs, thus in general preventing on the fly design, and

## 5 RF pulse design

more complicated numerical design. Nevertheless, for single transmit cases RF pulses typically can be computed off-line and stored in a pulse library on the MR scanner to be selected in the intended MR sequence. However, GPU parallelization has been shown to reduce the computation time dramatically from the range of hours down to several seconds [159]. This could be highly interesting in the context of parallel transmit where RF pulses have to be optimized for a patient specific  $B_1$  transmit map.

### 5.4 Variable-rate selective excitation

So far, the design of RF pulses is based on the assumption of no (Section 5.2) or a constant spatially variable field gradient (Section 5.3). For neglected relaxation the relation between RF amplitude and slice selective gradient can be exploited to reduce the overall RF power requirements. This is known as variable-rate selective excitation VERSE [160]. The reduction of the overall RF power comes with the drawback of increased sensitivity to off-resonance effects increase due to a time varying slice selective gradient shape with lower amplitudes. Later implementations extended this idea to reduce the pulse duration and apply it to reduce the peak RF amplitude [112] and power of SMS pulses [118]. A thoughtful derivation and further elaboration of VERSE can be found in [23].

To reduce the RF amplitude, a rectangular RF pulse can be stretched in time (see Section 5.2) which reduces the RF bandwidth. This change in RF bandwidth can be compensated by the same reduction of the amplitude of the slice selective gradient, see Eq. 5.2. This idea can be extended to a time varying RF pulse and slice selective gradient shape with a transformation function  $\lambda(t)$ . The VERSE transformation can be defined [23] by

$$B_{1,VERSE}(t) = \frac{2\pi}{\gamma G_s} B_1(k) \frac{dk}{dt}, \quad (5.18)$$

$$G_{s,VERSE}(t) = \frac{2\pi\Delta f}{\gamma\Delta z} \lambda(t) = G_s \lambda(t), \quad (5.19)$$

with

$$k(t) = \frac{\gamma}{2\pi} \int_0^t G_s(t') dt' = \frac{\gamma G_s}{2\pi} \int_0^t \lambda(t') dt' \quad (5.20)$$

being the RF k-space trajectory [23]. The transformation in Eq. 5.18 connects  $\lambda(t)$  with the slope of the RF pulse  $B_1(t)$  and the constant slice selective gradient amplitude  $G_s$ . This transformation results in a variable-rate slice selective gradient shape with a

## 5 RF pulse design

matched RF pulse that compensates the varying k-space velocity. For instance, when the slice selective gradient amplitude is small, the RF amplitude has to be reduced to compensate the slow k-space velocity.

The main question for the VERSE application is the determination of the transformation function  $\lambda(t)$ . The transformation function  $\lambda(t)$  can be defined by a manual selection of time points where the RF amplitude should be reduced, or by an iterative adaptation until all hardware constraints on the RF and slice selective gradient amplitude and slew rate are fulfilled [112]. This however should not be confused with the method described in Chapter 5.6 to jointly design RF and slice selective gradient shape with explicit hardware constraints.

Column 4 of Figure 5.5 shows the VERSE'd Hann filtered SLR RF pulse of Section 5.3 (re-sampled with a time discretization  $\tau = 2.36 \mu\text{s}$ , a factor of 10, to reduce the interpolation artefacts) and  $\lambda(t)$  composed out of two constant blocks and half a Sine period at the center where the RF pulse amplitude should be reduced. The area of the slice selective gradient has been scaled such that the gradient impact remains constant, thus leading to an almost identical slice profile before and after VERSE.

### 5.5 SMS RF pulse design

Conventional single slice selective MR imaging experiments acquire an integrated MR signal originating from protons of a specific slice or slab, a process which is repeated to acquire the entire k-space. Although TE for single- and multi-shot sequences lies in the sub-second range, the need to fill a spatially encoded two or three dimensional k-space in combination with relatively long  $T_1$  times typically results in long repetition times with a long dead time in between. This dead time can be used in conventional multi-slice imaging to multiplex the acquisition of spatially non-overlapping slices to increase the temporal acquisition efficiency [23]. Developments in parallel imaging enabled an extension of this idea of slice selective multi-slice imaging to acquire slice information simultaneously to further increase the acquisition efficiency and use coil sensitivities to separate the aliased slice information [95], [161]. Although the main idea of SMS was founded in 1988 [162], it took several years until SMS imaging became widely accepted as evidenced in various publications [95], [163]–[166] and pushed by pre-compiled SMS-MR sequences provided by the University of Minnesota (Center for Magnetic Resonance Research, CMMR) and the Massachusetts General Hospital (MGH, Boston). Today, SMS is commercially available as a clinically approved MRI sequence product.

## 5 RF pulse design

Besides parallel imaging based reconstruction [82], [167]–[172], special RF pulses that excite or refocus slices simultaneously are essential for SMS imaging [95]. The topic of this section deals with limitations influencing the slice acceleration factor, or multi-band MB factor. Different approaches are introduced to increase the slice acceleration while maintaining a minimal echo time to maximize the achievable MR signal.

SMS RF pulses can be computed by a simple superposition of individual RF pulses with a different carrier frequencies [162]. Originally, the resulting SMS pulses were combined with Hadamard encoding [161] to disentangle the aliased slice information by subtraction of raw images acquired with alternating phase patterns [162]. This implies that the required acquisitions to disentangle the aliased slice information increase by the power of the MB factor. To avoid multiple acquisitions, later implementations use parallel imaging reconstruction techniques [95]. Slice selective RF pulses, see Section 5.3, can be easily shifted along the slice direction  $z$  by a phase modulation of the RF pulse shape

$$B_{1,offset}(t) = B_1(t)e^{i\gamma G_s \Delta z t}, \quad (5.21)$$

for a given slice selective gradient amplitude  $G_s$  at each time-point  $t$  [95]. This allows superposition of phase modulated RF pulse shapes  $B_1(t)$  replicated in the slice direction for the desired spatial locations  $\Delta z_n$

$$B_{1,sp}(t) = \sum_{n=1}^{MB} B_1(t)e^{i\gamma G_s \Delta z_n t}, \quad (5.22)$$

with MB being the MB factor. This process is depicted in Figure 5.7 for a MB3 superposition pulses together with the Bloch simulation to visualize the position of the slice profile. The superposition results in a linear scaling of the maximal peak RF amplitude [95], thus easily reaching  $B_{1,max}$  and RF power.

### 5.5.1 Peak RF amplitude reduction

The linear  $B_1$  peak amplitude scaling of conventional superposition pulses competes with RF amplifier constraints, see Section 4. For typical 3 T in vivo MR systems the RF amplifiers are usually limited to 12 – 20  $\mu$ T. To fulfil this amplitude constraint, superposition pulses have to be stretched and can get unacceptably long since, the pulse duration competes with inherent  $T_2$  and  $T_2^*$  de-phasing, especially for high MB factors or high TBWP. The following methods assess the problem of peak amplitude

## 5 RF pulse design

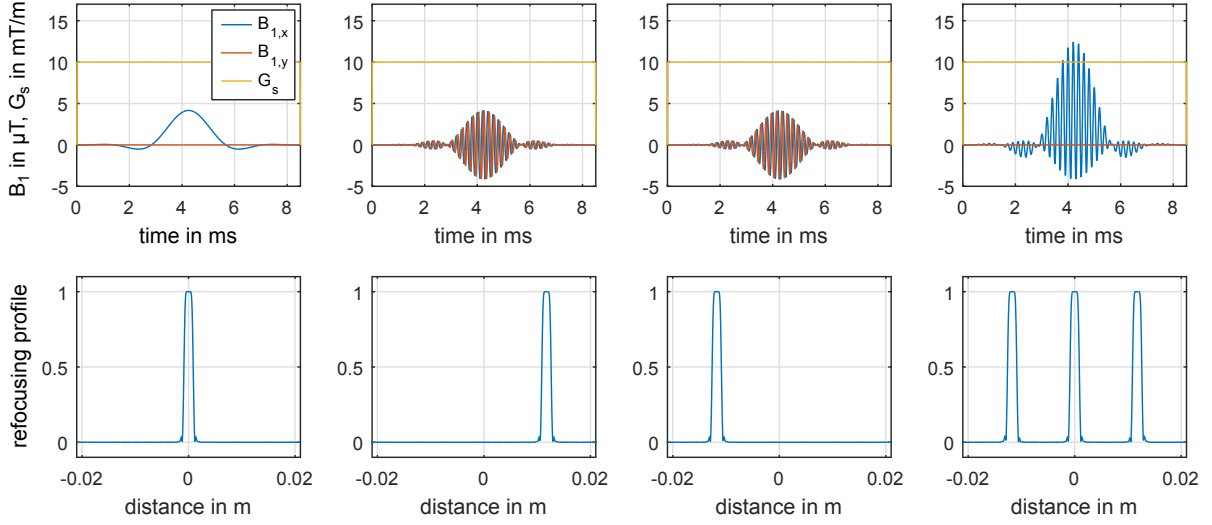


Figure 5.7: Principal composition of a SMS superposition pulse as a sum of different on-resonant and phase shifted single slice pulses.

increase without reducing the overall RF power requirements. A more extensive comparison of the presented design methods is given in [111], [173].

### Phase scrambling

The peak  $B_1$  amplitude of superposition SMS pulses can be reduced by a variation of the individual mean phase of each single slice RF pulse [174]. The phase variation results in a shift of the complex peak amplitudes such that the individual peaks do not overlap. Theoretically, the peak amplitude reduction then is proportional to the square root of the number of simultaneous slices  $\sqrt{MB}$  [174].

A slight modification of Equation 5.22 can be used to compute the RF shape

$$B_{1,ps}(t) = \sum_{n=1}^{MB} B_1(t) e^{i(\gamma G_s \Delta z_n t + \theta_n)}, \quad (5.23)$$

with  $\theta_n$  being the mean phase for each of the individual slices. The phase offsets up to a MB factor of 16 can be found at [174]. Column 2 of Figure 5.8 shows a phase scrambled superposition pulse with the mean phase  $\theta(n) = (0, 2.005, 1.674, 5.012, 5.736, 4.123)$  rad with a roughly 28% shorter pulse duration.

## 5 RF pulse design

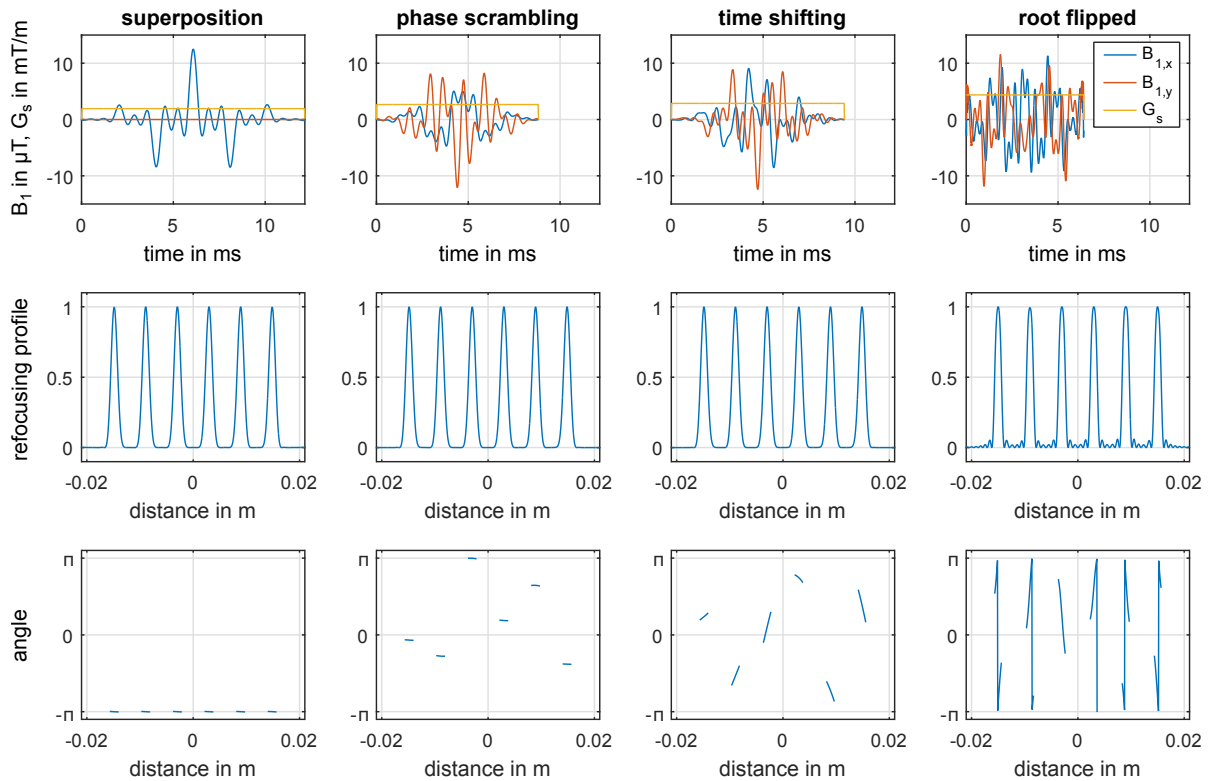


Figure 5.8: Overview of different SMS refocusing pulses ( $MB=6$ ,  $TBWP=2$ ) designed with superposition (Column 1), phase-scrambling (Column 2), time shifting (Column 3) and root flipping (Column 4) and maximal RF peak amplitude of  $12.5 \mu\text{T}$ . The Bloch simulations (magnitude and phase) are given in Row 2 and 3 respectively.

### Time shifting

The  $B_1$  peak amplitude of superposition pulses can be further reduced by a temporal shift of the individual sub pulses. This results in a better amplitude distribution and reduced peak amplitudes [175]. Column 3 of Figure 5.8 shows a time shifted superposition pulse with a roughly 32% reduced pulse duration. The individual sub-pulses are delayed by 0.25 ms. There is a nice overview and comparison of time-stretched, time-shifted and phase-scrambled superposition in [175]. Therein, it's shown that the combination of phase-scrambled and time-shifted sub-pulses results in the lowest peak amplitude and thereafter enables generation of even shorter pulses. Due to the different temporal shifts however, the individual slices are excited at different time points and the slice selection gradient can not re-phase all slices at the same echo time. This slice dependent echo time can be corrected with a matched second RF pulse e.g. to generate a uniform spin echo in all slices. Therefore the use of time shifted pulses is limited to the use of sequences with two RF pulses needed, for instance SE or TSE.

## Root flipping

Another approach to reduce the  $B_1$  peak amplitude using SLR theory is to generate asymmetric RF pulses whose peak amplitudes do not overlap [173]. This is achieved by flipping the roots of the sub pulse's beta polynomial such that the peak amplitude of the overall RF pulse is reduced. In addition to a slice dependent echo time, root flipped SMS pulses have a quadratic in-slice phase and require a second matched SMS RF pulse. Compared to phase optimization and pure time shifting, the use of root flipping reduces both the pass- and stop-band ripple amplification and yields significant shorter minimal RF pulse durations. A comparison of a representative SMS root flipping RF pulse is given in Column 4 of Figure 5.8 with roughly half the pulse duration compared to the superposition pulse in Column 1.

### 5.5.2 Peak RF amplitude and RF power reduction

In addition to the linear peak amplitude scaling the mean RF energy requirements of superposition pulses also scale linearly [95], hence limiting the the use of large MB factors. The mean energy  $S$  of an arbitrary RF pulse  $B_1(t)$  can be computed by

$$S = \tau \sum |B_1(t)|^2, \quad (5.24)$$

with the time discretization  $\tau$  for all temporal samples. The overall energy requirements of SMS RF pulses can be reduced analogous to single slice RF pulses by modifying the k-space trajectory via VERSE [112], [160], [172], see Section 5.4. It should be noted, however, that strong oscillations of the RF waveform might require additional smoothing of the otherwise too rapidly changing gradient waveform. The application of VERSE on the envelope of the SMS pulse resolves this limitation [176], [177].

A different approach to reduce peak RF amplitude and mean energy can be achieved via wavelet compression [178]. Alternatively, an inherent power reduction can be achieved by the PINS [131] or MultiPINS [179] method described in the following sections. A direct peak and power constrained RF design including in-slice error constraints was proposed with constrained convex optimization [180] or applying OC, see Section 5.6.

### PINS

An elegant way to set up the k-space trajectory by means of power efficiency is the power independent number of slices PINS technique [131]. Therein, RF pulse shape and the corresponding k-space trajectory are discretized and used after each other in an alternating scheme. The RF pulse is then a convolution of the continuous single slice pulse with a train of delta functions whereas the gradient are triangular blips. This results in a piecewise movement through excitation k-space with RF power deposition only at distinct k-space positions and periodic slice profiles. The alternating RF and slice selective gradient pattern, together with the slew rate limitations of the slice selective gradient system typically results in lengthy PINS pulses. The TBWP of PINS pulses is defined as [95]

$$\text{TBWP} = N_{sp} \text{THK} / z_{sep}, \quad (5.25)$$

with the number of PINS sub-pulses  $N_{sp}$ , the slice thickness THK and the slice separation  $z_{sep}$ . The PINS method can be directly applied to single slice RF pulses with a constant slice selective gradient shape. Figure 5.9 shows a superposition refocusing pulse (TBWP= 2.05, THK= 1 mm, MB= 11,  $z_{sep} = 20$  mm) and in comparison a PINS RF pulse (Number of gradient blips  $N_{sp} = 37$  with a duration  $\tau_{sp} = 0.2$  ms) based on the same single slice SLR pulse. It can be seen that both, the superposition and PINS pulse suffer from a large  $B_{1,max}$  of 41.13  $\mu\text{T}$  (superposition) and 31.72  $\mu\text{T}$  (PINS).

### Multi PINS

The comparison of PINS and superposition based RF pulses shows that both methods have different design targets. Therefore, the question arises when to use superposition pulses and when to use PINS based pulses. It has shown that the combination of conventional superposition pulses and PINS yields good intermediate results [179]. With Multi PINS it is possible to combine the beneficial low power requirements of PINS pulses with the higher TBWP of superposition pulses. This is realized by using VERSE on the superposition pulse and using the time of the slice selective gradient blips for RF transmission. This reduces peak RF amplitude and power and can be used to further reduce the overall RF pulse duration. Column 3 of Figure 5.9 shows a MultiPINS example with a mixing ratio of 0.5, see [179], reducing  $B_{1,max}$  from 31.72  $\mu\text{T}$  by roughly 50% to 15.99  $\mu\text{T}$ .

## 5 RF pulse design

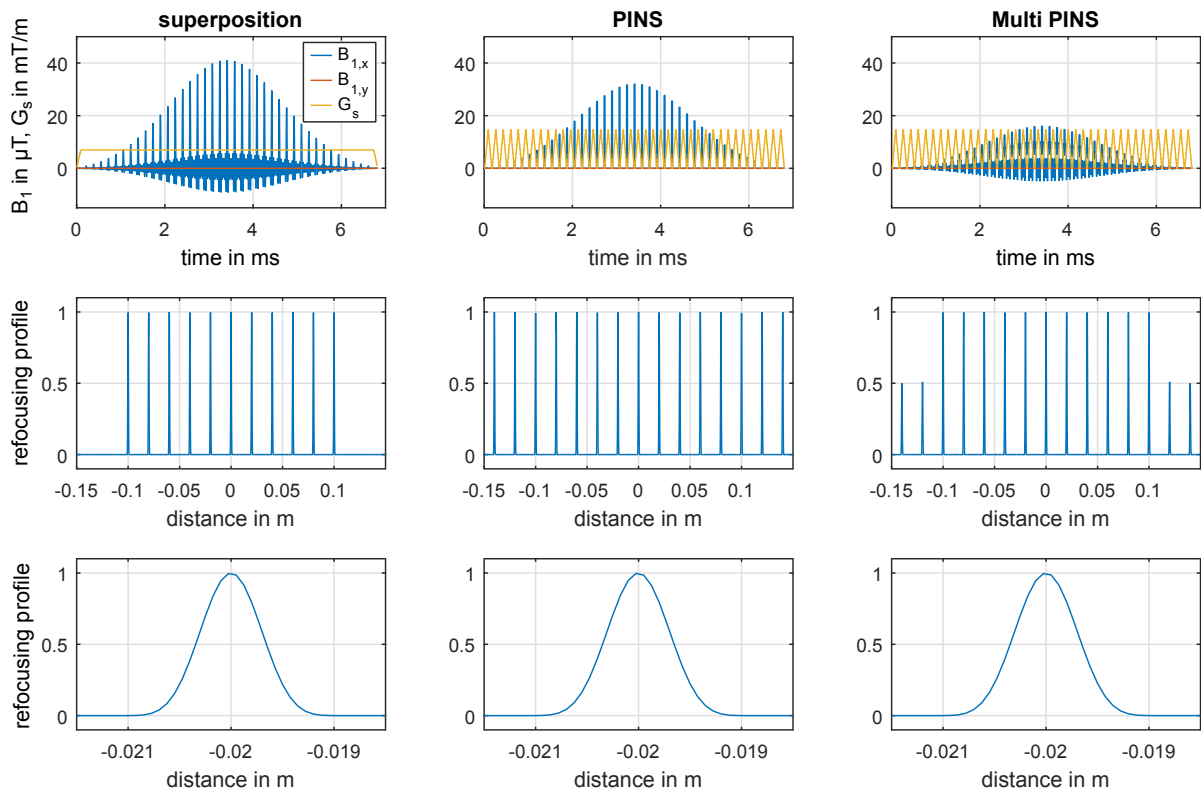


Figure 5.9: Comparison of superposition (Column 1), PINS (Column 2) and MultiPINS (Column 3) pulses with the same pulse duration and different peak RF amplitudes. The Bloch simulations (magnitude) are shown in Row 2 and 3 (zoom to one slice) respectively.

## 5.6 Slice selective RF pulse design via optimal control

Optimal control theory goes back to the 17th century and became widely used with the development of digital computers for various applications [181] including flight path optimization, feedback control and RF pulse design for NMR and MRI applications. This includes the design of RF pulses for slice selective excitation in MRI [120], coupled spin systems in NMR [155], [156], NMR and MRI contrast optimization [152], [182], multidimensional parallel transmission [47], [49] and robust 2D spatial selective excitation [153]. For modern OC theory the reader is referred to the monography [183]. There are various ways to compute the optimal solution and the following will therefore focus on the methods used in [1]–[3] to design RF pulses for single slice selective and SMS applications with and without constraints on the controls.

The general idea of optimal control based RF pulse design is to compute the RF and slice selective gradient shapes summarized by  $u(t)$  (control variables), that minimize a cost functional  $J(M, u)$  containing the discrepancy of the simulated and desired magnetization (state variables) and a penalty function related to the control variables. The Bloch equations in the rotating frame, see Section 2.5, are defined by the differential equation

$$\begin{cases} \dot{M}(t, z) = A(u(t), z)M(t, z) + b(z), & t > 0, \\ M(0, z) = M^0(z), \end{cases} \quad (5.26)$$

with the magnetization  $M$ , the controls  $u(t) = (B_{1,x}(t), B_{1,y}(t), G_s(t))^T$  describing the real and imaginary RF pulse and the slice selective gradient shape [26]. The system matrix  $A$  is defined as

$$A(u; z) = \begin{pmatrix} -\frac{1}{T_2} & \gamma G_s(t)z & -\gamma B_{1,y}(t) \\ -\gamma G_s(t)z & -\frac{1}{T_2} & \gamma B_{1,x}(t) \\ \gamma B_{1,y}(t) & -\gamma B_{1,x}(t) & -\frac{1}{T_1} \end{pmatrix}, \quad b(z) = \begin{pmatrix} 0 \\ 0 \\ \frac{M_0}{T_1} \end{pmatrix}, \quad (5.27)$$

for each time point  $t \in [0, T]$  and spatial point  $z \in [-z_{min}, z_{max}]$ .

The RF pulse design problem with a constant slice selective gradient waveform can be formulated as a quadratic tracking problem starting from a given initial magnetization  $M^0(z)$  and initial controls  $u^0(t) = (B_{1,x}(t), B_{1,y}(t))^T$  to find  $u(t)$  that

## 5 RF pulse design

results in a  $M(T, z)$  as close as possible to a desired magnetization  $M_d(z)$  for a spatial region covered by  $z_{min}$  and  $z_{max}$  at the read-out time  $T$ , for instance by solving

$$\min_{(u, M) \text{ s.t. (5.26)}} J(M, u) = \frac{1}{2} \int_{-z_{min}}^{z_{max}} |M(T, z) - M_d(z)|_2^2 dz + \frac{\mu_{RF}}{2} \int_0^T |u(t)|_2^2 dt, \quad (5.28)$$

with the regularization parameter  $\mu_{RF}$  to balance between slice profile accuracy and RF power requirements.

The first RF pulse design application for MRI via OC [120] were proposed in 1986 using a steepest descent approach to iteratively update the controls  $u(t)$ . This formulation comes with the hurdle of choosing an appropriate step size to determine the size of the update step. While a too small step size results in slow convergence and long computation times, large step sizes are associated with an instability issue [120]. The iterative steepest descent scheme is performed until the change of the cost  $J$  becomes close to zero, hence, fulfilling the first-order condition for an optimal set of controls  $u(t)$  in a local optimum. The final control variables  $u(t)$  then describe the optimal RF pulse with respect to the cost function  $J$ . The RF pulse design via optimal control can be achieved using various other minimization methods including gradient [47], [49] or approximate second-order methods [184].

The optimal control approaches presented in the following sections use Newton-type methods where the Newton equations are solved with the conjugate gradient method (CG) embedded in a Steihaug trust-region framework [185]. In the following sections two different applications, the design of single slice selective RF pulses (5.6.1) and slice selective SMS RF pulses (5.6.2) are presented. Therein, two different Bloch models, based on the fully time dependent Bloch equations in the magnetization domain [1] and the spin domain with neglected relaxation terms [2], [3] are used for a fixed [1], [2] and a variable pulse duration [3]. Different second-order methods are used in the optimization, including Newton [1], semismooth Newton or quasi-Newton methods [2], [3].

### 5.6.1 Single slice selective RF pulse design via OC

This chapter describes two optimal control approaches for the unconstrained and constrained design of RF pulse and slice selective gradient shapes for single slice selective excitation [1] based on the fully time dependent Bloch equations. The first

## 5 RF pulse design

section contains a brief description of the unconstrained optimal control framework and its limitation with respect to strict hardware limitations on the RF and slice selective gradient waveform. These limitations are included in the optimal control framework and described in the second section.

### Unconstrained joint design of RF pulse and slice selective gradient shape

First, only the real RF pulse waveform  $B_{1,x}(t)$  is optimized. The imaginary part of the RF pulse  $B_{1,y}(t)$  and the selective gradient shape  $G_s(t)$  are not part of the optimization and are set to zero and to a trapezoidal shape, respectively. Therefore, the controls  $u(t)$  are equivalent to  $B_{1,x}(t)$ . The optimization consists of minimizing the functional

$$\min_{(u, M) \text{ s.t. (5.26)}} J(M, u) = \frac{1}{2} \int_{z_{min}}^{z_{max}} |M(T, z) - M_d(z)|_2^2 dz + \frac{\mu_{RF}}{2} \int_0^T |B_{1,x}(t)|_2^2 dt, \quad (5.29)$$

at the end of the excitation time  $t = T$  that is evaluated at discrete spatial points  $z$  ranging from  $z_{min}$  to  $z_{max}$ .

The optimal RF shape  $B_{1,x}(t)$  is computed by minimizing  $J$ , see Eq. 5.29. In contrast to gradient methods that compute the update

$$u^{k+1} = u^k - s^k g(u^k), \quad (5.30)$$

for a step length  $s^k$  and the gradient  $g(u^k)$  of Eq.5.29, the application of the Newton's method requires an additional derivative. However, the computation of the full Hessian  $H(k)$  is in practice computationally expensive. The computation of the full Hessian can be prevented using Krylov methods such as CG that only require to compute the Hessian action  $H(u^k)h$  for a given direction  $h$  in each iteration. This reduces the computational effort dramatically to the cost of a gradient evaluation [1], [186]. To achieve accurate derivative information the gradient and the action of the Hessian are computed using the adjoint method. This is achieved solving the forward Bloch equations, see Eq. 5.26, and adjoint (backward in time) Bloch equations

$$\begin{cases} -\dot{P}(t; z) = A(u(t); z)^T P(t; z), & 0 \leq t < T, \\ P(T; z) = M(T; z) - M_d(z), \end{cases} \quad (5.31)$$

## 5 RF pulse design

with  $P$  being the solution to the adjoint Bloch equation. The gradient can be then calculated efficiently by

$$g(u^k)(t) = \mu_{RF}u(t) + \begin{pmatrix} \int_{-z_{min}}^{z_{max}} M(t;z)A_1P(t;z) dz \\ \int_{-z_{min}}^{z_{max}} M(t;z)A_2P(t;z) dz \end{pmatrix}, \quad 0 \leq t \leq T, \quad (5.32)$$

with

$$A_1 := \begin{pmatrix} 0 & 0 & 0 \\ 0 & 0 & -\gamma \\ 0 & \gamma & 0 \end{pmatrix}, \quad A_2 := \begin{pmatrix} 0 & 0 & -\gamma \\ 0 & 0 & 0 \\ \gamma & 0 & 0 \end{pmatrix}. \quad (5.33)$$

The computation of the Hessian action  $H(u^k)h$  is done accordingly by differentiating Eq. 5.32 with respect to  $u$  and  $h$ , see [1] and 9.1.2 in the Appendix. To ensure practical application of the CG Newton method and to guarantee convergence from any arbitrary initial  $u(t)$ , the Newton's method is embedded into a Steihaug CG trust-region [185] framework. This, however, does not imply the determination of the globally optimal solution, but the convergence to a local minimum is guaranteed. In the Steihaug CG trust-region framework a breakdown of the CG method is handled by a trust-region step. Additional checks before the application of the update step on curvature, step size and actual cost decrease allow us to use the CG method for minimizing a quadratic function with a trust-region radius that is adapted iteratively. The full algorithm and discretization required for numerical optimization are given in [1] as well as in 9.1.7 and 9.1.8 in the Appendix.

As an exemplary result, the optimal RF pulse shape  $B_{1,x}(t)$  with respect to a Gauss-filtered rectangular slice with a THK of 5 mm and a flip angle of  $90^\circ$  ( $M_d(z)$ ) is shown in Row 1 of Figure 5.10 [187]. The optimization is initialized with a zero RF pulse and has a fixed duration of 2.56 ms ( $\tau = 10 \mu\text{s}$ ). The refocusing gradient is not part of the optimization and is fixed to half of the gradient moment of the slice selective gradient. The spatial domain consists of 2001 equidistant discrete samples to incorporate a distance of  $\pm 0.2$  m. The Bloch simulation at the end of the gradient refocusing is shown and compared to experimental GRE magnitude reconstruction of the measured slice profile. The choice of the regularization parameter  $\mu_{RF}$  in Eq. 5.29 is done with respect to the best ratio between the slice profile accuracy, RF peak amplitude and RF power requirements. Figure 5.11 shows this for different optimization runs with different regularization parameters to find the best value for the optimization of a MB6 excitation pulse used in [1] and shown in Figure 5.16.

The extension to a joint design of both the RF shape and the slice selective gradient shape is straight forward. The vector notation of the optimization enables direct extension of the controls to include the slice selective gradient in the optimization as well. Besides tracking to a desired  $M_d$  this allows for reduction of the RF power

## 5 RF pulse design

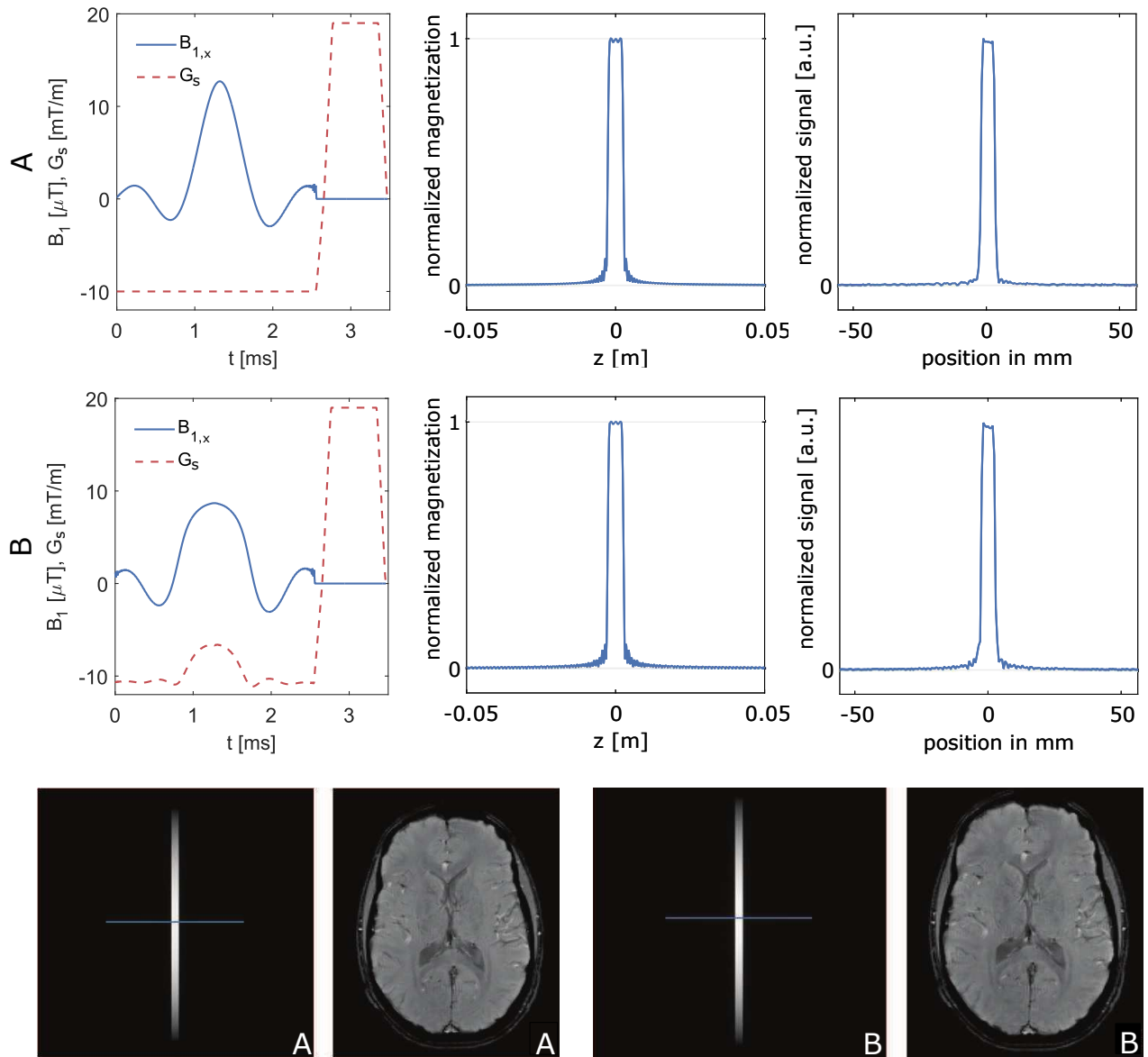


Figure 5.10: RF only (Row 1) and joint RF/ $G_s$  (Row 2) optimization (left) together with the simulated (middle) and measured transverse magnetization (right). Row 3 shows the experimental phantom and in vivo magnitude reconstructions using the RF and gradient shapes RF only (A) and joint RF/ $G_s$  (B) [187].

## 5 RF pulse design

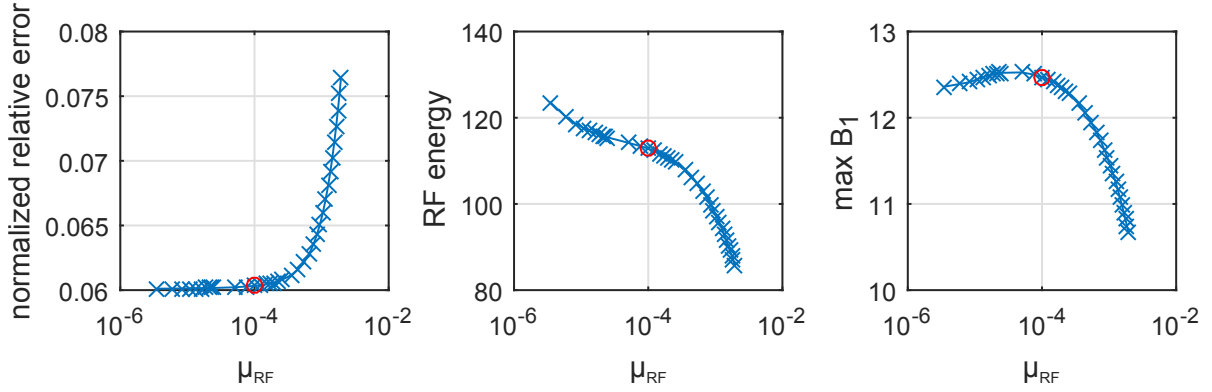


Figure 5.11: Optimized SMS pulses with different regularization parameter  $\mu_{RF}$ . The relative error is defined as the normalized point-wise Euclidean norm  $\|M - M_d\|_2^2 / \|M_d\|_2^2$  and the average RF energy is  $\|B_1\|_2^2$ . The red circle depicts the  $\mu_{RF}$  used in [1].

requirements of the RF pulse by changing the k-space velocity, a similar effect as described in Section 5.4 (VERSE). However, the slice selective gradient is changed here in each iteration simultaneously with the RF pulse.

The optimization results for a joint optimization of RF and slice selective gradient is depicted in Row 2 of Figure 5.10. Again, the optimization is started with a zero RF pulse and the trapezoidal slice selective gradient with respect to the same parameters as stated above. Now, the first 256 samples of the slice selective gradient are modified in the optimization, thus leading to simultaneous reduction and stretching of both, the RF and slice selective gradient shape to reduce the RF power present in the cost function Eq. 5.29. This reduces the RF power by 30% with only a low increase of the mean squared error (0.26% to 0.31%). The peak slew rate of the optimized gradient ( $120 \text{ T m}^{-1} \text{ s}^{-1}$ ) remains below the prescribed maximal rate ( $180 \text{ T m}^{-1} \text{ s}^{-1}$ ) of the used system. It should be noted, however, that the optimization is unconstrained and depending on the regularization parameters the optimized waveforms may violate MR scanner hardware limits. An experimental comparison of the two optimized results is depicted in Row 3 of Figure 5.10 for a standard GRE in vivo scan and a modified GRE phantom scan to directly measure the slice profile, see Section 4.2. The intersection line depicts the position of the profile. The joint design yields sharp slice profiles and reduced RF power requirements without the need of explicit power reduction techniques such as VERSE [112], see Section 5.4. The matrix-free implementation allows computation of a larger number of temporal and spatial control points compared to the gVERSE [188] approach that is limited with 15 spatial points. Depending on the regularization parameters it is possible to compute pulses with an even lower SAR depending on hardware limitations, in particular the gradient slew rate.

### Constrained joint design of RF pulse and slice selective gradient shape

The design approach described before enables an unconstrained optimization of both the RF pulse and slice gradient shape at a high spatial and temporal resolution [1]. However, the optimized results could exceed physical constraints and therefore may not be realized on a real MR scanner. To include hard constraints of actual MR hardware, the previously introduced framework is extended to a trust-region semismooth Newton method to include physical constraints such as the peak  $B_1$  amplitude of the RF pulse and the slew rate of the gradient system [2].

The optimization is again based on minimizing the difference between the forward Bloch simulation at the end of the pulse duration  $M(T, z)$  and the desired magnetization  $M_d(z)$ . Three additional cost terms model the power of the RF pulse  $B_{1,x}$ , the slew rate  $\dot{G}_s$  and the final amplitude of  $G_s$

$$\begin{aligned} \min_{(u, M) \text{ s.t. (5.26)}} J(M, u) = & \frac{1}{2} \int_{-z}^z |M(T; z) - M_d(z)|_2^2 dz + \frac{\mu_{RF}}{2} \int_0^T |B_{1,x}(t)|_2^2 dt \\ & + \frac{\mu_{G_s}}{2} \int_0^T |\dot{G}_s(t)|_2^2 dt + \frac{\mu_s}{2} |G_s(T)|_2^2, \end{aligned} \quad (5.34)$$

with the regularization parameters  $\mu_{RF}$ ,  $\mu_{G_s}$ ,  $\mu_s$ . To include peak RF and slew rate amplitude constraints, these are added as point-wise inequality constraints on the control variables  $u(t)$ :

$$|B_1|_\infty \leq B_{1,max} \quad \text{and} \quad |\dot{G}_s|_\infty \leq \dot{G}_{s,max}. \quad (5.35)$$

Now, the Newton method is not applicable any longer due to a resulting set of nonsmooth equations [2]. However, such problems can be efficiently solved with generalized semismooth Newton methods [190] based on projections without increasing the computational effort. The semismooth Newton-derivative can be evaluated for the Hessian action similar to the unconstrained design [1]. In addition to the efficient application, semismooth Newton methods converge locally superlinear which makes them an highly efficient method for OC problems with inequality constraints [2]. Again, the gradient and Hessian information are computed with the adjoint calculus. The generalized semismooth Newton method is embedded in a Steihaug CG trust-region framework [185], [191].

Figure 5.12 compares a conventional Hamming filtered SINC pulse with the results of the unconstrained optimization together with the constrained optimization (peak RF magnitude  $B_{1,max} = 13 \mu\text{T}$ , peak slew rate  $\dot{G}_s = 175 \text{ mT m}^{-1} \text{ s}^{-1}$ ) [189]. The Bloch simulations show a well-defined slice profile for all three examples. However, only

## 5 RF pulse design

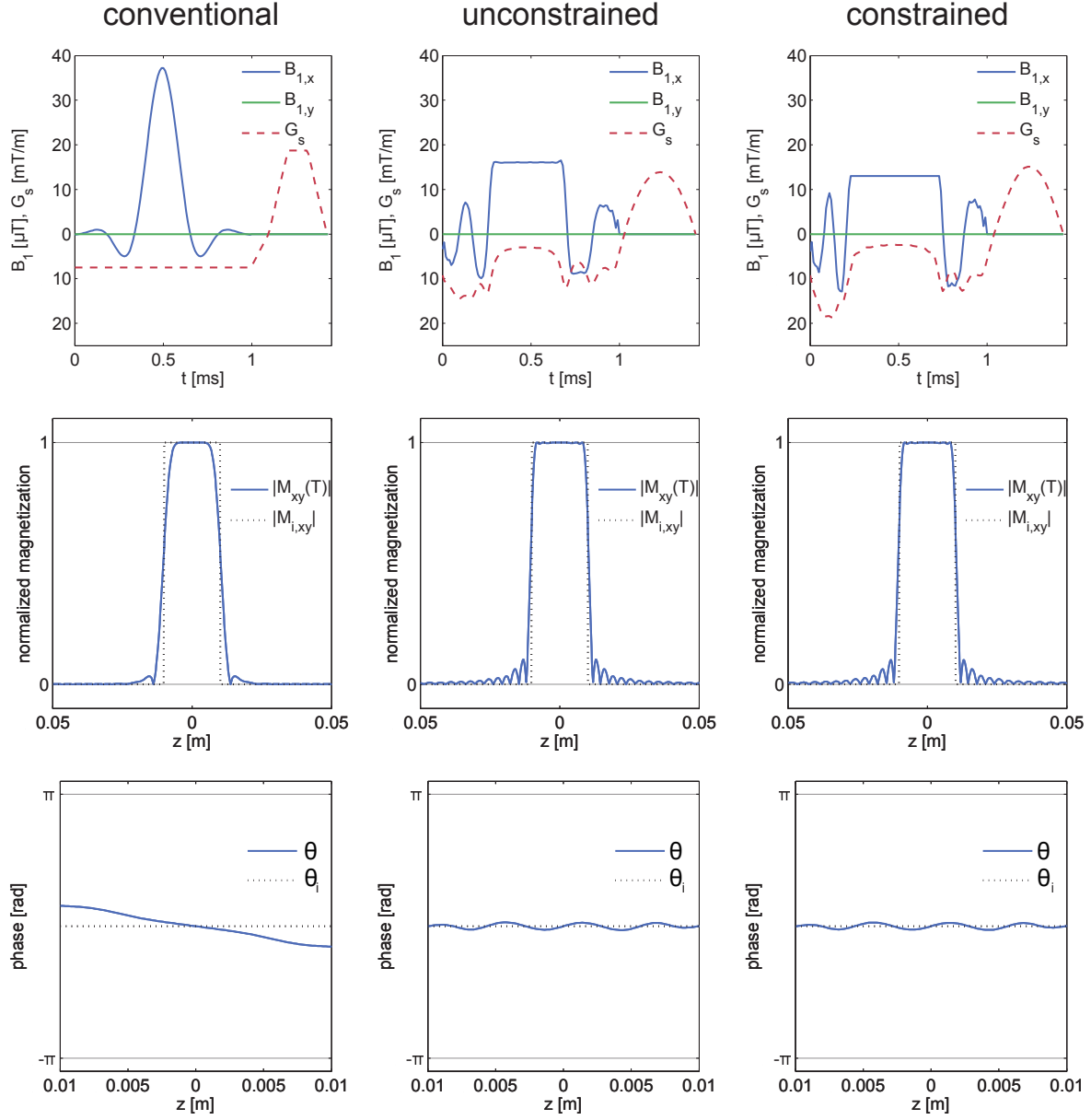


Figure 5.12: Conventional Hamming window filtered SINC with standard trapezoidal gradient slope, low SAR optimized unconstrained and constrained RF and  $G_s$  shapes (both with  $\mu_{RF} = 5e - 4$ ,  $\mu_{G_s} = 3e - 4$ ,  $\mu_s = 1.25$ ), second line: simulated ( $M_{xy}$ ) and ideal transverse magnetization ( $M_{i,xy}$ ), third line: simulated and ideal phase ( $\theta$  and  $\theta_d$ ) [189].

## 5 RF pulse design

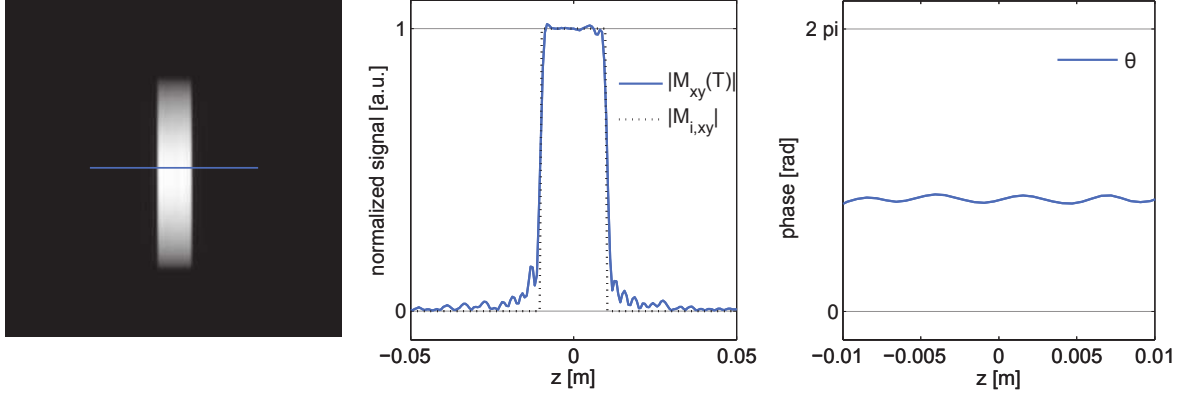


Figure 5.13: Measured phantom slice profile of the constrained optimized RF and slice selective gradient shape ( $B_{1,max} = 13 \mu\text{T}$ , peak slew rate  $\dot{G}_s = 175 \text{ mT m}^{-1} \text{ s}^{-1}$ ) together with the measured relative in-slice phase  $\theta$  [189].

Table 5.2: Comparison of  $B_1$  and  $\dot{G}_s$  peak,  $B_1$  power and root mean squared error (RMSE) and mean absolute error (MAE) for the optimized pulses [189].

	$\ B_{1,x}\ _\infty$ [ $\mu\text{T}$ ]	$\ \dot{G}_s\ _\infty$ [ $\text{Tm}^{-1}\text{s}^{-1}$ ]	$\ B_{1,x}\ _2^2$ [a.u.]	RMSE [a.u.]	MAE [a.u.]
conventional	37.18	170.5	191.6	0.0892	0.0232
unconstrained	16.49	214.4	129.3	0.0498	0.0113
constrained	13.0	175	114.7	0.0499	0.0113

## 5 RF pulse design

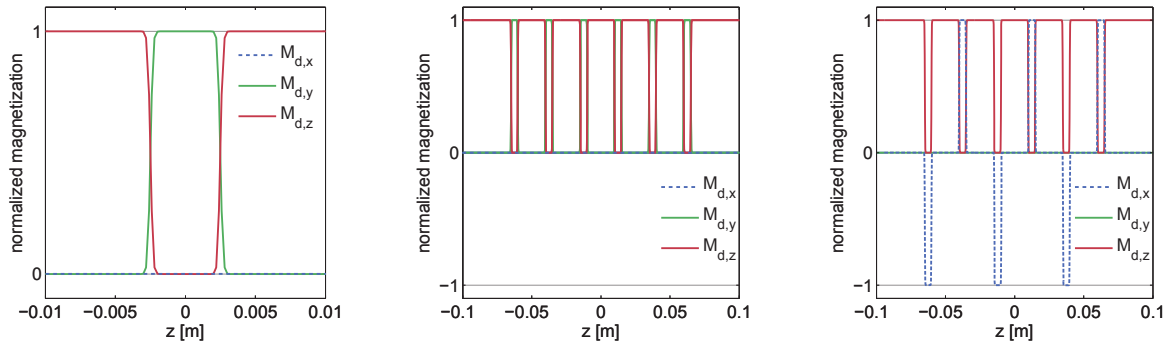


Figure 5.14: Desired magnetization  $M_d$  for single (a) and SMS design with 6 slices with different phase patterns (b,c) [1].

the constrained results are directly applicable on the MR scanner. The unconstrained results violate the hardware limitations and have to be stretched in time to reduce peak RF and slew rate of the slice selective gradient. The numerical simulations are validated by magnitude and phase images of experimental 3 T phantom measurements in Figure 5.13. The significant key features are summarized in Table 5.2. Despite using a constrained optimization, the optimized pulses achieve a similar slice profile compared to the unconstrained optimization while having the benefit of guaranteed practical applicability.

### 5.6.2 SMS RF pulse design via OC

The OC based design method introduced in the previous Section 5.6.1 can be easily extended to the design of SMS pulses and gradient shapes. For this purpose, the desired magnetization is changed to contain more than one slice, for instance six equidistant slices, as shown in Figure 5.14. The following sections describe the unconstrained and constrained design of SMS RF pulses with fixed pulse duration and optimized pulse duration.

#### Unconstrained SMS excitation

The unconstrained OC approach to design SMS RF pulse shapes is done in a similar way to Section 5.6.1 and consists of minimizing the discrepancy between the numerical solution of the fully time-dependent Bloch equations and a prescribed magnetization profile together with a cost term modeling the pulse power, see Eq. 5.29. The use of different desired magnetization patterns, see Figure 5.14, now results in SMS RF

## 5 RF pulse design

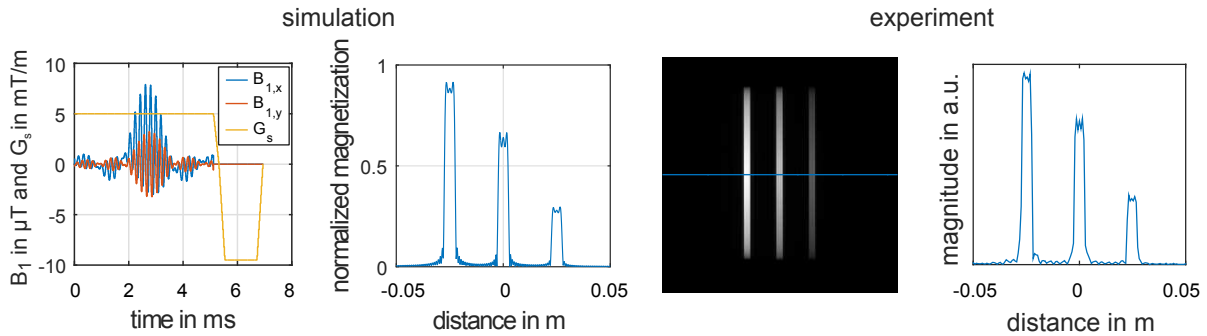


Figure 5.15: Optimized SMS RF pulse for three slices with different flip angles ( $\phi = (65, 35, 15)^\circ$ ) and experimental phantom reconstruction [193].

pulses. The source code used to generate the examples can be downloaded from <https://github.com/chaigner/rfcontrol/releases/v1.2> [1].

This approach was applied to compute RF pulses for a simultaneous excitation, considering a z-range of 400 mm with a spatial resolution of 0.02 mm and a thickness of 5 mm for each slice. The high spatial resolution is important to suppress a modulation of the magnetization. The pulses were designed for a total excitation time  $T = 2.56$  ms and consisted of 256 samples. For each slice, a flip angle of  $25^\circ$  [192] or  $90^\circ$  was specified [1], see also Figure 5.14. Alternatively, the OC-based design approach allows for the choice of any arbitrary desired magnetization pattern, for instance choosing different flip angles for individual slices [193]. This is exemplary shown in Figure 5.15 for an optimized complex SMS excitation pulse to excite three slices with different flip angles ( $\phi_i = (65, 35, 15)^\circ$ ). The numerical results are imported to the previously described GRE sequence to perform phantom and in vivo measurements.

Figure 5.16 shows optimized RF pulses ( $B_{1,x}$ ,  $B_{1,y}$ ) together with the prescribed slice selective gradient  $G_s$ , the corresponding simulated slice profiles and the central line of the reconstructed phantom magnitude images for a flip angle of  $90^\circ$ . To separate aliased slice information in the case of in vivo imaging, we use the slice-GRAPPA (sG) algorithm [172] with reference scans of 24 phase encoding lines per slice. Since the reconstruction starts to suffer from g-factor problems for more than three slices, we modified the above-described SMS pulses using a CAIPIRINHA-based excitation pattern [171], which alternates two different pulses to achieve phase-shifted magnetization vectors in order to increase the spatial distance of aliased voxels by a factor of  $\text{FOV}/2$  for every second slice. As it can be seen in Row 2 of Figure 5.16, the optimized pulses lead to the desired excitation pattern while the remaining columns show the sG reconstructions, which illustrate the uniform excitation and the applicability of the optimized pulses for in vivo experiments.

## 5 RF pulse design

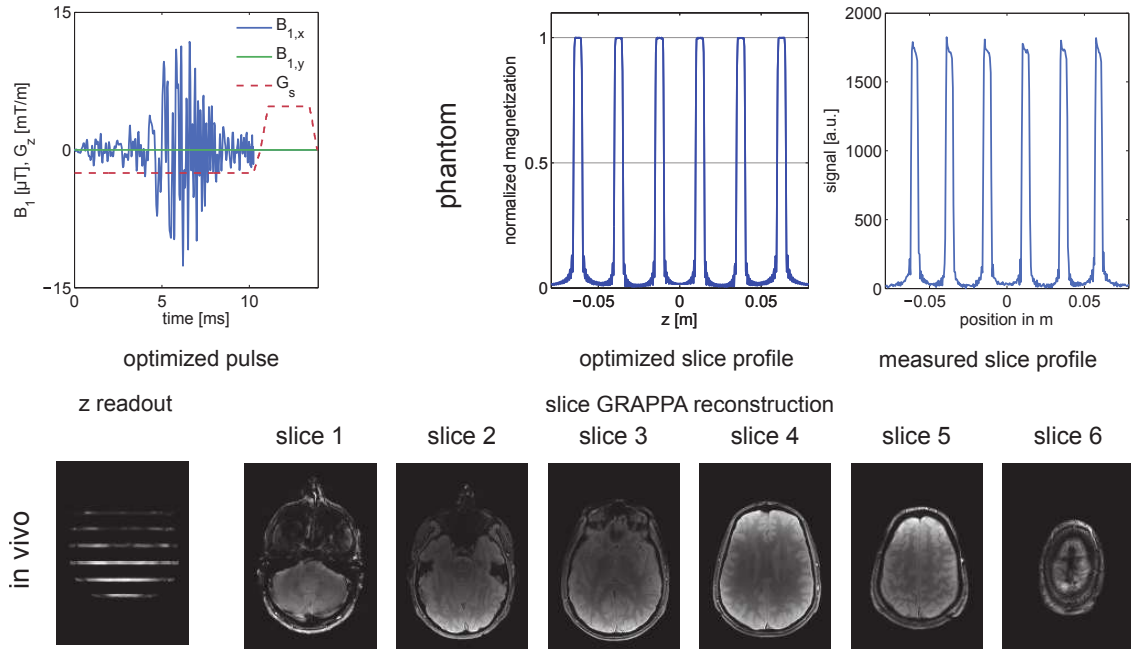


Figure 5.16: Optimized RF pulse for six slice profiles, each with a flip angle of  $90^\circ$  together with simulated magnetization patterns and experimental phantom measurements (Row 1). Cartesian and slice-GRAPPA reconstruction using CAIPIRINHA-based SMS excitation (Row 2) [1].

The simulation and optimization of the full time dependent Bloch equations with the Crank–Nicolson method [1] turned out to introduce numerical errors [71] that were not visible in the numerical simulations and experimental validation. This error increases for off-resonant positions and leads to a slice shift and dephasing. This numerical errors can be effectively reduced by increasing the temporal discretization. Figure 5.17 shows two optimization runs for six slices and compares forward simulations with the Crank–Nicolson method and spin domain Bloch simulations. The differences in the transversal magnetization are minimized by the finer temporal discretization in Row 2. A more extensive analysis of different numerical methods to solve the Bloch equations with and without relaxation times is covered in [68].

## 5 RF pulse design

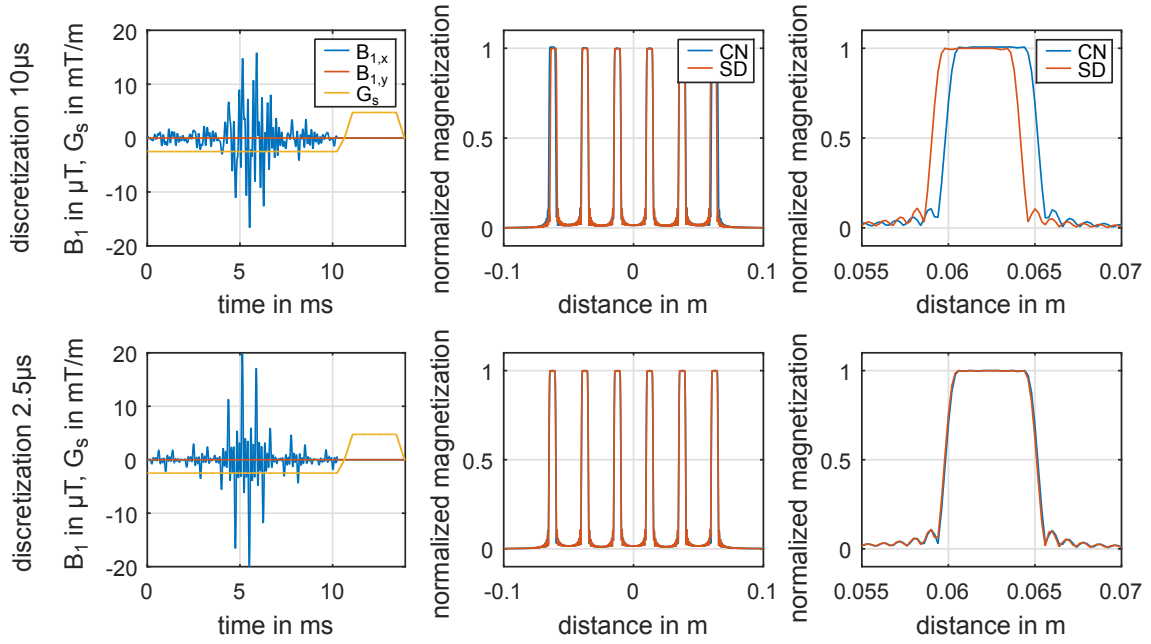


Figure 5.17: Optimized SMS excitation pulses using the numerical Bloch Crank–Nicolson (CN) model with different temporal sampling (Row 1:  $\tau = 10 \mu\text{s}$  and Row 2:  $\tau = 2.5 \mu\text{s}$ ) together with simulated transverse magnetization using Crank–Nicolson and spin domain (SD) Bloch equations.

### Constrained SMS refocusing

The joint design of RF and slice selective gradient shape via OC [1] can be extended to the spin domain Bloch equations using the Cayley-Klein parameters  $a$ ,  $b$  [2]

$$\begin{aligned} a_m &= \alpha_m a_{m-1} - \beta_m^* b_{m-1}, \\ b_m &= \beta_m a_{m-1} + \alpha_m^* b_{m-1}, \end{aligned} \quad (5.36)$$

and  $\alpha$ ,  $\beta$  defined in Eq. 3.15 together with the initial conditions  $a_0 = 1$ ,  $b_0 = 0$ . The controls  $x$  are the complex RF pulse  $B_{1,m} = r_m \exp(i\vartheta_m)$  and the slice selective gradient slew rate  $s_m = g_m - g_{m-1}/\tau$  for each discrete time point  $m$ . Contrary to the previously described design of single and SMS excitation pulses, SMS refocusing pulses are designed in the spin domain assuming perfect crusher gradients. Therefore, the desired refocusing profile (magnitude and phase) at the end of the refocusing time  $T$  is defined in-slice as  $1 - |\beta(z)|^2 \leq e_{\text{in}}$ , out-of-slice as  $|\beta(z)|^2 \leq e_{\text{out}}$  together with a in-slice phase constraint  $|\varphi - \bar{\varphi}| \leq e_{\text{ph}}$  with the phase  $\varphi$  and desired mean

## 5 RF pulse design

phase  $\bar{\varphi}$  based on the parameter relations in [66] and Tab. 5.1. The optimization is done to minimize the RF energy requirements by minimizing the functional

$$\begin{aligned} \min_{(x) \text{ s.t. (5.36)}} J = & \frac{\tau}{2} \sum_{m=1}^{N_t} r_m^2 + \zeta \vartheta_m^2 + \zeta g_m^2 \\ & + \frac{\delta\mu_{\text{out}}}{2p} \sum_{z_j \in \Omega_{\text{out}}} \left( \frac{|b_{N_t}|^2}{e} \right)^p + \frac{\delta\mu_{\text{in}}}{2p} \sum_{z_j \in \Omega_{\text{in}}} \left( \frac{|b_{N_t}|^2 - 1}{e} \right)^p \\ & + \frac{\delta\mu_p}{p} \sum_{l=1}^L \sum_{z_j \in S_l} \left( \frac{\varphi - \bar{\varphi}_l}{e_p} \right)^p + \frac{\tau\mu_g}{p} \sum_{m=2}^{N_t} \left( \frac{g_m - g_{m-1}}{\tau s_{\text{max}}} \right)^p, \end{aligned}$$

where  $x$  are the control variables,  $p$  is an even positive integer,  $r_m$  the RF amplitude,  $\vartheta_m$  the RF phase,  $g_m$  the slice selective gradient and  $\zeta$ ,  $\mu_{\text{out}}$ ,  $\mu_{\text{in}}$ ,  $\mu_p$  and  $\mu_g$  being the regularization parameters. The regularization parameters are initialized with  $\zeta = 0.01$ ,  $\mu_{\text{out}} = 1e5$ ,  $\mu_{\text{in}} = 1e4$ ,  $\mu_p = 1$  and  $\mu_g = 1$ . To balance between the different terms the regularization parameters are being adapted throughout the optimization [2]. Hard amplitude constraints on the RF amplitude ( $0 \leq r \leq B_{1,\text{max}}$ ), RF phase ( $-\pi \leq \vartheta \leq \pi$ ) and slew rate of the slice selective gradient ( $-s_{\text{max}} \leq g_m - g_{m-1} \leq s_{\text{max}}$ ) are included for the controls. The resulting set of nonsmooth equations are solved for a fixed  $p$  by a semismooth quasi-Newton method [190] that is embedded in a Steihaug CG trust-region framework [185], [191]. Throughout the optimization, the parameter  $p$  is successively increased starting with a small number, for instance  $p = 2$ , until the minimum pulse energy is found. For a full description refer to [2], or 9.2.2, 9.2.3 and 9.2.7 in the Appendix.

The proposed algorithm is tested to reduce the power requirements of different SMS pulses including superposition, PINS and root flipping as well as examples given by the ISMRM Challenge 2015 test set [83] for a fixed pulse duration [2]. To guarantee practical applicability on the MR system used, the time discretization is fixed to a gradient raster time of  $\tau = 10 \mu\text{s}$ . Throughout the optimization, the parameter  $p$  is iteratively increased with a decrease of all  $\mu$  in Eq. 5.37 to find a minimal RF power solution. Figure 5.18 shows an optimized result for SMS refocusing with a MB factor of 6, a THK of 1.75 mm and a TBWP of 4 starting from a root flipping [173] initial for peak RF amplitude  $B_{1,\text{max}} = 13 \mu\text{T}$ , a peak slew rate  $\dot{G}_{s,\text{max}} = 200 \text{ T m}^{-1} \text{ s}^{-1}$ , and a maximum refocusing error of 5% (in-slice) and 4% (out-slice). The phase of the refocusing profiles was not included since root flipping pulses do not have a linear phase profile [173]. Other optimized results are presented in [2] and in 9.2.4 of the Appendix. Optimized SMS pulses with a MB factor of 3 and 10 respectively are implemented on a 3 T MR scanner (Magnetom Skyra, Siemens Healthcare, Erlangen, Germany) using a spin echo sequence with a conventional superposed  $90^\circ$  SLR based SMS excitation pulse. These results are depicted in Figure 5.19 for phantom

## 5 RF pulse design

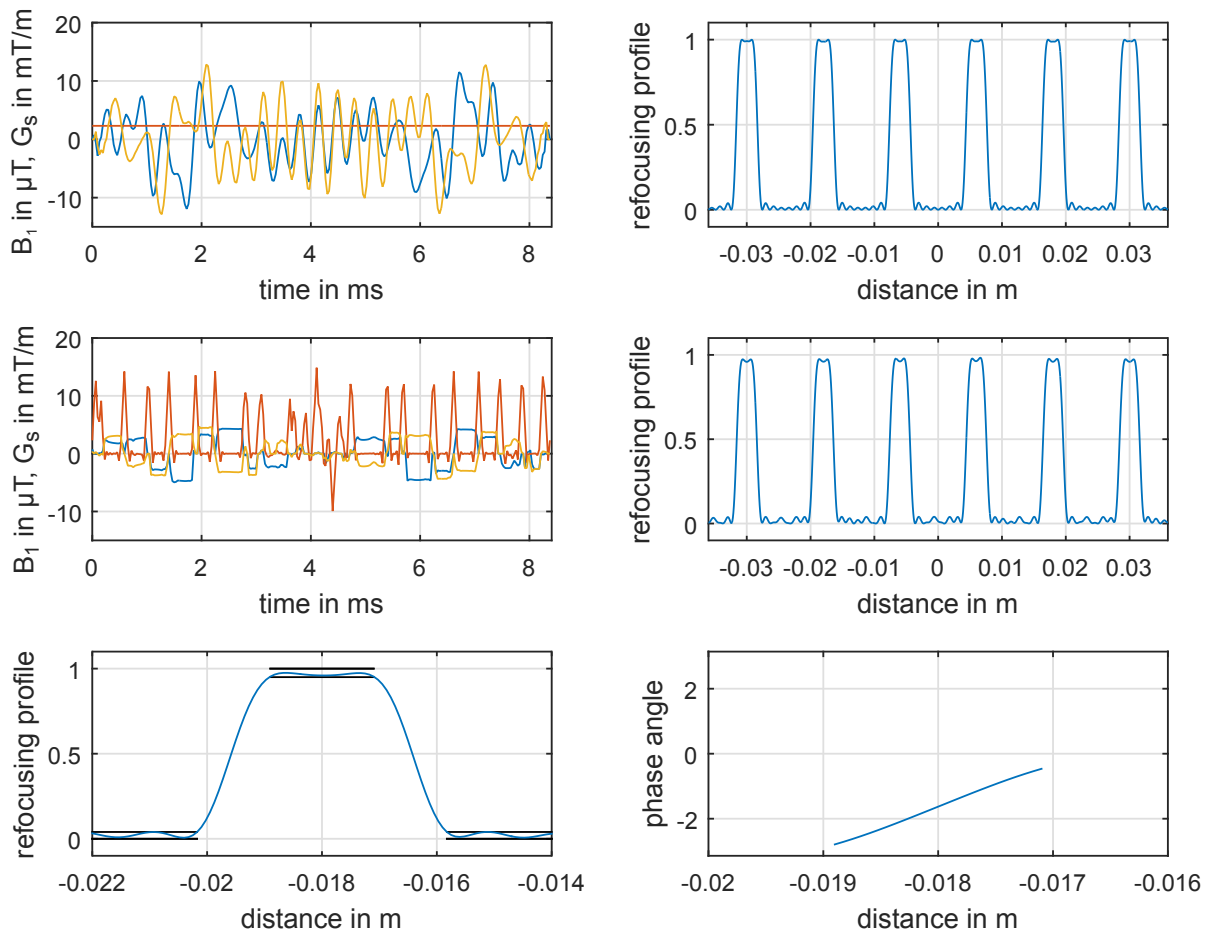


Figure 5.18: Numerical optimization results and spin domain Bloch simulations for a MB6 pulse. Initial (Row 1) and optimized (Row 2) RF and  $G_s$  (Re(RF) in blue, Im(RF) in yellow and  $G_s$  in red) with refocusing profile  $|b_{N_t}|^2$ . Zoom of the central slice (black lines mark the in-slice/out-of-slice error tolerance) with phase angle( $b_{N_t}$ ) (not part of the optimization) for the optimized pulse (Row 3) [2].

and in vivo measurements (TR/TE= 100/25 – 30 ms, FOV= 300 × 300 mm, matrix= 1536 × 1536 with 922 phase encoding steps) and an in vivo scan (TR/TE= 200/15 ms, FOV= 300 × 300 mm, matrix= 512 × 512). The reconstructed high resolution experimental phantom data is further directly compared with the numerical results, thereby validating the Bloch simulations. Across a wide range of parameters the pulse power is dramatically reduced. Both the phantom and in vivo measurements show well defined slices and validate the Bloch simulations, demonstrating the ability to jointly design RF and slice selective gradient shapes with hard inequality constraints.

## 5 RF pulse design

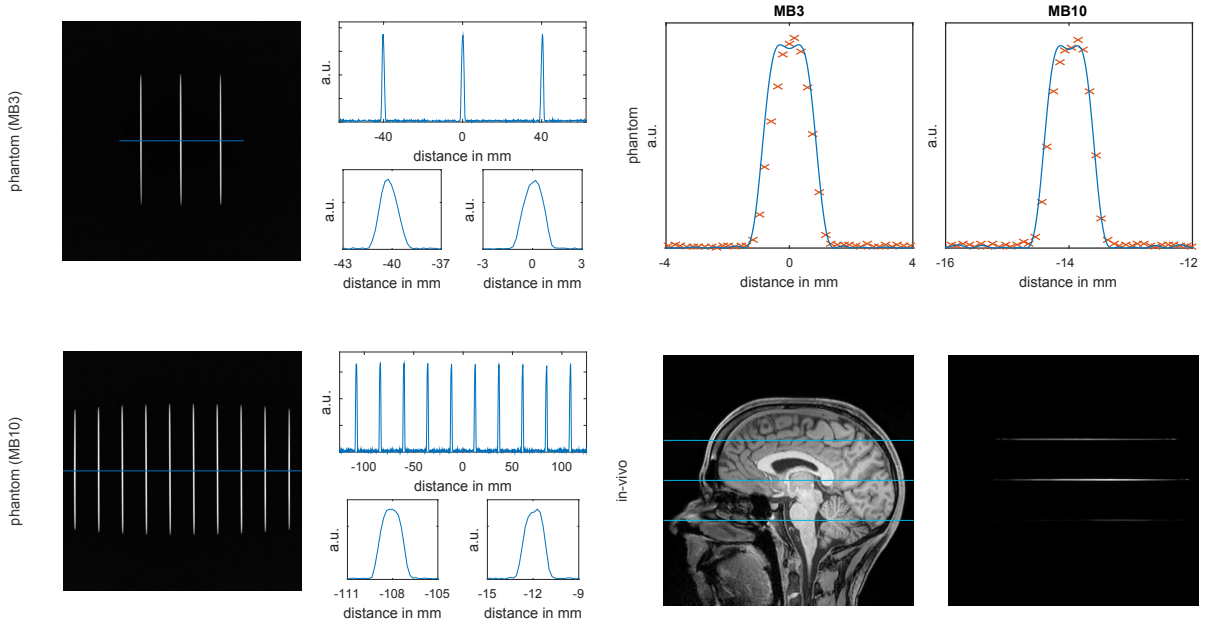


Figure 5.19: Measured experimental data for optimized MB<sub>3</sub> and MB<sub>10</sub> pulses (left). Simulated refocusing profile (solid line) and experimental phantom data (crosses) of the phantom measurements and reconstructed experimental data for in vivo measurements using the optimized MB<sub>3</sub> pulse [2].

### Constrained time optimal SMS refocusing

The constrained joint design of RF pulse and slice selective gradient shape for a fixed pulse duration  $T$  [2] can be extended to reduce the pulse duration  $T$  by a time-OC formulation of the Bloch equations in the spin domain [3]. The terminal time  $T$  is iteratively reduced in a bi-level fashion in the upper-level. The lower-level problem is computed with a fixed  $T$  analogous to the previous Section (Constrained SMS refocusing) until the prescribed constraints on the refocusing profile, refocusing phase and maximal slice selective peak amplitudes are fulfilled and the energy of the RF pulse is sufficiently reduced. Again, hard amplitude constraints on the RF amplitude ( $0 \leq r \leq B_{1,max}$ ), RF phase ( $-\pi \leq \vartheta \leq \pi$ ) and slew rate of the slice selective gradient ( $-s_{max} \leq g_m - g_{m-1} \leq s_{max}$ ) are included for the controls. The reduction of the time duration  $T$  is done in the upper-level by deleting appropriate time points that result in the best performance after deletion followed by an optimization with a fixed  $T$  using a trust-region semismooth quasi-Newton method [2] until an admissible solution has been found. To minimize the deletion effects on the slice profile the deleted RF and slice selective amplitudes are symmetrically distributed to the neighbouring time instances. To exploit all constraints the parameter  $p$  is increased in the upper-level problem throughout the optimization. The performed optimization runs revealed that a further refinement of the time grid in the course of the optimization results

## 5 RF pulse design

in even shorter pulse durations. The refinement, however, has to be used with care with respect to gradient raster time of the MR system. For a full description refer to [3], or 9.3.2 in the Appendix. The source code can be downloaded from <https://github.com/rundar/mr.control>.

To test the general applicability of the proposed design method, we minimized the pulse duration in the test set of 31 cases from the 2015 ISMRM pulse design challenge [83]. The iterative optimization was initialized with PINS [131]-based RF and triangular slice selective gradient shapes with respect to a  $B_{1,max} = 18 \mu\text{T}$ , and  $\dot{G}_{s,max} = 200 \text{ T m}^{-1} \text{ s}^{-1}$ , and a maximum refocusing error of 3% and 2% for in- and out-slice regions respectively. A representative optimized TSE result (MB= 12, TBWP= 3, THK= 1 mm) is depicted in Figure 5.20. The exploitation of the hardware constraints, see Row 1 of Figure 5.20, and a  $p$  driven to large even numbers, allowed for determination of the shown result with a pulse duration  $T$  reduced by 75% from 12.92 ms to 3.16 ms compared to the initial PINS pulse that still fulfils all control constraints. An overview of all optimized 31 examples of the ISMRM challenge [83]

Table 5.3: Comparison of the optimized pulse duration (in ms) with the duration of the PINS initial guess for all examples without constraints on the refocusing phase.

	MB3		MB4		MB5	
THK mm	PINS ms	opt ms	PINS ms	opt ms	PINS ms	opt ms
2.00	16.870	2.155	15.090	2.285	13.560	2.414
1.75	18.460	2.155	16.400	2.448	14.140	2.502
1.50	21.260	2.336	18.470	2.539	16.090	2.651
1.25	24.370	2.470	21.180	2.673	18.320	2.404
1.00	28.840	2.650	25.250	2.805	21.180	2.938

is summarized in Tables 5.3 and 5.4 and compare the time optimal pulse duration with the used PINS initial guesses. The optimized slice selective gradient resulted in a varying k-space trajectory that makes the pulse possibly prone to  $B_0$  off-resonance influences and  $B_1$  inhomogeneities. Figure 5.21 shows Bloch simulations with a constant global  $B_0$  off-resonance variation of  $\pm 200$  Hz and  $B_1$  variation of 75%-125% with stable slice profiles below  $\pm 100$  Hz. To validate the numerical results, the optimized pulses were computed for the gradient raster time of  $\tau = 10 \mu\text{s}$ , which results in a pulse duration of  $T = 3.3$  ms on the 3 T MR scanner (Magnetom Skyra, Siemens Healthcare, Erlangen, Germany) used and imported to a spin echo sequence. Phantom experiments were performed with a conventional SLR based  $90^\circ$  SMS excitation pulse acquiring high-resolution phantom scans ( $TR/TE = 300/30$  ms,  $FOV = 300 \times 300$  mm, matrix =  $960 \times 960$ ) where the phase encoding is applied in slice-direction. The experimental results are shown in Figure 5.22. To validate the

## 5 RF pulse design

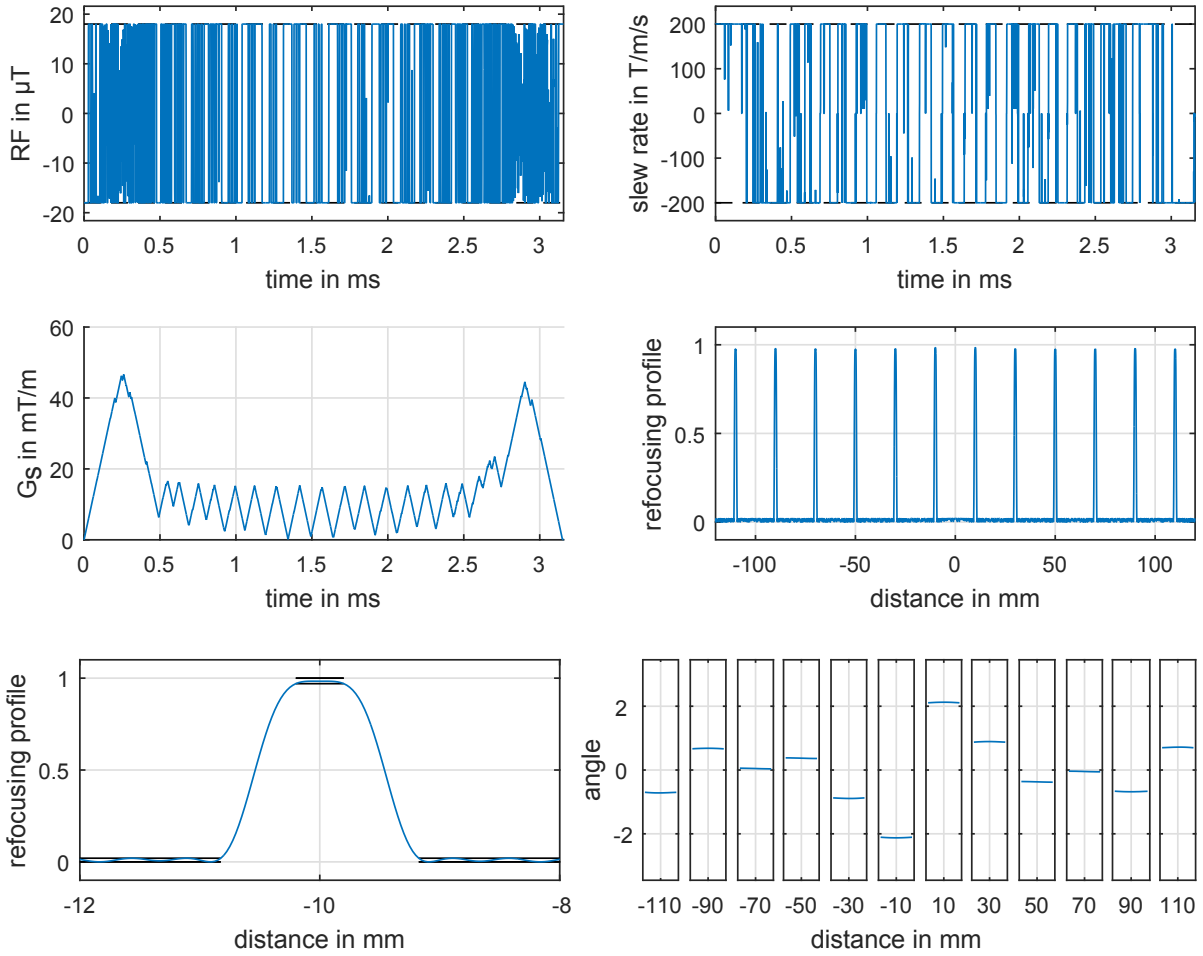


Figure 5.20: Optimization results and Bloch simulations for one representative TSE example. The first row shows the control variables  $B_1$  amplitude and slew rate of the slice selective gradient for the refocusing duration of  $T = 3.16$  ms. The second row depicts the slice selective gradient shape, and the corresponding simulated refocusing profile  $|b_{N_i}|^2$ . The last row shows a detail zoom of one slice to see the refocusing profile together with the error corridor (black), and the phase angle  $\arg(b_{N_i}^2)$  per slice [3].

Table 5.4: Comparison of the optimized pulse duration (in ms) with the duration of the PINS initial guess for all TSE examples.

		MB8		MB10		MB12		MB14	
THK	PINS	opt	PINS	opt	PINS	opt	PINS	opt	
mm	ms	ms	ms	ms	ms	ms	ms	ms	
2.0	10.640	2.742	9.460	2.856	8.810	2.728	8.710	2.809	
1.5	13.260	3.295	11.110	3.213	10.890	3.286	10.300	3.296	
1.0	18.040	3.958	15.170	4.122	14.460	4.120	14.110	3.996	
0.5	32.420	6.106	27.390	6.113	25.230	6.080	24.520	6.189	

## 5 RF pulse design

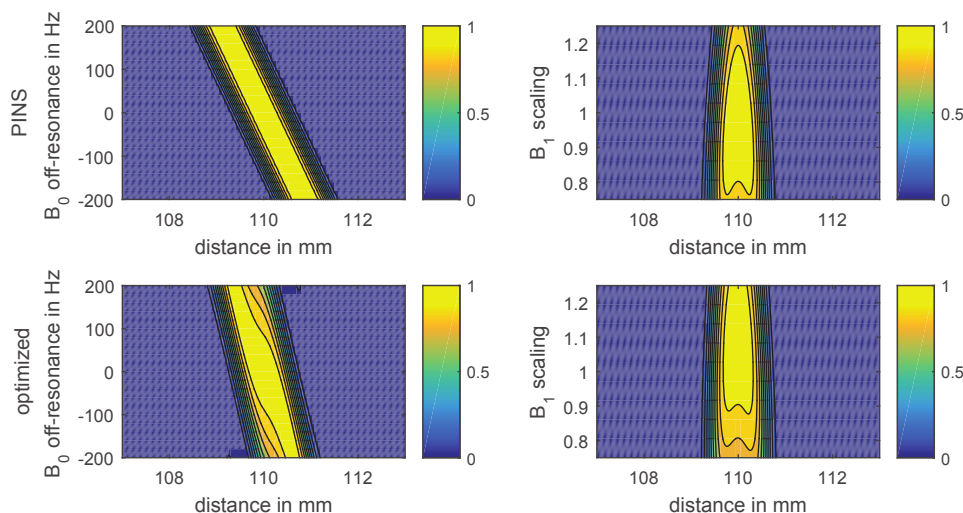


Figure 5.21: Simulated refocusing profiles  $|b_{N_z}|^2$  (zoom to the outermost slice with comparable refocusing profiles across all individual slices) for a variation in the off-resonance and  $B_1$  inhomogeneity for the PINS-based initial and the optimized pulse shown in Figure 5.20 [3].

numerical Bloch simulations the measured slice profiles were normalized for spatial  $B_1$  transmit/receive and signal variations resulting from the used spherical phantom by a fully non-selective reference scan. These normalized slice profiles are depicted in Rows 5 and 6 of Figure 5.22 together with the simulated refocusing profiles (solid). Despite rapidly varying RF and slice selective gradient shapes only minor slice profile degradation can be observed. The small deviations of the outermost slice are likely to be an effect of non-ideal gradients, see Section 4.3 and [119]. In general, the proposed design of minimum duration RF pulse and slice selective gradient shape in the presence of physical and technical constraints guarantees practical applicability and allows the optimized pulses to be integrated in existing EPI or TSE sequences to reduce the echo-spacing or effective echo time. Moreover, the proposed method resulted in the first place in the ISMRM SMS RF pulse design challenge [83] (October 2015 to May 2016, <http://challenge.ismrm.org/node/71>).

### Application to Wave-CAIPIRINHA encoded TSE

The previously introduced constrained time-OC design of SMS pulses was extended to prescribe a fixed mean phase for each individual slice to fulfil the CPMG condition [23] and applied to the design of a Wave-CAIPIRINHA encoded TSE sequence [194]. Therefore, a SMS refocusing pulse (MB = 15, THK = 1 mm, slice gap = 17 mm, TBWP = 2.37) was optimized using a PINS initial guess with respect to  $B_{1,max} = 18$

## 5 RF pulse design

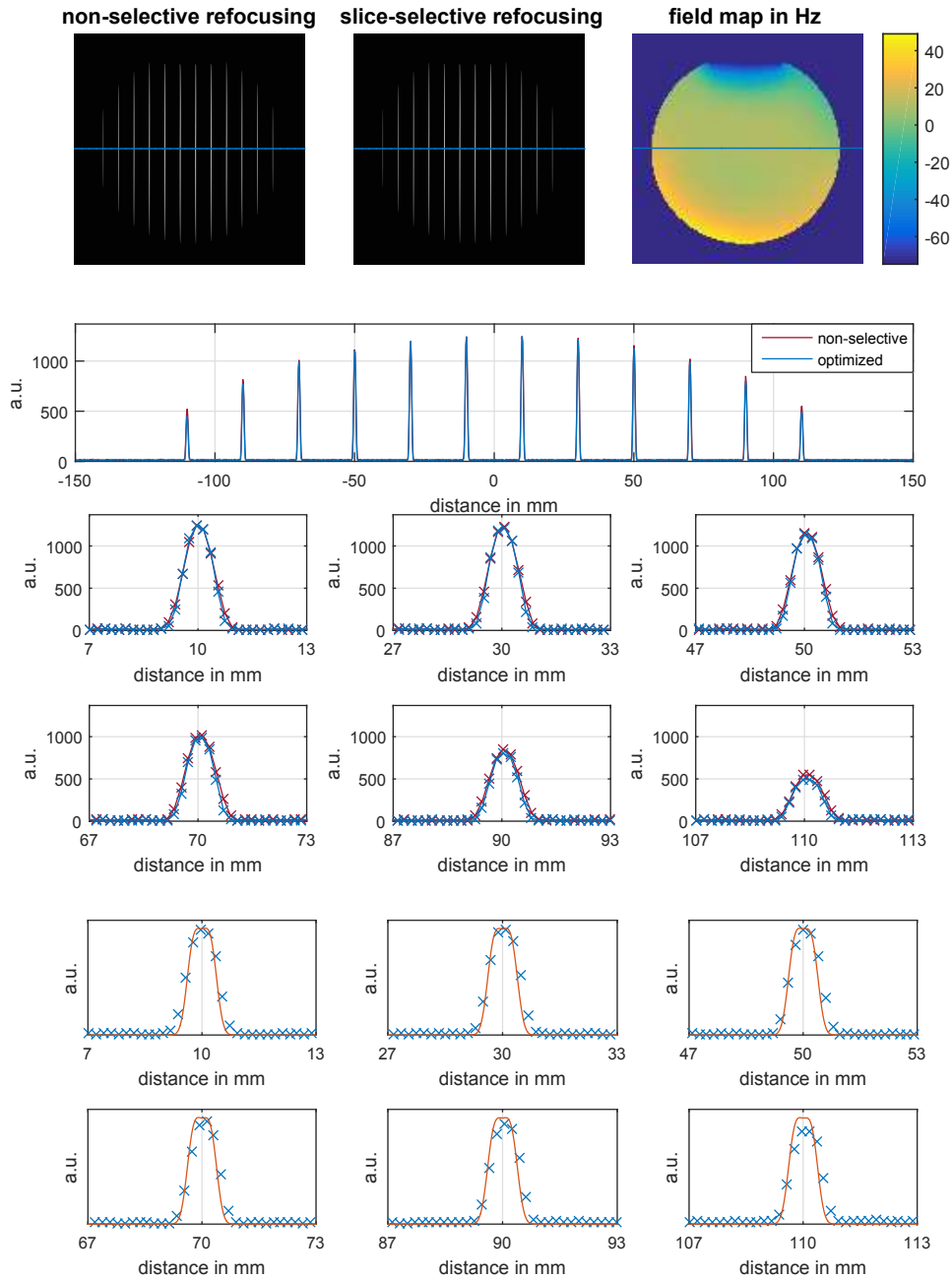


Figure 5.22: Reconstructed experimental spin echo data for MB12 refocusing with a slice thickness of 1 mm using a spherical phantom. Two different pairings are used: slice selective excitation and non-selective refocusing (non-selective), and slice selective excitation and optimized slice selective refocusing. Row 5 and 6 show a comparison of the experimental data (exp) with optimized refocusing normalized by a fully non-selective SE measurement and the Bloch simulations (sim) for slice selective excitation and optimized MB12 refocusing [3].

## 5 RF pulse design

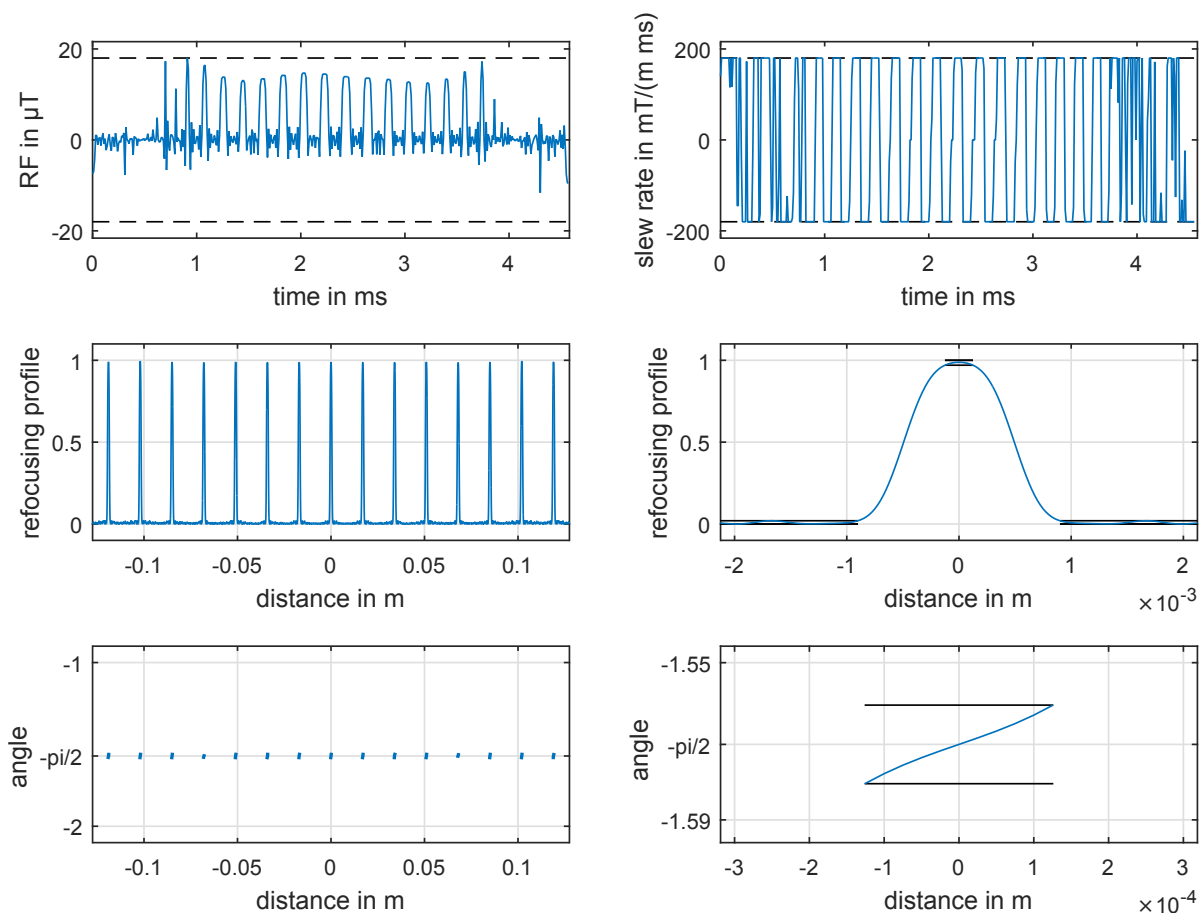


Figure 5.23: Time-optimal RF and slew rate of the slice selective gradient (1st row), refocusing profile ( $|b_{N_i}|^2$ ) with zoom (2nd row), and phase angle  $\arg(b_{N_i}^2)$  per slice with zoom (3rd row) [194].

$\mu\text{T}$ ,  $G_{s,\max} = 35 \text{ mT m}^{-1}$ ) and  $\dot{G}_{s,\max} = 180 \text{ T m}^{-1} \text{ s}^{-1}$ . To ensure the CPMG condition we added an additional constraint for the in-slice phase and prescribe the global mean phase of the refocusing pulse to be  $-\pi/2$ .

Figure 5.23 depicts the time optimal results that are imported into a Wave-CAIPIRINHA encoded TSE sequence [195] ( $\text{TR}/\text{TE} = 4000/100 \text{ ms}$ , bandwidth = 130 Hz/pixel, turbo factor = 12, MB = 15) with wave gradients during the readout to create a corkscrew trajectory due to  $G_{s,\max} = 6 \text{ mT m}^{-1}$ ,  $\dot{G}_{s,\max} = 50 \text{ T m}^{-1} \text{ s}^{-1}$ , 7 sinusoidal cycles) to maximize the spatial distance of aliased voxels and reduce the g-factor.

In contrast to the optimized result shown in Figure 5.20, the strict SAR and  $B_1$  amplitude constraints of this example prevent a further reduction of the refocusing pulse in time. Again, the simulated refocusing profile fulfils the magnitude and phase

## 5 RF pulse design

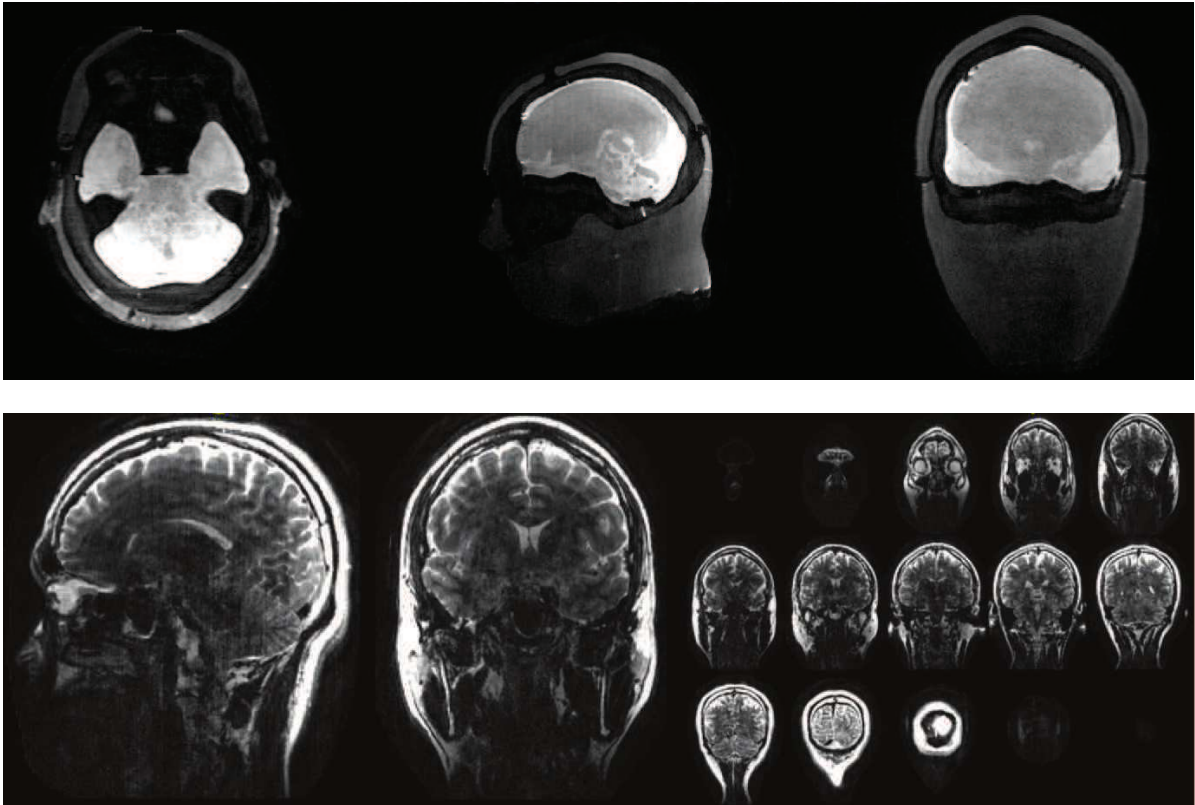


Figure 5.24: Phantom (Row 1) and in vivo (Row 2) RARE/TSE measurement using the optimized pulse shown in Figure 5.23 after Wave-CAIPINHA reconstruction [194].

constraints in the observed slice regions. Measurements are performed on a 3 T MR Scanner (Magnetom Trio, Siemens Healthcare, Erlangen, Germany) for a phantom and in vivo. The Wave-CAIPINHA reconstruction of the optimized RF pulse is shown in Figure 5.24 for a phantom (Row 1) and in vivo (Row 2). The optimized RF pulse and slice selective gradient fulfil the hard constraints given by actual scanner hardware and safety measures that ensures a simple replacement of existing pulses and is well suited to further decrease the echo spacing in TSE/RARE sequences. The combination of optimized pulses for large MB factors with a Wave-CAIPINHA reconstruction allows for fast acquisition of whole head TSE/RARE imaging in 70 s.

## 6 Discussion

This thesis presents different methods to design RF pulse and slice selective gradient shapes. The focus was placed on single slice and SMS applications with and without explicit hardware constraints for the full Bloch equations including relaxation effects and the spin domain Bloch equations with neglected relaxation terms. A summarised discussion of the key results is presented below.

Compared to standard RF design methods, OC approaches are flexible in the problem formulation and can be modified to prescribe various problem parameters ranging from a point-wise description of the desired magnetization [1] to maximal error and amplitude bounds on the state and control variables [2]. The theory is described for both, the full [1] and the spin domain Bloch equations [2], [3], while most of the optimization runs are done with neglected relaxation times. For standard in vivo imaging of the human head, this is a valid assumption since the relaxation times are very long compared to the RF pulse duration. Nevertheless, the inclusion of relaxation times is possible using the design approach based on the full time dependent Bloch equations [1]. More details on the theory and the employed methods can be found in the Appendix.

The increased computational effort of numerical optimization is kept low by an efficient computation of exact or approximate second order information to speed up convergence and by using a trust region framework for robustness and numerical efficiency. Large numbers of spatial points are efficiently computed by means of GPU or CPU parallelization. The RF and slice selective gradient shapes are treated in the optimization as piecewise constant functions. This form of modelling reflects how external fields are implemented in MR sequences.

The performed studies show that the OC based design of RF pulse shapes increases the slice profile accuracy without major RF power reduction [1]. The RF power requirements can be reduced, however, by a joint design of RF and slice selective gradient waveforms [2]. This is in good accordance with the VERSE theory and comes with the benefits of a constant raster time and single step formulation, rather than splitting the design of RF and slice selective gradient. Therefore, jointly optimized RF and slice selective gradient shapes do not have to be interpolated to match the

## 6 Discussion

raster time, which saves interpolation errors. Additionally, the joint optimization does not require a scaling function and the balance between slice profile accuracy and RF power requirements can be adjusted with the regularization parameters. These observations can be transferred to SMS pulse design where RF amplitude, power and duration are highly limited parameters [1].

The Crank–Nicolson scheme used to discretize the Bloch equations [1] showed slight slice profile differences as a function of the spatial position that remained undetected by the initial experimental validation [71]. Compared to the Bloch solution with rotation matrices, off resonant spatial positions experienced a slice shift and dephasing. Spins close to the isocenter, however, are affected by a much smaller content. It seems, that the precession of spins far away from the isocenter becomes too large for an adequate solution by the Crank-Nicolson method. This inaccuracy can be effectively reduced choosing finer temporal discretization as shown exemplarily by Figure 5.17. However, the optimization framework and methods are independent of the chosen Bloch solver, and hence can be extended easily to more expensive and accurate Bloch solvers, for instance to symmetric operator splitting or piecewise constant analytic solution, which was done in [68]. Alternatively, the spin domain formulation can be used to accurately solve the Bloch equations with neglected relaxation terms [2]. The decreased computational effort compared to a numerical solution allows looping of the optimization to address new issues, for instance a reduction of the overall pulse duration [3].

While the proposed optimal control approaches use highly efficient numerical methods, the computational effort is significantly greater than, for instance, SLR-based approaches. The optimized examples are therefore computed offline within in the minute to hour range [1]–[3] using parallel CPU computing. A proof-of-concept GPU implementation indicates that this gap can be sufficiently narrowed to make patient-specific design feasible [1].

The use of unconstrained optimization requires checking the admissibility of optimized results which may result in the need for manual tuning of the regularization parameters or post optimal adjustment efforts [1]. This is no longer necessary when explicit hardware constraints are included in the optimization. The constraint formulation proved to facilitate the optimization and guarantees practical applicability [2]. The extension to a bi-level optimization with an iterative reduction of the pulse duration further allows the design of time optimal SMS pulses [3]. Compared to conventional superposed frequency shifted and PINS based pulse candidates, the duration can be reduced drastically by roughly 80%. This reduces the effective echo time or echo spacing which increases signal quality and motion robustness and increases the temporal acquisition efficiency. Moreover, the discussed time optimal design was declared the winning method of the ISMRM Challenge on RF pulse design [83].

## 6 Discussion

The optimized RF and slice selective gradient shapes are implemented on different 3 T MR scanners. The experimental results validate the numerical simulations with various phantom and in vivo experiments. Using the specific hardware constraints of the MR system used in the optimization simplifies the application of optimized pulses since no further transformations have to be done that could reduce the slice profile accuracy or violate hardware constraints.

The joint design of RF and slice selective gradient results in time varying slice selective gradient shapes that are known to introduce sensitivity with respect to  $B_0$  inhomogeneity. However, the slice profile fidelity remains almost unchanged ( $\pm 500$  Hz for fixed duration and  $\pm 100$  Hz for time optimization). With respect to  $B_1$  variations the optimized RF shapes behave similar to conventional RF pulses [3].

Although the optimized results fulfil all prescribed hardware constraints on the RF and slice selective gradient, the optimized slice selective gradient shape might exceed the bandwidth of the slice selective gradient system. Despite a highly fluctuating slice selective gradient shape, influences from gradient imperfections are hardly visible in the acquired experimental data [2], [3]. However, the same optimized results showed clearly visible deviations on a different MR system of a different vendor [119] as a result of a lower effective gradient system bandwidth. These gradient system imperfections can be corrected by an inclusion of the GIRF in the optimization [119] which is currently in progress.

The optimization is formulated and has been performed for excitation in the magnetization domain [1] and refocusing with crusher gradients in the spin domain [2], [3]. To cover other RF examples such as inversion or saturation, or to address additional effects such as  $B_0$  or  $B_1$  inhomogeneities, the discussed cost functions have to be adapted. Finally, the presented OC based RF pulse design methods outperforms previously proposed design methods in terms of flexibility and shows that it is possible to greatly reduce the RF power and pulse duration while fulfilling hardware constraints. The numerical results are validated in various experiments and demonstrate its practical use to design short, low power and accurate RF and slice selective gradient shapes for single and SMS applications.

## 7 Outlook

The OC based RF design methods described in the previous chapters and listed in the Appendix show different numerical strategies to design short and low power RF and slice selective gradient shapes for clinically relevant sequences with respect to physical constraints given by current scanner hardware. The presented approaches form the basis of new research projects targeting different directions.

Translating the time optimal solutions to different MR systems revealed that the rapid varying slice selective gradient shapes might outperform the gradient amplifier bandwidth and together with gradient imperfections caused by eddy currents or time delays could be an obstacle for practical application of optimized RF pulses. Preliminary results in Figure 7.1 show that the inclusion of the time-invariant GIRF [115] in the optimization completely corrects these gradient imperfections and should allow the design of short RF and slice selective gradient shapes for precise SMS refocusing [119].

The OC design framework can be extended to jointly design RF pulses and slice selective gradient shapes for multi-dimensional and multi-channel pTx excitation. In addition to the known hardware constraints, we add a minimum local 10 g SAR constraint based on the Q-matrix formalism to limit potential SAR hot spots. Preliminary simulations with a homogenous spherical phantom showed that both, local SAR and peak RF power can be reduced significantly while maintaining a low slice profile error [139]. Figure 7.2 shows the initial and SAR optimized independent RF and slice selective gradient shapes. Both, Bloch and electromagnetic simulations to computing the local SAR (XFDTD 7.4, Remcom, State College, USA) show the feasibility to jointly compute complex RF and slice selective gradient shapes for large flip angle pTx excitation which forms the basis for future projects.

Finally, future work will be done on the extension of more complicated Bloch models such as the Bloch Torrey equation [196] or the Bloch McConnell equation [197] to model more comprehensive physical processes, such as diffusion or chemical exchange during RF application.

## 7 Outlook

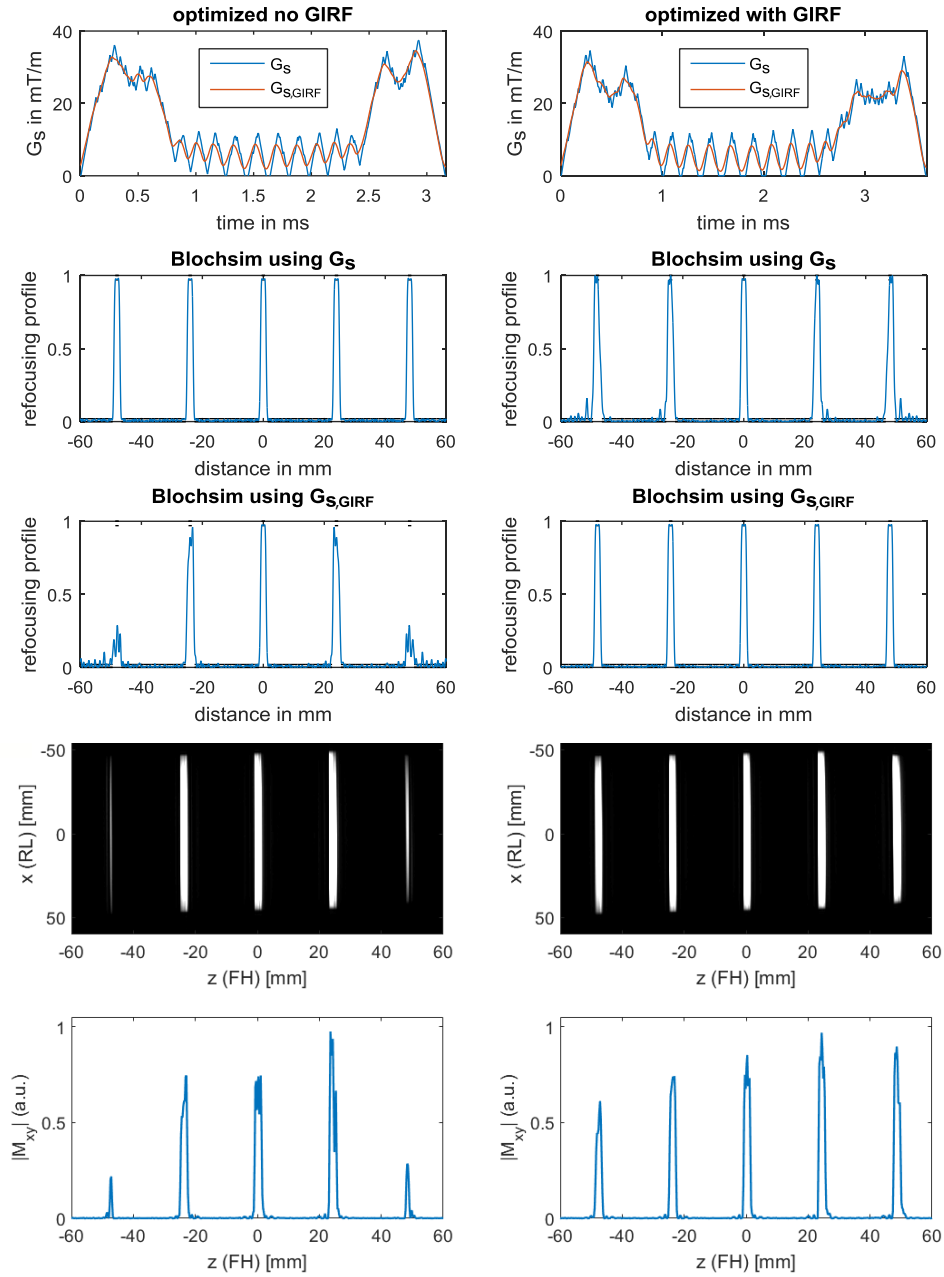


Figure 7.1: Comparison of the two optimized slice selective gradient shapes before ( $G_S$ ) and after convolution with the GIRF ( $G_{S,GIRF}$ ) with a duration of 3.17 ms (optimized without GIRF) and 3.6 ms (optimized with GIRF). Row 2 and 3 show the simulated refocusing profiles  $|b(z)|^2$  in the spin domain without and with convolution. Row 4 and 5 show slice profile measurements on a phantom bottle, in a spin-echo sequence using the time-optimal control refocusing pulses and conventional multiband excitation pulses [119].

## 7 Outlook

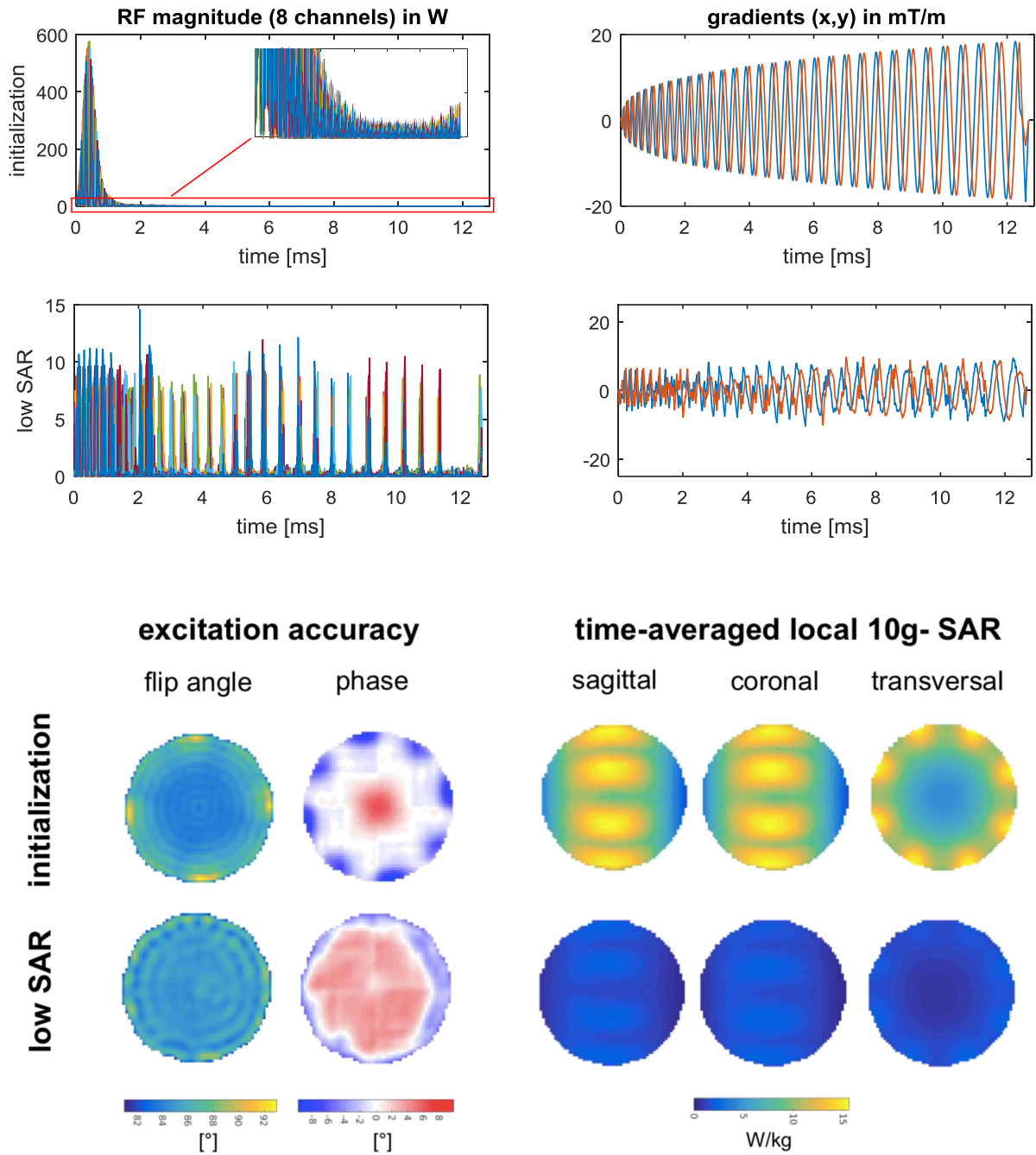


Figure 7.2: Comparison of RF magnitude and gradient shapes of the initialization and the optimized case (note the different scaling on the y-axis for the RF pulse magnitude) and simulated two dimensional in-ROI flip angle and phase distributions together with corresponding maximum intensity projections of the time-averaged local 10 g-SAR in three directions compared for the initial pulse and the optimized pulse [139].

## 8 List of Publications

### Peer reviewed full journal publications

1. D. Bagga, **C.S. Aigner**, J.L. Reichert, C. Cecchetto, F.P.S. Fischmeister, P. Holzer, C. Moissl-Eichinger and V. Schöpf. "Influence of 4-week multi strain probiotic administration on resting-state functional connectivity in healthy volunteers". *European Journal of Nutrition*, Early view May 2018, doi: <https://doi.org/10.1007/s00394-018-1732-z>
2. D. Bagga, J.L. Reichert, K. Koschutnig, **C.S. Aigner**, P. Holzer, K. Koskinen, C. Moissl-Eichinger and V. Schöpf. "Probiotics drive gut microbiome triggering emotional brain signatures". *Gut Microbes*, Early view May 2018, doi: <https://doi.org/10.1080/19490976.2018.1460015>
3. G. Pfurtscheller, A. Schwerdtfeger, A. Seither-Preisler, C. Brunner, **C.S. Aigner**, J. Calisto, J. Gens and A. Andrade. "Synchronization of intrinsic 0.1-Hz blood-oxygen-level dependent (BOLD) oscillations in amygdala and prefrontal cortex in subjects with increased state anxiety". *European Journal of Neuroscience*, Volume 47:5, March 2018, Pages 417-426, doi: <https://doi.org/10.1111/ejn.13845>
4. A. Rund<sup>†</sup>, **C.S. Aigner**<sup>†</sup>, K. Kunisch, and R. Stollberger. "Simultaneous multislice refocusing via time optimal control". *Magnetic Resonance in Medicine*, Early view: February 2018, doi: <https://doi.org/10.1002/mrm.27124>
5. A. Rund, **C.S. Aigner**, K. Kunisch, and R. Stollberger. "Magnetic Resonance RF pulse design by optimal control with physical constraints". *IEEE Transactions on Medical Imaging*, Volume 37:2, February 2018, Pages 461-472, doi: [10.1109/TMI.2017.2758391](https://doi.org/10.1109/TMI.2017.2758391)
6. S.M. Spann, K.S. Kazimierski, **C.S. Aigner**, M. Kraiger, K. Bredies, R. Stollberger. "Spatio-temporal TGV denoising for ASL perfusion imaging". *NeuroImage*, Volume 157, August 2017, Pages 81-96, doi: <https://doi.org/10.1016/j.neuroimage.2017.05.054>
7. G. Pfurtscheller, A. Schwerdtfeger, A. Seither-Preisler, C. Brunner, **C.S. Aigner**, J. Brito, M.P. Carmo, A. Andrade. "Brain-heart communication: Evidence for

---

<sup>†</sup>Armin Rund and Christoph Stefan Aigner have contributed equally to the paper

## 8 List of Publications

- "central pacemaker" oscillations with a dominant frequency at 0.1 Hz in the cingulum". *Clinical Neurophysiology*, Volume 128:1, January 2017, Pages 183–193, doi: <https://doi.org/10.1016/j.clinph.2016.10.097>
8. G. Pfurtscheller, A. Schwerdtfeger, C. Brunner, **C.S. Aigner**, D. Fink, J. Brito, M.P. Carmo, A. Andrade. "Distinction between Neural and Vascular BOLD Oscillations and Intertwined Heart Rate Oscillations at 0.1 Hz in the Resting State and during Movement". *PLoS ONE* 12(1): e0168097, January 2017, doi: <https://doi.org/10.1371/journal.pone.0168097>
  9. **C.S. Aigner**, C. Clason, A. Rund and R. Stollberger. "Efficient high-resolution RF pulse design applied to simultaneous multi-slice excitation". *Journal of Magnetic Resonance*, Volume 263, February 2016, Pages 33–44, doi: <https://doi.org/10.1016/j.jmr.2015.11.013>

### Peer reviewed conference proceedings

1. D. Bagga, **C.S. Aigner**, C. Cecchetto, F. Fischmeister, A. Specht, F. Schwaerzel and V. Schöpf. "The interplay between gender, GABA levels, and nicotine addiction: A proton MRS investigation". *Annual OHBM Meeting*, Singapore, Singapore, June 2018
2. **C.S. Aigner**, A. Rund, S. Abo Seada, S. Malik, J.V. Hajnal, K. Kunisch and R. Stollberger. "Time-optimal control based RF pulse design under gradient imperfections". *Proc. Intl. Soc. Mag. Reson. Med.* 26, Paris, France, June 2018 
3. A. Rund, **C.S. Aigner**, L. Nohava, R. Frass-Kriegl, E. Laistler, K. Kunisch and R. Stollberger. "Optimal control based design of parallel transmission RF pulses with minimum local SAR". *Proc. Intl. Soc. Mag. Reson. Med.* 26, Paris, France, June 2018
4. S.M. Spann, **C.S. Aigner**, M. Schlögl, A. Lesch, K. Bredies, R. Stefan, D. Pinter, L. Pirpamer and R. Stollberger. "Acceleration of arterial spin labeling data using spatio-temporal total generalized variation (TGV) reconstruction". *Proc. Intl. Soc. Mag. Reson. Med.* 26, Paris, France, June 2018 
5. S.M. Spann, M. Schlögl, **C.S. Aigner**, K. Koschutnig, M. Holler, K. Bredies and R. Stollberger. "Denoising of functional Arterial Spin Labeling (fASL) perfusion data using infimal convolution of total generalized variation functionals (ICTGV)". *Proc. Intl. Soc. Mag. Reson. Med.* 26, Paris, France, June 2018 

## 8 List of Publications

6. A. Rund, **C.S. Aigner**, K. Kunisch and R. Stollberger. "Magnetic Resonance Radiofrequency Pulse Design by Optimal Control". *9th Vienna Conference on Mathematical Modelling*, Vienna, Austria, January 2018
7. L. Nohava, A. Kuehne, **C.S. Aigner**, A. Rund, E. Moser, E. Laistler and R. Frass Kriegl. "Evaluation of RF pulses for 8-channel pTx systems at 7T with respect to hardware constraints and the trade-off between local 10g SAR and excitation accuracy". *34th ESMRMB Annual Scientific Meeting*, Barcelona, Spain, October 2017
8. D. Bagga, K. Koschutnig, B. Mohan, **C.S. Aigner**, J. Reichert, P. Holzer and V. Schöpf. "When gut speaks, brain listens: Exploring the influence of gut microbiota on emotional decision making". *Annual OHBM Meeting*, Vancouver, Canada, June 2017
9. **C.S. Aigner**, A. Rund, B. Bilgic, B. Gagoski, K. Setsompop, K. Kunisch and R. Stollberger. "Application of time-optimal Simultaneous Multi-Slice refocusing to TSE/RARE". *Proc. Intl. Soc. Mag. Reson. Med.* 25, Hawaii, USA, April 2017
10. A. Rund, **C.S. Aigner**, K. Kunisch and R. Stollberger. "Simultaneous multislice refocusing by time-optimal control". *Proc. Intl. Soc. Mag. Reson. Med.* 25, Hawaii, USA, April 2017
11. A. Rund, **C.S. Aigner**, K. Kunisch and R. Stollberger. "RF pulse design by optimal control with physical constraints". *Proc. Intl. Soc. Mag. Reson. Med.* 25, Hawaii, USA, April 2017
12. A. Petrovic, **C.S. Aigner** and R. Stollberger. "A time domain signal equation for multi-echo spin-echo sequences with arbitrary excitation and refocusing angle and phase". *Proc. Intl. Soc. Mag. Reson. Med.* 25, Hawaii, USA, April 2017
13. M. Schloegl, S. Spann, **C.S. Aigner**, M. Holler, K. Bredies and R. Stollberger. "Improved Denoising of Dynamic Arterial Spin Labeling with Infimal Convolution of Total Generalized Variation Functionals (ICTGV)". *Proc. Intl. Soc. Mag. Reson. Med.* 25, Hawaii, USA, April 2017
14. S.M. Spann, K.S. Kazimierski, **C.S. Aigner** and R. Stollberger. "A denoising method for arterial spin labeling data based on total generalized variation (TGV) with a spatial varying regularization parameter". *Proc. Intl. Soc. Mag. Reson. Med.* 25, Hawaii, USA, April 2017
15. D. Bagga, K. Koschutnig, B. Mohan, **C.S. Aigner**, J. Reichert, P. Holzer and V. Schöpf. "The Gut-Brain-Axis: from gut feelings to gut memory". *Proc. Intl. Soc. Mag. Reson. Med.* 25, Hawaii, USA, April 2017
16. **C.S. Aigner**, C. Clason, A. Rund, A. Petrovic and R. Stollberger. "Design of complex RF pulse shapes for asymmetric excitation patterns via optimal control". *BMT 2016 „Dreiländertagung“ Swiss, Austrian and German Societies of Biomedical Engineering*, Basel, Switzerland, October 2016

## 8 List of Publications

17. S.M. Spann, K.S. Kazimierski, **C.S. Aigner**, M. Kraiger and R. Stollberger; "Influence of denoising techniques on the absolute CBF quantification of ASL perfusion data". *BMT 2016 „Dreiländertagung“ Swiss, Austrian and German Societies of Biomedical Engineering*, Basel, Switzerland, October 2016
18. M. Bödenler, **C.S. Aigner**, A. Rund, C. Clason and R. Stollberger. Fast Optimization of RF Excitation. *33rd ESMRMB Annual Scientific Meeting*, Vienna, Austria, October 2016
19. S.M. Spann, **C.S. Aigner**, K.S. Kazimierski, Markus Kraiger and R. Stollberger. "Total generalized variation (TGV) for spatio-temporal denoising of high resolution ASL perfusion data". *33rd ESMRMB Annual Scientific Meeting*, Vienna, Austria, October 2016
20. **C.S. Aigner**, C. Clason, A. Rund and R. Stollberger. "Low SAR RF-pulse design by joint optimization of RF and gradient shape with physical constraints". *Proc. Intl. Soc. Mag. Reson. Med. 24*, Singapore, Singapore, May 2016
21. **C.S. Aigner**, C. Clason, A. Rund and R. Stollberger. "RF pulse design for simultaneous multislice excitation with highly reduced B<sub>1</sub> peak amplitude". *Proc. Intl. Soc. Mag. Reson. Med. 23*, Toronto, Canada, June 2015;  magna cum laude award
22. **C.S. Aigner**, C. Clason, A. Rund and R. Stollberger. "SAR reduced excitation by joint design of RF pulse and slice selective gradient shape". *Proc. Intl. Soc. Mag. Reson. Med. 23*, Toronto, Canada, June 2015
23. A. Lesch, A. Petrovic, T.J. Sumpf, **C.S. Aigner** and R. Stollberger. "Fast and Accurate Quantification of T<sub>1</sub>, T<sub>2</sub> and Proton Density using IR bSSFP with Slice Profile Correction and Model Based Reconstruction". *Proc. Intl. Soc. Mag. Reson. Med. 23*, Toronto, June 2015
24. **C.S. Aigner**, C. Clason, A. Rund and R. Stollberger. "Validation of a flexible optimal control approach for RF-pulse-design including relaxation effects and SAR". *Annual Meeting of the Austrian Society for Biomedical Engineering*, Hall in Tirol, Austria, September 2014
25. **C.S. Aigner**, C. Clason, A. Rund and R. Stollberger. "RF pulse design for low SAR simultaneous multislice (SMS) excitation using optimal control". *Proc. Intl. Soc. Mag. Reson. Med. 22*, Milano, Italy, May 2014
26. **C.S. Aigner**, C. Diwojky and R. Stollberger. "Development of a pulseoximeter to measure the oxygen saturation and the heartrate of sedated mice". *BMT 2013 „Dreiländertagung“ Swiss, Austrian and German Societies of Biomedical Engineering*, Graz, Austria, 2013

## Oral Presentations

1. **C.S. Aigner**, A. Rund, S. Abo Seada, S. Malik, J.V. Hajnal, K. Kunisch and R. Stollberger. "Time-optimal control based RF pulse design under gradient imperfections". *Intl. Soc. Mag. Reson. Med.* 26 Power Pitch presentation, Paris, France, June 2018 
2. **C.S. Aigner**. "Spin Dance – On the Forefront of MRI Signal Generation". *2nd Human- and Biotechnology FoE Day*, Graz, Austria, October 2017
3. **C.S. Aigner**, A. Rund, K. Kunisch and R. Stollberger. "RF-Pulse Design with Physical Constraints". *Czech-Austrian MR Workshop*, Semmering, Austria, May 2017
4. **C.S. Aigner**, A. Rund. "Optimal Control Based Design of Tailored RF Pulses". *Invited Talk at the Medical University of Vienna*, Vienna, Austria, October 2016
5. **C.S. Aigner**. "Slice selective RF pulse design via optimal control". *Invited Talk at the University Medical Center Freiburg*, Freiburg, Germany, October 2016
6. **C.S. Aigner**, C. Clason, "Design of complex RF pulse shapes for asymmetric excitation patterns via optimal control". *BMT 2016 „Dreiländertagung“ Swiss, Austrian and German Societies of Biomedical Engineering*, Basel, Switzerland, October 2016
7. **C.S. Aigner**, A. Rund. "Towards tailored refocusing in minimum time: Results and Application". *Imaging with Modulated/Incomplete Data*, Graz, Austria, September 2016
8. **C.S. Aigner**, C. Clason, A. Rund and R. Stollberger. "Low SAR RF-pulse design by joint optimization of RF and gradient shape with physical constraints". *Intl. Soc. Mag. Reson. Med.* 24, *Joint Study Group Session: High Field Systems and Applications and MR Safety*, Singapore, Singapore, May 2016
9. **C.S. Aigner**, Christian Clason, Armin Rund and Rudolf Stollberger. "RF Pulse Design With Optimal Control - Current and Future Applications". *SFB Statusseminar 2016*, Admont, Austria, April 2016
10. **C.S. Aigner**. "Optimal Control – vom Raum zum Spin". *MRI research in Graz*, Graz, Austria, March 2015
11. **C.S. Aigner**, Christian Clason, Armin Rund and Rudolf Stollberger. "RF Pulse Optimization via Optimal Control – Summary and Outlook". *SFB Networking Seminar 2014*, Graz, Austria, September 2014
12. **C.S. Aigner**, C. Clason, A. Rund and R. Stollberger. "RF pulse design for simultaneous multislice excitation with highly reduced B<sub>1</sub> peak amplitude". *Proc. Intl. Soc. Mag. Reson. Med.* 23, Toronto, Canada, June 2015; magna cum laude award 

## 8 List of Publications

13. **C.S. Aigner**, C. Clason, A. Rund and R. Stollberger. "Validation of a flexible optimal control approach for RF-pulse-design including relaxation effects and SAR". *Annual Meeting of the Austrian Society for Biomedical Engineering*, Hall in Tirol, Austria, September 2014
14. **C.S. Aigner**, Christian Clason, Armin Rund and Rudolf Stollberger. "Optimal control for advanced 1D RF-pulse-design: Results and Challenges". *SFB Statusseminar 2013*, Admont, Austria, November 2013
15. **C.S. Aigner**, Christian Clason, Armin Rund and Rudolf Stollberger. "An optimal control approach for advanced 1D RF-pulse-design including relaxation effects". *BMT 2013 „Dreiländertagung“ Swiss, Austrian and German Societies of Biomedical Engineering*, Graz, Austria, September 2013

## Prices, Awards and Stipends

1. Magna cum laude award ISMRM 26 (2018), Paris, France
2. 1st place in the ISMRM RF pulse design challenge 2015: Simultaneous Multislice Acquisition. Member of the winning team "rfcontrol" together with A.Rund, C.Clason, K.Kunisch and R. Stollberger; (2015-2016), Singapore  
MRM Highlights: Q&A with 2015 ISMRM Challenge Winners, (<http://www.ismrm.org/rf-pulse-design-challenge/>)  
MRM full paper: W. Grissom and K. Setsompop et al., MRM 2016. (<https://doi.org/10.1002/mrm.26512>)
3. Magna cum laude award ISMRM 23 (2015), Toronto, Canada
4. ISMRM Educational Stipend 2014, 2015 and 2016

# 9 Appendix

## 9.1 Efficient high-resolution RF pulse design applied to simultaneous multi-slice excitation

Christoph Stefan Aigner<sup>1,2</sup>, Christian Clason<sup>3</sup>, Armin Rund<sup>4</sup> and Rudolf Stollberger<sup>1,2</sup>

This is a preprint of the publication "Efficient high-resolution RF pulse design applied to simultaneous multi-slice excitation". *Journal of Magnetic Resonance*, Volume 263, February 2016, Pages 33–44, doi: <https://doi.org/10.1016/j.jmr.2015.11.013>

### Abstract

RF pulse design via optimal control is typically based on gradient and quasi-Newton approaches and therefore suffers from slow convergence. We present a flexible and highly efficient method that uses exact second-order information within a globally convergent trust-region CG-Newton method to yield an improved convergence rate. The approach is applied to the design of RF pulses for single- and simultaneous multi-slice (SMS) excitation and validated using phantom and in-vivo experiments on a 3 T scanner using a modified gradient echo sequence.

---

<sup>1</sup>Institute of Medical Engineering, Graz University of Technology, Stremayrgasse 16, 8010 Graz, Austria

<sup>2</sup>BioTechMedGraz, 8010 Graz, Austria

<sup>3</sup>Faculty of Mathematics, University of Duisburg-Essen, 45117 Essen, Germany

<sup>4</sup>Institute for Mathematics and Scientific Computing, University of Graz, Heinrichstrasse 36, 8010 Graz, Austria

### 9.1.1 Introduction

For many applications in MRI there is still demand for the optimization of selective RF excitation, e.g., for simultaneous multi-slice excitation [163], [166], UTE imaging [198], or velocity selective excitation [128]. To achieve a well-defined slice profile at high field strength while meeting  $B_1$  peak amplitude limitations is a challenge for RF pulse design and becomes especially critical for quantitative methods.

Correspondingly, many approaches for general pulse design have been proposed in the literature. RF pulses with low flip angles can be designed using the small tip angle simplification [43], which makes use of an approximation of the Bloch equation to compute a pulse via the Fourier transform of the desired slice profile. However, this simplification breaks down for large flip angles. The resulting excitation error for large flip angle pulses can be reduced by applying the Shinnar–Le Roux (SLR) technique [66] or optimization methods, e.g., simulated annealing, evolutionary approaches or optimal control [47], [120], [147], [149], [152], [153], [199]. The SLR method is based on the hard pulse approximation and a transformation of the excitation problem, allowing to solve the excitation problem recursively by applying fast filter design algorithms such as the Parks–McClellan algorithm [66]. Originally, this approach only covered special pulses such as  $90^\circ$  and  $180^\circ$  excitation or refocusing, but Lee [200] generalized this approach to arbitrary flip angles with an exact parameter relation. Despite its limitations due to neglected relaxation terms and sensitivity to  $B_1$  inhomogeneities, it found widespread use (see, e.g., [200]–[203]) and is considered to be the gold standard for large tip angle pulse design. An alternative approach is based on optimizing a suitable functional; see, e.g., [47], [66], [145], [151], [154]. In particular, optimal control (OC) approaches involve the solution of the Bloch equation describing the evolution of the magnetization vector in an exterior magnetic field [47], [49], [120], [152], [153], [155], [156], [182]. They often lead to better excitation profiles due to a more accurate design model and are increasingly used in MRI, for instance, to perform multidimensional and multichannel RF design [47], [49], robust 2D spatial selective pulses [153] and saturation contrast [152]. In addition, arbitrary flip angles and target slice profiles, as well as inclusion of additional physical effects such as, e.g., relaxation can be handled. However, so far OC approaches are limited by the computational effort and require a proper modeling of the objective. In particular, standard gradient-based approaches suffer from slow convergence, imposing significant limitations on the accuracy of the obtained slice profiles. On the other hand, Newton methods show a locally quadratic convergence, but require second-order information which in general is expensive to compute [157]. Approximating the Hessian using finite differences causes loss of quadratic convergence due to the lack of exact second-order information and typically requires significantly more iterations. Superlinear convergence can be obtained using quasi-Newton methods based on exact gradients

[204], although their performance can be sensitive to implementation details. The purpose of this work is to demonstrate that for the OC approach to pulse design, it is in fact possible to use exact second-order information while avoiding the need of computing the full Hessian, yielding a highly efficient numerical method for the optimal control of the full time-dependent Bloch equation. In contrast to [157] (which uses black-box optimization method and symbolically calculated Hessians based on an effective-matrix approximation of the Bloch equation), we propose a matrix-free Newton–Krylov method [186] using first- and second-order derivatives based on the adjoint calculus [205] together with a trust-region globalization [185]; for details we refer to Section 9.1.2. Recently, similar matrix-free Newton–Krylov approaches with line search globalization were presented for optimal control of quantum systems in the context of NMR pulse sequence design [206], [207]. In comparison, the proposed trust-region framework significantly reduces the computational effort, particularly for the initial steps far away from the optimum. The effectiveness of the proposed method is demonstrated for the design of pulses for single and simultaneous multi-slice excitation (SMS).

SMS excitation is increasingly used to accelerate imaging experiments [163]–[166]. Conventional design approaches, based on a superposition of phase-shifted sub-pulses [162] or sinusoidal modulation [163], typically result in a linear scaling of the  $B_1$  peak amplitude, a quadratic peak power and a linear increase in the overall RF power [131], [175]. The required maximal  $B_1$  peak amplitude of conventional multi-slice pulses therefore easily exceeds the transmit voltage of the RF amplifier. In this case, clipping will occur, while rescaling will decrease and limit the maximal flip angle of such a pulse. On the other hand, restrictions of the specific absorption rate limit the total (integrated)  $B_1$  power and therefore the maximal number of slices as well as the pulse duration and flip angle. The increase of  $B_1$  power can be addressed by the Power Independent of Number of Slices (PINS) technique [131], which was extended to the kT-PINS method [208] to account for  $B_1$  inhomogeneities. This approach leads to a nearly slice-independent power requirement, but the periodicity of the resulting excitation restricts the slice orientation and positioning. Furthermore, the slice profile accuracy is reduced [165], and a limited ratio between slice thickness and slice distance may further restrict possible applications. The combination of PINS with regular multi-band pulses was shown to reduce the overall RF power by up to 50% (MultiPINS [179]) and was applied to refocusing pulses in a multi-band RARE sequence with 13 slices [195].

A different way to reduce the maximum  $B_1$  amplitude is to increase the pulse length; however, this stretching increases the minimal echo and repetition times and decreases the RF bandwidth, thus reducing the slice profile accuracy [175]. Applying variable rate selective excitation [160], [209] avoids this problem but leads to an increased sensitivity to slice profile degradations at off-resonance frequencies. In addition, they

## 9 Appendix

require specific sequence alterations, e.g., variable slice gradients or gradient blips. Instead of using the same phase for all sub-slices, the peak power can be reduced by changing the uniform phase schedule to a different phase for each individual slice [174]. Alternative approaches [173], [210] using phase-matched excitation and refocusing pairs show that a nonlinear phase pattern can be corrected by a subsequent refocusing pulse. Another way to reduce the power deposition and SAR of SMS pulses is to combine them with parallel transmission [211]. This allows to capitalize transmit sensitivities in the pulse design and leads to a more uniform excitation with an increased power efficiency [212], [213]. Recently, Guerin et al. [214] demonstrated that it is possible to explicitly control both global and local SAR as well as the peak power using a spokes-SMS-pTx pulse design.

The focus of this work, however, is on single channel imaging, where we apply our OC-based pulse design for efficient SMS pulse optimization using a direct description of the desired magnetization pattern. Its flexible formulation allows a trade-off between the slice profile accuracy and the required pulse power and is well suited for the reduction of power and amplitude requirements of such pulses, even for a large number of slices or large flip angles or in presence of relaxation. The efficient implementation of the proposed method allows to optimize for SMS pulses with a high spatial resolution to achieve accurate excitation profiles. The RF pulses are designed to achieve a uniform effective echo time and phase for each slice and use a constant slice-selective gradient, allowing to insert the RF pulse into existing sequences and opening up a wide range of applications.

### 9.1.2 Theory

This section is concerned with the description of the optimal control approach to RF pulse design as well as of the proposed numerical solution approach.

#### Optimal control framework

Our OC approach is based on the full time-dependent Bloch equation, which describes the temporal evolution of the ensemble magnetization vector  $M(t) = (M_x(t), M_y(t), M_z(t))^T$  due to a transient external magnetic field  $B(t)$  as the solution of the ordinary differential equation (ODE)

$$\begin{cases} \dot{M}(t) = \gamma B(t) \times M(t) + R(M(t)), & t > 0, \\ M(0) = M^0, \end{cases} \quad (9.1)$$

## 9 Appendix

where  $\gamma$  is the gyromagnetic ratio,  $M^0$  is the initial magnetization and

$$R(M(t)) = (-M_x(t)/T_2, -M_y(t)/T_2, -(M_z(t) - M_0)/T_1)^T \quad (9.2)$$

denotes the relaxation term with relaxation times  $T_1, T_2$  and the equilibrium magnetization  $M_0$ . To encode spatial information in MR imaging, the external magnetic field  $B$  (and thus the magnetization vector) depends on the slice direction  $z$ , hence the Bloch equation can be considered as a parametrized family of three-dimensional ODEs. In the on-resonance case and ignoring spatial field inhomogeneities, the Bloch equation can be expressed in the rotating frame as

$$\begin{cases} \dot{M}(t; z) = A(u(t); z)M(t; z) + b(z), & t > 0, \\ M(0; z) = M^0(z), \end{cases} \quad (9.3)$$

where the control  $u(t) = (u_x(t), u_y(t))$  describes the RF pulse,

$$A(u; z) = \begin{pmatrix} -\frac{1}{T_2} & \gamma G_z(t)z & \gamma u_y(t)B_1 \\ -\gamma G_z(t)z & -\frac{1}{T_2} & \gamma u_x(t)B_1 \\ -\gamma u_y(t)B_1 & -\gamma u_x(t)B_1 & -\frac{1}{T_1} \end{pmatrix}, \quad b(z) = \begin{pmatrix} 0 \\ 0 \\ \frac{M_0}{T_1} \end{pmatrix}, \quad (9.4)$$

and  $G_z$  is the slice-selective gradient; see, e. g., [26, Chapter 6.1].

The OC approach consists in computing for given initial magnetization  $M^0(z)$  the RF pulse  $u(t)$ ,  $t \in [0, T_u]$ , that minimizes the squared error at read-out time  $T > T_u$  between the corresponding solution  $M(T; z)$  of (9.3) and a prescribed slice profile  $M_d(z)$  for all  $z \in [-a, a]$  together with a quadratic cost term modeling the SAR of the pulse, i.e., solving

$$\min_{(u, M) \text{ satisfying (9.3)}} J(M, u) = \frac{1}{2} \int_{-a}^a |M(T; z) - M_d(z)|_2^2 dz + \frac{\alpha}{2} \int_0^{T_u} |u(t)|_2^2 dt. \quad (9.5)$$

The parameter  $\alpha > 0$  controls the trade-off between the competing goals of slice profile attainment and SAR reduction.

### Adjoint approach

The standard gradient method for solving (9.5) consists of computing for given  $u^k$  the gradient  $g(u^k)$  of  $j(u) := J(M(u), u)$  and setting  $u^{k+1} = u^k - s^k g(u^k)$  for some

## 9 Appendix

suitable step length  $s^k$ . The gradient can be calculated efficiently using the adjoint method, which in this case yields

$$\begin{aligned} g(u^k)(t) &= \alpha u(t) + \gamma B_1 \left( \int_{-a}^a M_z(t; z) P_y(t; z) - M_y(t; z) P_z(t; z) dz \right. \\ &\quad \left. - \int_{-a}^a M_z(t; z) P_x(t; z) - M_x(t; z) P_z(t; z) dz \right) \\ &=: \alpha u(t) + \left( \int_{-a}^a M(t; z) A_1 P(t; z) dz \right. \\ &\quad \left. - \int_{-a}^a M(t; z) A_2 P(t; z) dz \right), \quad 0 \leq t \leq T_u, \end{aligned} \quad (9.6)$$

where  $M$  is the solution to (9.3) for  $u = u^k$  and  $0 < t \leq T$ ,  $P$  is the solution to the adjoint (backward in time) equation

$$\begin{cases} -\dot{P}(t; z) = A(u(t); z)^T P(t; z), & 0 \leq t < T, \\ P(T; z) = M(T; z) - M_d(z), \end{cases} \quad (9.7)$$

and for the sake of brevity, we have set

$$A_1 := \gamma B_1 \begin{pmatrix} 0 & 0 & 0 \\ 0 & 0 & -1 \\ 0 & 1 & 0 \end{pmatrix}, \quad A_2 := \gamma B_1 \begin{pmatrix} 0 & 0 & -1 \\ 0 & 0 & 0 \\ 1 & 0 & 0 \end{pmatrix}. \quad (9.8)$$

However, this method requires a line search to converge and usually suffers from slow convergence close to a minimizer. This is not the case for Newton's method (which is a second-order method and converges locally quadratically), where one additionally computes the Hessian  $H(u^k)$  of  $j$  at  $u^k$ , solves for  $\delta u$  in

$$H(u^k)\delta u = -g(u^k), \quad (9.9)$$

and sets  $u^{k+1} = u^k + \delta u$ . While the full Hessian  $H(u^k)$  is very expensive to compute in practice, solving (9.9) using a Krylov method such as conjugate gradients (CG) only requires computing the Hessian *action*  $H(u^k)h$  for a given direction  $h$  per iteration; see, e.g., [186]. The crucial observation in our approach is that the adjoint method allows computing this action exactly (e.g., without employing finite difference approximations) and without knowledge of the full Hessian. Since Krylov methods usually converge within very few iterations, this so-called "matrix-free" approach amounts to significant computational savings. To derive a procedure for computing the Hessian action  $H(u^k)h$  for a given direction  $h$  directly, we start by differentiating (9.6) with respect to  $u$  in direction  $h$  and applying the product rule. This yields

## 9 Appendix

$$[H(u^k)h](t) = \alpha h(t) + \left( \int_{-a}^a \delta M(t; z) A_1 P(t; z) + M(t; z) A_1 \delta P(t; z) dz \right) + \left( \int_{-a}^a \delta M(t; z) A_2 P(t; z) + M(t; z) A_2 \delta P(t; z) dz \right), \quad 0 \leq t \leq T_u, \quad (9.10)$$

where  $\delta M$  – corresponding to the directional derivative of  $M$  with respect to  $u$  – is given by the solution of the linearized state equation

$$\begin{cases} \delta \dot{M}(t; z) = A(u^k; z) \delta M(t; z) + A'(h) M, & 0 < t \leq T, \\ \delta M(0; z) = (0, 0, 0)^T, \end{cases} \quad (9.11)$$

with

$$A'(h) = \gamma B_1 \begin{pmatrix} 0 & 0 & h_y(t) \\ 0 & 0 & h_x(t) \\ -h_y(t) & -h_x(t) & 0 \end{pmatrix}, \quad (9.12)$$

and  $\delta P$  – corresponding to the directional derivative of  $P$  with respect to  $u$  – is the solution of the linearized adjoint equation

$$\begin{cases} -\delta \dot{P}(t; z) = A(u^k; z)^T \delta P(t; z) + A'(h)^T P, & 0 \leq t < T, \\ \delta P(T; z) = \delta M(T; z). \end{cases} \quad (9.13)$$

This characterization can be derived using formal Lagrangian calculus and rigorously justified using the implicit function theorem; see, e.g., [215, Chapter 1.6]. Since (9.10) can be computed by solving the two ODEs (9.11) and (9.13), the cost of computing a single Hessian action is comparable to that of a gradient evaluation; cf. (9.6). This has already been observed in the context of seismic imaging [216], meteorology [217], and optimal control of partial differential equations [205], but has received little attention so far in the context of optimal control of ODEs.

One difficulty is that the Bloch equation (9.3) is bilinear since it involves the product of the unknowns  $u$  and  $M$ . Hence, the optimal control problem (9.5) is not convex and the Hessian  $H(u)$  is not necessarily positive definite (or even invertible), thus precluding a direct application of the CG-Newton method. We therefore embed Newton's method into the trust-region framework of Steihaug [185], where a breakdown of the CG method is handled by a trust-region step and the trust region radius is continually adapted. This allows global convergence (i.e., for any starting point) to a local minimizer as well as transition to fast quadratic convergence; see [185]. As an added advantage, computational time is saved since the CG method is usually not fully resolved far away from the optimum. The full algorithm is given in Appendix 9.1.7.

## Discretization

For the numerical computation of optimal controls, both the Bloch equation (9.3) and the optimal control problem in (9.5) need to be discretized. Here, the time interval  $[0, T]$  is replaced by a time grid  $0 = t_0 < \dots < t_N = T$  with time steps  $\Delta t_m := t_m - t_{m-1}$ , chosen such that  $t_{N_u} = T_u < T$  for some  $N_u < N$ . The domain  $[-a, a]$  is replaced by a spatial grid  $-a = z_1 < \dots < z_Z = a$  with grid sizes  $\Delta z_m := z_m - z_{m-1}$ . We note that for each  $z_i$ , the corresponding ODEs can be solved independently and in parallel. The Bloch equation is discretized using a Crank–Nicolson method, where the state  $M$  is discretized as continuous piecewise linear functions with values  $M_m := M(t_m)$ , and the controls  $u$  are treated as piecewise constant functions, i.e.,  $u = \sum_{m=1}^{N_u} u_m \chi_{(t_{m-1}, t_m]}(t)$ , where  $\chi_{(a,b]}$  is the characteristic function of the half-open interval  $(a, b]$ .

For the efficient computation of optimal controls, it is crucial that both the gradient and the Hessian action are computed in a manner consistent with the chosen discretization. This implies that the adjoint state  $P$  has to be discretized as piecewise constant using an appropriate time-stepping scheme [218], and that the linearized state  $\delta M$  and the linearized adjoint state  $\delta P$  have to be discretized in the same way as the state and adjoint state, respectively. Furthermore, the conjugate gradient method has to be implemented using the scaled inner product  $\langle u, v \rangle := \sum_{m=1}^{N_u} \Delta t_m u_m v_m$  and the corresponding induced norm  $\|u\|^2 := \langle u, u \rangle$ . For completeness, the resulting schemes and discrete derivatives are given in Appendix 9.1.8.

### 9.1.3 Methods

This section describes the computational implementation of the proposed pulse design and the experimental protocol for its validation.

#### Pulse design

The OC approach described in Section 9.1.2 is implemented in MATLAB (The MathWorks, Inc., Natick, USA) using the Parallel Toolbox for parallel solution of the (linearized) Bloch and adjoint equation for different values of  $z_i$ . In the spirit of reproducible research, the code used to generate the results in this paper can be downloaded from <https://github.com/chaigner/rfcontrol/releases/v1.2>.

## 9 Appendix

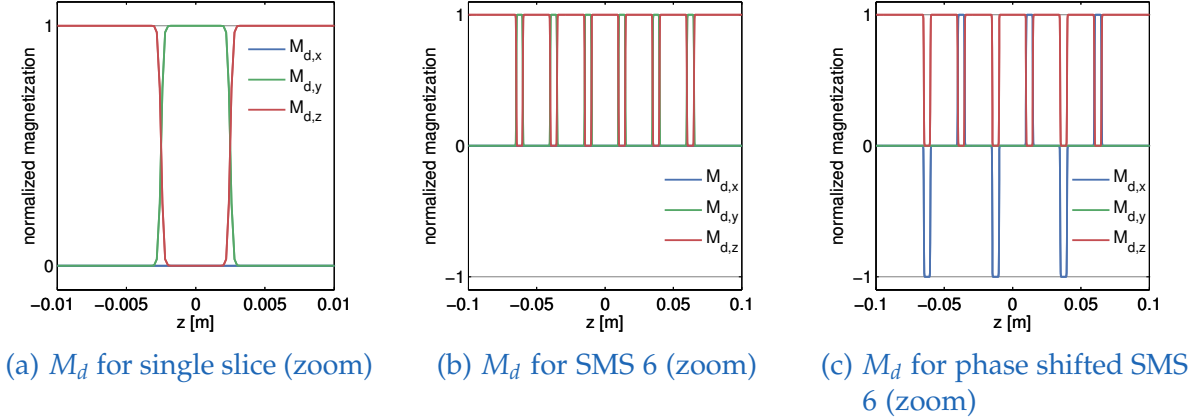


Figure 9.1: Desired magnetization for single- (a) and multi-slice (b,c) pulse design

The initial magnetization vector is set to equilibrium, i.e.,  $M^0(z) = M_0(0,0,1)^T$ . The slice-selective gradient  $G_z(t)$  is extracted out of a standard Cartesian GRE sequence simulation and consists of a trapezoidal shape of length 2.56 ms that is followed by a re-phasing part of length 0.92 ms to correct the phase dispersion using the maximal slew rate; i.e.,  $T_u = 2.56$  ms and  $T = 3.48$  ms with a temporal resolution of  $\Delta t = 5$   $\mu$ s for the single-slice excitation (see dashed line in Figure 9.2a) and  $T_u = 10.24$  ms and  $T = 13.92$  ms with a temporal resolution of  $\Delta t = 20$   $\mu$ s for the SMS excitation (see dashed line in Figure 9.4a). This corresponds in both cases to  $N = 697$  uniform time steps for the time interval  $[0, T]$  and  $N_u = 512$  time steps for the control interval  $[0, T_u]$ . For the spatial computational domain,  $a = 0.5$  m is chosen to consider typical scanner dimensions; the domain  $[-a, a]$  is discretized using  $Z = 5001$  equidistant points to achieve a homogeneous spatial resolution of  $\Delta z = 0.2$  mm.

For the desired magnetization vector, we consider three examples:

**Single-slice excitation** To validate the design procedure, we compute an optimized pulse for a single slice of a given thickness  $\Delta_w$  and a flip angle of  $90^\circ$ , i.e., we set

$$\tilde{M}_d(z) = \begin{cases} (0, \sin(90^\circ), \cos(90^\circ))^T & \text{if } |z| < \Delta_w/2, \\ (0, 0, 1)^T & \text{else,} \end{cases} \quad (9.14)$$

as visualized in Figure 9.1a. To reduce Gibbs ringing, this vector is filtered before the optimization with a Gaussian kernel with a full width at half maximum of 1.6 mm. For comparison, an SLR pulse [66], [200] with an identical temporal resolution and pulse duration is designed to the same specification (slice width, flip angle, full width at half maximum) using the Parks–McClellan (PM) algorithm [66] with a 1% in-

## 9 Appendix

and out-of slice ripple as usual [66] and a bandwidth of 2.35 kHz. To achieve a fully refocused magnetization, the refocusing area of the slice selective gradient for the SLR pulse is increased by 4.1 percent compared to the OC pulse (Figure 9.2a).

**SMS excitation: phantom** RF pulses for the simultaneous excitation of two, four, and six equidistant rectangular slices with a flip angle of  $90^\circ$  are computed, i.e., we set

$$\tilde{M}_d(z) = \begin{cases} (0, \sin(90^\circ), \cos(90^\circ))^T & \text{if } z \text{ in slice,} \\ (0, 0, 1)^T & \text{if } z \text{ out of slice,} \end{cases} \quad (9.15)$$

and apply Gauss filtering; see Figure 9.1b for the case of six slices.

Since PINS pulses are not suitable for axial or axial-oblique slice preference as they generate a periodic slice pattern extending outside the field of interest [166], the optimized pulses are compared with conventional SMS pulses obtained using superposed phase-shifted sinc-based excitation pulses, again for the same slice width, flip angle and full width at half maximum.

**SMS excitation: in-vivo** Since multi-slice in-vivo imaging using slice-GRAPPA starts to suffer from g-factor problems for more than three slices, we modify the above-described SMS pulses using a CAIPIRINHA-based excitation pattern [171], which alternates two different pulses to achieve phase-shifted magnetization vectors in order to increase the spatial distance of aliased voxels. Here, the first vector and pulse are identical to those designed for the phantom. For odd slice numbers, the second vector is modified by adding a phase term of  $\pi$  to every second slice of the desired magnetization, i.e.,

$$\tilde{M}_d(z) = \begin{cases} (0, \pm \sin(90^\circ), \cos(90^\circ))^T & \text{if } z \text{ in odd/even slice,} \\ (0, 0, 1)^T & \text{if } z \text{ out of slice} \end{cases} \quad (9.16)$$

(before filtering). For even slice numbers, the transverse pattern has to be further shifted by  $\frac{\pi}{2}$ , i.e.,

$$\tilde{M}_d(z) = \begin{cases} (\pm \sin(90^\circ), 0, \cos(90^\circ))^T & \text{if } z \text{ in even/odd slice,} \\ (0, 0, 1)^T & \text{if } z \text{ out of slice,} \end{cases} \quad (9.17)$$

see Figure 9.1c for the case of six slices. The additional phase shift is balanced before reconstruction by subtracting a phase of  $\frac{\pi}{2}$  from every second phase-encoding line of the measured k-space data. Since typical relaxation times in the human brain are

## 9 Appendix

at least an order of magnitude bigger than the pulse duration, relaxation effects are neglected in the optimization.

The starting point for the optimization is chosen in all cases as  $u^0 = [0, \dots, 0]$ . The control cost parameter is fixed at  $\alpha = 10^{-4}$  for both the single-slice and the multi-slice optimization. The parameters in Algorithm 1 are set to  $\text{tol}_N = 10^{-9}$ ,  $\text{maxit}_N = 5$ ,  $\text{tol}_C = 10^{-6}$ ,  $\text{maxit}_C = 50$ ,  $\rho_0 = 1$ ,  $\rho_{\max} = 2$ ,  $q = 2$ ,  $\sigma_1 = 0.03$ ,  $\sigma_2 = 0.25$ ,  $\sigma_3 = 0.7$ .

All calculations are performed on a workstation with a four-core 64 bit processor with 3.1 GHz (Intel i5-3350P) and 16 GB of RAM.

### Experimental validation

Fully sampled experimental data for a phantom and a healthy volunteer were acquired on a 3 T MR scanner (Magnetom Skyra, Siemens Healthcare, Erlangen, Germany) using the built-in body coil to transmit the RF pulse. The MR signals were received using a body coil for the phantom experiments and a 32-channel head coil for the in-vivo experiments. A standard Cartesian GRE sequence was modified to import and apply external RF pulses. By changing the read-out gradient from the frequency-axis to the slice direction, the excited slice can be measured and visualized. The single-slice excitation was measured using a water filled sphere with a diameter of 170 mm. To acquire a high resolution in z-direction, we used a matrix size of  $512 \times 384$  with a FOV of  $250 \text{ mm} \times 187 \text{ mm}$  and a bandwidth of 390 Hz. The echo time was  $T_E = 5 \text{ ms}$  and the repetition time  $T_R = 2000 \text{ ms}$  to get fully relaxed magnetization before the next excitation. The SMS phantom experiments were performed using a homogeneous cylinder phantom with diameter of 140 mm, length of 400 mm, and relaxation times  $T_1 = 102 \text{ ms}$ ,  $T_2 = 81 \text{ ms}$ , and  $T_2^* = 70 \text{ ms}$ . The sequence parameters were  $T_E = 10 \text{ ms}$ ,  $T_R = 1000 \text{ ms}$ , bandwidth 390 Hz, matrix size  $512 \times 288$ , and a field of view of  $250 \text{ mm} \times 141 \text{ mm}$ .

To verify the in-vivo applicability, human brain images of a healthy volunteer were acquired using the above described GRE sequence modified to include the optimized CAIPIRINHA-based pulses. The sequence parameters were set to  $T_E = 10 \text{ ms}$ ,  $T_R = 4000 \text{ ms}$ , bandwidth 390 Hz, matrix size  $192 \times 120$  and FOV  $300 \text{ mm} \times 187 \text{ mm}$ . After acquisition, the k-space data of the individual slices were separated using an offline slice-GRAPPA (32 coils, kernel size of  $4 \times 4$ ) reconstruction [172], [219]. The reference scans used in the slice-GRAPPA reconstruction were performed with the same sequence using an optimized single-slice pulse (not shown here). To decrease the scanning time, we acquired 25 k-space lines (1/5 of the full dataset) around the

k-space center for each reference scan. After this separation, a conventional Cartesian reconstruction was performed individually for each slice.

### 9.1.4 Results

**Single-slice excitation** Figure 9.2 shows the results of the design of an RF pulse for the excitation of a single slice of width  $\Delta_w = 5$  mm; see Figure 9.1a. The computed pulse (after 4 Newton iterations and a total number of 28 CG steps taking 989 s on the above-mentioned workstation is shown in Figure 9.2a. (To indicate the sequence timing, the slice-selective gradient  $G_z$  – although not part of the optimization – is shown dashed.) It can be seen that  $u_x(t)$  is similar, but not identical, to a standard sinc shape, and that  $u_y(t)$  is close to zero, which is expected due to the symmetry of the prescribed slice profile. Figure 9.2b contains a detail of the corresponding transverse magnetization  $M_{xy}(T) = (M_x(T)^2 + M_y(T)^2)^{1/2}$  obtained from the numerical solution of the Bloch equation, which is confirmed by experimental phantom measurements in Figure 9.2c,d. Both simulation and measurement show an excitation with a steep transition between the in- and out-of-slice regions and a homogeneous flip angle distribution across the target slice.

Figure 9.3 compares the optimized (OC) pulse with a standard SLR pulse by showing details of the corresponding simulated magnetizations (Figure 9.3a for OC and Figure 9.3b for SLR; in both cases the targeted ideal magnetization is shown dashed). It can be seen that the in-slice magnetization of the optimized pulse has oscillations of higher frequency but of much smaller amplitude than that of the SLR pulse. This becomes especially visible when comparing the resulting in-slice phases (Figure 9.3c).

This is achieved by allowing higher ripples close to the slice while decreasing the amplitude monotonically away from the slice. (Note that only a small central segment of this region is shown in the figures.) This leads to the total root mean squared error (RMSE) and the mean absolute error (MAE) with the ideal rectangular magnetization pattern (Figure 9.3d) matching the full width at half maximum of both pulses being smaller for the OC pulse ( $1.46 \times 10^{-2}$  and  $1.10 \times 10^{-4}$ , respectively) compared to the SLR pulse ( $1.62 \times 10^{-2}$  and  $2.27 \times 10^{-4}$ , with an equal power demand for both pulses).

**SMS excitation: phantom** Figure 9.4 shows the results of the design of RF pulses for simultaneous excitation of two, four and six equidistant slices with a separation

## 9 Appendix

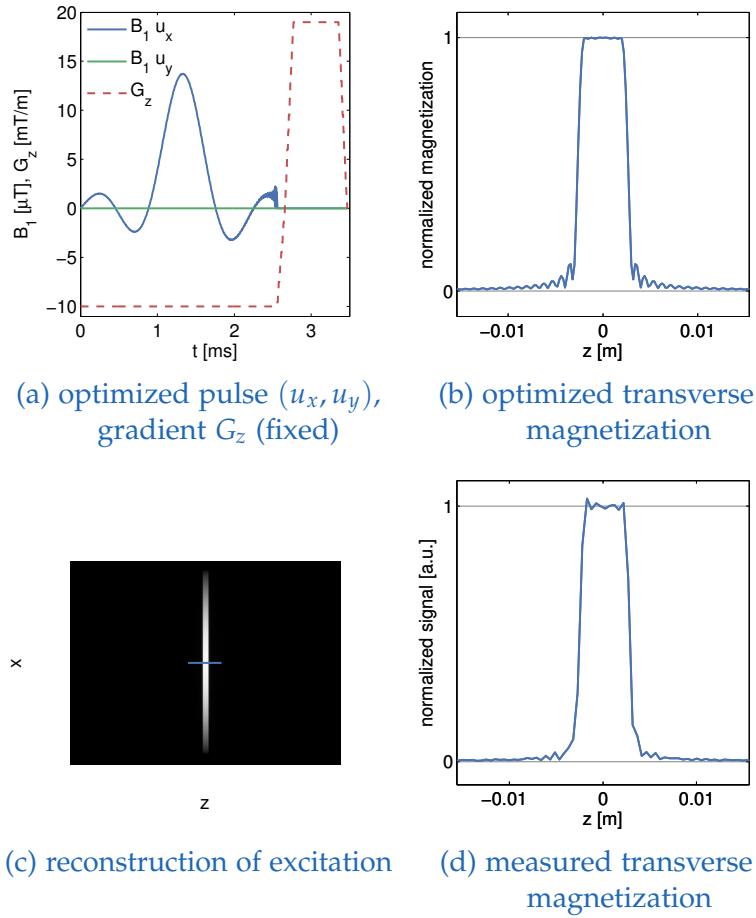


Figure 9.2: Optimized pulse and slice profile for single-slice excitation

of 25 mm and a thickness  $\Delta_w = 5$  mm; see Figure 9.1b. The computational effort in all cases is similar to that in the single-slice case. The corresponding computed pulses are shown in Figures 9.4a–c. A graphical analysis shows that instead of higher amplitudes, the optimization distributes the total RF power (which increases with the number of slices) more uniformly over the pulse length. A central section of the corresponding optimized slice profiles are given in Figures 9.4d–f. It can be seen that all slices have a sharp profile which does not deteriorate as the number of slices increases (although it decreases slightly farther from the center and the bandwidth is slightly reduced). These results are validated by the experimental phantom measurements using the computed pulses: Figures 9.4g–i show the reconstructed excitation inside the phantom, while Figures 9.4j–l show the measured slice profiles along a cut parallel to the  $x$ -axis in the center of the previous images.

## 9 Appendix

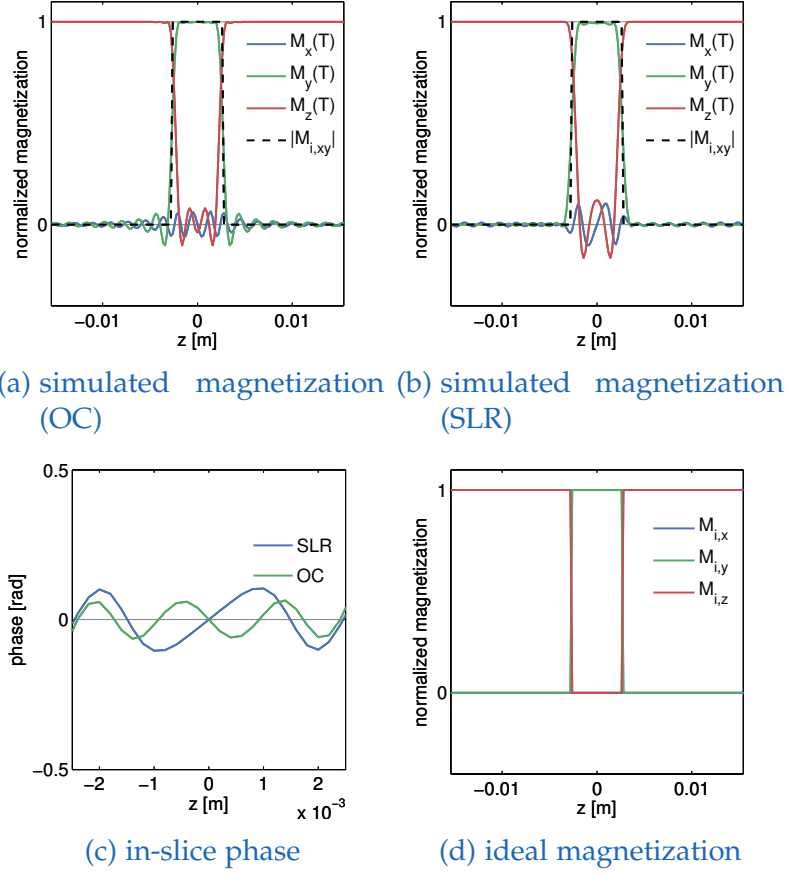


Figure 9.3: Comparison of SLR and OC pulse

A quantitative comparison of SLR and OC-based SMS pulses from one to six simultaneous slices is given in Table 9.1, which shows both the power requirement of the computed pulses, both in total  $B_1$  energy

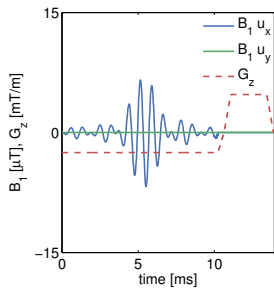
$$\|B_{1,x}\|_2^2 = \int_0^T |B_1 u_x(t)|^2 dt \quad (9.18)$$

and in peak  $B_1$  amplitude

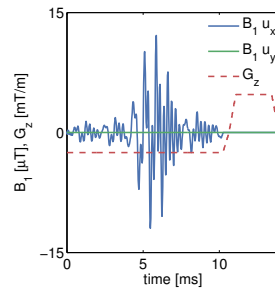
$$\|B_{1,x}\|_\infty = \max_{t \in [0, T]} |B_1 u_x(t)|, \quad (9.19)$$

as well as the mean absolute error (MAE) with respect to the ideal (unfiltered) slice profiles for the in-slice and the out-of-slice regions. While both methods lead to a linear increase of the total energy with the number of slices, the peak amplitude increases more slowly for the OC pulses than for the conventional pulses. Furthermore, we remark that the peak  $B_1$  amplitude for four, five and six slices remain similar.

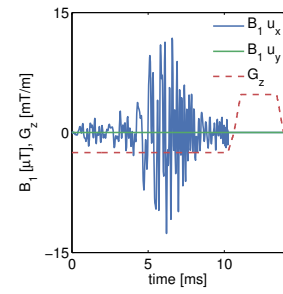
## 9 Appendix



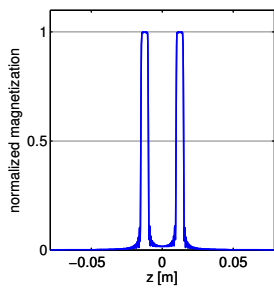
(a) optimized pulse (2 slices)



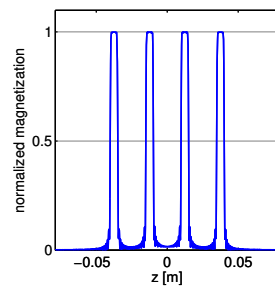
(b) optimized pulse (4 slices)



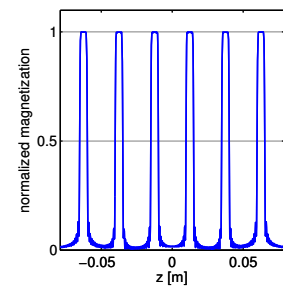
(c) optimized pulse (6 slices)



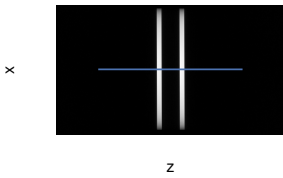
(d) optimized slice profile (2)



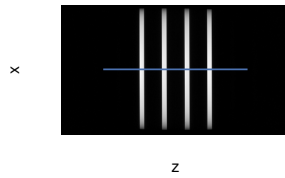
(e) optimized slice profile (4)



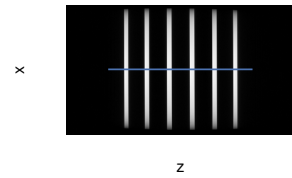
(f) optimized slice profile (6)



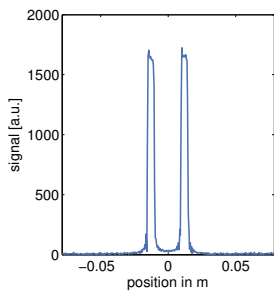
(g) reconstructed excitation (2)



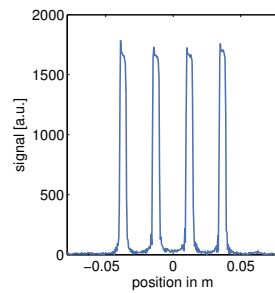
(h) reconstructed excitation (4)



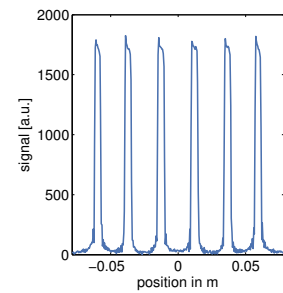
(i) reconstructed excitation (6)



(j) measured slice profile (2)



(k) measured slice profile (4)



(l) measured slice profile (6)

Figure 9.4: Optimized pulses and slice profiles for SMS excitation (phantom)

## 9 Appendix

Regarding the corresponding slice profiles, the OC pulses lead to a significantly lower MAE in both the in-slice and out-of-slice regions compared to the SLR pulses. Visual inspection of Figure 9.4d–f shows that this is due to the fact that the out-of-slice ripples are concentrated around the in-slice regions while quickly decaying away from them.

Table 9.1: Comparison of  $B_1$  power and the mean absolute error (MAE) of the transverse magnetization after excitation for conventional and OC based SMS pulses

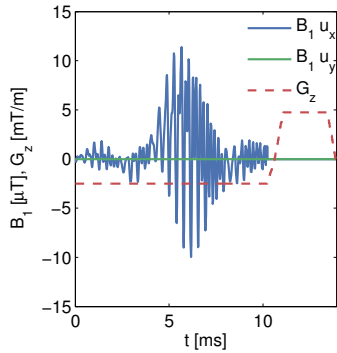
slices	$\ B_{1,x}\ _2^2$ [a.u.]		$\ B_{1,x}\ _\infty$ [ $\mu\text{T}$ ]		MAE in-slice [a.u.]		MAE out-of-slice [a.u.]	
	conv	OC	conv	OC	conv	OC	conv	OC
1	19.5	19.5	3.5	3.49	0.062	0.052	0.0039	0.0014
2	38.9	38.1	7.0	6.78	0.060	0.052	0.0040	0.0018
3	58.4	57.2	10.5	10.02	0.054	0.053	0.0039	0.0030
4	77.9	76.3	14.0	12.13	0.065	0.045	0.0086	0.0031
5	97.3	95.5	17.5	11.38	0.059	0.053	0.0078	0.0051
6	116.8	113.9	21.0	12.63	0.068	0.053	0.0075	0.0067

Finally, we illustrate the influence of the regularization parameter  $\alpha$  in Table 9.2, where the root of mean square error (RMSE), the total  $B_1$  energy as well as the  $B_1$  peak of the OC SMS 6 pulses is shown for different values of the control cost parameter  $\alpha$ . As can be seen, a bigger  $\alpha$  leads to an increase in the error between desired and controlled magnetization while both the total  $B_1$  power and the peak  $B_1$  amplitude are reduced, although these effects amount to less than 20 percent over a range of parameters spanning two orders of magnitude. This demonstrates that the results presented here are robust with respect to the choice of the control cost parameter.

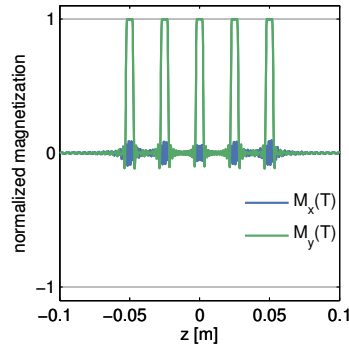
Table 9.2: Comparison of RMSE,  $B_1$  power and  $B_1$  peak for different values of  $\alpha$

$\alpha$ [a.u.]	RMSE [a.u.]	$\ B_{1,x}\ _2^2$ [a.u.]	$\ B_{1,x}\ _\infty$ [ $\mu\text{T}$ ]
$1 \times 10^{-5}$	$2.374 \times 10^{-2}$	117.0	12.75
$5 \times 10^{-5}$	$2.375 \times 10^{-2}$	115.1	12.71
$1 \times 10^{-4}$	$2.377 \times 10^{-2}$	113.9	12.62
$5 \times 10^{-4}$	$2.437 \times 10^{-2}$	106.7	12.14
$1 \times 10^{-3}$	$2.591 \times 10^{-2}$	98.9	11.63

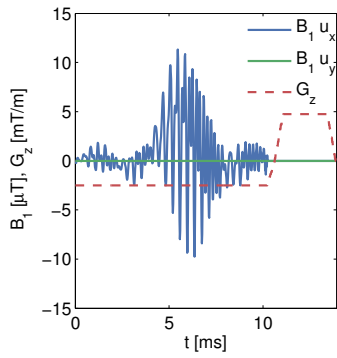
## 9 Appendix



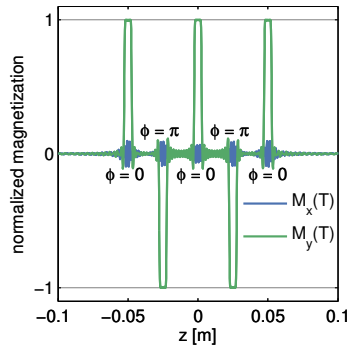
(a) optimized pulse (no shift)



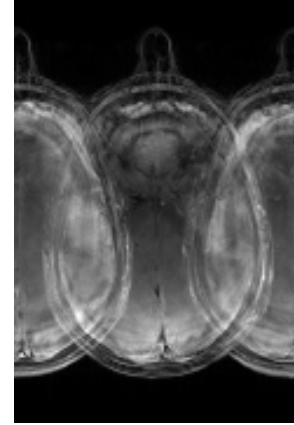
(b) optimized slice profile of (a)



(c) optimized pulse (phase shift)



(d) optimized slice profile of (c)



(e) slice-aliased reconstruction

Figure 9.5: Optimized pulses, slice profiles and slice-aliased Cartesian reconstruction for CAIPIRINHA-based SMS excitation pattern (five slices)

**SMS excitation: in-vivo** The CAIPIRINHA-based modifications to the SMS pulse design (see Figure 9.1c) are illustrated in Figure 9.5 (showing the case of five slices for the sake of variation). Figure 9.5a shows the unmodified pulse, which differs in structure from the cases with an even number of slices in, e.g., Figure 9.4c due to the different symmetry of the slice profile (see Figure 9.5b). On the other hand, the pulse is very similar to the modified pulse for the alternating phase shift; see Figure 9.5c for the computed pulse and Figure 9.5d for the resulting slice profile. For illustration, a slice-aliased reconstruction of the acquired in-vivo data using this pulse sequence is shown in Figure 9.5e.

Figure 9.6 shows the image reconstruction using optimized RF pulses for simultaneous excitation of two, four and six slices with the same slice separation and thickness as above. As can be seen clearly in the first column, all three pulses lead to the desired excitation pattern in-vivo as well. The remaining columns show the slice-GRAPPA

## 9 Appendix

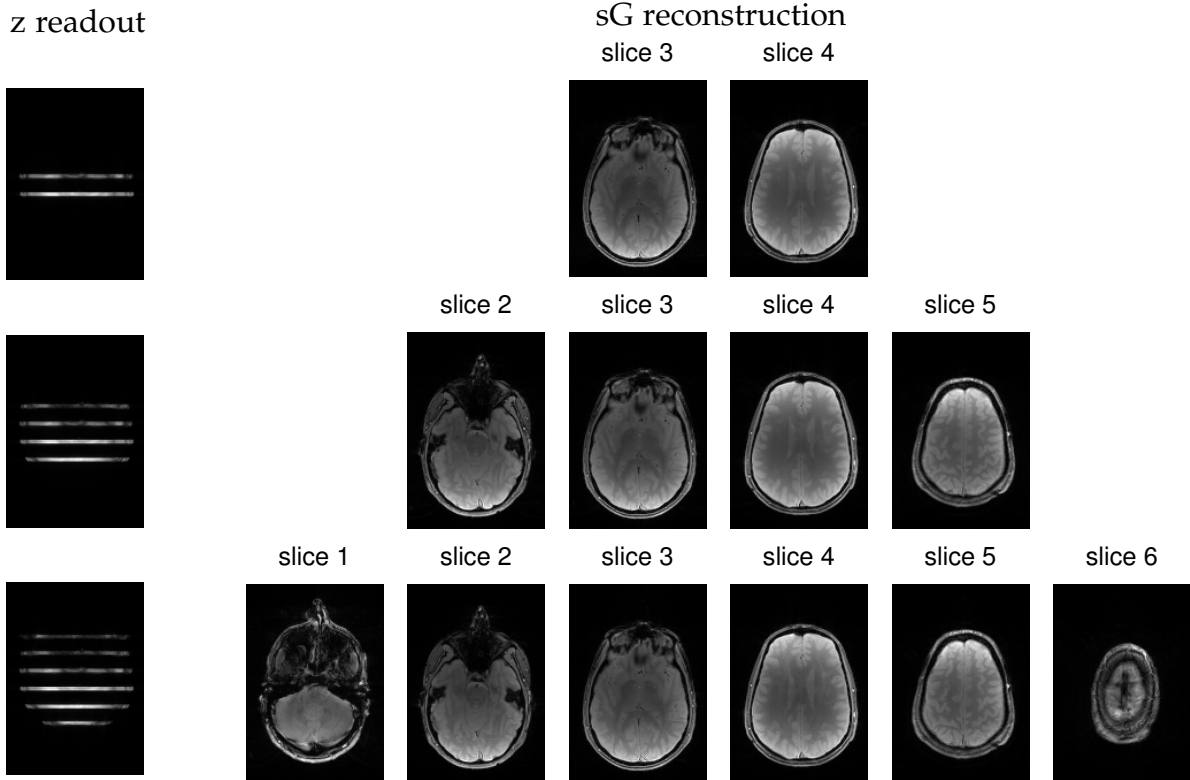


Figure 9.6: Slice-GRAPPA reconstruction of in-vivo data using CAIPIRINHA-based SMS excitation pattern for two (top), four (middle) and six (bottom) slices (left: conventional reconstruction showing the collapsed data in slice-encoding direction; right: reconstruction of GRAPPA-separated slices)

reconstructions, which illustrate that the excitation is uniform across the field of view.

### 9.1.5 Discussion

Our optimization approach is related to the basic ideas presented by Conolly et al. [120]. In the context of MRI, the implementation of this principle was also carried out by other groups using gradient [47], [49] and quasi-Newton [153] methods. However, these methods do not make full use of second-order information and therefore achieve at best superlinear convergence. In contrast, our Newton method makes use of exact second derivatives and is therefore quadratically convergent. In particular, the main contribution of our work is the efficient computation of exact Hessian actions using the adjoint approach and its implementation in a matrix-free trust-region CG-Newton method. The use of exact derivatives speeds up convergence of the CG method, while

## 9 Appendix

the trust-region framework guarantees global convergence and terminates the CG method early especially at the beginning of the optimization. Both techniques save CG steps and therefore computations of Hessian actions, allowing the use of second-order information with limited computational effort and memory requirements. Since computing a Hessian action incurs the same computational cost as a gradient evaluation (i.e., the solution of two ODEs; compare (9.6) with (9.10)), we were able to compute a minimizer, e.g., for the single-slice example, with a computational effort corresponding to 32 gradient evaluations (4 for the right-hand side in each Newton iteration and 28 for the Hessian action in each CG iteration). This is less than the same number of iterations of a gradient or quasi-Newton method with line search (required in this case for global convergence), demonstrating the efficiency of the proposed approach. Therefore, our method can be used to compute RF pulses with a high temporal resolution, allowing the design of pulses for a desired magnetization on a very fine spatial scale, in particular for the excitation of a sharp slice profile.

Furthermore, the proposed algorithm does not require an educated initial guess for global convergence (to a local minimizer, which might depend on the initial guess if more than one exists) and allows for pulse optimization in non-standard situations where no analytic RF pulse exists (e.g., for large flip angles). Compared to design methods using a simplification or approximation of the Bloch equation [43], [66], our OC based approach is capable of including relaxation terms. However, for standard in-vivo imaging applications of the human head, the relevant relaxation times are very long compared to the RF pulse duration. Thus, in our examples the influence of relaxation during excitation on the designed pulses is insignificant and has been neglected in the optimization process (although the inclusion may be indicated for other applications). The presented direct design approach allows to specify the desired magnetization in x-, y- and z-direction independently for every point in the field of view. This spatial independence of each control point allows to directly apply parallel computing to speed up the optimization process. While real-time optimization was not the aim of this work, a proof-of-concept implementation of the proposed approach on a GPU system (CUDA, double precision, GeForce GTX 550 Ti with 192 cores and 1024 MB of RAM) shows an average speedup of 135 (e.g., 6.8 s instead of 989 s for the single-slice example) while yielding identical results, thus making patient-specific design feasible as well as making the gap between OC and SLR pulse design nearly negligible. This allows efficient and fast generation of accurate slice profiles – important for minimal slice gaps, optimal contrast and low systematic errors in quantitative imaging – for arbitrary flip angles and even for specialized pulses such as refocusing or inversion.

In particular, our approach can be used to design pulses for the simultaneous excitation of multiple slices, which increases the temporal efficiency of advanced imaging techniques such as diffusion tensor imaging, functional imaging or dynamic scans.

## 9 Appendix

In these contexts, SMS excitation is successfully used to reduce the total imaging time [163]–[166]; however, the peak  $B_1$  amplitude of conventional SMS pulses is one of the main restrictions of applying SMS imaging to high-field systems [166]. The performed studies show that compared to conventional SMS design, the presented procedure yields pulses with a reduced  $B_1$  peak amplitude (e.g., 40% reduction for six simultaneous slices). Depending on the desired temporal resolution, the bandwidth and the slice profiles of the outer slices are slightly changed, which results in a decreased  $B_1$  peak amplitude. It could be shown that the peak  $B_1$  amplitude does not increase linearly with the number of slices, while the power requirement per slice remains constant and the overall power consumption is comparable to that of conventional pulses. To further reduce the SAR it is necessary to either change the excitation velocity using a time-varying slice selective gradient [160], or to extend the pulse design to parallel transmit [211]–[214]. Furthermore, our OC-based pulses produce sharp slice profiles with a lower mean absolute error compared to the used PM-based SLR pulse, both in- and out-of-slice, at the cost of slightly larger out-of-slice ripples close to the in-slice regions. Of course, the ripple behavior of the SLR pulse can be balanced with the transition steepness by using different digital filter design methods (i.e. PM for minimizing the maximum ripple or a least squares linear-phase FIR filter for minimizing integrated squared error). The OC ripple amplitude close to the transition band can be further controlled by using offset-dependent weights as demonstrated by Skinner et al. [220]. In addition, the computational complexity of OC methods is significantly higher than for direct or linearized methods. This implies that OC-based pulse design is advantageous in situations where high in-slice contrast and low  $B_1$  peak amplitude are important, while SLR pulses should be used when minimal near-slice excitation and computational effort are crucial.

The presented OC approach is able to avoid some possible disadvantages of previously proposed design methods for SMS excitation. In particular, the OC design method prescribes each slice with the same uniform echo-time and phase in comparison to time-shifted [175], phase relaxation [174] and nonlinear phase design techniques [173], [210]. On the other hand, some of their features such as different echo times [175] or a non-uniform phase pattern [173], [174], [210] (e.g., for spin echo experiments) can be incorporated in our approach to further reduce the  $B_1$  peak amplitude. It also should be possible to combine the OC design method with other techniques analogous to MultiPINS [179], [195] that combine PINS with conventional multiband pulses for a further reduction of SAR. Finally, the phantom and in-vivo experiments demonstrate that it is possible to simply replace standard pulses by optimized pulses in existing imaging sequences, and that the proposed method is therefore well suited for application in a wide range of imaging situations in MRI.

### 9.1.6 Conclusions

This paper demonstrates a novel general-purpose implementation of RF pulse optimization based on the full time-dependent Bloch equation and a highly efficient second-order optimization technique assuring global convergence to a local minimizer, which allows large-scale optimization with flexible problem-specific constraints. The power and applicability of this technique was demonstrated for SMS, where a reduced  $B_1$  peak amplitude allows exciting a higher number of simultaneous slices or achieving a higher flip angle. Phantom and in-vivo measurements (on a 3 T scanner) verified these findings for optimized single- and multi-slice pulses. Even for a large number of simultaneously acquired slices, the reconstructed images show good image quality and thus the applicability of the optimized RF pulses for practical imaging applications. While the computational requirements for optimal control approaches are of course significantly greater than for, e.g., SLR-based approaches, a proof-of-concept GPU implementation indicates that this gap can be sufficiently narrowed to make patient-specific design feasible.

Due to the flexibility of the optimal control formulation and the efficiency of our optimization strategy, it is possible to consider field inhomogeneities ( $B_1$ ,  $B_0$ ), design complex RF pulses for parallel transmit, or to extend the framework to include pointwise constraints due to hardware limits such as peak  $B_1$  amplitude and slew rate.

### Acknowledgments

This work is funded and supported by the Austrian Science Fund (FWF) in the context of project "SFB F3209-18" (Mathematical Optimization and Applications in Biomedical Sciences). Support from BioTechMed Graz and NAWI Graz is gratefully acknowledged. We would like to thank Markus Bödenler from the Graz University of Technology for the CUDA implementation of our algorithm.

## 9.1.7 Trust-region algorithm

**Algorithm 1:** Trust-region CG-Newton algorithm

---

**Input:** Trust region parameters  $\text{tol}_N, \text{maxit}_N, \text{tol}_C, \text{maxit}_C, \rho_0, \rho_{\max}, q > 1,$   
 $0 < \sigma_1 < \sigma_2 < \sigma_3 < 1$

**Output:** Control  $u$

Set  $u^0 \equiv 0, k = 0, g \equiv 1, \rho = \rho_0$  // initialization

**while**  $\|g\| > \text{tol}_N$  and  $k < \text{maxit}_N$  **do** // TR-Newton step

  Compute gradient  $g(u^k)$

  Set  $p^0 = r^0 = -g(u^k), \delta u = 0, i = 0$

**while**  $\|r^i\| > \text{tol}_C \|r^0\|$  and  $i < \text{maxit}_C$  **do** // TR-CG step

    Compute  $H(u^k)p^i$

**if**  $\langle p^i, H(u^k)p^i \rangle < \varepsilon$  **then** // negative curvature: CG fails

      Compute  $\max\{\tau : \|\delta u + \tau p^i\| \leq \rho\}$  // go to boundary of trust region

      Set  $\delta u = \delta u + \tau p^i$ ; **break**

**end**

    Compute  $\alpha = \|r^i\| / \langle p^i, H(u^k)p^i \rangle$

**if**  $\|\delta u + \alpha p^i\| \geq \rho$  **then** // step too large: model not trusted

      Compute  $\max\{\tau : \|\delta u + \tau p^i\| \leq \rho\}$  // go to boundary of trust region

      Set  $\delta u = \delta u + \tau p^i$ ; **break**

**end**

    Set  $r^{i+1} = r^i - \alpha H(u^k)p^i$

    Set  $p^{i+1} = r^{i+1} + \|r^{i+1}\|^2 / \|r^i\|^2 p^i$

    Set  $\delta u = \delta u + \alpha p^i, i = i + 1$

**end**

  Compute  $\delta J_a = J(u^k) - J(u^k + \delta u)$  // actual function decrease

  Compute  $\delta J_m = -\frac{1}{2} \langle \delta u, H(u^k) \delta u \rangle - \langle \delta u, g(u^k) \rangle$  // predicted function decrease

**if**  $\delta J_a > \varepsilon$  and  $\delta J_a > \sigma_1 \delta J_m$  **then** // sufficient decrease

    Set  $u^{k+1} = u^k + \delta u$  // accept step

**end**

**if**  $\delta J_a > \varepsilon$  and  $|\delta J_a / \delta J_m - 1| \leq 1 - \sigma_3$  **then** // step accepted, model good

    Set  $\rho = \min\{q\rho, \rho_{\max}\}$  // increase radius

**else if**  $\delta J_a \leq \varepsilon$  **then** // step rejected, no decrease

    Set  $\rho = \rho/q$  // decrease radius

**end**

**else if**  $\delta J_a < \sigma_2 \delta J_m$  **then** // model bad

    Set  $\rho = \rho/q$  // decrease radius

**end**

**end**

---

### 9.1.8 Discretization

**Cost functional:**

$$J(M, u) = \frac{1}{2} \sum_{i=1}^Z \Delta z_i |M_{N,i} - M_d(z_i)|_2^2 + \frac{\alpha}{2} \sum_{m=1}^N \Delta t_m |u_m|_2^2$$

**Bloch equation** for all  $i = 1, \dots, Z$ :

$$\begin{aligned} \left[ I - \frac{\Delta t_m}{2} A(u_m; z_i) \right] M_{m,i} &= \left[ I + \frac{\Delta t_m}{2} A(u_m; z_i) \right] M_{m-1,i} + \Delta t_m b, \quad m = 1, \dots, N \\ M_{0,i} &= M^0(z_i) \end{aligned}$$

**Adjoint equation** for all  $i = 1, \dots, Z$ :

$$\begin{aligned} \left[ I - \frac{\Delta t_m}{2} A(u_m; z_i)^T \right] P_{m,i} &= \left[ I + \frac{\Delta t_{m+1}}{2} A(u_{m+1}; z_i)^T \right] P_{m+1,i}, \quad m = 1, \dots, N-1 \\ \left[ I - \frac{\Delta t_N}{2} A(u_N; z_i)^T \right] P_{N,i} &= M_{N,i} - M_d(z_i) \end{aligned}$$

**Discrete gradient** for all  $m = 1, \dots, N_u$ :  $\bar{M}_m := \frac{1}{2}(M_m + M_{m-1})$ ,

$$g_m = \alpha u_m + \gamma B_1 \begin{pmatrix} \sum_{i=1}^Z \Delta z_i \left( P_{m,i}^T A_1 \bar{M}_{m,i} \right) \\ \sum_{i=1}^Z \Delta z_i \left( P_{m,i}^T A_2 \bar{M}_{m,i} \right) \end{pmatrix}$$

**Linearized state equation** for all  $i = 1, \dots, Z$ :

$$\begin{aligned} \left[ I - \frac{\Delta t_m}{2} A(u_m; z_i) \right] \delta M_{m,i} &= \left[ I + \frac{\Delta t_m}{2} A(u_m; z_i) \right] \delta M_{m-1,i} + \Delta t_m A'(\delta u_m) \bar{M}_{m,i}, \quad m = 1, \dots, N \\ \delta M_{0,i} &= 0 \end{aligned}$$

## 9 Appendix

**Linearized adjoint equation** for all  $i = 1, \dots, Z$ :

$$\begin{aligned} \left[ I - \frac{\Delta t_m}{2} A(u_m; z_i)^T \right] \delta P_{m,i} &= \left[ I + \frac{\Delta t_{m+1}}{2} A(u_{m+1}; z_i)^T \right] \delta P_{m+1,i} + \frac{\Delta t_m}{2} A'(\delta u_m)^T P_{m,i} \\ &\quad + \frac{\Delta t_{m+1}}{2} A'(\delta u_{m+1})^T P_{m+1,i}, \quad m = 1, \dots, N-1 \\ \left[ I - \frac{\Delta t_N}{2} A(u_N; z_i)^T \right] \delta P_{N,i} &= \delta M_{N,i} + \frac{\Delta t_N}{2} A'(\delta u_N)^T P_{N,i} \end{aligned}$$

**Discrete Hessian action** for all  $m = 1, \dots, N_u$ :  $\delta \bar{M}_m := \frac{1}{2}(\delta M_m + \delta M_{m-1})$

$$[H(u)h]_m = \alpha h_m + \gamma B_1 \left( \begin{array}{c} \sum_{i=1}^Z \Delta z_i \left( \delta P_{m,i}^T A_1 \bar{M}_{m,i} + P_{m,i}^T A_1 \delta \bar{M}_{m,i} \right) \\ \sum_{i=1}^Z \Delta z_i \left( \delta P_{m,i}^T A_2 \bar{M}_{m,i} + P_{m,i}^T A_2 \delta \bar{M}_{m,i} \right) \end{array} \right)$$

## 9.2 Magnetic Resonance RF pulse design by optimal control with physical constraints

Armin Rund<sup>1,2</sup>, Christoph Stefan Aigner<sup>3,2</sup>, Karl Kunisch<sup>1,4</sup> and Rudolf Stollberger<sup>3,2</sup>

This is a preprint of the publication "Magnetic Resonance RF pulse design by optimal control with physical constraints". *IEEE Transactions on Medical Imaging*, Volume 37:2, February 2018, Pages 461-472, doi: 10.1109/TMI.2017.2758391

### Abstract

Optimal control approaches have proved useful in designing RF pulses for large tip-angle applications. A typical challenge for optimal control design is the inclusion of constraints resulting from physiological or technical limitations, that assure the realizability of the optimized pulses. In this work we show how to treat such inequality constraints, in particular, amplitude constraints on the B1 field, the slice-selective gradient and its slew rate, as well as constraints on the slice profile accuracy. For the latter a pointwise profile error and additional phase constraints are prescribed. Here, a penalization method is introduced that corresponds to a higher-order tracking instead of the common quadratic tracking. The order is driven to infinity in the course of the optimization. We jointly optimize for the RF and slice-selective gradient waveform. The amplitude constraints on these control variables are treated efficiently by semismooth Newton or quasi-Newton methods.

The method is flexible, adapting to many optimization goals. As an application we reduce the power of refocusing pulses, which is important for spin echo based applications with a short echo spacing. Here, the optimization method is tested in numerical experiments for reducing the pulse power of simultaneous multislice refocusing pulses. The results are validated by phantom and in-vivo experiments.

---

<sup>1</sup>Institute for Mathematics and Scientific Computing, University of Graz, Heinrichstr. 36, 8010 Graz, Austria

<sup>2</sup>BioTechMed-Graz, 8010 Graz, Austria

<sup>3</sup>Institute of Medical Engineering, Graz University of Technology, Stremayrgasse 16/III, 8010 Graz, Austria

<sup>4</sup>Johann Radon Institute for Computational and Applied Mathematics (RICAM), Austrian Academy of Sciences, Altenbergstraße 69, 4040 Linz, Austria

### 9.2.1 Introduction

Magnetic resonance imaging at high field strength is restricted by the specific absorption rate (SAR) and technical limitations of the hardware. For single transmit MR imaging the SAR is proportional to the overall or global pulse power. SAR limitations apply mainly for sequences with larger flip angles (e.g. turbo or multi spin echo) or short TR (e.g. True FISP, SSFP).

Various methods exist to design slice-selective RF pulses [23]. For small flip angles the Bloch equation can be approximated by the inverse Fourier transform, while large flip angles require the full Bloch equation. Neglecting the relaxation terms and assuming pointwise constancy, the Bloch equation can be expressed in the spin domain [67] and inverted by the Shinnar Le-Roux transform for large tip angle RF pulse design [66].

In the context of Simultaneous Multislice (SMS) imaging [95] the global RF power typically increases linearly with the multiband (MB) factor, while the increase in the maximum  $B_1$  peak amplitude can be reduced by phase scrambling[174], time shifting[175] or root flipping[173]. Using sampling and replication properties from the Fourier transform, the PINS method[131] allows for a refocusing of many periodic slices without a power increase at the cost of a reduced bandwidth and long pulse durations, which makes PINS or its enhancement MultiPINS[179] the gold standard for large MB factors. A different approach to reduce the power of a given RF pulse with a distinct slice profile can be accomplished by applying the VERSE principle[112], [176], [221]. Alternatively, the pulse can be improved iteratively by optimal control approaches [1], [152], [153], [202]. Here, one typically minimizes a quadratic objective subject to the Bloch equations.

The aim of this work is to introduce new models and optimal control methods for minimizing the global RF power while restricting the maximal slice profile error. To effectively reduce the pulse power, both the RF pulse and the slice-selective gradient (Gs) are controlled jointly. For ensuring the practical applicability of the optimized pulses, technical constraints on the MR hardware are included into the optimization. Among these are amplitude constraints on Gs and its slew rate, as well as amplitude constraints on the RF pulse. In contrast to existing optimal control approaches, the proper excitation/refocusing pattern is modeled in a detailed way using an error band around a desired pattern. Accordingly we cast the design objectives as inequality constraints rather than as quadratic tracking type functionals. New methods for solving the resulting inequality-constrained optimal control problems for RF pulse design are introduced. Since a reduced pulse power is highly important especially in SMS acquisition[95], test examples from this field are chosen for numerical experiments, as well as phantom and in-vivo measurements.

In our preceding work [1] we set up efficient second-order optimization methods for optimal control of the Bloch equations with relaxation. Here we show how to extend second-order methods to different types of inequality constraints. Semismooth Newton and quasi-Newton methods are introduced and combined with new penalization techniques for assuring the profile accuracy. Furthermore, we extend the optimization framework to the common spin-domain description [66], [67] at the cost of neglecting the relaxation.

## 9.2.2 Theory

The nuclear magnetization vector  $\mathbf{M}$  is described by the Bloch equation (without relaxation) in the on-resonance case  $\dot{\mathbf{M}}(t, z) = \gamma \mathbf{B}(t, z) \times \mathbf{M}(t, z)$ . The external magnetic field  $\mathbf{B}(t, z) = (\text{Re}(B_1(t)), \text{Im}(B_1(t)), g(t)z)$  depends on the complex-valued RF pulse  $B_1(t)$  and the amplitude  $g(t)$  of Gs, as well as the spatial position  $z$  and time  $t \in (0, T)$ . The aim of the optimization will be to control  $B_1(t)$  and  $g(t)$  jointly in order to approximately reach a space-dependent desired magnetization pattern at the terminal time  $T$  with a minimum pulse power. The optimization model will be defined in the spin domain.

### Spin domain Bloch equation

Assuming the external magnetic field to be piecewise constant in time, this Bloch equation can be solved in the spin domain [66], [67] as a sequence of rotations, where the magnetization vector  $\mathbf{M}$  can be described by the complex-valued Cayley-Klein parameters  $(a_m), (b_m), m = 1, \dots, N_t$  with evolution

$$\begin{aligned} a_m &= \alpha_m a_{m-1} - \beta_m^* b_{m-1}, \\ b_m &= \beta_m a_{m-1} + \alpha_m^* b_{m-1}, \end{aligned} \tag{9.20}$$

and with initial conditions  $a_0 = 1, b_0 = 0$ .

The RF pulse is described in polar coordinates  $B_1(t) = r(t) \exp(i\vartheta(t))$  with RF amplitude  $r(t)$ , RF phase  $\vartheta(t)$  and imaginary unit  $i$ . An equidistant time grid  $t_k = k\tau, k = 0, \dots, N_t$  with step size  $\tau = T/N_t$  is chosen with piecewise constant RF pulse

## 9 Appendix

and Gs described by  $(r_m, \vartheta_m, g_m)$ ,  $m = 1, \dots, N_t$ . The coefficients  $a_m, b_m$  are then given by

$$\begin{aligned}\alpha_m &= \cos(\phi_m/2) + i\gamma\tau z g_m \sin(\phi_m/2)/\phi_m, \\ \beta_m &= i\gamma\tau r_m \exp(i\vartheta_m) \sin(\phi_m/2)/\phi_m,\end{aligned}\tag{9.21}$$

with  $\phi_m = -\gamma\tau\sqrt{r_m^2 + (z g_m)^2}$  and the gyromagnetic ratio  $\gamma$ . Here, the variables  $a_m, b_m, \alpha_m, \beta_m, \phi_m$  depend on the spatial coordinate  $z \in \Omega = [-L, L]$  in slice direction based on an equidistant spatial discretization  $-L = z_1 < \dots < z_{N_z} = L$  with step size  $\delta$ .

### Optimal control of the Bloch equation in the spin-domain

The slice-selective excitation or refocusing is modeled as optimal control problem with inequality constraints. We jointly optimize for the RF pulse and Gs amplitude, hence we define the control vector

$\mathbf{x} = (r_1, \dots, r_{N_t}, \vartheta_1, \dots, \vartheta_{N_t}, g_2, \dots, g_{N_t-1})^T$ . The boundary values for the Gs amplitude are fixed  $g_1 = g_0$  and  $g_{N_t} = g_T$  with given  $g_0, g_T \in \mathbb{R}$ . The optimal control problem is to minimize the pulse power

$$\min_{\mathbf{x}} \quad \frac{\tau}{2} \sum_{m=1}^{N_t} r_m^2\tag{9.22}$$

subject to the spin domain Bloch equation (9.20) in every spatial point  $z_j, j = 1, \dots, N_z$ , and an amplitude constraint on the Gs slew rate

$$|g_m - g_{m-1}| \leq \tau s_{\max}, \quad m = 2, \dots, N_t,\tag{9.23}$$

with given  $s_{\max} > 0$ . Additionally, we prescribe amplitude constraints  $r(t) \leq r_{\max}$  with  $r_{\max} > 0$  and bounds for Gs  $g_{\min} \leq g(t) \leq g_{\max}$  denoted by  $g_{\max} > 0$  and  $g_{\min} < g_{\max}$ . They are collected in the pointwise control constraints

$$\mathbf{c}_{\min} \leq \mathbf{x} \leq \mathbf{c}_{\max}\tag{9.24}$$

with vectorized lower and upper bound

$$\begin{aligned}\mathbf{c}_{\min} &= (0, \dots, 0, -\pi, \dots, -\pi, g_{\min}, \dots, g_{\min})^T \\ \text{and } \mathbf{c}_{\max} &= (r_{\max}, \dots, r_{\max}, \pi, \dots, \pi, g_{\max}, \dots, g_{\max})^T.\end{aligned}$$

The slice profile accuracy is now modeled by constraints on the profile and on the phase according to the type of the RF pulse, see [23, Tab 2.3] for excitation, inversion

## 9 Appendix

or refocusing pulses. Below, we concentrate on a spin-echo profile for SMS refocusing with initial magnetization  $(0, M_0, 0)^T$  and ideal crusher gradients. The refocusing profile at the terminal time  $T$  is described by  $|b_{N_t}(z)|^2$  using the last Cayley-Klein parameter  $b_{N_t} = b_{N_t}(z)$  in (9.20). It is enforced to stay in a neighborhood of the ideal rectangular refocusing for all  $z$  in the observation domain  $\Omega_{\text{obs}} \subset \Omega$ , which is partitioned into the in-slice and out-of-slice domain  $\Omega_{\text{obs}} = \Omega_{\text{in}} \cup \Omega_{\text{out}}$ .

$$\begin{aligned} |b_{N_t}(z)|^2 - 1 &\leq e(z), & \forall z \in \Omega_{\text{in}}, \\ |b_{N_t}(z)|^2 &\leq e(z), & \forall z \in \Omega_{\text{out}}, \end{aligned} \quad (9.25)$$

with tolerance  $e = e(z) > 0$  that may depend on  $z$ . In particular a different in-slice and out-of-slice error can be prescribed. The profile is not fixed in between the two regions i.e. on  $\Omega \setminus (\Omega_{\text{in}} \cup \Omega_{\text{out}})$ . For ease of notation we do not write the dependence on  $z_j$  below and introduce the vector  $\mathbf{b} = (b_{N_t}(z_1), \dots, b_{N_t}(z_{N_z}))$ . In case of  $N_{\text{MB}}$  slices with in-slice domain  $S_l, l = 1, \dots, N_{\text{MB}}$ ,  $\Omega_{\text{in}} = \cup_{l=1}^{N_{\text{MB}}} S_l$  a constant phase per slice can be modeled as

$$|\varphi(b(z)) - \bar{\varphi}_l(\mathbf{b})| \leq e_p, \quad \forall z \in S_l, \quad l = 1, \dots, N_{\text{MB}}, \quad (9.26)$$

with phase  $\varphi(b(z)) = \arg(b_{N_t}^2(z))$  and arithmetic mean of the phase  $\bar{\varphi}_l(\mathbf{b})$  in slice  $l$ , and tolerance  $e_p = e_p(z) > 0$ .

The control constraints (9.24) and the state constraints (9.25), (9.26) need different solution techniques. Below, we suggest semismooth Newton techniques for the pointwise control constraints (9.24), which is computationally very inexpensive. In contrast, (9.23) and the state constraints (9.25, 9.26) will be treated by an iterative penalization method.

### Penalization

State-constrained optimal control problems are known to be challenging since the Lagrange multipliers are typically irregular, which may lead to a decrease of the convergence speed and accuracy of numerical solution methods. To address these difficulties, regularization techniques within Newton-type methods for state-constrained optimal control problems were introduced by several authors, in particular primal-dual active-set strategies applied to a Moreau-Yosida regularization [222], [223], which are under appropriate conditions equivalent to a semismooth Newton method [224]. Solution by interior-point methods were proposed in [225]. For further investigations of the topic we refer to [226] and the references therein.

## 9 Appendix

Here we suggest a related but different method, which is designed to facilitate the convergence and globalization properties of the problem at hand. We suggest an  $L^p$ -penalization of the state constraints (9.25) with parameters  $\mu_{\text{out}}, \mu_{\text{in}} > 0$ , and an integer exponent  $p \geq 1$ , which is driven to  $\infty$  as we approach the optimizer. Therefore, we eliminate (9.25) and add

$$\frac{\delta\mu_{\text{out}}}{2p} \sum_{z_j \in \Omega_{\text{out}}} \left( \frac{|b_{N_t}|^2}{e} \right)^p + \frac{\delta\mu_{\text{in}}}{2p} \sum_{z_j \in \Omega_{\text{in}}} \left| \frac{|b_{N_t}|^2 - 1}{e} \right|^p \quad (9.27)$$

to the objective with parameters  $\mu_{\text{in}}, \mu_{\text{out}} > 0$  and the spatial step size  $\delta > 0$ . While  $p = 1$  corresponds to the widespread quadratic tracking, the power- $p$  penalty recovers the original state constraint (9.25) for  $p \rightarrow \infty$ . This follows from the simple observation that  $|s|^p \rightarrow \infty$  for  $|s| > 1$  and  $|s|^p \rightarrow 0$  for  $|s| < 1$  if  $p \rightarrow \infty$ . We propose a loop around the optimization where  $p$  is increased successively until the minimum pulse power solution is attained. We do not start with large  $p$  from the beginning, since a small value of  $p$  turns out to be advantageous for the globalization, as will be shown in the results section.

The constraints on  $g$  in (9.23) and on the in-slice phase in (9.26) are treated analogously. For algorithmic purposes we also add a small regularization for the controls  $\vartheta_m, g_m$  with parameter  $\zeta > 0$ , which is driven to 0 as we approach the optimizer. To avoid absolute values we restrict  $p > 0$  to be even. Altogether the penalized objective is defined as

$$\begin{aligned} J(\mathbf{x}, \mathbf{b}) = & \frac{\tau}{2} \sum_{m=1}^{N_t} r_m^2 + \zeta \vartheta_m^2 + \zeta g_m^2 \\ & + \frac{\delta\mu_{\text{out}}}{2p} \sum_{z_j \in \Omega_{\text{out}}} \left( \frac{|b_{N_t}|^2}{e} \right)^p + \frac{\delta\mu_{\text{in}}}{2p} \sum_{z_j \in \Omega_{\text{in}}} \left( \frac{|b_{N_t}|^2 - 1}{e} \right)^p \\ & + \frac{\delta\mu_p}{p} \sum_{l=1}^L \sum_{z_j \in S_l} \left( \frac{\varphi - \bar{\varphi}_l}{e_p} \right)^p + \frac{\tau\mu_g}{p} \sum_{m=2}^{N_t} \left( \frac{g_m - g_{m-1}}{\tau s_{\text{max}}} \right)^p \end{aligned} \quad (9.28)$$

with parameters  $\zeta, \mu_p, \mu_g > 0$ .

### 9.2.3 Methods

#### Semismooth (quasi-)Newton method

Semismooth Newton methods are a generalization of Newton's method for specific nonsmooth equations. In the context of optimal control problems they were introduced by [190], [224], see also the monographs [227], [228]. With local superlinear convergence, these methods turned out to be highly efficient for optimal control problems with pointwise control or (regularized) state constraints, with sparsity, or with variational inequalities. Here, the penalized optimal control problem (9.20,9.24,9.28) for a fixed  $p$  is solved with semismooth Newton methods. Semismooth Newton methods fulfill the remaining inequality constraints efficiently based on projections. This procedure allows for the inclusion of these constraints into the optimization code without increasing the computational effort. For efficiency the optimization is done purely on the controls  $\mathbf{x}$ , while the state variables are eliminated using the discrete Bloch and auxiliary equations. We introduce the reduced objective

$$j(\mathbf{x}) = J(\mathbf{x}, \mathbf{b}(\mathbf{x}), \mathbf{w}(\mathbf{x})) = \frac{1}{2} \mathbf{x}^T E \mathbf{x} + F(\mathbf{x}),$$

with the diagonal matrix  $E = \tau \text{diag}(1, \dots, 1, \zeta, \dots, \zeta, \zeta, \dots, \zeta)$  and penalization terms  $F$ . With its gradient  $\mathbf{j}'(\mathbf{x}) = E\mathbf{x} + \mathbf{F}'(\mathbf{x})$  the first order necessary optimality conditions for  $\min_{\mathbf{c}_{\min} \leq \mathbf{x} \leq \mathbf{c}_{\max}} j(\mathbf{x})$  are given by

$$\mathbf{x} = P_{\text{ad}}(-E^{-1}\mathbf{F}'(\mathbf{x})), \quad (9.29)$$

where  $P_{\text{ad}} = \min(\mathbf{c}_{\max}, \max(\mathbf{c}_{\min}, z))$  denotes the componentwise projection to the feasible set.  $\mathbf{F}'(\mathbf{x})$  is given in terms of a forward and backward solve using a Lagrange calculus in Appendix 9.2.7. The calculations are done with the Wirtinger calculus [229], which for the spin domain description allows for an efficient derivation and a compact form of both, the equations and the subsequent code. We reformulate (9.29) equivalently by introducing  $\mathbf{c} := -E^{-1}\mathbf{F}'(\mathbf{x})$  as independent variable and parametrize the control  $\mathbf{x} = P_{\text{ad}}(\mathbf{c})$ . Then a minimizer has to fulfill  $\mathbf{G}(\mathbf{c}) := E\mathbf{c} + \mathbf{F}'(P_{\text{ad}}(\mathbf{c})) = 0$ .  $\mathbf{G}$  is nonsmooth but semismooth, which allows for the semismooth Newton iteration  $\mathbf{c}^{k+1} = \mathbf{c}^k + \delta\mathbf{c}$ ,

$$D_N G(\mathbf{c}^k) \delta\mathbf{c} = -\mathbf{G}(\mathbf{c}^k). \quad (9.30)$$

Therein,  $D_N G(\mathbf{c}^k) \delta\mathbf{c}$  is the generalized Newton-derivative of  $G$  applied to the direction  $\delta\mathbf{c}$  in the current point  $\mathbf{c}^k$ . While the assembling of the full matrix  $D_N G(\mathbf{c}^k)$  is computationally expensive, it is well-known that the evaluation of a matrix vector

## 9 Appendix

product can be performed efficiently, without knowledge of the full matrix. This technique is basis of matrix-free Newton-Krylov methods, where the Newton equation is solved iteratively using a Krylov method. We already presented this technique in [1] in the absence of inequality constraints and for the Crank-Nicolson Bloch solver. Here, we apply the technique in the spin domain, generalize the Newton method to the semismooth case with inequality constraints, and to quasi-Newton methods. By the calculus for Newton derivatives [227], the left-hand side of (9.30) can be computed as

$$D_N G(\mathbf{c}^k) \delta \mathbf{c} = E \delta \mathbf{c} + F''(P_{\text{ad}}(\mathbf{c}^k)) D_N P_{\text{ad}}(\mathbf{c}^k) \delta \mathbf{c} \quad (9.31)$$

where  $D_N P_{\text{ad}}(\mathbf{c}^k)$  is the Newton-derivative of the projection  $P_{\text{ad}}$  at the current iterate  $\mathbf{c}^k$ . The second summand can be realized by a forward backward solve consisting in a linearized Bloch equation and its adjoint analogously to [1, eq. (6,7)]. We introduce the inactive set  $\mathcal{I} = \{m \mid -c_{\min,m} < c_m < c_{\max,m}\}$  and its characteristic function  $\chi_{\mathcal{I}}(m)$  which is 1 for  $m \in \mathcal{I}$  and 0 otherwise. Then it holds that  $D_N P_{\text{ad}}(\mathbf{c}) = \chi$  with  $\chi = \text{diag}(\chi_{\mathcal{I}}(1), \dots, \chi_{\mathcal{I}}(3N_t - 2))$ . In order to save computational effort, the system is firstly solved on the inactive set  $\mathcal{I}$ , where  $D_N G(\mathbf{c})$  is symmetric, using the Steihaug-cg method [230]. Finally the components on the active set can be easily obtained by adding the last residual, for background see [191, Algorithm 2]. Steihaug-cg is embedded into a trust-region framework based on [230] and [191, Algorithm 3].

In case of a semismooth quasi-Newton method we approximate  $F''$  using the Broyden-Fletcher-Goldfarb-Shanno (BFGS) formula [231]

$$B_{k+1} = B_k - \frac{B_k \mathbf{s}_k \mathbf{s}_k^T B_k}{\mathbf{s}_k^T B_k \mathbf{s}_k} + \frac{\mathbf{y}_k \mathbf{y}_k^T}{\mathbf{y}_k^T \mathbf{s}_k}, \quad (9.32)$$

with  $\mathbf{s}_k = \mathbf{x}^{k+1} - \mathbf{x}^k$  and  $\mathbf{y}_k = \mathbf{F}'(P_{\text{ad}}(\mathbf{c}^{k+1})) - \mathbf{F}'(P_{\text{ad}}(\mathbf{c}^k))$ . The expression  $D_N G(\mathbf{c}) \delta \mathbf{c}$  is then replaced by  $(E + B_{k+1} \chi) \delta \mathbf{c}$ . The update is skipped if the trust-region step is rejected. For efficiency, we apply  $B_{k+1}$  in the (matrix-free) limited-memory BFGS method using the compact form of [231] and [232], which requires less storage and computational effort by storing only data from the last  $L_{\text{BFGS}}$  steps with a fixed limit  $L_{\text{BFGS}} \in \mathbb{N}$ .

We note that the presented trust-region semismooth Newton method coincides with the trust-region Newton method of [1] in the absence of control constraints (9.24). In this case  $P_{\text{ad}}(\mathbf{c}) = \mathbf{c}$ , and the active set is empty.

## Implementation

The optimal control approach is implemented in MATLAB (The MathWorks, Inc., Natick, USA). The Bloch state and adjoint solvers are parallelized in C using OpenMP and included using a MEX file. The computations are done on one node of the HPC Cluster "RADON 1" (RICAM Linz, Austria) with 16 CPU cores with 2.4 GHz.

The parameters of the penalized objective are adapted automatically throughout the optimization. Therefore, the maximum errors in the constraints (9.23), (9.25), (9.26) are defined

$$\begin{aligned}
 \varepsilon_g &= \max_{m=2,\dots,N_t} |g_{m-1} - g_m| / (\tau s_{\max}), \\
 \varepsilon_{\text{out}} &= \max_{z \in \Omega_{\text{out}}} |b_{N_t}|^2 / e, \\
 \varepsilon_{\text{in}} &= \max_{z \in \Omega_{\text{in}}} (1 - |b_{N_t}|^2) / e, \\
 \varepsilon_{\text{ph}} &= \max_{l=1,\dots,L} \max_{z \in S_l} |\varphi - \bar{\varphi}_l| / e_p.
 \end{aligned} \tag{9.33}$$

Note that these errors are dimensionless and scaled to 1. Every 20th optimization step we adapt the parameter  $\mu_g$  by multiplication with  $\min(10, \max(0.3, 1 + 10(\varepsilon_g - 1)))$ . Accordingly we increase  $\mu_g$  if  $g$  is not admissible to the slew rate constraint ( $\varepsilon_g > 1$ ), keep  $\mu_g$  if  $g$  is admissible but active ( $\varepsilon_g = 1$ ), and reduce it if the slew rate constraint is not active at all ( $\varepsilon_g < 1$ ). The other parameters ( $\mu_{\text{out}}, \mu_{\text{in}}, \mu_p$ ) are adapted in the same way by exchanging  $\varepsilon_g$  with  $\varepsilon_{\text{out}}, \varepsilon_{\text{in}}, \varepsilon_{\text{ph}}$ . This technique ensures that the different penalty terms remain balanced, and that the results are insensitive to the initialization of the parameters. Initially we set  $\mu_{\text{out}} = 10^5$ ,  $\mu_{\text{in}} = 10^4$ ,  $\mu_p = 1$ , and  $\mu_g = 1$ .

### 9.2.4 Results

In this section we demonstrate the application of the proposed design method to reduce the overall RF pulse power using different initial guesses in the field of SMS refocusing. We consider four different experiments for a varying number of slices and slice thicknesses. The initial pulses are designed with six different state of the art methods for SMS RF pulse design [95] including a conventional superposition [162], superposition with VERSE[112], [160], PINS[131], PINS with VERSE, MultiPINS[179] and root-flipped SMS design [173]. For all simulations we assume perfect spoiling for the computed refocusing profile in the spin-domain description [66]. Tab. 9.3 lists the parameters of the four examples. The peak amplitudes are generally set to  $r_{\max} = 18$

## 9 Appendix

Table 9.3: Parameters of the experiments

Example	MB factor	$T$ ms	$N_t$	$L$ mm	$N_z$	transition region mm	$s_{\max}$ $T m^{-1} s^{-1}$	$e _{\Omega_{\text{in}}}$	$e _{\Omega_{\text{out}}}$	$e_p$
SUP MB3	3	10.42	515	60	2401	1.1	200	0.03	0.02	$\infty$
Root-flipped MB6	6	8.41	258	36	961	1.2	200	0.05	0.04	$\infty$
PINS MB10	10	9.46	946	120	4801	1.2	200	0.03	0.02	0.01
Comparison MB5	5	6.02	602	125	5001	1.8	200	0.03	0.02	0.01

$\mu\text{T}$  for  $B_1$ ,  $g_{\max} = 24 \text{ mT m}^{-1}$  for the gradient, and  $200 \text{ T m}^{-1} \text{ s}^{-1}$  for the gradient slew rate. The minimum gradient value  $g_{\min}$  is set to  $-g_{\max}$ . However, the second example below investigates the influence of the choice of  $s_{\max}$  and  $g_{\min}$  on the optimal solution. Typical spatial and the temporal discretizations are chosen (50 to 75  $\mu\text{m}$  and 10 to 40  $\mu\text{s}$ ). The excluded transition regions are listed in Tab. 9.3 and shown graphically in Row 3 of Fig. 9.7-9.11 where black lines mark the in-slice/out-of-slice error tolerance. In all examples we set  $g_T = g_0$  determined by the used initial guess. To compare the overall pulse power of the initials and the optimized RF pulse candidates, we compute the (scaled) pulse power using

$$S = 10^4 \tau \sum_{m=1}^{N_t} r_m^2, \quad [S] = 10^{-5} \text{T}^2 \text{s}. \quad (9.34)$$

As standard parameters for the optimization the exponent  $p$  in the penalization is initially set to 2 and increased by a factor of 2 every 350th iteration of the quasi-Newton method (with  $L_{\text{BFCS}} = 30$ ), which is shown below to be the preferable strategy in general. In addition, we give the best results using individually tuned parameters per example. Whenever  $p$  is increased,  $\zeta$  is divided by 10 starting from  $\zeta = 0.01$ .

### Superposition (SUP) MB3

We designed a 180 degree single slice refocusing pulse based on the SLR [66] (in-slice and out-of-slice error of 0.02, time bandwidth product (TBP) = 2.8 and slice thickness of 2 mm). To generate a SMS refocusing pulse with a MB factor of three, we superposed three partially phase shifted subpulses together with a constant Gs amplitude. The symmetry of the slices around the isocenter leads to a real valued pulse, rather than a complex pulse. This RF pulse was scaled to a maximal peak  $B_1$  amplitude of 18  $\mu\text{T}$  resulting in a pulse duration of 10.42 ms and is shown, together with a Bloch simulation, in the first row of Figure 9.7. The optimized results for this

## 9 Appendix

Table 9.4: Optimization results: optimized pulse power in dependence of the choice rule for  $p$  (in MATLAB colon notation).  $p$  is increased every maxit iteration (or stopping in case of maximum  $p$ )

choice rule for $p$	maxit	optimized pulse power $S$		
		SUP MB3	RF MB6	PINS MB10
2	3500	1.859	4.501	1.697
$2^5$	3500	0.931	3.087	1.087
$2^{10}$	3500	1.298	4.501	0.929
$2^{1:10}$	350	0.767	2.199	0.819
$4^{1:5}$	700	0.768	2.240	0.828
$2^{4:10}$	500	0.770	2.232	0.851
$8^{1:4}$	875	0.799	2.433	0.879
$2^{1:10}$	100	1.577	2.632	1.697
$2^{1:10}$	250	0.771	2.237	0.840
$2^{1:10}$	350	0.767	2.199	0.819
$2^{1:10}$	450	0.797	2.184	0.816
$2^{1:10}$	500	0.805	2.168	0.914

example are given in the second row of Figure 9.7. The simulated refocusing profile is shown for the full field of view (FOV) of 120 mm and in detail for the central slice in the third row of Figure 9.7 with the non-optimized but still stable phase. The overall pulse power is reduced by 59% from initially  $S = 1.859$  to  $S = 0.767$  after the optimization.

Different strategies for choosing the penalty exponent  $p$  were tested, see Tab. 9.4. In the upper seven cases 3500 quasi-Newton iterations are performed in total. The optimized values of  $S$  for the first three examples presented in this paper are depicted. As can be seen in the first three rows, constant values of  $p$  do not allow to find a small pulse power. Especially, the classical quadratic tracking in the first row cannot improve  $S$  within 3500 iterations. In contrast, the proposed strategy of increasing  $p$  from a small initial value to a large value performs well, independently of the particular protocol, see rows four to seven. The best results were gained with the strategy  $p = 2^k, k = 1, \dots, 10$ . The lower part shows that the number of 350 iterations is a reasonable choice for that strategy. Therefore, this strategy is applied for all other optimization results throughout the paper. We observed that larger values  $p > 1024$  lead to many more iterations without a significant gain. However, we mention the best observed run for this example, which yielded a power  $S = 0.744$  with individually tuned parameters  $p = 2^k, k = 1, \dots, 12$  with maxit = 500 and  $L_{\text{BFGS}} = 180$ .

## Root-flipped MB6

For this example we used a SMS refocusing pulse designed with the root-flipped method[173] as an initial guess for the numerical optimization together with a constant  $G_s$  amplitude. This complex RF pulse refocuses six slices with a slice thickness of 1.75 mm and  $TBP = 4$ . Scaled to a peak  $B_1$  amplitude of 13  $\mu\text{T}$ , the pulse duration results in 9.46 ms with  $S = 4.501$ . By optimization the pulse power was reduced down to approximately  $S = 2.2$  corresponding to a SAR reduction of 51%. Below we show that the reduction can even be increased to 77%. This best solution is plotted together with the initial guess in Figure 9.8. Bloch simulations at the terminal time of the spoiled refocusing profile are given for the full  $FOV = 72$  mm and in detail for one slice together with the refocusing phase. Please note, that the phase was intentionally not part of the optimization.

Here, we compare different values of the limit parameter  $L_{\text{BFGS}}$  for the limit-memory BFGS, as well as the full semismooth Newton method, see Tab. 9.5. As can be seen from the table,  $L_{\text{BFGS}} = 10$  does not improve the pulse power satisfactorily. In contrast,  $L_{\text{BFGS}} = 30$  already yields very small values in a computation time of 2.3 min. Further increasing the limit in the BFGS method yields slightly better results at the costs of a higher computational effort. Due to this trade-off we decided to use  $L_{\text{BFGS}} = 30$  in all other optimization results. However, if much more computational time can be invested, the SAR of the MB6 pulse can be even reduced by 74% using individually tuned parameters. Then, the pulse power is reduced to  $S = 1.166$  using  $p = 2^k, k = 1, \dots, 10$  with  $\text{maxit} = 5000$  and  $L_{\text{BFGS}} = 200$  leading to a computation time of 55 min. On the other hand, the exact Hessian within the semismooth Newton method allows for the best power values that were observed at the cost of an increased numerical effort. Here, we find  $S = 1.471$  in the standard configuration (300 iterations per step for  $p = 2^k, k = 2, \dots, 7$ ) with a computation time of about 2h (with standard MATLAB parallelization instead of C/OpenMP). With individually tuned parameters the semismooth Newton method gives  $S = 1.041$  which is a reduction of 77% of the pulse power.

The influences of the maximum slew rate  $s_{\text{max}}$  and the minimum gradient  $g_{\text{min}}$  on the gain of the optimal solution are depicted in Tab. 9.6. With smaller  $s_{\text{max}}$  the SAR reduction decreases slightly from 51% down to 40%. An increase of  $g_{\text{min}}$  up to 1 does not influence the optimal SAR significantly, which is related to the given boundary conditions  $g_0 = g_T = 2.31$ . However, larger values decrease the SAR reduction significantly. The optimal solutions for different  $s_{\text{max}}$  are depicted in Fig. 9.9. It can be seen that the slew rate is hitting the constraint at many time instances and in all settings. With smaller  $s_{\text{max}}$  the gradient waveform gets smoother, while the maximum RF amplitude increases slightly. All optimal solutions show a good slice profile, one that is admissible to the underlying inequality constraints. Up to now the lower

## 9 Appendix

Table 9.5: Optimization results: optimal pulse power in dependence of the optimization method. maxit is the iteration per step for  $p$ , i.p. denotes individually tuned parameters per example.

optimization method	maxit	optimized pulse power $S$		
		SUP	RF	PINS
		MB3	MB6	MB10
semism. Newton, $p = 2^{2:7}$	300		1.471	
semism. Newton	i.p.		1.041	
semism. BFGS, $L_{\text{BFGS}} = 10$	350	0.790	2.257	0.997
semism. BFGS, $L_{\text{BFGS}} = 30$	350	0.767	2.199	0.819
semism. BFGS, $L_{\text{BFGS}} = 50$	350	0.763	2.172	0.813
semism. BFGS, $L_{\text{BFGS}} = 80$	350	0.761	2.163	0.808
semism. BFGS, $L_{\text{BFGS}} = 200$	i.p.	0.744	1.166	0.803

constraint on  $g$  was never active due to  $g_{\min} = -24$ . In contrast, Figure 9.10 shows the optimized results with different tight constraints on the minimal gradient amplitude ( $\{0, 1, 2.31\} \text{ mT m}^{-1}$ ) and standard parameters. As can be seen, the lower bound constraint on  $g$  is active at many time instances, especially for  $g_{\min} = 2.31$ .

### PINS MB10

For the third example we designed a SMS refocusing pulse applying the PINS method [131] on a SLR based 180 degree refocusing pulse (in-slice and out-of-slice error of 0.02, TBP = 3, slice thickness of 2 mm). Accordingly, the  $G_s$  amplitude is built up of regular PINS blips, see the upper left plot of Figure 9.11. Here, we include phase constraints with a maximum phase deviation of  $e_p = 0.01$  rad from the mean phase per slice. This PINS refocusing pulse was scaled to a peak  $B_1$  amplitude of 18  $\mu\text{T}$  producing  $T = 10.36$  ms. The optimized real valued controls are given in Figure 9.11 together with the used initial and Bloch simulations with  $FOV = 240$  mm.

The power of the shown RF pulse was reduced to  $S = 0.819$  by roughly 53% compared to the initial PINS guess. With individually tuned parameters we even find  $S = 0.803$  with  $p = 2^k, k = 1, \dots, 12$ , maxit = 500 and  $L_{\text{BFGS}} = 170$ . For each example the reduction of the required pulse power is depicted in Tab. 9.7. The last three rows of Tab. 9.7 contain the optimization results without joint control, i.e. when only the RF pulse is controlled while  $g$  is kept fix at its initialization. For the superposition pulse with a fixed and constant  $g$  the reduction in the pulse power  $S$  is limited, while for the root-flipped pulse we observe a good reduction of 35% (compared to 51% reduction for joint control). In case of PINS initialization, keeping the non-constant  $g$

## 9 Appendix

Table 9.6: Optimization results for a MB6 pulse: optimal pulse power  $S$  in dependence of the maximum slew rate  $s_{\max}$  and the minimum gradient field  $g_{\min}$ .

$s_{\max}$	$g_{\min}$	optimized $S$	SAR reduction
200	-24	2.199	51.1%
100	-24	2.248	50.1%
50	-24	2.357	47.6%
30	-24	2.458	45.4%
10	-24	2.683	40.4%
200	-24	2.199	51.1%
200	0	2.211	50.9%
200	1	2.289	49.1%
200	2	2.621	41.8%
200	2.3	2.896	35.7%
200	2.3091	2.901	35.6%

fixed yields a reduction of 46% which is just slightly below the value of 53% that was observed for joint control.

### Comparison of different initializations for MB5

In a final study we compare the performance of the optimization method for different initializations (superposition, superposition with VERSE, PINS, PINS with VERSE, and MultiPINS). For an intermediate MB factor of 5, these five initializations can be designed with the same duration ( $T = 6.02$  ms) and comparable slice profile properties (slice thickness 2 mm, TBP = 2, maximum in-slice and out-of-slice error, and maximum phase error, see Tab.9.3) resulting in different peak  $B_1$  amplitudes and RF power (see Tab.9.8). The boundary conditions are in general set to  $g_0 = g_T = 0$ , which is implemented with a ramp-up/ramp down for the superposition pulse to reach the constant gradient of  $4.65 \text{ mT m}^{-1}$ , respectively  $5.00 \text{ mT m}^{-1}$  with VERSE. Furthermore, the peak  $B_1$  for the superposition pulse is projected down to the allowed maximum of  $18 \text{ } \mu\text{T}$ . The optimized pulse power  $S$  is shown in the last two columns of Tab.9.8 for standard parameters in the optimization (column  $S$ ) and for  $L_{\text{BFGS}} = 200$ ,  $p = 2^k, k = 1, \dots, 12$  with each 350 iterations (column  $S$  best). Depicted are also the maximum errors of the slice profile.

In the first two rows the superposition pulse without and with VERSE are compared. We see that the version with VERSE allows for a smaller pulse power  $S$  after optimization. The last three rows show that the optimization method yields the best

## 9 Appendix

Table 9.7: Pulse power  $S$  of initial and optimized pulse with standard parameters and with individually tuned parameters/method.

Example	initial $S$	optimized $S$	SAR reduction
PINS	1.724	0.819	52.5%
PINS best	1.724	0.803	53.4%
SUP	1.859	0.767	58.7%
SUP best	1.859	0.744	60.0%
Root-flipped	4.501	2.199	51.1%
Root-flipped best	4.501	1.041	76.9%
PINS ( $g$ fixed)	1.724	0.925	46.3%
SUP ( $g$ fixed)	1.859	1.471	20.9%
Root-flipped ( $g$ fixed)	4.501	2.927	35.0%

power values for PINS, PINS with VERSE and MultiPINS pulses. While their initial values for  $S$  are different, the optimized values in the last column coincide for these three initialization. However, the optimized pulses behind these power values are very different. The maximum errors in the optimum are increased out-of-slice and in the phase, however, the maximum allowed errors are in most cases not attained. The maximum in-slice errors of the initializations and the optima agree and are at the bound 0.03.

### Experimental validation

Figure 9.12 contains the experimental validation of the optimized refocusing pulse and  $G_s$  shape for MB<sub>3</sub> using a superposition initial (Figure 9.7), MB<sub>5</sub> using a MultiPINS initial (not shown) and MB<sub>10</sub> using a PINS initial (Figure 9.11), on a 3T MR scanner (Magnetom Skyra, Siemens Healthcare, Erlangen, Germany). The data is acquired with a 2D spin echo sequence (TE = 25 – 30 ms, TR = 100 ms, FOV = 300 mm × 300 mm, matrix = 1536 pixel × 1536 pixel (922 phase encoding steps), readout bandwidth = 130 Hz/pixel) with conventional superposed SMS excitation pulses using a cylindrical phantom. Figure 9.13 contains a zoomed view to one slice of the experimental phantom data shown in Figure 9.12 and compares it to numerical Bloch simulations of the optimized refocusing pulses. Figure 9.14 shows the in-vivo reconstruction of the measured slice profiles (optimized MB<sub>3</sub>) as described above with a TR = 200 ms and a matrix of 512 pixel × 512 pixel with a measured head SAR of 0.288 W kg<sup>-1</sup> (0.512 W kg<sup>-1</sup> for the initial MB<sub>3</sub> pulse).

## 9 Appendix

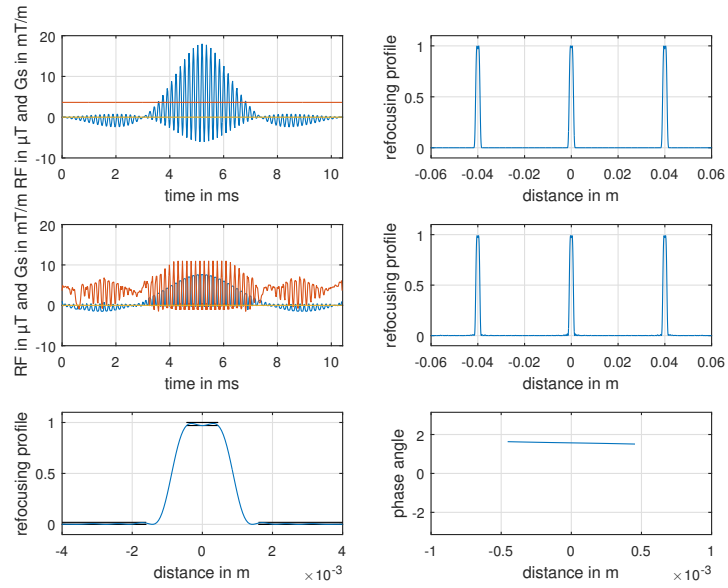


Figure 9.7: Optimization results and spin domain Bloch simulations for a MB3 pulse. Initial (Row 1) and optimized (Row 2) RF and Gs (Re(RF) in blue, Im(RF) in yellow and Gs in red) with refofocusing profile  $|b_{N_i}|^2$ . Zoom of the central slice (black lines mark the in-slice/out-of-slice error tolerance) with phase angle( $b_{N_i}$ ) (not part of the optimization) for the optimized pulse (Row 3).

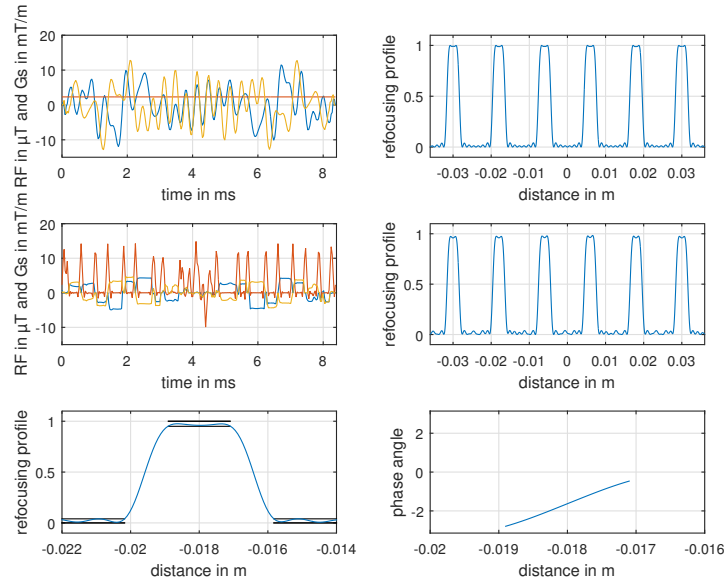


Figure 9.8: Optimization results and spin domain Bloch simulations for a MB6 pulse. Initial (Row 1) and optimized (Row 2) RF and Gs (Re(RF) in blue, Im(RF) in yellow and Gs in red) with refofocusing profile  $|b_{N_i}|^2$ . Zoom of the central slice (black lines mark the in-slice/out-of-slice error tolerance) with phase angle( $b_{N_i}$ ) (not part of the optimization) for the optimized pulse (Row 3)

## 9 Appendix

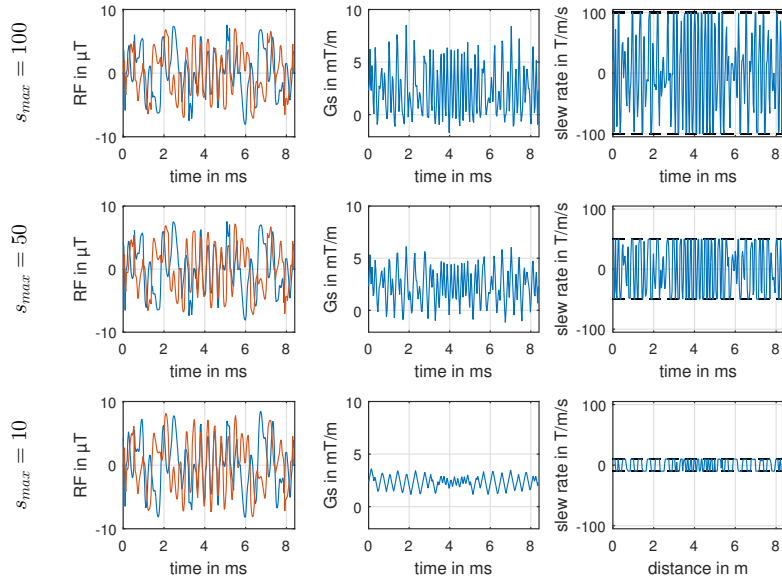


Figure 9.9: Optimized MB6 RF pulse (Re(RF) in blue, Im(RF) in red), slice-selective gradient Gs and gradient slew rate for different maximum values of  $s$ :  $s_{max} \in \{100, 50, 10\} \text{ T m}^{-1} \text{ s}^{-1}$ .

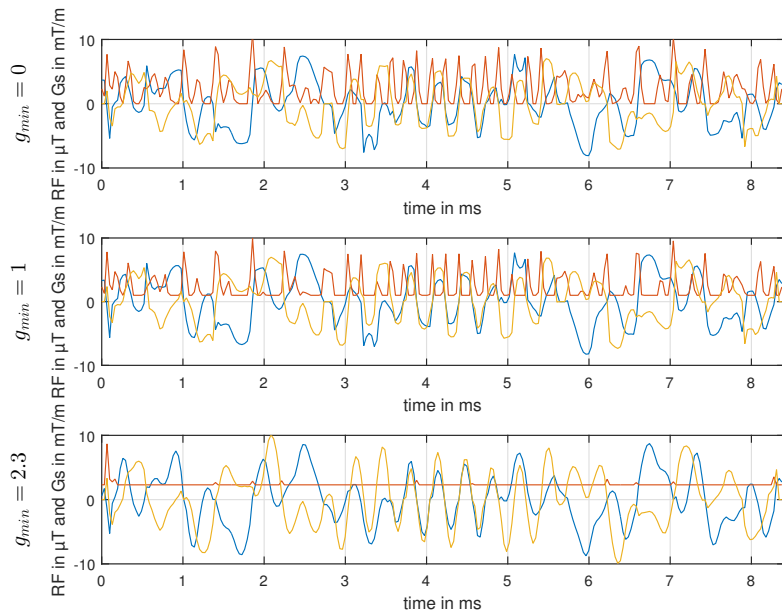


Figure 9.10: Optimized MB6 RF pulse and slice-selective gradient shape (Re(RF) in blue, Im(RF) in yellow and Gs in red) for different minimal values of  $G_s$ :  $g_{min} \in \{0, 1, 2.3\} \text{ mT m}^{-1}$ .

## 9 Appendix

Table 9.8: Performance of the optimization method for different initializations for an MB5 example. Depicted are the maximum errors and the pulse power  $S$  both for the initial and optimized pulse. The maximum errors were constrained by 0.03 in-slice , by 0.02 out-of-slice , and by 0.01 in the phase constraint.

Initialization	initial					optimized				
	error in-slice	error out-of-slice	error phase	$\max  B_1 $ $\mu\text{T}$	$S$ $10^{-5}\text{T}^2\text{s}$	error in-slice	error out-of-slice	error phase	$S$ $10^{-5}\text{T}^2\text{s}$	$S$ best $10^{-5}\text{T}^2\text{s}$
SUP	0.0318	0.0142	0.0031	18	1.9531	0.0300	0.0066	0.0100	0.7712	0.7677
SUP VERSE	0.0297	0.0016	0.0010	14	1.4461	0.0300	0.0200	0.0032	0.5603	0.5556
PINS	0.0294	0.0010	0.0009	13	1.1301	0.0300	0.0116	0.0030	0.4163	0.4108
PINS VERSE	0.0297	0.0014	0.0008	13	0.9967	0.0300	0.0146	0.0093	0.4578	0.4093
MultiPINS	0.0297	0.0016	0.0009	8	0.7262	0.0300	0.0200	0.0032	0.4144	0.4127

### 9.2.5 Discussion

We presented a general framework for optimal control based joint design of RF pulses and gradient waveforms for MRI. The framework is flexible in the primary optimization goal, which was chosen as SAR reduction in the examples above, and in the desired magnetization profile. The latter can range from a conventional single slice in the isocenter, to asymmetric or off-resonance profiles, or SMS. While we included the most important inequality constraints for RF pulse design, it is possible to add other constraints and treat them with the presented penalization method. Otherwise, constraints can also be turned off by choosing an infinite bound.

The examples were chosen in the context of SMS imaging, where the pulse power and peak  $B_1$  amplitude are easily exceeded and complying the hardware constraints is crucial for practical applications. Therefore, the optimal control method was tested in the numerical experiments focusing on SAR reduction of several SMS refocusing pulses for various slice thicknesses, time bandwidth products and a slice acceleration factor ranging from MB3 to MB10. The initial pulses are designed with different methods, with conventional superposition[162], VERSE[112], [160], root flipping[173], PINS[131] and MultiPINS [179] with SLR based subpulses[66]. We investigated four different examples for low (MB3), intermediate (MB5 and MB6) and large (MB10) slice acceleration factors. PINS pulses for low MB factors and superposition pulses for large MB factors typically have a very long pulse duration. Therefore we chose to use MB3 superposition pulses for low and MB10 PINS pulses for large MB factors only and compare different initialization methods (SUP, SUP VERSE, PINS, PINS VERSE and MultiPINS) for the intermediate MB5 case. The root flipping pulse is excluded from this comparison and investigated separately for MB6 as it creates refocusing profiles with a non linear phase.

## 9 Appendix

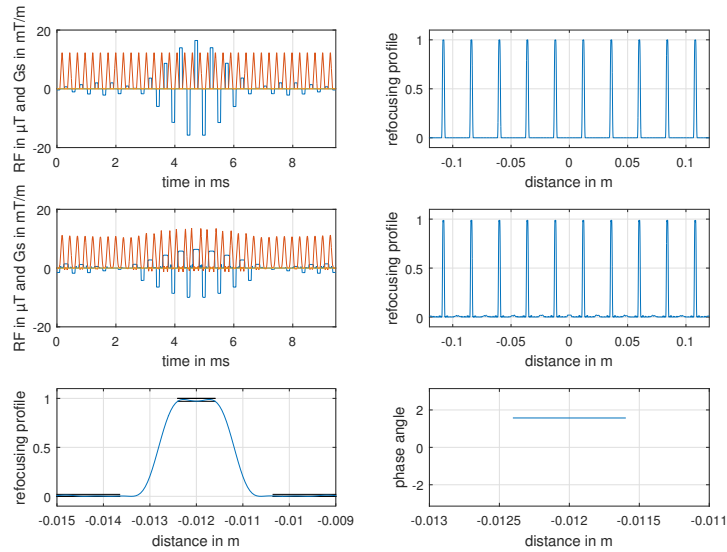


Figure 9.11: Optimization results and spin domain Bloch simulations for a MB10 pulse. Initial (Row 1) and optimized (Row 2) RF and gradient waveform (Re(RF) in blue, Im(RF) in yellow and Gs in red) with refocusing profile  $|b_{N_i}|^2$ . Zoom of the central slice (black lines mark the in-slice/out-of-slice error tolerance) with phase angle( $b_{N_i}$ ) for the optimized pulse (Row 3)

The results show that the proposed optimal control model and method can reduce the pulse power dramatically. The overall power of the initial pulses was reduced by roughly 58 percent for SUP MB3 and 52 percent for PINS MB10 (and by 77 percent for the RF MB6 pulse with a higher tolerance  $e_{in}$  and  $e_{out}$ , see Tab. 9.3). Please note that the initial power of the PINS pulse already lies in the range of the MB3 pulse designed with superposition. As can be seen in the Figures 9.7-9.11 the optimal waveforms vary in their shape, and hence depend on the initialization. The figures show that the maximum and mean  $B_1$  amplitude is reduced and the slice-selective gradient is modulated. While the initial PINS already uses a time varying Gs, the optimized superposition and in particular the optimized root flipped example introduce fluctuating Gs curves from constant initializations. The extent of the fluctuations in Gs changes with the prescribed maximum gradient slew rate, see Fig.9.9, and small fluctuations give a slightly reduced but still significant reduction in the pulse power, see Tab. 9.6. Even a constant and fixed Gs allows for a significant reduction of the pulse power for the root flipped initialization, but only a slight reduction for the superposition pulse, see Tab. 9.7. Keeping the non-constant Gs from PINS initialization fixed allows for nearly the same reduction of the pulse power as with the joint control. Accordingly, joint control is always beneficial, but the gain varies with the specific examples.

9 Appendix

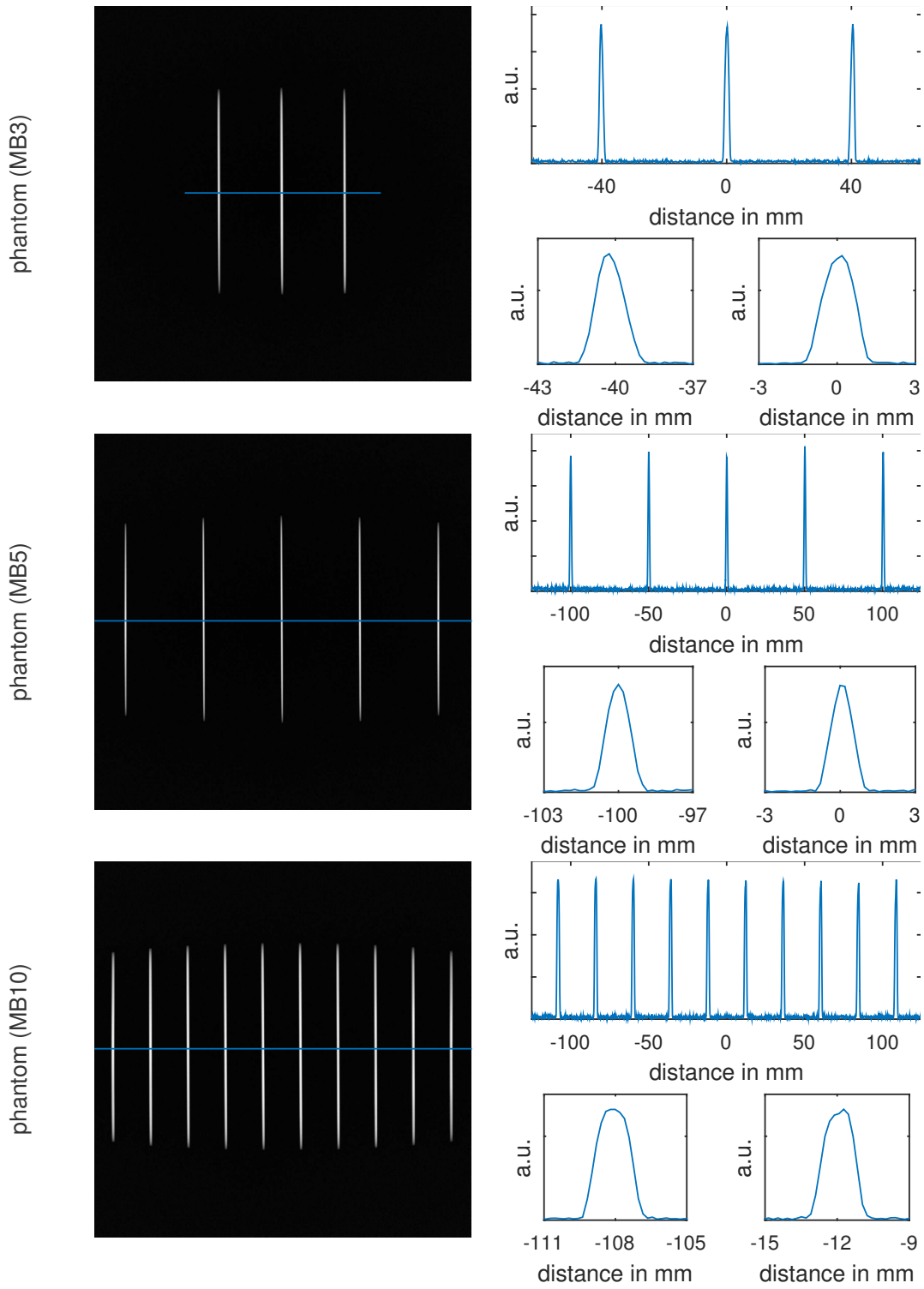


Figure 9.12: Reconstructed experimental data for the optimized MB3, MB5 and MB10 candidates.

## 9 Appendix

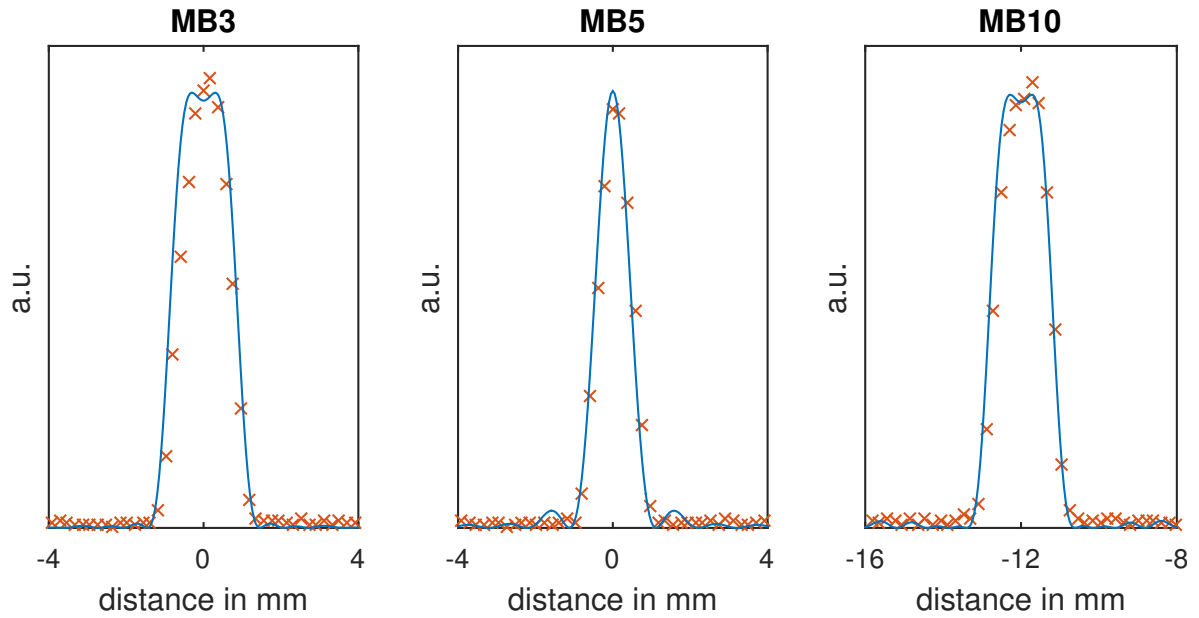


Figure 9.13: Simulated refocusing profile (solid line) and experimental phantom data (crosses) of the phantom measurements shown in Figure 9.12 for MB3 (zoom to one slice).

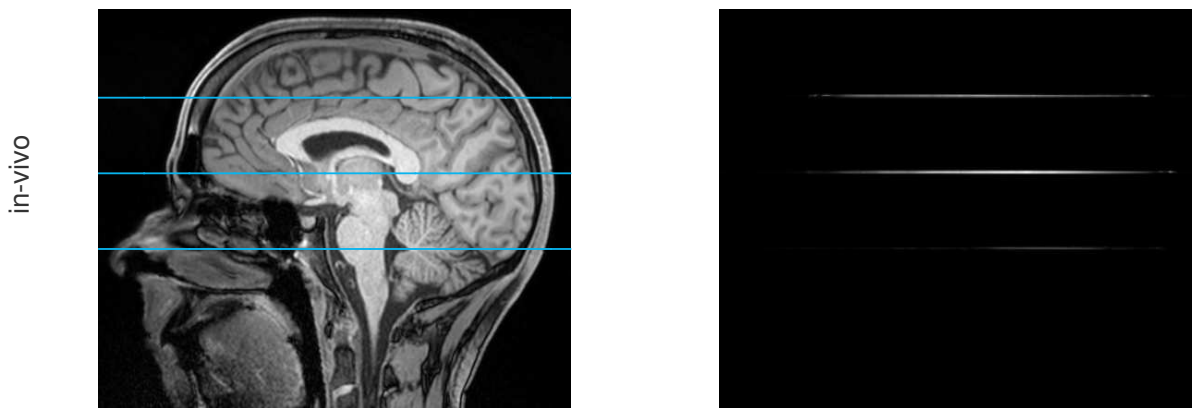


Figure 9.14: Reconstructed experimental data for in-vivo measurements using the optimized MB3 pulse.

## 9 Appendix

Five different initializations were compared for an intermediate MB factor of 5 with a uniform pulse duration and comparable error properties. The pulse power was heavily reduced in all cases while the maximal in-slice errors  $\varepsilon_{\text{in}}$  remained the same. An increase in the out-of-slice errors  $\varepsilon_{\text{out}}$  and phase errors  $\varepsilon_{\text{ph}}$  was observed, but it remained below the prescribed error bounds of 2% and 0.01 radians, respectively. A superposition pulse with VERSE yielded  $S \approx 0.56$  and therefore outperformed the same pulse without VERSE ( $S \approx 0.77$ ). However, much better power values of  $S \approx 0.41$  were observed for optimized PINS, PINS with VERSE and MultiPINS pulses. Therefore, it seems that the optimal control method performs best with PINS based initializations, especially for large MB factors.

These improvements in the pulse power were possible by allowing a *controlled deviation* of 3% and 5% for the slice profile accuracy along with 2% and 4% for the out-of-slice region compared to an ideal rectangular refocusing with a transition zone excluded from the optimization. For two of the examples (SUP MB3 and PINS MB10) this formulation results in a slightly steeper refocusing profile for the optimized refocusing compared to the initial. Figures 9.7-9.11 show that the controlled deviation is not exceeded anywhere in the observation domain. In other words, the profile constraints are fulfilled exactly, which is an achievement of the presented penalization technique.

Two second-order methods of numerical optimal control were introduced, that both use adjoint-based exact discrete derivatives, also for the second derivative. The precise derivative information allows for better progress when approaching the minimizer. For robustness of the optimization method w.r.t. the initialization and the problem parameters we embedded the Newton-type method into a trust-region framework using the Steihaug-CG method. Additionally, Steihaug-CG reduces the computational effort of Newton-type methods, since it saves many Hessian evaluations in the first phase of the optimization. In the second phase of the optimization both methods profit from an increased convergence order compared to first-order methods. To save computational effort, both methods were applied as a Newton-Krylov method with a matrix-free evaluation of the Hessian. By semismooth Newton techniques the inequality constraints on the control variables were included into the optimization without increasing the numerical effort. The parameters of the optimization method were adapted automatically, or calibrated in the numerical experiments shown above. With these parameters the semismooth quasi-Newton method yields good results in short computational time. In contrast, the semismooth Newton method which uses increased computation time gives the best results.

Two examples for turbo spin echo sequences included explicit phase constraints, whereas the two other examples, intended for double refocused diffusion sequences, did not constrain the phase of the refocusing profile. The influence of the phase

## 9 Appendix

constraints on the optimal solutions is less severe than expected and the optimized cases lead to similar power reductions in the range of 50% for the standard constraints (Tab. 9.6).

The prescribed amplitude constraints on the optimized RF pulse, the gradient and its slew rate ensure practical applicability on MR scanners. Due to the semismooth Newton method as well as the penalization technique, all these constraints are never exceeded in the optimum. More closely, the results show that the maximum values for the  $B_1$  amplitude and gradient strength were not attained in the optimal solution. This is due to the fact, that the reduction of the pulse power and the boundary conditions for the gradient already pull the maximum value downwards. However, both these constraints become active for examples with smaller maximum values, different boundary conditions, and especially for smaller pulse durations. In contrast, we observe that the slew rate constraint is active in any of the investigated scenarios, which can e.g. be seen in Fig. 9.9. A nonnegative minimum gradient value is also in effect for large pulse durations, as can be seen in Fig. 9.10. If the minimum gradient value gets too large, the possible reduction of the pulse power is decreased significantly, as can be seen for  $g_{\min} = 2.31$  in Tab. 9.6.

The pulses were designed based on the spin-domain description neglecting the relaxation effects. To justify this simplification we performed full Bloch simulations [233] for the optimized pulses and compared the simulations to the spin-domain results. The relaxation times were set to those of the cylindrical phantom ( $T_1 = 102$  ms,  $T_2 = 81$  ms) used in the experiment. In all simulations, the refocusing profiles of the optimized examples do not degenerate significantly in the presence of relaxation. We see a simple scaling of the refocusing profiles, similar to conventional RF pulses for short  $T_2$  values. The effects of  $T_1$  is an increase of the refocusing error outside of the slices, which is compensated by the  $T_2$  relaxation and remains below the allowed deviation for each example. Since the  $T_1$  relaxation times of typical in-vivo tissue are even higher and their influence on the refocusing profiles are negligible. These findings have been verified by the experimental phantom measurements.

The experimental validation was done on a 3T scanner exchanging the excitation and refocusing pulse of a standard crushed spin echo sequence for a cylindrical phantom (MB3, MB5 and MB10) and in-vivo (MB3). Changing the readout gradient to the slice direction allows for a direct measurement of the simultaneous excited and refocused slices. The small inter slice ripples of the optimized refocusing pulses can be neglected for a real measurement as standard excitation pulses produce no marked transversal magnetization at these inter slice positions and the refocused magnetization would be weighted by a factor of  $\sin(\theta/2)^2$  with a spatially dependent but low inter slice refocusing flip angle  $\theta$ . Due to the adequate choice and implementation of the slew rate constraint, the fluctuating Gs shapes were implementable, and the measured slice

profiles fit very well to the Bloch simulations for all measurements. The measured whole body SAR includes the non optimized excitation pulse and is therefore lower than the calculated power reduction of the optimized MB3 refocusing pulse. The good accordance of the simulations and the measurements shows the practical applicability of the optimized pulses on a standard clinical scanner. Using the specific hardware constraints of the desired MR system simplifies the application of optimized pulses since no further modifications or transformations have to be done, that moreover could reduce the optimality.

In simulations we compared the robustness of the optimized pulses w.r.t. inhomogeneities in  $B_0$  and  $B_1$  to the one of the initial pulses. The initial pulse and gradient pairs have a constant k-space excitation velocity and constant  $B_0$  inhomogeneities lead to a constant spatial shift. Despite the time varying slice-selective gradient of the optimized examples, which is known to be prone to off-resonance effects, the profile fidelity remains almost unchanged in the range of  $\pm 500$  Hz and the impact of the chemical shift (400 Hz at 3 T) is negligible. For applications with larger  $B_0$  inhomogeneities, the minimal amplitude constraint of the slice selective gradient can be increased or Gs can be fixed to enhance off-resonance robustness at the cost of a decreased power reduction. To investigate the influences of a temporal mismatch between the RF and slice selective gradient and eddy currents on the refocusing profiles, Bloch simulations were performed using a temporal shift of the slice selective gradient shape with respect to the RF pulse (up to 10  $\mu$ s) and a first order low pass filtering (normalized numerator and denominator of 0.5) of the slice selective gradient shape. Both effects led to a symmetric decrease of the refocusing efficiency in dependence of the distance to the isocenter. Compared to the used initials with constant or repetitive gradient functions, the fast changes in the optimized slice selective gradient are more prone to these effects. However, such a behavior is not observable in the experimental phantom measurements and leads to the conclusion that the optimized examples can be successfully implemented on the used MR scanner without special compensation techniques. To decrease the sensitivity of gradient imperfections of the optimized results, it should be possible to incorporate this directly in the optimization by enforcing a smoothness constraint on the slice selective gradient or to directly include the gradient impulse response[234]. In the context of  $B_1$  inhomogeneities all optimized examples behave similar as the initial pulses and lead to a smooth transition of higher and lower flip angles for a static  $B_1$  increase or reduction, respectively. Furthermore, we do not expect an additional proneness to small in-plane and through-plane motion compared to conventional RF pulses. The same holds for movements between the excitation and the read-out. However, to reduce the influences of motion artifacts it should be considered to reduce the overall refocusing time.

If the pulse power is not the primary restriction, then the pulse duration can be decreased instead while keeping the pulse power. The reduction of the refocusing

time is of high importance in SMS imaging and was chosen to be the topic of the 2015 ISMRM Challenge[4]. In this direction the next step is to minimize the pulse duration by time-optimal control [235] in order to find the shortest possible pulses that fulfill the given inequality constraints.

### 9.2.6 Conclusions

The modeling of the profile accuracy with inequality constraints together with a customized solution method allows for the computation of optimal RF pulses and slice-selective gradients, that outperform other approaches in the performance index. Moreover, the usage of constrained optimization guarantees for practical applicability and a direct implementation in clinical MR sequences.

### Acknowledgments

This work is partially funded by the Austrian Science Fund (FWF) in the context of project "SFB F3209-18" (Mathematical Optimization and Applications in Biomedical Sciences). Partial support from BioTechMed-Graz and NAWI Graz is gratefully acknowledged. The authors thank Christian Clason from the University of Duisburg-Essen for many fruitful discussions on the topic of the paper.

### 9.2.7 Lagrange calculus in the spin domain

The adjoint based derivative is set up using a real-valued Lagrangian together with the Wirtinger calculus. Therefore we introduce the complex RF pulse  $U_m = u_m + iv_m = r_m e^{i\theta_m}$ . The Lagrange multipliers for the discrete Bloch equation (9.20) are called  $p_m, q_m \in \mathbb{C}$  for  $m = 1, \dots, N_t$ . The control constraints (9.24) are kept explicitly. The Lagrangian of the penalized problem is defined in the usual way depending on the

## 9 Appendix

control variables  $r_m, \vartheta_m, g_m$ , the state variables  $a_m, b_m$  and the Lagrange multipliers  $p_m, q_m$  as

$$\begin{aligned}
 \mathcal{L} = & \frac{\tau}{2} \sum_{m=1}^{N_t} r_m^2 + \zeta \vartheta_m^2 + \zeta g_m^2 + \frac{\delta \mu_{\text{out}}}{2p} \sum_{z_j \in \Omega_{\text{out}}} \left( \frac{|b_{N_t}|^2}{e} \right)^p \\
 & + \frac{\delta \mu_{\text{in}}}{2p} \sum_{z_j \in \Omega_{\text{in}}} \left( \frac{|b_{N_t}|^2 - 1}{e} \right)^p + \frac{\delta \mu_p}{p} \sum_{l=1}^L \sum_{z_j \in S_l} \left( \frac{\varphi - \bar{\varphi}_l}{e_p} \right)^p \\
 & + \frac{\tau \mu_g}{p} \sum_{m=2}^{N_t} \left( \frac{g_m - g_{m-1}}{\tau s_{\text{max}}} \right)^p \\
 & - \sum_{z_j \in \Omega} \text{Re} \left\{ \sum_{m=1}^{N_t} (a_m - \alpha_m a_{m-1} + \beta_m^* b_{m-1}) p_m^* \right. \\
 & \left. + (b_m - \beta_m a_{m-1} - \alpha_m^* b_{m-1}) q_m^* \right\}.
 \end{aligned}$$

A compact form of the first-order necessary conditions can be derived efficiently using the Wirtinger calculus. In particular, for a Lagrangian of the form  $\mathcal{L} = \text{Re}(\mathcal{L}_{\mathbb{C}})$  with a complex-valued expression  $\mathcal{L}_{\mathbb{C}}$  the derivatives w.r.t the real and imaginary part  $Z_1, Z_2$  of a complex variable  $Z = Z_1 + iZ_2$  can be combined to

$$\frac{\partial \mathcal{L}}{\partial Z_1} + i \frac{\partial \mathcal{L}}{\partial Z_2} = \frac{\partial \mathcal{L}_{\mathbb{C}}}{\partial Z^*} + \left( \frac{\partial \mathcal{L}_{\mathbb{C}}}{\partial Z} \right)^*$$

using the Wirtinger derivatives [229] of a function  $f : \mathbb{C} \rightarrow \mathbb{C}, Z = Z_1 + iZ_2 \mapsto f(Z)$

$$\frac{\partial f}{\partial Z} = \frac{1}{2} \left( \frac{\partial f}{\partial Z_1} - i \frac{\partial f}{\partial Z_2} \right), \quad \frac{\partial f}{\partial Z^*} = \frac{1}{2} \left( \frac{\partial f}{\partial Z_1} + i \frac{\partial f}{\partial Z_2} \right).$$

In our case  $\mathcal{L}_{\mathbb{C}}$  does not depend on  $p_m, q_m, a_m^*, b_m^*$ . Therefore the state equations (9.20) are easily recovered by differentiation w.r.t.  $p_m^*, q_m^*$ . Analogously differentiating w.r.t.  $a_m$  and  $b_m$  and complex conjugation gives the adjoint Bloch equations

$$\begin{aligned}
 p_m &= \alpha_{m+1}^* p_{m+1} + \beta_{m+1}^* q_{m+1}, \\
 q_m &= -\beta_{m+1} p_{m+1} + \alpha_{m+1} q_{m+1},
 \end{aligned}$$

## 9 Appendix

for  $m = 1, \dots, N_t - 1$  and pointwise in each  $z_j \in \Omega$ . For the terminal condition in case of a refocusing pulse both Wirtinger derivatives w.r.t.  $b_{N_t}$  and  $b_{N_t}^*$  have to be evaluated. Depending on the location  $z_j$  we find  $p_{N_t} = 0$  and

$$\begin{aligned} q_{N_t} &= \frac{\mu_{\text{out}}\delta}{e} \chi_{\Omega_{\text{out}}} \left( \frac{|b_{N_t}|^2}{e} \right)^{p-1} b_{N_t} \\ &+ \frac{\mu_{\text{in}}\delta}{e} \chi_{\Omega_{\text{in}}} \left( \frac{|b_{N_t}|^2 - 1}{e} \right)^{p-1} b_{N_t} + \left\{ \sum_{l=1}^{N_{\text{MB}}} \chi_{S_l} \frac{\delta\mu_p}{e} \right. \\ &\left. \left[ \left( \frac{\varphi - \bar{\varphi}_l}{e_p} \right)^{p-1} - \frac{1}{N_l} \sum_{z_k \in S_l} \left( \frac{\varphi(z_k) - \bar{\varphi}_l}{e_p(z_k)} \right)^{p-1} \right] \right\} 2 \frac{ib_{N_t}}{b_{N_t}^* b_{N_t}}. \end{aligned}$$

The last fraction stems from the chain rule using the derivative of the arctan function in  $\varphi = \arg(b_{N_t}^2)$ . Moreover,  $\chi_{S_l}$  is the characteristic function of the in-slice set  $S_l = \{z_1^l, \dots, z_{N_l}^l\}$  with  $N_l$  points and mean phase  $\bar{\varphi}_l = \sum_{k=1}^{N_l} \varphi(z_k^l) / N_l$ .

The gradient of the reduced objective  $\mathbf{j}' = E\mathbf{x} + \mathbf{F}'(\mathbf{x})$  is given by the partial derivatives w.r.t the control variables. Its components are given by chain rule for the polar coordinates

$$\begin{aligned} \frac{\partial \mathcal{L}}{\partial r_m} &= \tau r_m + \frac{\partial \mathcal{L}}{\partial u_m} \cos(\vartheta_m) + \frac{\partial \mathcal{L}}{\partial v_m} \sin(\vartheta_m), \\ \frac{\partial \mathcal{L}}{\partial \vartheta_m} &= \zeta \tau \vartheta_m - \frac{\partial \mathcal{L}}{\partial u_m} r_m \sin(\vartheta_m) + \frac{\partial \mathcal{L}}{\partial v_m} r_m \cos(\vartheta_m), \end{aligned}$$

for  $m = 1, \dots, N_t$  and by  $\frac{\partial \mathcal{L}}{\partial g_m}$ ,  $m = 2, \dots, N_t - 1$ , which is computed below. Each first term is collected in  $E\mathbf{x}$ , and the other terms constitute  $\mathbf{F}'(\mathbf{x})$ . In these equations we need

$$\frac{\partial \mathcal{L}}{\partial u_m} = \text{Re} \left( \frac{\partial \mathcal{L}_{\mathcal{C}}}{\partial U_m} + \frac{\partial \mathcal{L}_{\mathcal{C}}}{\partial U_m^*} \right), \quad \frac{\partial \mathcal{L}}{\partial v_m} = \text{Im} \left( \frac{\partial \mathcal{L}_{\mathcal{C}}}{\partial U_m^*} - \frac{\partial \mathcal{L}_{\mathcal{C}}}{\partial U_m} \right).$$

With  $\frac{\partial \alpha_m^*}{\partial \phi_m} = \left( \frac{\partial \alpha_m}{\partial \phi_m} \right)^*$  and analogously for  $\beta_m$  the result is

$$\begin{aligned} \frac{\partial \mathcal{L}}{\partial u_m} &= \gamma^2 \tau^2 u_m R_m - \gamma \tau \text{Im}(Q_m), & m = 1, \dots, N_t, \\ \frac{\partial \mathcal{L}}{\partial v_m} &= \gamma^2 \tau^2 v_m R_m - \gamma \tau \text{Re}(Q_m), & m = 1, \dots, N_t, \end{aligned}$$

## 9 Appendix

with

$$Q_m = \sum_{z_j \in \Omega} \sin(\phi_m/2) \frac{1}{\phi_m} (a_{m-1}q_m^* - b_{m-1}^*p_m),$$

$$R_m = \sum_{z_j \in \Omega} \frac{1}{\phi_m} \operatorname{Re} \left\{ (a_{m-1}p_m^* + b_{m-1}^*q_m) \frac{\partial \alpha_m}{\partial \phi_m} \right.$$

$$\left. + (a_{m-1}q_m^* - b_{m-1}^*p_m) \frac{\partial \beta_m}{\partial \phi_m} \right\},$$

$$\frac{\partial \alpha_m}{\partial \phi_m} = i \frac{\gamma \tau z g_m}{\phi_m} \left( \frac{\cos(\phi_m/2)}{2} - \frac{\sin(\phi_m/2)}{\phi_m} \right) - \frac{\sin(\phi_m/2)}{2},$$

$$\frac{\partial \beta_m}{\partial \phi_m} = i \frac{\gamma \tau (u_m + iv_m)}{\phi_m} \left( \frac{\cos(\phi_m/2)}{2} - \frac{\sin(\phi_m/2)}{\phi_m} \right).$$

Differentiation w.r.t.  $g_m$  gives finally

$$\frac{\partial \mathcal{L}}{\partial g_m} = \zeta \tau g_m + \sum_{z_j \in \Omega} \operatorname{Re} \left\{ (a_{m-1}p_m^* + b_{m-1}^*q_m) \frac{\partial \alpha_m}{\partial g_m} \right.$$

$$\left. + (a_{m-1}q_m^* - b_{m-1}^*p_m) \frac{\partial \beta_m}{\partial g_m} \right\}$$

$$+ \frac{\mu_g}{s_{\max}} \left( \frac{g_m - g_{m-1}}{\tau s_{\max}} \right)^{p-1} - \frac{\mu_g}{s_{\max}} \left( \frac{g_{m+1} - g_m}{\tau s_{\max}} \right)^{p-1},$$

for  $m = 2, \dots, N_t - 1$  and with

$$\frac{\partial \alpha_m}{\partial g_m} = \frac{\gamma \tau z}{\phi_m} \left( i \sin(\phi_m/2) + \gamma \tau z g_m \frac{\partial \alpha_m}{\partial \phi_m} \right),$$

$$\frac{\partial \beta_m}{\partial g_m} = \frac{(\gamma \tau z)^2}{\phi_m} g_m \frac{\partial \beta_m}{\partial \phi_m}.$$

## 9.3 Simultaneous Multislice Refocusing via Time Optimal Control

Armin Rund<sup>1,2,†</sup>, Christoph Stefan Aigner<sup>3,†</sup>, Karl Kunisch<sup>1,2,4</sup> and Rudolf Stollberger<sup>2,3</sup>

This is a preprint of the publication "Simultaneous multislice refocusing via time optimal control". *Magnetic Resonance in Medicine*, Early view: February 2018, doi: <https://doi.org/10.1002/mrm.27124>

### Abstract

**Purpose:** Joint design of minimum duration RF pulses and slice-selective gradient shapes for MRI via time optimal control with strict physical constraints, and its application to simultaneous multislice (SMS) imaging.

**Theory and Methods:** The minimization of the pulse duration is cast as a time optimal control problem with inequality constraints describing the refocusing quality and physical constraints. It is solved with a bilevel method, where the pulse length is minimized in the upper level, and the constraints are satisfied in the lower level. To address the inherent nonconvexity of the optimization problem, the upper level is enhanced with new heuristics for finding a near global optimizer based on a second optimization problem.

**Results:** A large set of optimized examples shows an average temporal reduction of 87.1% for double diffusion and 74% for turbo spin echo pulses compared to PINS pulses. The optimized results are validated on a 3T scanner with phantom measurements.

**Conclusion:** The presented design method computes minimum duration RF pulse and slice-selective gradient shapes subject to physical constraints. The shorter pulse duration can be used to decrease the effective TE in existing EPI or echo spacing in TSE sequences.

---

<sup>1</sup>Institute for Mathematics and Scientific Computing, University of Graz, Heinrichstr. 36, 8010 Graz, Austria

<sup>2</sup>BioTechMed-Graz, 8010 Graz, Austria

<sup>†</sup>Armin Rund and Christoph Stefan Aigner have contributed equally to the paper

<sup>3</sup>Institute of Medical Engineering, Graz University of Technology, Stremayrgasse 16/III, 8010 Graz, Austria

<sup>4</sup>Johann Radon Institute for Computational and Applied Mathematics (RICAM), Austrian Academy of Sciences, Altenbergstraße 69, 4040 Linz, Austria

### 9.3.1 Introduction

Simultaneous Multislice (SMS) imaging acquires the information of different slices simultaneously to reduce the overall acquisition time and is an emerging imaging technique with various applications such as multi-directional diffusion tensor imaging [209], short echo time (TE) functional imaging [236] and clinically important turbo spin echo (TSE) based sequences [195]. Contrary to pure in-plane accelerated parallel imaging, SMS acceleration in slice direction acquires signal for every extra slice measured and has only a minimal signal-to-noise penalty [95]. Recently, the application of Wave-CAIPI [237], originally proposed for 3D encoding, to SMS imaging allowed an increase in the number of simultaneous slices, called the multiband (MB) factor, to 13 without major g-factor penalties [195]. On the other hand, SMS refocusing pulses with a low MB factor but a good refocusing profile are beneficial for high resolution diffusion imaging [173], [238], [239].

However, SMS imaging requires RF pulses that simultaneously excite or refocus slices, which typically result in RF amplitudes and power which are too high, or in very long pulse durations [95]. Historically, the first SMS RF pulse design method is based on a superposition of frequency shifted sub-pulses [162]. To overcome the limitation of a linear scaling of the  $B_1$  peak amplitude and overall RF power with the MB factor [95], [163], different groups proposed design methods via phase modulation [174], time shifted superposition [175], root-flipping [173] and use of the wavelet domain [178]. After the pulse design, additional  $B_1$  and power reduction can be achieved by applying variable-rate selective excitation (VERSE) [112], [160], [172]. However, high MB factors lead to a strong oscillation of the RF amplitude and a direct VERSE application might require additional smoothing of the otherwise too rapidly changing gradient waveform, which was resolved by applying VERSE on the overall RF pulse envelope [176]. Alternatively, an inherent power reduction in the pulse design is possible using the power independent number of slices (PINS) [131] method that utilizes periodic excitation patterns, with the limitation that a low time-bandwidth product (TBP) is generally used in order to avoid long pulse durations.

The combination of PINS pulses with conventional SMS pulses, MultiPINS [179], combines both approaches to reduce the overall pulse duration and increase the bandwidth of PINS pulses.

In addition, SMS RF pulses can also be designed by optimal control methods. Optimal Control (OC) has proven to be successful in NMR and MRI to design accurate excitation profiles based on different models such as the Liouville-von Neumann equation [155], [156], [158], the Bloch equations [1], [157], [184], [240], or the Bloch spin-domain model [49].

## 9 Appendix

To encourage researchers to focus on new methods that compute short SMS pulses with a low  $B_1$  peak and SAR, while achieving accurate excitation/refocusing profiles, SMS pulse design was chosen to be the topic of the 2015 ISMRM challenge [4] (October 2015 to May 2016, <http://challenge.ismrm.org/node/71>). The method described in this paper was developed and applied in its SMS design subchallenge.

In our preceding work [2], [241] we introduced an optimal control method for RF pulse design subject to different equality and inequality constraints using a fixed time horizon. In contrast, we present here a new time optimal control modeling for designing RF pulses with minimum duration under technical constraints. Due to the free terminal time, the solution of time optimal control problems [242] is algorithmically involved and different methods are needed. We introduce a new bilevel method with time grid adaption and warm-start algorithms. Moreover, globalization plays a central role, since both the free terminal time and the bilinear Bloch equation lead to a nonconvex optimization problem. Here, we introduce new heuristics for finding a near global optimizer. The optimization method is tested on 31 SMS refocusing examples. The numerical results are validated by experimental phantom measurements on a 3T MR system.

### 9.3.2 Theory

In the following, refocusing in minimum time is posed as a time optimal control problem with inequality constraints for slice profile fidelity and MR hardware restrictions. The constraints were inspired by the ISMRM Challenge [4].

#### Optimal control framework

We jointly optimize for the time horizon/pulse duration  $T$ , as well as the RF pulse and slice-selective gradient (Gs) slew rate values at each time sample. Applying an equidistant time grid  $t_m = m\tau, m = 0, \dots, N_t$  with step size  $\tau = T/N_t$ , the RF pulse is described as  $B_{1,m} = r_m \exp(i\vartheta_m)$  with amplitude  $r_m$ , phase  $\vartheta_m$  and the imaginary unit  $i$ . The Gs amplitude  $g_m$  is given via the slew rate  $s_m$  as

$$g_m = g_{m-1} + \tau s_{m-1}, \quad m = 2, \dots, N_t - 1 \quad (9.35)$$

with given boundary conditions  $g_1, g_{N_t}$ . The Bloch equation is solved exactly in the spin-domain, see [66], [67], neglecting relaxation effects, which is reasonable

## 9 Appendix

for short  $T$ . The evolution of the magnetization is described by the complex-valued Cayley-Klein parameters

$$a_m = \alpha_m a_{m-1} - \beta_m^* b_{m-1}, \quad b_m = \beta_m a_{m-1} + \alpha_m^* b_{m-1}, \quad (9.36)$$

for  $m = 1, \dots, N_t$  with  $a_0 = 1, b_0 = 0$ , the gyromagnetic ratio  $\gamma$ , and coefficients

$$\begin{aligned} \alpha_m &= \cos(\phi_m/2) + i\gamma\tau z g_m \sin(\phi_m/2) / \phi_m, \\ \beta_m &= i\gamma\tau B_{1,m} \sin(\phi_m/2) / \phi_m, \\ \phi_m &= -\gamma\tau \sqrt{r_m^2 + (z g_m)^2}. \end{aligned}$$

Therein, the spatial point  $z$  covers the field of view (FOV)  $\Omega$  which is discretized equidistantly as  $z_j, j = 1, \dots, N_z$  with the spatial resolution  $\delta$ .  $\Omega$  is separated into the in-slice domain  $\Omega_{\text{in}} = \cup_{l=1}^{N_{\text{MB}}} S_l$  containing the interior  $S_l$  of each of the  $N_{\text{MB}}$  slices, the out-of-slice domain  $\Omega_{\text{out}}$ , and a free transition region in between. For refocusing in minimum time we optimize the control  $\mathbf{x} = (r_1, \dots, r_{N_t}, \vartheta_1, \dots, \vartheta_{N_t}, s_1, \dots, s_{N_t-2})$  and the pulse duration  $T$  in order to

$$\min_{T>0, \mathbf{x}} T \quad \text{subject to (9.35),} \quad (9.37)$$

$$(9.36) \quad \text{for } z = z_j, j = 1, \dots, N_z, \quad (9.38)$$

$$|b_{N_t}|^2 - 1 \leq e \quad \text{for } z_j \in \Omega_{\text{in}}, \quad |b_{N_t}|^2 \leq e \quad \text{for } z_j \in \Omega_{\text{out}}, \quad (9.39)$$

$$|\varphi - \bar{\varphi}_l| \leq e_p, \quad \text{for } z_j \in S_l, \quad l = 1, \dots, N_{\text{MB}}, \quad (9.40)$$

$$0 \leq r_m \leq r_{\text{max}}, \quad |s_m| \leq s_{\text{max}}, \quad -\pi \leq \vartheta_m \leq \pi, \quad (9.41)$$

$$|g_m| \leq g_{\text{max}}, \quad \left| \frac{g_{N_t} - g_{N_t-1}}{\tau} \right| \leq s_{\text{max}}, \quad (9.42)$$

$$\text{SAR}_e = \text{SAR}_{\text{coileff}} f_p \tau \sum_{m=1}^{N_t} r_m^2 \leq S_{\text{max}}. \quad (9.43)$$

The inequalities model the slice profile accuracy in magnitude and phase, amplitude and SAR constraints. In (9.39) the slice profile is prescribed with a tolerance  $e > 0$  (that may depend on the spatial location) around a perfect refocusing. Here, ideal crusher gradients are assumed to completely dephase the free induction decay produced by the refocusing pulse [23], [66]. In (9.40) the phase  $\varphi = \arg(b_{N_t}^2)$  is allowed to vary only up to a tolerance  $e_p = e_p(z_j) > 0$  from the arithmetic mean  $\bar{\varphi}_l$  of the phase in slice  $S_l$ . MR hardware restrictions are included as amplitude constraints in (9.41), (9.42) with maximum amplitudes  $r_{\text{max}}, g_{\text{max}}, s_{\text{max}} > 0$ . The last inequality in (9.42) incorporates the given terminal condition  $g_{N_t}$ . Since a low SAR and a short pulse duration are competing goals, a SAR limit  $S_{\text{max}} > 0$  is prescribed. For single transmit MR imaging, it is here reasonable to apply a SAR estimate  $\text{SAR}_e$  ( $\text{W kg}^{-1}$ ) based on

## 9 Appendix

the global pulse power with constant  $\text{SAR}_{\text{coileff}}$  ( $\text{W}/\text{kg}/\mu\text{T}^2$ ) and constant pulse rate  $f_p$ .

This optimization problem is a pure time optimal control problem with control and state constraints. Such problems tend to possess bang-bang solutions, where the control constraint is active all the time but the value jumps between the upper and lower bound, see e.g. [242]. To approximate such optimal controls reliably we suggest an  $L^2$ -regularization of the controls with parameters  $\alpha, \zeta > 0$ . Furthermore, pointwise state-constrained optimal control problems are known to be involved since the Lagrange multiplier is irregular which leads to a decrease of the convergence speed and accuracy of numerical solution methods, see e.g. [226]. To reduce these effects we apply the  $L^p$ -penalization of the state constraints from [2] and drive the exponent  $p \rightarrow \infty$  in a homotopy loop as we approach the optimizer. Therefore, we define the penalized objective

$$\begin{aligned} \min_{T>0, \mathbf{x}} J = & T + \frac{\tau}{2} \sum_{m=1}^{N_t} \alpha r_m^2 + \zeta \vartheta_m^2 + \frac{\zeta \tau}{2} \sum_{m=1}^{N_t-2} s_m^2 + \frac{\delta \mu_{\text{out}}}{2p} \sum_{z_j \in \Omega_{\text{out}}} \left( \frac{|b_{N_t}|^2}{e} \right)^p \\ & + \frac{\delta \mu_{\text{in}}}{2p} \sum_{z_j \in \Omega_{\text{in}}} \left( \frac{|b_{N_t}|^2 - 1}{e} \right)^p + \frac{\delta \mu_p}{p} \sum_{l=1}^L \sum_{z_j \in \mathcal{S}_l} \left( \frac{\varphi - \bar{\varphi}_l}{e_p} \right)^p \\ & + \frac{\tau \mu_w}{p} \sum_{m=2}^{N_t-1} \left( \frac{g_m}{g_{\text{max}}} \right)^p + \frac{\mu_T}{p} \left( \frac{g_{N_t} - g_{N_t-1}}{\tau s_{\text{max}}} \right)^p \end{aligned} \quad (9.44)$$

with even number  $p$  and parameters  $\mu_{\text{out}}, \mu_{\text{in}}, \mu_p, \mu_w, \mu_T > 0$ .  $\alpha$  is automatically adapted to fulfill the SAR constraint (9.43),  $\zeta$  is decreased as the optimizer is approached. This penalized objective has to be minimized subject to (9.35), (9.36), (9.43), and the pointwise control constraints (9.41). For a fixed  $T$  this problem can be solved with established methods of numerical optimal control. We apply the trust-region semismooth quasi-Newton method from [2], which features robustness and adjoint-based exact discrete derivatives. It also handles the automatic adaption of the penalty parameters  $\mu_{\text{out}}, \mu_{\text{in}}, \mu_p, \mu_w, \mu_T$ . However, we still have to take care of the free terminal time  $T$ .

### Bilevel method for time optimal control

Time-optimal control problems can be solved by different approaches. In our approach, the control  $\mathbf{x}$  and  $T$  are separated in a bilevel method, where  $T$  is kept fixed in the lower level problem. Alternatively, both can be treated at once using time transformations, see e.g. [243]. For the Bloch equation on equidistant time grids,

## 9 Appendix

numerical studies showed that a bilevel method prevails, since it facilitates keeping a good slice profile pattern after a time reduction. Furthermore, it offers more flexibility in the time reduction, which is exploited for finding an improved minimizer.

The bilevel method is initialized using an existing method for SMS pulse design, e.g. conventional superposition [162], phase scrambling [174], root-flipped pulses [173], PINS [131] or MultiPINS [179]. Then, we alternately reduce the terminal time (upper level) and fulfill the constraints (lower level). For the former we keep the time step constant and reduce the terminal time by deleting one time point. The latter is done by minimization of the penalized objective (9.44) for a fixed  $T$  using the trust-region semismooth quasi-Newton method of [2] with the following changes. First, we do not fully iterate until a relative or absolute stopping criteria is fulfilled, but terminate as soon as we have found an admissible solution to (9.39)–(9.43). Second,  $p$  is not changed during the course of the semismooth quasi-Newton method, but altered in the upper level of the bilevel method in order to have a monotonicity of  $p$  towards the optimum. Sometimes in the alternation of lower and upper level we decide to increase  $p$  and might apply a refinement of the time grid (depending on the allowed raster time). The resulting bilevel method reads:

- Step 1: Initialize control  $\mathbf{x}_0$  and duration  $T_0$  with a conventional RF pulse design method, choose  $p$  and set  $n = 1$ .
- Step 2: Upper level: Choose to delete one time instance  $t_k$  applying the heuristics for an improved optimizer (9.45). Reduce the terminal time to  $T_n < T_{n-1}$  and warm-start  $\mathbf{x}_n = f(\mathbf{x}_{n-1}, k)$ .
- Step 3: Lower level: Minimize the penalized objective (9.44) for a fixed terminal time  $T_n$  by a trust-region semismooth quasi-Newton method until an admissible solution to the inequality constraints (9.39)–(9.43) is found. The resulting control is  $\mathbf{x}_n$ .
- Step 4: Decide to increase  $p$ , decrease  $\zeta$  and/or to refine the time grid. Set  $n = n + 1$  and repeat from Step 2.

Finally, we present the technical details of the time reduction. At deletion of a time point  $t_k$ , the current control  $\mathbf{x}_{n-1}$  is represented on the new time grid  $\mathbf{x}_n = f(\mathbf{x}_{n-1}, k)$  using a transfer function  $f$  that performs a good warm-start for the next lower level optimization. In particular, for maintaining a good slice profile this transfer function distributes the values of  $g_k$  and the real and imaginary part of  $B_{1,k}$  at the deleted time instance  $t_k$  symmetrically to the neighboring time instances. While doing so, we fulfill the constraints (9.41), (9.42). For technical details of  $f$  we refer to its source code, which we published together with the software (see below). The time point  $t_k$  to be deleted is chosen based on new heuristics for finding a near global optimizer. We choose the time point that allows the best performance after deletion, warm-start

## 9 Appendix

and  $N_g$  steps of the lower level solver. More precisely, the time  $t_k$  is determined as the global solution to the optimization problem

$$\min_{m \in \{1, \dots, N_t^n\}} J(T_n, Q(f(\mathbf{x}_{n-1}, m))), \quad (9.45)$$

where  $Q$  is an abstract function that stands for solving the lower level problem with the trust-region semismooth quasi-Newton method of [2] in at most  $N_g$  iterations. Obviously, a larger  $N_g$  gives a better minimizer at the end, but increases the runtime of the code. We use  $N_g = 0$  for fast runs and  $10 \leq N_g \leq 20$  otherwise. Then the global minimizer of this auxiliary problem is computed exactly by total enumeration, or approximately by reusing information from previous upper level steps.

### 9.3.3 Methods

#### Simulations and pulse design

To test the general applicability of the proposed design method, we minimized the pulse duration in the test set of 31 cases given by the organizers of the ISMRM Challenge [4]. It contains different problem parameters (i.e. MB factor and slice thickness (THK)) and 13 different constraints (i.e.  $B_1$  peak, slew rate of Gs, maximum refocusing errors and SAR limits). For the sake of completeness the most important problem parameters and constraints are repeated below. A full description is given by the ISMRM 2015 challenge homepage and [4].

The maximum refocusing error  $e$  was set to 0.02 out-of-slice and 0.03 in-slice. For the design of all SMS refocusing pulses we assumed perfect crusher gradients. The space was discretized equidistantly with a resolution  $\delta = THK/400$ . Two different example classes were considered for the optimization, double refocused diffusion and TSE/RARE imaging, each with different problem parameters (see Supporting Table S1). The global SAR constraint for all cases was set to be  $S_{\max} = 3.2 \text{ W kg}^{-1}$ . The SAR estimate  $SAR_e$  used an expected SAR efficiency of a 3T birdcage coil  $SAR_{\text{coileff}}$  of  $0.25 \text{ W/kg}/\mu\text{T}^2$  and the assumed pulse rate  $f_p$  for the two different scenarios (see Supporting Table S1). The influence of amplitude constraints on the optimization was analyzed by using three different constraint settings given by actual hardware limits (see Supporting Table S2).

**Diffusion pulses (DIFF).** This example class asked for refocusing pulses for double refocused diffusion sequences [143] with a small MB factor (3–5) and THK (1–2 mm), see Supporting Table S1. The number of spatial points  $N_z$  varied from 2401

## 9 Appendix

(MB = 3, THK = 2 mm) to 4801 (MB = 5, THK = 1 mm) to define a FOV of 120 mm. The SAR estimate  $SAR_e$  used a repetition time (TR) of 120 ms with two identical refocusing pulses per repetition, resulting in a pulse rate  $f_p = 16.67/s$ . The phase of the refocusing profile was not considered in the optimization.

**Turbo spin echo pulses (TSE).** Here the task was to generate SMS refocusing pulses with a large number of simultaneous and thin slices (MB = 8–14, THK = 0.5–2 mm, TBP = 3) for a repeated application in a TSE/RARE based sequence. A phase constraint with a maximal deviation of  $e_p = 0.01$  radian from the mean phase per slice was added according to (9.40). The bigger FOV of 240 mm resulted in more degrees of freedom in the spatial direction, ranging from 4801 (MB = 8, THK = 2 mm) up to 19201 (MB = 14, THK = 0.5 mm). For all TSE cases a turbo factor of 12 and a TR of 220 ms was assumed resulting in a pulse rate  $f_p = 54.55/s$ .

The optimization was in general started from RF and Gs waveforms based on the PINS method [131]. The sub-pulse envelope was computed by the SLR algorithm [66] using  $d_1 = e/4$  (in-slice) and  $d_2 = e/\sqrt{2}$  (out-of-slice). For  $\tau = 10 \mu s$  the initial pulse durations  $T_{init}$  ranged from 8.710 ms (MB = 14, THK = 2 mm) to 32.42 ms (MB = 8, THK = 0.5 mm), see Table 9.9 and 9.10.

The optimization method was implemented in MATLAB (The MathWorks, Inc, Natick, USA). A version of it can be downloaded from [https://github.com/rundar/mr\\_control](https://github.com/rundar/mr_control). Initially a small penalty exponent  $p = 6$  was chosen, which was doubled towards the optimum gradually to about  $10^3$  to  $10^4$  based on previous experience [2]. The trust-region semismooth quasi-Newton method [2] calibrated and adapted the other parameters in the objective (9.44) automatically. The time step size was initially set to  $\tau = 10 \mu s$ , and gradually decreased by a factor of two as long as the optimizer stayed below 20000 sampling points. For the challenge we typically

Table 9.9: Comparison of the optimized pulse duration (in ms) with the duration of the PINS initial guess for all DIFF examples.

	MB3		MB4		MB5		
	THK mm	PINS ms	opt ms	PINS ms	opt ms	PINS ms	opt ms
	2.00	16.870	2.155	15.090	2.285	13.560	2.414
	1.75	18.460	2.155	16.400	2.448	14.140	2.502
	1.50	21.260	2.336	18.470	2.539	16.090	2.651
	1.25	24.370	2.470	21.180	2.673	18.320	2.404
	1.00	28.840	2.650	25.250	2.805	21.180	2.938

## 9 Appendix

chose  $N_g = 20$  for the auxiliary optimization problem of the best time reduction, and reused the information several times. All calculations were done in parallel on the high-performance-computing-cluster “RADON 1” (RICAM, Linz, Austria) using one node ( $2 \times$  Xeon E5-2630v3 with in total 16 cores and 128 GB of RAM) for each case. Two examples were analyzed and described in more detail. One diffusion case with  $MB = 3$  and  $THK = 1.75$  mm and one TSE/RARE case with  $MB = 12$  and  $THK = 1$  mm.

### Experiments

To validate the numerical simulations, phantom measurements were performed on a 3T MR scanner (Magnetom Skyra, Siemens Healthcare, Erlangen, Germany) using the transmit/receive body-coil (birdcage). A standard crushed spin echo (SE) sequence was modified to import arbitrary RF and Gs shapes, and to measure the slice profile by changing the phase encoding to the slice direction. We created three SE sequences, non-selective excitation and refocusing, slice-selective MB excitation with non-selective refocusing, and slice-selective MB excitation with optimized slice-selective MB refocusing (applying the proposed optimization method). We implemented two optimized refocusing pulses and slice-selective gradient shapes, both shown in Figure 9.17 (“scanner 2”), optimized for the hardware constraints that comply with the MR system used. Their durations were  $T = 3.38$  ms (DIFF MB3) and  $T = 5.78$  ms (TSE MB12) using a temporal grid of  $10 \mu\text{s}$  equivalent to the gradient raster time of the MR system.

The utilized non-selective rectangular block pulses were 0.8 ms long for both, excitation and refocusing. The slice-selective MB excitation pulses were created applying superposition with phase shifted SLR sub-pulse envelopes[66] resulting in a pulse

Table 9.10: Comparison of the optimized pulse duration (in ms) with the duration of the PINS initial guess for all TSE examples.

	MB8		MB10		MB12		MB14	
THK mm	PINS ms	opt ms	PINS ms	opt ms	PINS ms	opt ms	PINS ms	opt ms
2.0	10.640	2.742	9.460	2.856	8.810	2.728	8.710	2.809
1.5	13.260	3.295	11.110	3.213	10.890	3.286	10.300	3.296
1.0	18.040	3.958	15.170	4.122	14.460	4.120	14.110	3.996
0.5	32.420	6.106	27.390	6.113	25.230	6.080	24.520	6.189

## 9 Appendix

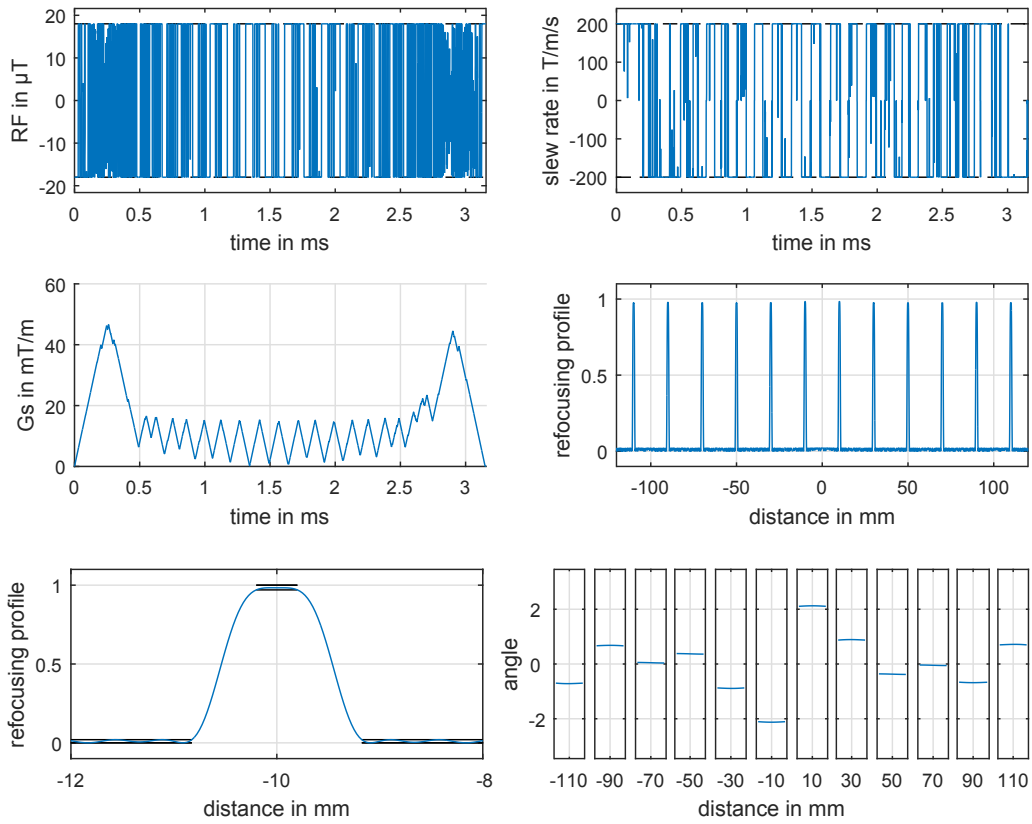


Figure 9.15: Optimization results and Bloch simulations for one representative TSE example. The first row shows the control variables  $B_1$  amplitude and slew rate of Gs for the refocusing duration of 3.16 ms. The second row depicts Gs shape, and the corresponding simulated refocusing profile  $|b_{N_i}|^2$ . The last row shows a detail zoom of one slice to see the refocusing profile together with the error corridor (black), and the phase angle  $\arg(b_{N_i}^2)$  per slice.

duration of  $T = 5.58$  ms and a constant slice-selective gradient of 10 mT/m for the DIFF MB3 case. For the TSE MB12 case we have  $T = 10.92$  ms and 5 mT/m.

The experiments were performed using a spherical phantom with a diameter of 240 mm filled with 0.011 g MACROLEX blue per liter MARCOL-oil ( $T_1 \approx 200$  ms and  $T_2 \approx 100$  ms). High resolution data were acquired in the transversal plane with a matrix size of  $1536 \times 1536$  (1536 phase encoding steps) and a FOV of  $300 \times 300$  mm resulting in a voxel size of  $0.2 \times 0.2$  mm. For both cases we used  $\text{TR} = 300$  ms. The TE was set to 23 ms (DIFF MB3) and 30 ms (TSE MB12) for both the non-selective and optimized SE experiments. The TE of the fully non-selective SE was set to 15.5 ms. All measurements were acquired after a manual shim with a sampling bandwidth of 130 Hz and were repeated five times to compute the median with an increased signal to noise ratio. The experimental data using the optimized slice-selective refocusing

were normalized by the fully non-selective SE measurement using a masked noise cut-off of 0.1.

### 9.3.4 Results

Below we present the results of our contribution to the ISMRM challenge. In particular, we show the real-valued RF pulses ( $B_{1,m} \in \mathbb{R}$  for all times) which were submitted for the challenge.

#### Simulations

Supporting Figure S1 summarizes the numerical results of an optimized diffusion example to refocus 5 slices with a thickness of 1.25 mm equally distributed over a FOV of 120 mm at a temporal resolution of  $\tau = 0.625 \mu\text{s}$ . The overall terminal time could be reduced to 2.404 ms, which is a reduction of 86.9% compared to the initial PINS pulse with 18.32 ms and a reduction of 90.3% compared to a valid pulse candidate based on conventional superposition with 24.85 ms (not shown). The optimized RF amplitude and slew rate are given in the first row of Supporting Figure S1. The second row additionally shows the Gs shape, and the simulated refocusing profile for the whole FOV. A zoomed image in the third row shows, that the profile always remains inside the black error corridor. The last plot shows the phase of each refocusing profile, which was not constrained here.

Figure 9.15 shows the analogous plots, this time for the optimized TSE refocusing (MB12, THK= 1 mm, FOC= 240 mm,  $\tau = 0.625 \mu\text{s}$ ). The optimization was done here without a constraint on the SAR. The pulse duration was reduced by 75% from 12.92 ms to 3.16 ms compared to the initial PINS pulse. Again, the gradient amplitude in the third plot shows a large hump at the beginning and the end, and a small zigzagging in between that remained from the initial PINS pulse. The slice profile fulfills the constraints, with an equiripple error in the out-of-slice region, which can be seen in the zoomed plot in the third row for one slice. The last plot shows the additional phase constraint for the TSE/RARE examples. The refocusing phase is nearly constant per slice, but each slice shows a different mean phase.

A summary for the total pulse duration of the PINS based initial guesses  $T_{\text{init}}$  compared to the time optimal pulse durations  $T$  is given in Table 9.9 (DIFF) and Table 9.10 (TSE). Here, all 31 examples were solved with the SAR constraint. The achieved temporal reduction for the diffusion example is 86.9% (from 18.32 ms to

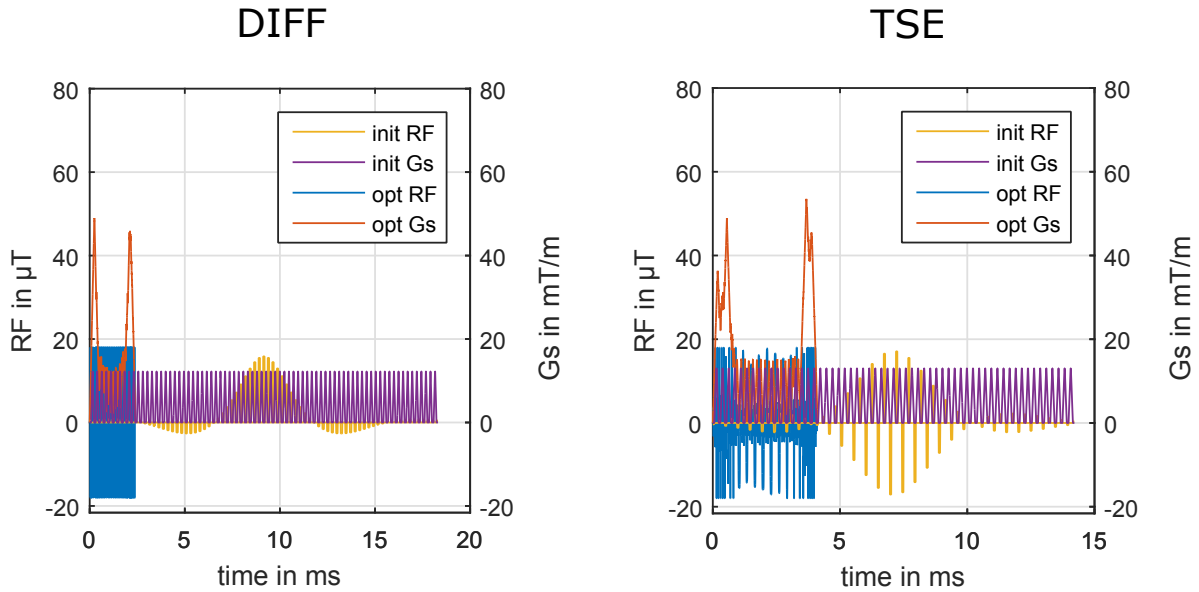


Figure 9.16: Comparison of the optimized results shown in Figure 9.15 and Supporting Figure S1 with the initial guess from PINS.

2.404 ms) and for the TSE example 71% (from 14.21 ms to 4.12 ms). Overall, an average reduction of 87.1% could be achieved for all diffusion cases and 74% for all TSE cases. All 15 DIFF examples show very short pulse durations  $2 < T < 3$  ms. More closely, the optimized durations increase slightly with decreasing THK and with increasing MB factor. The SAR constraints of all optimized DIFF examples are not active and do not restrict the temporal reduction. The case with the maximum SAR observed in the optimum was  $MB = 4$  with  $THK = 1$  mm and a SAR of 3.16. In contrast, all TSE examples show an active SAR constraint in the optimum that limits a further temporal reduction. As a consequence, TSE examples with small slice thickness show a larger pulse duration of up to 6 ms, and the optimized durations depend mainly on the slice thickness. For example, the RF pulses shown in Figure 9.16 have a  $SAR_e$  of  $3.03 \text{ W kg}^{-1}$  (DIFF optimized) and  $3.19 \text{ W kg}^{-1}$  (TSE optimized). The initial PINS pulses feature a lower SAR estimate ( $1.47 \text{ W kg}^{-1}$  (DIFF init) and  $2.46 \text{ W kg}^{-1}$  (TSE init)), mainly due to the much longer pulse duration. The 31 optimized pulses behind this Figure fulfill all constraints of the optimization model exactly, since the software rejects pulses with even minor violation in any constraint.

Figure 9.17 shows the optimized RF and Gs shapes for one DIFF and one TSE example using three different hardware constraints given in Supporting Table S2. Here,  $\tau$  is set to the minimal gradient raster time of  $10 \mu\text{s}$  of the 3T MR scanner used later in the experimental validation. The computation times (scanner 2) of these pulses are

## 9 Appendix

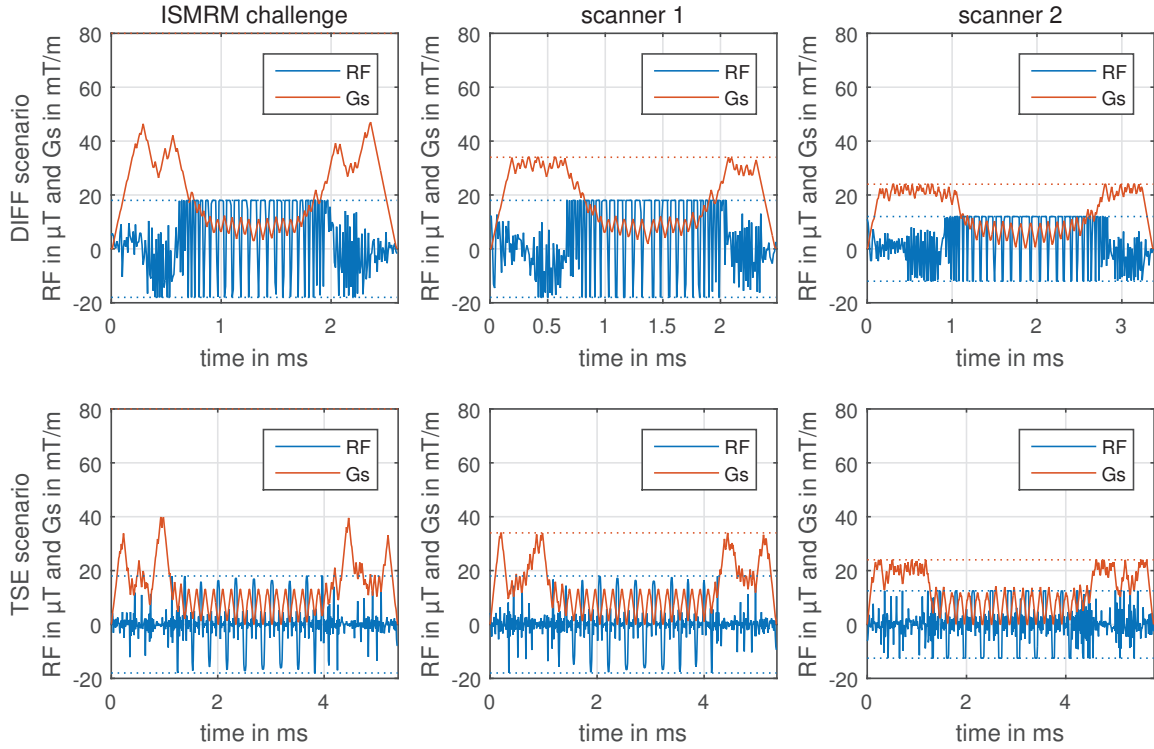


Figure 9.17: Optimized RF and Gs shapes for different hardware constraints (shown dotted) summarized in Supporting Table S2 (left: ISMRM challenge, middle: scanner 1, right: scanner 2) and a fixed temporal resolution of  $10 \mu\text{s}$ . The upper row shows a DIFF pulse for 3 slices with a thickness of 1.75 mm and the lower row shows a TSE pulse for 12 slices with a thickness of 1 mm.

approximately 2h (DIFF) and 2.5h (TSE) using MPI on the hardware (16 CPU cores) described above.

Next, we investigated the influence of time-invariant  $B_0$  and  $B_1$  inhomogeneities on the two optimized pulses shown in Figure 9.15 and Supporting Figure S1. Bloch simulations were performed with an off-resonance range of  $p_m 200$  Hz and a  $B_1$  variation of 75 – 125%. The results for the optimized pulses and the corresponding initial PINS pulse are depicted in Supporting Figure S2.

The optimized results do not change significantly w.r.t. the time resolution of the PINS initial guess or the initialization of the objective parameters, as long as the final time sampling rate is the same. In contrast, a coarser time discretization at the end generally leads to an increased pulse duration. For instance, the shortest diffusion candidate in Figure 9.17 optimized for a temporal discretization of  $\tau = 10$

## 9 Appendix

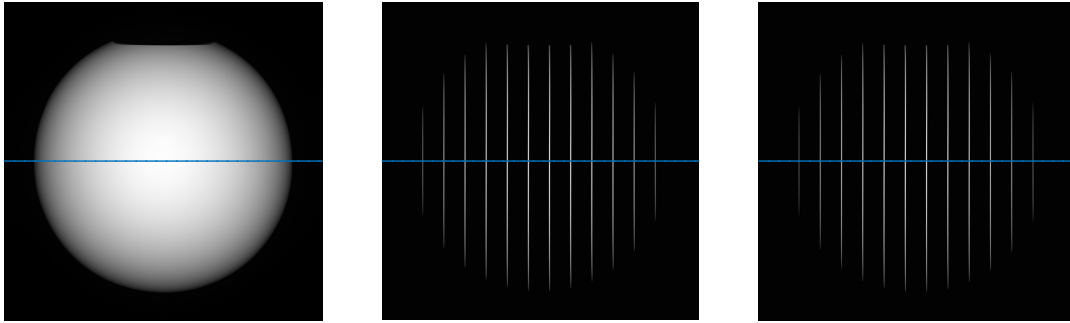


Figure 9.18: Reconstructed experimental spin echo data using a spherical oil phantom. Three different pairings are used: non-selective excitation and refocusing (left), slice-selective MB12 excitation and non-selective refocusing (middle), and slice-selective MB12 excitation and optimized refocusing (right). The intersection is shown in Figure 9.19 in detail.

$\mu$ s is about 17% longer ( $T = 2.61$  ms) than the optimized candidate with a temporal discretization of  $0.625$   $\mu$ s shown in Table 9.9 with  $T = 2.155$  ms.

### Experiments

Figure 9.18 shows the image reconstructions (magnitude) of the three SE experiments using a spherical oil phantom in the above mentioned 3T MR scanner. The optimized refocusing is based on the RF and Gs shapes of Figure 9.17 (“scanner 2”). The measured and reconstructed magnitude signal along the blue intersection line is plotted in detail in Figure 9.19 for the two slice-selective SE experiments.

There, the first and third row show the median of the high resolution DIFF and TSE phantom measurements, whereas the second, fourth and fifth row display zoomed images of the slices displaying both the median (solid) and the measurements points (crosses). The median is computed out of five individual measurements with minor noise variations. There is a good agreement between the different SE experiments with a small signal reduction for the outermost OC TSE slices, visible in the lowest right plot of Figure 9.19. The larger span in slice direction of the TSE example (240 mm) led to a comparable slice shift for both, the non-selective and optimized refocused data.

Figure 9.20 shows the intersection of the optimized SE experiment (median) normalized by the median of the non-selective SE experiment (shown for TSE in Figure

## 9 Appendix

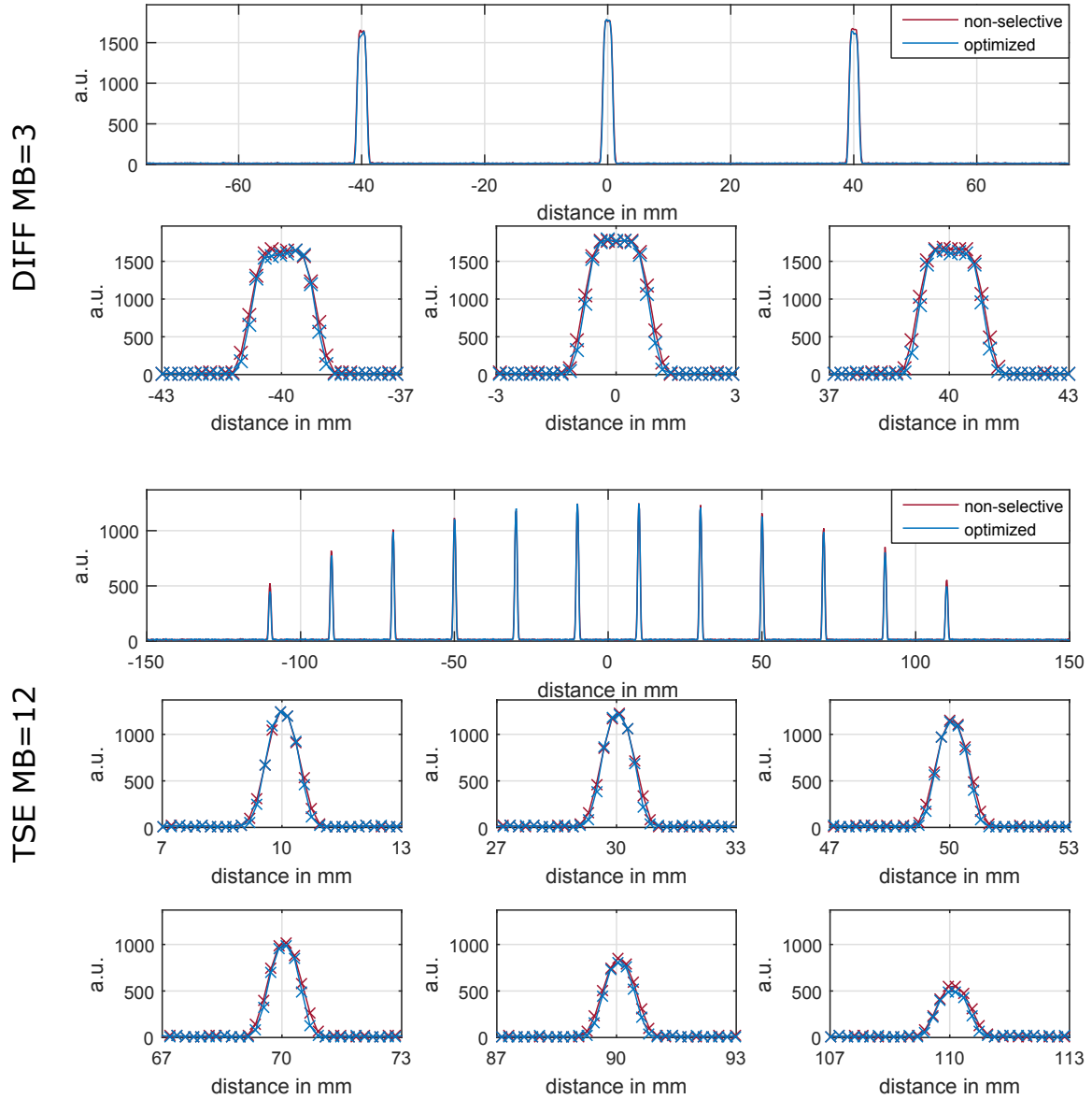


Figure 9.19: Reconstructed experimental spin echo data for DIFF MB = 3 and TSE MB = 12 refocusing with a slice thickness of 1.75 mm and 1 mm using a spherical phantom. Two different pairings are used: slice-selective excitation and non-selective refocusing (non-selective), and slice-selective excitation and optimized refocusing (optimized). Row one and three show the median of four individual measurements per curve. Row two, four and five show a zoom into the slices where the measurement points are additionally plotted (crosses).

## 9 Appendix

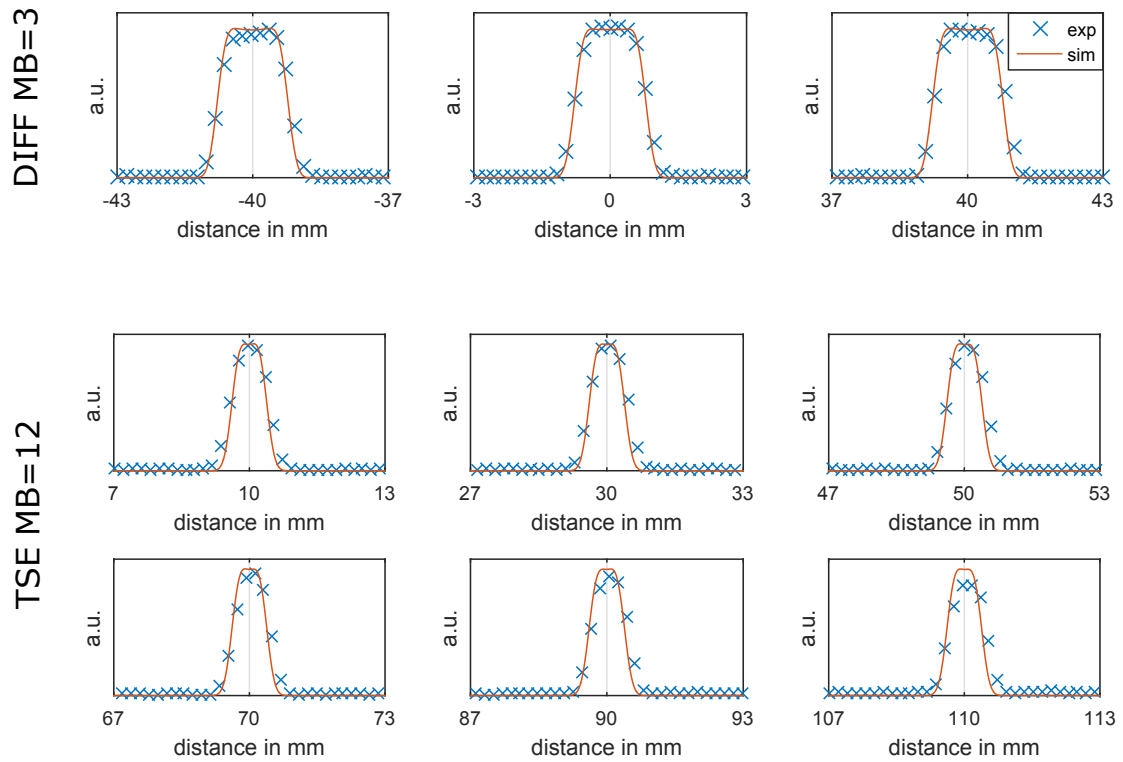


Figure 9.20: Comparison of the experimental data (exp) with optimized refocusing normalized by a fully non-selective SE measurement and the Bloch simulations (sim) for slice-selective excitation and optimized DIFF MB = 3 and TSE MB = 12 refocusing.

9.18). This normalization corrects for spatial  $B_1$  transmit/receive and signal variations resulting from the spherical phantom. The normalized data points were compared to the numerical Bloch simulations of the used excitation and optimized refocusing (solid).

### 9.3.5 Discussion

In addition to strict hardware and safety constraints, the minimal excitation or refocusing duration is a critical and important parameter. Specifically in the context of SMS imaging, RF pulses tend to have unacceptable long pulse durations limiting the applications and capabilities of SMS imaging. This work presented a time optimal control method, that, together with constrained optimization [2], can be applied to drastically reduce the pulse duration of SMS refocusing pulses while still fulfilling the hardware constraints and slice profile accuracy. The methods were tested on the 31 examples of the ISMRM Challenge on RF pulse design [4]. Compared to the given initialization of the ISMRM challenge (conventional superposed frequency shifted candidates for the diffusion cases, PINS for the TSE cases) the sum of the pulse durations for the 31 examples was reduced from 520.4 ms down to 102.4 ms, which is a reduction of 80.3%.

The proposed time optimal control method was tested for different problem parameters (Supporting Table S1) and constraints (Supporting Table S2). It robustly delivered pulses that exploit the allowed error bands to significantly shorten the pulse duration. This robustness w.r.t. the parameters and initializations is a consequence of using a trust-region globalization of the Newton-type method in the lower level problem. During the Challenge we tested the optimizer on different initializations computed by frequency shifted superposition, phase modulation and PINS. In all cases the pulses were shortened significantly. The shortest pulse durations were in most cases obtained for PINS based initial pulses, however, other educated guesses may outperform the presented results. We note that different initializations can be tested by the user in the published software.

The simulations of the optimized SMS pulses show accurate refocusing profiles with errors below the prescribed error bounds. Both, the treatment of the control constraints (i.e. peak  $B_1$  amplitude and the peak slew rate of Gs) by a semismooth quasi-Newton method and the treatment of the state constraints (profile accuracy, phase constraints, amplitude of Gs) by an  $L^p$  penalization with an iteratively increased  $p \rightarrow \infty$  allowed for full exploitation of the inequality constraints [2]. The precise derivative information (exact discrete derivatives using adjoint calculus, second-order

## 9 Appendix

method) enabled additional progress in reducing the pulse duration, when many of the constraints were already active. In contrast to the SAR minimization for fixed pulse duration in [2] the RF amplitude constraint is much more important in the time optimal case. In particular, the optimized controls in Figure 9.15 and Supporting Figure S1 show that (if the SAR and peak gradient constraint are not active) all the constraints are active wherever it is possible, resulting in equiripple error distributions and bang-bang controls. This is a typical behavior of solutions of pure time optimal control problems, and it underlines the local optimality of the presented results. With stronger constraints on the SAR or the peak gradient amplitude, optimized durations increase. In this case the optimal RF amplitude is at its bounds only in certain points during the time interval, see Figure 9.17.

In all examples, the pulse duration can be further decreased by a temporal refinement at the cost of an increased computational effort. For example the diffusion case shown in Figure 9.17 yielded a minimum pulse duration of 2.61 ms for a typical time grid ( $\tau = 10 \mu\text{s}$ ) and of 2.155 ms after four further refinement steps ( $\tau = 2.5 \mu\text{s}$ ). For the SE measurements the temporal refinement was done only up to the minimal gradient raster time of the particular MR scanner.

All optimized examples are designed and evaluated for a distinct FOV. We would like to mention here that both the PINS initial and optimized pulses create refocusing slices outside the FOV of interest. If this is unacceptable, the use of different initial guesses such as superposition pulses allows to increase the FOV and further restricts the refocusing profiles.

Optimized pulse durations of under 3 ms were observed throughout all diffusion examples, see Table 9.9. Here, the SAR was never at its bounds, mainly because of the low pulse rate. The maximum amplitude  $g_{\max}$  for the Gs amplitude was only reached in 3 of the 15 examples. In contrast, all optimized RF amplitudes and gradient slew rates were at their bounds almost everywhere with small exceptions around the two time points of maximum gradient amplitude.

For the TSE examples, the initial PINS pulses already combine a good refocusing profile with a small RF power that is exploited in the temporal reduction. Due to a higher pulse rate, the SAR constraint has a strong influence on the pulse duration here and is the main limiting factor for the temporal reduction. All 16 cases show an active SAR constraint in the optimum and outperform the initial PINS pulses in terms of the required refocusing duration. For the case given in Figure 9.15, the optimizer computes an admissible pulse candidate with a minimal pulse duration of 3.155 ms without a SAR constraint, compared to 4.120 ms with a SAR constraint, see Figure 9.16 and Table 9.10, of  $3.2 \text{ W kg}^{-1}$  - a factor of roughly 25%. This results in less exploited RF shape where the RF envelope differs from the block shape of examples

## 9 Appendix

without an active power constraint, e.g. the DIFF MB5 case shown in Figure 9.16. As a consequence of the active SAR constraint, the minimum durations turn out to be independent of the MB factor, see Table 9.10. Instead, they mainly depend on the slice thickness.

In total we applied the proposed optimization method to design SMS refocusing pulses with a wide range of MB factors (3–14) and THK (0.5–2 mm). All optimized pulses show a dramatically reduced pulse duration, on average by 87.1% for the diffusion and by 74.5% for the TSE examples, which allows significant reduction of the minimal TE of both, diffusion and TSE/RARE sequences.

Compared to state-of-the-art minimum duration design methods such as root-flip design [173], the achieved reduction of the proposed method is still significantly higher. For instance, the DIFF pulse used in the experiment (see Figure 9.17) is 57.4% shorter than a root-flipped pulse ( $T = 6.11$  ms) designed with equivalent design parameters (512 time-points with  $\tau = 11.93$   $\mu$ s,  $MB = 3$ ,  $TBP = 4$ ,  $THK = 1.75$  mm,  $r_{max} = 12.5$   $\mu$ T and a refocusing error of 0.02 out-of-slice and 0.03 in-slice).

Comparison of DIFF examples without a distinct phase constraint with the TSE examples designed with a pointwise phase constraint of the refocusing slices revealed that the additional constraint only has a minor effect on the overall pulse duration. Although this is not shown in this work, the phase constraint can obviously be changed to treat all slices at once to comply with the CPMG condition [244], [245].

With the current CPU based MPI implementation the pulses need to be precomputed and provided on the MR scanner. To reduce the current computation time, a speed-up of a factor 31 has been reported by using GPU parallelization[159]. Both optimized SE measurements were in a good accordance with the non-selective refocusing.

For comparison of simulated and measured slice profiles, the transmit/receive sensitivity variations and spatial signal differences arising from the used spherical oil phantom were removed by normalization of the measurements with a fully non-selective SE reference scan. Then, comparisons between the normalized slice profiles with optimized refocusing and the Bloch simulations were performed (Figure 9.20).

In general, rapidly-varying RF pulses can be distorted by the limited bandwidth of the RF system[246]. To reduce this RF distortion, we design real valued RF pulses that are less prone to RF distortions[111]. Additionally we used a time grid of 10  $\mu$ s, 400 times the minimal RF duration of 25 ns. Therefore we do not expect significant alterations of the RF chain on the optimized RF shapes. This is supported by the measured slice profiles. The question, whether time-optimal complex-valued RF pulses can outperform the real-valued ones will be part of future work. For systems with different RF specifications or for the optimization of complex RF pulses, an

additional constraint on the RF slew rate, analogous to the presented Gs slew rate constraint, could be included in the optimization.

The question arises how the optimized pulses perform in the presence of gradient imperfections. Besides an identical slice shift for both refocusing examples (see Figure 9.19) the slices of the optimized refocusing are attenuated with the distance to the isocenter. After a manual shim there are only minor  $B_0$  inhomogeneities in the phantom and the slice shift mainly results from non-linear gradients at the boundary of the field of view. The minor signal attenuations of the outermost slices are likely caused by gradient distortions [115], [118]. The inclusion of gradient and amplifier imperfections for different MR systems in the optimization will be future work.

An additional gradient echo phase scan (not shown) showed a slightly asymmetric  $B_0$  field that explains spatial signal differences between data from non-selective excitation and data from slice-selective excitation. However, these residual  $B_0$  inhomogeneities are not strong enough to explain the observed signal loss. The robustness of the optimized pulses w.r.t.  $B_0$  and  $B_1$  inhomogeneities was investigated in simulations in comparison to the initial pulses (Supporting Figure S2). In general the slice displacement for both optimized cases are lower compared with the initial PINS pulses. This is mainly due to the heavily decreased pulse duration which reduces the  $B_0$  sensitivity. Due to a variable k-space velocity of the optimized examples, the refocusing profiles are thinned out with increasing off-resonance, but remain stable below  $p_m 100$  Hz. In the context of  $B_1$  inhomogeneities, all examples share the principle that the thickness of the refocusing profile is broadened for lower  $B_1$  scaling and thinned out for a higher  $B_1$  scaling similar to other studies [247]. Depending on the application, an inclusion of  $B_0/B_1$  robustness into the optimization framework will be focus of future work.

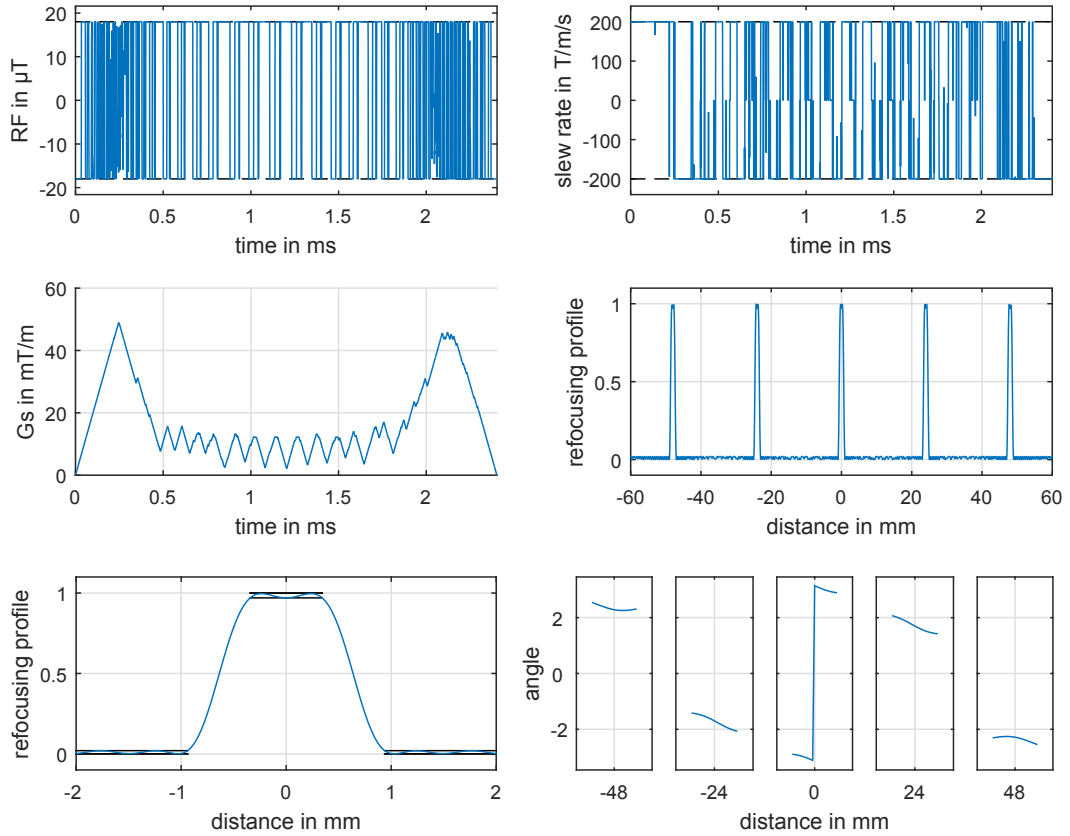
### 9.3.6 Conclusions

The proposed time optimal design method yields optimized SMS refocusing pulses for clinical sequences with very short pulse durations with respect to representative physical constraints given by current scanner hardware. The time optimal refocusing pulses will be beneficial for a broad range of SMS applications such as diffusion and spin echo based sequences to reduce the echo spacing and increase the signal quality in terms of amplitude and robustness to motion.

## Acknowledgments

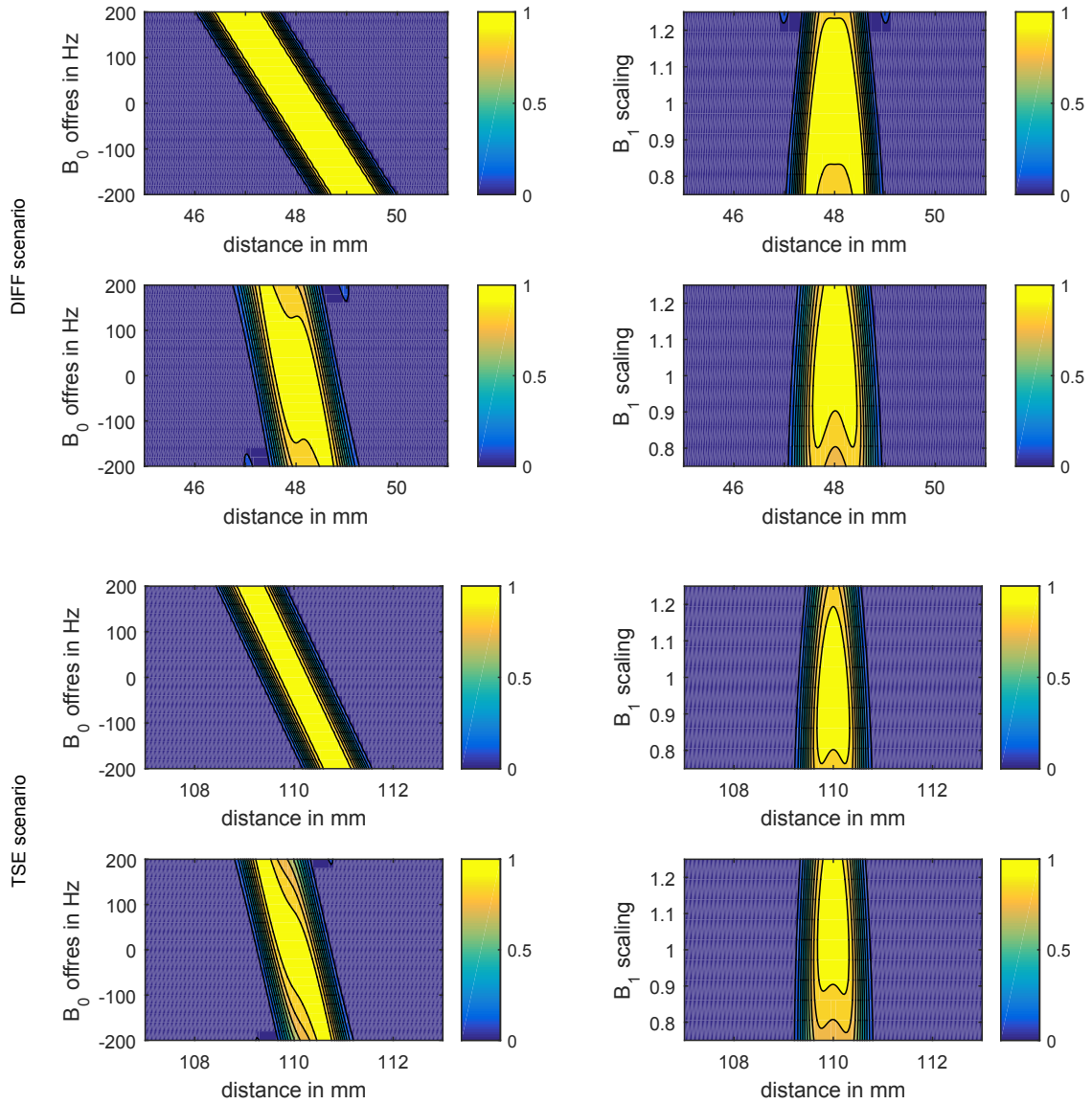
Partial support from "SFB F32-N18" and BioTechMed-Graz are gratefully acknowledged. This work was in part supported by the ERC advanced grant 668998 (OCLOC) under the EU's H2020 research program. The authors thank Christian Clason from the University of Duisburg-Essen for many fruitful discussions on the topic of the paper.

## Supporting Information



Supporting Figure S.1: Optimization results and Bloch simulations for a representative diffusion example. The first row shows the control variables  $B_1$  amplitude and slew rate of  $G_s$  with a total duration of 2.404 ms. The second row depicts  $G_s$  shape, and the corresponding simulated refocusing profile  $|b_{N_i}|^2$ . The last row shows a detail zoom of one slice to see the refocusing profile together with the error corridor (black), and the phase angle  $\arg(b_{N_i}^2)$  per slice.

## 9 Appendix



Supporting Figure S.2: Simulated refocusing profiles  $|b_{N_i}|^2$  (zoom to the outermost slice with comparable refocusing profiles across all individual slices) for a variation in the off-resonance and  $B_1$  inhomogeneity for four different pulses: the PINS-based initial pulses (first and third row) and the optimized pulses shown in Supporting Figure S1 (second row) and Figure 1 (fourth row), respectively.

## 9 Appendix

Supporting Table S.1: Overview of the problem parameters for TSE and diffusion (DIFF).

	MB factor [a.u.]	FOV mm	THK mm	TBP [a.u.]	$f_p$ 1/s	phase [a.u.]
TSE	8 : 2 : 14	240	0.5 : 0.5 : 2.0	3	54.55	constant
DIFF	3 : 1 : 5	120	1.0 : 0.25 : 2.0	4	16.67	free

Supporting Table S.2: Overview of the physical constraints used in the optimization.

	$g_{\max}$ mT/m	$s_{\max}$ mT/m/ms	$r_{\max}$ $\mu\text{T}$
ISMRM challenge	80.0	200	18.0
scanner 1	34.0	200	18.0
scanner 2	24.0	180	12.5

## Bibliography

- [1] C. S. Aigner, C. Clason, A. Rund, and R. Stollberger, "Efficient high-resolution RF pulse design applied to simultaneous multi-slice excitation", *J Magn Reson*, vol. 263, pp. 33–44, 2016. DOI: <http://dx.doi.org/10.1016/j.jmr.2015.11.013> (cit. on pp. 1, 2, 15, 27, 39, 50, 59–62, 64, 65, 68–71, 81–83, 118, 119, 124, 146).
- [2] A. Rund, C. S. Aigner, K. Kunisch, and R. Stollberger, "Magnetic resonance rf pulse design by optimal control with physical constraints", *IEEE Trans Med Imaging*, vol. 37, no. 2, pp. 461–472, 2018, ISSN: 0278-0062. DOI: 10.1109/TMI.2017.2758391 (cit. on pp. 1, 2, 15, 27, 39, 41, 50, 59, 60, 65, 71–74, 81–83, 147, 149–152, 161, 162).
- [3] A. Rund, C. S. Aigner, K. Kunisch, and R. Stollberger, "Simultaneous multislice refocusing via time optimal control", *Magn Reson Med*, n/a–n/a, DOI: 10.1002/mrm.27124 (cit. on pp. 1, 2, 15, 27, 32, 33, 35–37, 39, 41, 50, 59, 60, 74–78, 81–83).
- [4] W. A. Grissom, K. Setsompop, S. A. Hurley, J. Tsao, J. V. Velikina, and A. A. Samsonov, "Advancing RF pulse design using an open-competition format: Report from the 2015 ISMRM challenge", *Magn Reson Med*, pp. 1–10, 2016, ISSN: 1522-2594. DOI: 10.1002/mrm.26512 (cit. on pp. 1, 141, 147, 151, 161).
- [5] I. I. Rabi, "On the process of space quantization", *Phys Rev*, vol. 49, pp. 324–328, 4 1936. DOI: 10.1103/PhysRev.49.324 (cit. on p. 3).
- [6] —, "Space quantization in a gyrating magnetic field", *Phys Rev*, vol. 51, pp. 652–654, 8 1937. DOI: 10.1103/PhysRev.51.652 (cit. on p. 3).
- [7] C. P. Slichter, *Principles of Magnetic Resonance*. Springer-Verlag Berlin Heidelberg, 1990. DOI: 10.1007/978-3-662-09441-9 (cit. on p. 3).
- [8] M. E. Haacke, R. Brown, M. Thompson, and R. Venkatesan, *Magnetic resonance imaging: physical principles and sequence design*. Wiley-Liss, 1999 (cit. on pp. 3, 5–12, 15, 16, 23, 28).
- [9] F. Bloch, "Nuclear induction", *Phys Rev*, vol. 70, pp. 460–474, 7-8 1946. DOI: 10.1103/PhysRev.70.460 (cit. on pp. 3, 11, 13, 27).
- [10] M. H. Levitt, *Spin Dynamics: Basics of Nuclear Magnetic Resonance*. Wiley, 2008 (cit. on pp. 3, 5–11, 23).

## Bibliography

- [11] L. G. Hanson, "Is quantum mechanics necessary for understanding magnetic resonance?", *Concepts Magn Reson Part A*, vol. 32A, no. 5, pp. 329–340, 2008. DOI: 10.1002/cmr.a.20123 (cit. on pp. 3, 7).
- [12] D. P. Zeeman, "On the influence of magnetism on the nature of the light emitted by a substance", *Philos Mag*, vol. 43, no. 262, pp. 226–239, 1897. DOI: 10.1080/14786449708620985 (cit. on p. 4).
- [13] W. Gerlach and O. Stern, "Der experimentelle nachweis der richtungsquantelung im magnetfeld", *Zeitschrift für Physik*, vol. 9, no. 1, pp. 349–352, 1922, ISSN: 0044-3328. DOI: 10.1007/BF01326983 (cit. on p. 4).
- [14] G. E. Uhlenbeck and S. Goudsmit, "Spinning electrons and the structure of spectra", *Nature*, vol. 117, 1926. DOI: 10.1038/117264a0 (cit. on p. 4).
- [15] "The quantum theory of the electron", *Proc Royal Soc of London*, vol. 117, no. 778, pp. 610–624, 1928. DOI: 10.1098/rspa.1928.0023 (cit. on p. 4).
- [16] P. J. Mohr, D. B. Newell, and B. N. Taylor, "CODATA recommended values of the fundamental physical constants: 2014", *Rev Mod Phys*, vol. 88, p. 035009, 3 2016. DOI: 10.1103/RevModPhys.88.035009 (cit. on p. 4).
- [17] *The nist reference on fundamental physical constants*, <https://physics.nist.gov/cgi-bin/cuu/Value?gp>, Accessed: 2018-05-08 (cit. on p. 4).
- [18] J. Fessler, "MRI notes, p. 1-33", lecture notes for EECS 516, 2009 (cit. on pp. 5, 17).
- [19] "Pd: Proton density of tissue water", in *Quantitative MRI of the Brain*. John Wiley and Sons, Ltd, 2004, pp. 83–109. DOI: 10.1002/0470869526.ch4 (cit. on p. 6).
- [20] E. Moser, "Ultra-high-field magnetic resonance: Why and when?", *World J Radiol*, vol. 2, pp. 37–40, 1 2010. DOI: 10.4329/wjr.v2.i1.37 (cit. on p. 8).
- [21] M. K. Woo, R. L. Lagore, L. DelaBarre, B. Y. Lee, Y. Eryaman, J. Radder, A. Erturk, G. Metzger, P. F. van de Moortele, K. Ugurbil, and G. Adriany, "A 16-channel transceiver loop dipole antennas head array for human head imaging at 10.5t", in *Proc ICEAA*, 2017, pp. 1649–1652. DOI: 10.1109/ICEAA.2017.8065607 (cit. on pp. 8, 26).
- [22] O. Kraff and H. H. Quick, "7t: Physics, safety, and potential clinical applications", *J Magn Reson Imaging*, n/a–n/a, 2017. DOI: 10.1002/jmri.25723 (cit. on p. 8).
- [23] M. A. Bernstein, K. F. King, and X. J. Zhou, *Handbook of MRI Pulse Sequences*. Elsevier Academic Press, 2004. DOI: <http://dx.doi.org/10.1016/B978-012092861-3/50003-0> (cit. on pp. 8, 9, 15, 17, 22, 23, 28, 31, 36, 39–41, 43, 44, 46, 49–52, 77, 118, 120, 148).

## Bibliography

- [24] I. I. Rabi, N. F. Ramsey, and J. Schwinger, "Use of rotating coordinates in magnetic resonance problems", *Rev Mod Phys*, vol. 26, pp. 167–171, 2 1954. DOI: 10.1103/RevModPhys.26.167 (cit. on p. 9).
- [25] J. Wang, W. Mao, M. Qiu, M. B. Smith, and R. T. Constable, "Factors influencing flip angle mapping in mri: Rf pulse shape, slice-select gradients, off-resonance excitation, and bo inhomogeneities", *Magn Reson Med*, vol. 56, no. 2, pp. 463–468, 2006. DOI: 10.1002/mrm.20947 (cit. on pp. 10, 36).
- [26] D. G. Nishimura, *Principles of Magnetic Resonance Imaging*. Stanford University, 1996 (cit. on pp. 11, 59, 97).
- [27] A. Abragam, *The Principles of Nuclear Magnetism*. Clarendon Press, 1983 (cit. on p. 11).
- [28] M. Goldman, "Formal theory of spin-lattice relaxation", *J Magn Reson*, vol. 149, no. 2, pp. 160–187, 2001. DOI: <https://doi.org/10.1006/jmre.2000.2239> (cit. on p. 11).
- [29] G. J. Stanisz, E. E. Odobina, J. Pun, M. Escaravage, S. J. Graham, M. J. Bronskill, and R. M. Henkelman, "T<sub>1</sub>, t<sub>2</sub> relaxation and magnetization transfer in tissue at 3t", *Magn Reson Med*, vol. 54, no. 3, pp. 507–512, 2005. DOI: 10.1002/mrm.20605 (cit. on p. 12).
- [30] J. Z. Bojorquez, S. Bricq, C. Acquitte, F. Brunotte, P. M. Walker, and A. Lalande, "What are normal relaxation times of tissues at 3 t?", *J Magn Reson Imaging*, vol. 35, pp. 69–80, 2017. DOI: <https://doi.org/10.1016/j.mri.2016.08.021> (cit. on p. 12).
- [31] G. B. Chavhan, P. S. Babyn, B. Thomas, M. M. Shroff, and E. M. Haacke, "Principles, techniques, and applications of t<sub>2</sub>\*-based mr imaging and its special applications", *RadioGraphics*, vol. 29, no. 5, pp. 1433–1449, 2009. DOI: 10.1148/rg.295095034 (cit. on pp. 13, 15, 28).
- [32] F. A. Anet, D. J. O'Leary, C. G. Wade, and R. D. Johnson, "Nmr relaxation by the antisymmetric component of the shielding tensor: A longer transverse than longitudinal relaxation time", *Chem Phys Lett*, vol. 171, no. 5, pp. 401–405, 1990. DOI: [https://doi.org/10.1016/0009-2614\(90\)85237-7](https://doi.org/10.1016/0009-2614(90)85237-7) (cit. on p. 13).
- [33] H. M. Sevian and J. L. Skinner, "T<sub>2</sub> can be greater than 2t<sub>1</sub>", *The J Chem Phys*, vol. 91, no. 3, pp. 1775–1782, 1989. DOI: 10.1063/1.457648 (cit. on p. 13).
- [34] D. D. Traficante, "Relaxation. can t<sub>2</sub>, be longer than t<sub>1</sub>?", *Concepts Magn Reson*, vol. 3, no. 3, pp. 171–177, 1991. DOI: 10.1002/cmr.1820030305 (cit. on p. 13).
- [35] L. N. Baldwin, K. Wachowicz, S. D. Thomas, R. Rivest, and B. G. Fallone, "Characterization, prediction, and correction of geometric distortion in 3t mr images", *Med Phys*, vol. 34, no. 2, pp. 388–399, 2007. DOI: 10.1118/1.2402331 (cit. on p. 14).

## Bibliography

- [36] J. R. Reichenbach, R. Venkatesan, D. A. Yablonskiy, M. R. Thompson, S. Lai, and E. M. Haacke, "Theory and application of static field inhomogeneity effects in gradient-echo imaging", *J Magn Reson Imaging*, vol. 7, no. 2, pp. 266–279, 1997. DOI: 10.1002/jmri.1880070203 (cit. on p. 15).
- [37] J. F. Schenck, "The role of magnetic susceptibility in magnetic resonance imaging: Mri magnetic compatibility of the first and second kinds", *Med Phys*, vol. 23, no. 6, pp. 815–850, 1996. DOI: 10.1118/1.597854 (cit. on p. 15).
- [38] "Composite pulses", in *eMagRes*. John Wiley and Sons, Ltd, 2007. DOI: 10.1002/9780470034590.emrstm0086 (cit. on pp. 15, 40, 41).
- [39] S. Hidalgo-Tobon, "Theory of gradient coil design methods for magnetic resonance imaging", *Concept Magn Reson A*, vol. 36A, no. 4, pp. 223–242, 2010. DOI: 10.1002/cmr.a.20163 (cit. on pp. 15, 29, 36).
- [40] P. C. Lauterbur, "Image formation by induced local interactions: Examples employing nuclear magnetic resonance", *Nature*, vol. 242, p. 190, 1973. DOI: 10.1038/242190a0 (cit. on p. 15).
- [41] A. G. Webb, Ed., *Magnetic Resonance Technology, Hardware and System Component Design*, ser. New Developments in NMR. The Royal Society of Chemistry, 2016, pp. 1–385. DOI: 10.1039/9781782623878 (cit. on pp. 15, 26, 27).
- [42] P. A. Bottomley and C. J. Hardy, "Two dimensional spatially selective spin inversion and spin echo refocusing with a single nuclear magnetic resonance pulse", *J Appl Phys*, vol. 62, no. 10, pp. 4284–4290, 1987. DOI: 10.1063/1.339103 (cit. on pp. 15, 40).
- [43] J. Pauly, D. Nishimura, and A. Macovski, "A k-space analysis of small-tip-angle excitation", *J Magn Reson*, vol. 213, no. 2, pp. 544–557, 1989. DOI: 10.1016/0022-2364(89)90265-5 (cit. on pp. 15, 17, 18, 40, 44, 94, 111).
- [44] J. Pauly, D. Spielman, and A. Macovski, "Echo-planar spin-echo and inversion pulses", *Magn Reson Med*, vol. 29, no. 6, pp. 776–782, 1993. DOI: 10.1002/mrm.1910290609 (cit. on pp. 15, 40).
- [45] S. Rieseberg, J. Frahm, and J. Finsterbusch, "Two-dimensional spatially-selective rf excitation pulses in echo-planar imaging", *Magn Reson Med*, vol. 47, no. 6, pp. 1186–1193, 2002. DOI: 10.1002/mrm.10157 (cit. on pp. 15, 40).
- [46] V. A. Stenger, F. E. Boada, and D. C. Noll, "Multishot 3d slice-select tailored rf pulses for mri", *Magn Reson Med*, vol. 48, no. 1, pp. 157–165, 2002. DOI: 10.1002/mrm.10194 (cit. on pp. 15, 40).
- [47] D. Xu, K. F. King, Y. Zhu, G. C. McKinnon, and Z.-P. Liang, "Designing multichannel, multidimensional, arbitrary flip angle RF pulses using an optimal control approach", *Magn Reson Med*, vol. 59, no. 3, pp. 547–560, 2008. DOI: 10.1002/mrm.21485 (cit. on pp. 15, 40, 50, 59, 60, 94, 110).

## Bibliography

- [48] D. Lee, M. Lustig, W. A. Grissom, and J. M. Pauly, "Time-optimal design for multidimensional and parallel transmit variable-rate selective excitation", *Magn Reson Med*, vol. 61, no. 6, pp. 1471–1479, 2009. DOI: 10.1002/mrm.21950 (cit. on pp. 15, 40).
- [49] W. A. Grissom, D. Xu, A. B. Kerr, J. A. Fessler, and D. C. Noll, "Fast large-tip-angle multidimensional and parallel RF pulse design in MRI", *IEEE Trans Med Imaging*, vol. 28, no. 10, pp. 1548–1559, 2009. DOI: 10.1109/TMI.2009.2020064 (cit. on pp. 15, 40, 50, 59, 60, 94, 110, 146).
- [50] T. R. Brown, B. M. Kincaid, and K. Ugurbil, "Nmr chemical shift imaging in three dimensions", *Proc National Academy of Sciences USA*, vol. 79, no. 11, pp. 3523–3526, 1982 (cit. on pp. 15, 28).
- [51] S. Ljunggren, "A simple graphical representation of fourier-based imaging methods", *J Magn Reson*, vol. 54, no. 2, pp. 338–343, 1983. DOI: [https://doi.org/10.1016/0022-2364\(83\)90060-4](https://doi.org/10.1016/0022-2364(83)90060-4) (cit. on pp. 15, 28).
- [52] D. B. Twieg, "The k-trajectory formulation of the nmr imaging process with applications in analysis and synthesis of imaging methods", *Med Phys*, vol. 10, no. 5, pp. 610–621, 1983. DOI: 10.1118/1.595331 (cit. on pp. 15, 29).
- [53] Z.-P. Liang and P. C. Lauterbur, *Principles of magnetic resonance imaging: a signal processing perspective*, ser. IEEE Press series in biomedical engineering. IEEE Press, 2000, ISBN: 9780819435163 (cit. on pp. 15, 16, 19, 25).
- [54] B. Tahayori, L. Johnston, I. Mareels, and P. Farrell, "The bloch equation revisited through averaging under adiabatic passages", *Proc IFAC*, vol. 44, no. 1, pp. 9650–9655, 2011. DOI: <https://doi.org/10.3182/20110828-6-IT-1002.00884> (cit. on p. 16).
- [55] S. Balac and L. Chupin, "Fast approximate solution of bloch equation for simulation of rf artifacts in magnetic resonance imaging", *Math Comp Modelling*, vol. 48, no. 11, pp. 1901–1913, 2008. DOI: <https://doi.org/10.1016/j.mcm.2007.05.021> (cit. on p. 16).
- [56] G. Sebastiani and P. Barone, "Mathematical principles of basic magnetic resonance imaging in medicine", *Signal Processing*, vol. 25, no. 2, pp. 227–250, 1991. DOI: [https://doi.org/10.1016/0165-1684\(91\)90065-Q](https://doi.org/10.1016/0165-1684(91)90065-Q) (cit. on p. 16).
- [57] P. K. Madhu and A. Kumar, "Bloch equations revisited: New analytical solutions for the generalized bloch equations", *Concept Magn Reson A*, vol. 9, no. 1, pp. 1–12, 1997. DOI: 10.1002/(SICI)1099-0534(1997)9:1<1::AID-CMR1>3.0.CO;2-2 (cit. on p. 16).
- [58] T. Stoecker, K. Vahedipour, D. Pflugfelder, and N. J. Shah, "High-performance computing mri simulations", *Magn Reson Med*, vol. 64, no. 1, pp. 186–193, 2010. DOI: 10.1002/mrm.22406 (cit. on pp. 16, 32).

## Bibliography

- [59] J. P. Grivet, "Simulation of magnetic resonance experiments", *Am J Phys*, vol. 61, no. 12, pp. 1133–1139, 1993. DOI: 10.1119/1.17309 (cit. on p. 16).
- [60] J. Bittoun, J. Taquin, and M. Sauzade, "A computer algorithm for the simulation of any nuclear magnetic resonance (nmr) imaging method", *J Magn Reson Imaging*, vol. 2, no. 2, pp. 113–120, 1984. DOI: [https://doi.org/10.1016/0730-725X\(84\)90065-1](https://doi.org/10.1016/0730-725X(84)90065-1) (cit. on pp. 16, 19, 25).
- [61] R. M. Summers, L. Axel, and S. Israel, "A computer simulation of nuclear magnetic resonance imaging", *Magn Reson Med*, vol. 3, no. 3, pp. 363–376, 1986. DOI: 10.1002/mrm.1910030302 (cit. on p. 16).
- [62] H. Benoit-Cattin, G. Collewet, B. Belaroussi, H. Saint-Jalmes, and C. Odet, "The simri project: A versatile and interactive mri simulator", *J Magn Reson*, vol. 173, no. 1, pp. 97–115, 2005. DOI: <https://doi.org/10.1016/j.jmr.2004.09.027> (cit. on pp. 16, 19, 25).
- [63] I. Drobnjak, D. Gavaghan, E. Süli, J. Pitt-Francis, and M. Jenkinson, "Development of a functional magnetic resonance imaging simulator for modeling realistic rigid-body motion artifacts", *Magn Reson Med*, vol. 56, no. 2, pp. 364–380, 2006. DOI: 10.1002/mrm.20939 (cit. on p. 16).
- [64] M. Weigel, "Extended phase graphs: Dephasing, rf pulses, and echoes - pure and simple", *J Magn Reson Imaging*, vol. 41, no. 2, pp. 266–295, 2015. DOI: 10.1002/jmri.24619 (cit. on p. 16).
- [65] I. R. Cole, "Modelling cpv", PhD Dissertation, Loughborough University, 2015 (cit. on p. 19).
- [66] J. Pauly, P. Le Roux, D. Nishimura, and A. Macovski, "Parameter relations for the Shinnar–Le Roux selective excitation pulse design algorithm", *IEEE Trans Med Imaging*, vol. 10, no. 1, pp. 53–65, 1991. DOI: 10.1109/42.75611 (cit. on pp. 20, 21, 23, 39, 48, 49, 72, 94, 101, 102, 111, 118, 119, 125, 126, 134, 147, 148, 152, 153).
- [67] E. Jaynes, "Matrix treatment of nuclear induction", *Phys Rev*, vol. 98, no. 4, pp. 1099–1105, 1955 (cit. on pp. 21, 118, 119, 147).
- [68] C. Graf, "On the numerical solution of the bloch equation with relaxation", Master thesis, 2018 (cit. on pp. 24, 25, 70, 82).
- [69] S. Hirsch, J. Braun, and I. Sack, "Simulating the bloch equations", in *Magnetic Resonance Elastography*. Wiley-VCH Verlag GmbH and Co. KGaA, 2016, pp. 355–356. DOI: 10.1002/9783527696017.app1 (cit. on p. 24).
- [70] C. Moler and C. V. Loan, "Nineteen dubious ways to compute the exponential of a matrix, twenty-five years later", *SIAM Review*, vol. 45, no. 1, pp. 3–49, 2003. DOI: 10.1137/S00361445024180 (cit. on p. 24).

## Bibliography

- [71] K. Majewski, "Rotation relaxation splitting for optimizing parallel rf excitation pulses with  $t_1$ - and  $t_2$ -relaxations in mri", *J Magn Reson*, vol. 288, pp. 43–57, 2018, ISSN: 1090-7807. DOI: <https://doi.org/10.1016/j.jmr.2018.01.005> (cit. on pp. 24, 70, 82).
- [72] D. G. Nishimura, *Principles of Magnetic Resonance Imaging*. Stanford Univ, 2010 (cit. on p. 25).
- [73] B. Blümich, P. Blünder, C. Fülber, U. Scheler, and F. Weigand, "Nmr imaging and materials research", *Macromolecular Symposia*, vol. 87, no. 1, pp. 187–193, 1994. DOI: 10.1002/masy.19940870120 (cit. on p. 26).
- [74] O. Pecher, J. Carretero-González, K. J. Griffith, and C. P. Grey, "Materials' methods: Nmr in battery research", *Chem Mater*, vol. 29, no. 1, pp. 213–242, 2017. DOI: 10.1021/acs.chemmater.6b03183 (cit. on p. 26).
- [75] R. E. Botto and Y. Sanada, *Magnetic Resonance of Carbonaceous Solids*, B. R. E. and S. Yuzo, Eds. Washington, DC: J Am Chem Soc, 1992. DOI: 10.1021/ba-1993-0229 (cit. on p. 26).
- [76] A. Denic, S. I. Macura, P. Mishra, J. D. Gamez, M. Rodriguez, and I. Pirko, "Mri in rodent models of brain disorders", *Neurotherapeutics*, vol. 8, no. 1, pp. 3–18, 2011. DOI: 10.1007/s13311-010-0002-4 (cit. on p. 26).
- [77] P. Marzola, F. Boschi, F. Moneta, A. Sbarbati, and C. Zancanaro, "Preclinical in vivo imaging for fat tissue identification, quantification, and functional characterization", *Front Pharmacol*, vol. 7, p. 336, 2016. DOI: 10.3389/fphar.2016.00336 (cit. on p. 26).
- [78] R. M. Botnar and M. R. Makowski, "Chapter 8 - cardiovascular magnetic resonance imaging in small animals", in *Animal Models of Molecular Pathology*, ser. Progress in Molecular Biology and Translational Science, P. Conn, Ed., vol. 105, Academic Press, 2012, pp. 227–261. DOI: <https://doi.org/10.1016/B978-0-12-394596-9.00008-1> (cit. on p. 26).
- [79] C. Albanese, O. C. Rodriguez, J. VanMeter, S. T. Fricke, B. R. Rood, Y. Lee, S. S. Wang, S. Madhavan, Y. Gusev, E. F. Petricoin, and Y. Wang, "Preclinical magnetic resonance imaging and systems biology in cancer research: Current applications and challenges", *Am J Pathol*, vol. 182, no. 2, pp. 312–318, 2013. DOI: <https://doi.org/10.1016/j.ajpath.2012.09.024> (cit. on p. 26).
- [80] N. Beckmann, T. Mueggler, P. R. Allegrini, D. Laurent, and M. Rudin, "From anatomy to the target: Contributions of magnetic resonance imaging to pre-clinical pharmaceutical research", *Anat Rec*, vol. 265, no. 2, pp. 85–100, 2001. DOI: 10.1002/ar.1059 (cit. on p. 26).
- [81] S. D. Wolff and R. S. Balaban, "Magnetization transfer contrast (mtc) and tissue water proton relaxation in vivo", *Magn Reson Med*, vol. 10, no. 1, pp. 135–144, 1989. DOI: 10.1002/mrm.1910100113 (cit. on p. 26).

## Bibliography

- [82] D. J. Larkman and R. G. Nunes, "Parallel magnetic resonance imaging", *Phys Med Biol*, vol. 52, no. 7, R15, 2007 (cit. on pp. 26, 53).
- [83] W. A. Grissom, K. Setsompop, S. A. Hurley, J. Tsao, J. V. Velikina, and A. A. Samsonov, "Advancing rf pulse design using an open-competition format: Report from the 2015 ismrm challenge", *Magn Reson Med*, vol. 78, no. 4, pp. 1352–1361, 2017. DOI: 10.1002/mrm.26512 (cit. on pp. 26, 72, 75, 77, 82).
- [84] S. Posse, R. Otazo, S. R. Dager, and J. Alger, "Mr spectroscopic imaging: Principles and recent advances", *J Magn Reson Imaging*, vol. 37, no. 6, pp. 1301–1325, 2013. DOI: 10.1002/jmri.123945 (cit. on p. 26).
- [85] P. Stroman, *Essentials of Functional MRI*. Boca Raton: CRC Press, 2011 (cit. on pp. 26, 30).
- [86] C. Meriles, D. Sakellariou, and A. Trabesinger, "Theory of mri in the presence of zero to low magnetic fields and tensor imaging field gradients", *J Magn Reson*, vol. 182, no. 1, pp. 106–114, 2006. DOI: <https://doi.org/10.1016/j.jmr.2006.06.018> (cit. on p. 26).
- [87] Y. Eryaman, P. Zhang, L. Utecht, K. Kose, R. L. Lagore, L. DelaBarre, J. Kulesa, L. E. Eberly, G. Adriany, T. L. Iles, P. A. Iaizzo, J. T. Vaughan, and K. Ugurbil, "Investigating the physiological effects of 10.5 tesla static field exposure on anesthetized swine", *Magn Reson Med*, vol. 79, no. 1, pp. 511–514, 2018. DOI: 10.1002/mrm.26672 (cit. on p. 26).
- [88] M. D. Bird, I. R. Dixon, and J. Toth, "Large, high-field magnet projects at the nhmfl", *IEEE Trans Appl Supercond*, vol. 25, no. 3, pp. 1–6, 2015. DOI: 10.1109/TASC.2014.2367470 (cit. on p. 26).
- [89] E. Moser, E. Laistler, F. Schmitt, and G. Kontaxis, "Ultra-high field nmr and mri—the role of magnet technology to increase sensitivity and specificity", *Front Phys*, vol. 5, p. 33, 2017. DOI: 10.3389/fphy.2017.00033 (cit. on p. 26).
- [90] J. Enders, M. Rief, E. Zimmermann, P. Asbach, G. Diederichs, C. Wetz, E. Siebert, M. Wagner, B. Hamm, and M. Dewey, "High-field open versus short-bore magnetic resonance imaging of the spine: A randomized controlled comparison of image quality", *PLOS ONE*, vol. 8, no. 12, pp. 1–10, 2014. DOI: 10.1371/journal.pone.0083427 (cit. on p. 26).
- [91] W. T. Sobol, "Recent advances in mri technology: Implications for image quality and patient safety", *Saudi J Ophthalmol*, vol. 26, no. 4, pp. 393–399, 2012. DOI: <https://doi.org/10.1016/j.sjopt.2012.07.005> (cit. on p. 26).
- [92] E. M. Purcell, H. C. Torrey, and R. V. Pound, "Resonance absorption by nuclear magnetic moments in a solid", *Phys Rev*, vol. 69, pp. 37–38, 1-2 1946. DOI: 10.1103/PhysRev.69.37 (cit. on p. 27).

## Bibliography

- [93] N. Bloembergen, E. M. Purcell, and R. V. Pound, "Relaxation effects in nuclear magnetic resonance absorption", *Phys Rev*, vol. 73, pp. 679–712, 7 1948. DOI: 10.1103/PhysRev.73.679 (cit. on p. 27).
- [94] E. L. Hahn, "Spin echoes", *Phys Rev*, vol. 80, pp. 580–594, 4 1950. DOI: 10.1103/PhysRev.80.580 (cit. on pp. 27, 28).
- [95] M. Barth, F. Breuer, P. Koopmans, D. Norris, and B. Poser, "Simultaneous multislice (SMS) imaging techniques", *Magn Reson Med*, vol. 81, pp. 63–81, 2016. DOI: 10.1002/mrm.25897 (cit. on pp. 28, 52, 53, 56, 57, 118, 125, 146).
- [96] K. F. King and P. R. Moran, "A unified description of nmr imaging, data-collection strategies, and reconstruction", *Med Phys*, vol. 11, no. 1, pp. 1–14, 1984. DOI: 10.1118/1.595470 (cit. on p. 29).
- [97] J. Pauly, *Non-cartesian reconstruction*, 2005 (cit. on p. 29).
- [98] A. Haase, J. Frahm, D. Matthaei, W. Hanicke, and K.-D. Merboldt, "Flash imaging. rapid nmr imaging using low flip-angle pulses", *J Magn Reson*, vol. 67, no. 2, pp. 258–266, 1986. DOI: [https://doi.org/10.1016/0022-2364\(86\)90433-6](https://doi.org/10.1016/0022-2364(86)90433-6) (cit. on p. 29).
- [99] K. Scheffler and S. Lehnhardt, "Principles and applications of balanced ssfp techniques", *Eur Radiol*, vol. 13, no. 11, pp. 2409–2418, 2003. DOI: 10.1007/s00330-003-1957-x (cit. on p. 29).
- [100] J. Hennig, A. Nauerth, and H. Friedburg, "Rare imaging: A fast imaging method for clinical mr", *Magn Reson Med*, vol. 3, no. 6, pp. 823–833, 1986. DOI: 10.1002/mrm.1910030602 (cit. on p. 29).
- [101] P. Mansfield, "Multi-planar image formation using nmr spin echoes", *Journal of Physics C: Solid State Physics*, vol. 10, no. 3, p. L55, 1977 (cit. on p. 29).
- [102] M. Poustchi-Amin, S. A. Mirowitz, J. J. Brown, R. C. McKinstry, and T. Li, "Principles and applications of echo-planar imaging: A review for the general radiologist", *RadioGraphics*, vol. 21, no. 3, pp. 767–779, 2001. DOI: 10.1148/radiographics.21.3.g01ma23767 (cit. on p. 29).
- [103] R. C. Semelka, N. L. Kelekis, D. Thomasson, M. A. Brown, and G. A. Laub, "Haste mr imaging: Description of technique and preliminary results in the abdomen", *J Magn Reson Imaging*, vol. 6, no. 4, pp. 698–699, DOI: 10.1002/jmri.1880060420 (cit. on p. 29).
- [104] S. J. Holdsworth, S. Skare, R. D. Newbould, R. Guzman, N. H. Blevins, and R. Bammer, "Readout-segmented epi for rapid high resolution diffusion imaging at 3t", *Eur J Radiol*, vol. 65, no. 1, pp. 36–46, 2008, 3 Tesla MR. DOI: <https://doi.org/10.1016/j.ejrad.2007.09.016> (cit. on p. 31).

## Bibliography

- [105] K. Oshio and D. A. Feinberg, "Grase (gradient-and spin-echo) imaging: A novel fast mri technique", *Magn Reson Med*, vol. 20, no. 2, pp. 344–349, 1991. DOI: 10.1002/mrm.1910200219 (cit. on p. 31).
- [106] B. Slayman, K. King, and P. Licato, *Nutation angle measurement during mri prescan*, US Patent 5,416,412, 1995. [Online]. Available: <https://www.google.si/patents/US5416412> (cit. on p. 34).
- [107] T. Feiweier, P. Heubes, and T. Speckner, *Method and magnetic resonance system for adjustment of the field strength of rf pulses*, US Patent App. 11/612,802, 2007. [Online]. Available: <https://www.google.com/patents/US20070145975> (cit. on p. 34).
- [108] D. O. Brunner, B. E. Dietrich, M. Çavuşoğlu, B. J. Wilm, T. Schmid, S. Gross, C. Barmet, and K. P. Pruessmann, "Concurrent recording of rf pulses and gradient fields – comprehensive field monitoring for mri", *NMR Biomed*, vol. 29, no. 9, pp. 1162–1172, 2016. DOI: 10.1002/nbm.3359 (cit. on p. 36).
- [109] "Radiofrequency power amplifiers for nmr and mri", in *eMagRes*. John Wiley and Sons, Ltd, 2007. DOI: 10.1002/9780470034590.emrstm1138 (cit. on pp. 36, 37).
- [110] R. A. de Graaf, *In Vivo NMR Spectroscopy: Principles and Techniques*. John Wiley and Sons, Ltd, 2013 (cit. on pp. 37, 40, 41, 50).
- [111] S. Abo Seada, A. N. Price, J. V. Hajnal, and S. J. Malik, "Optimized amplitude modulated multiband rf pulse design", *Magn Reson Med*, vol. 78, no. 6, pp. 2185–2193, 2017. DOI: 10.1002/mrm.26610 (cit. on pp. 37, 54, 163).
- [112] B. A. Hargreaves, C. H. Cunningham, D. G. Nishimura, and S. M. Conolly, "Variable-rate selective excitation for rapid mri sequences", *Magn Reson Med*, vol. 52, no. 3, pp. 590–597, 2004. DOI: 10.1002/mrm.20168 (cit. on pp. 37, 51, 52, 56, 64, 118, 125, 134, 146).
- [113] C. Boesch, R. Gruetter, and E. Martin, "Temporal and spatial analysis of fields generated by eddy currents in superconducting magnets: Optimization of corrections and quantitative characterization of magnet/gradient systems", *Magn Reson Med*, vol. 20, no. 2, pp. 268–284, 1991. DOI: 10.1002/mrm.1910200209 (cit. on p. 37).
- [114] Q. Liu, D. G. Hughes, and P. S. Allen, "Quantitative characterization of the eddy current fields in a 40-cm bore superconducting magnet", *Magn Reson Med*, vol. 31, no. 1, pp. 73–76, 1994. DOI: 10.1002/mrm.1910310112 (cit. on p. 37).
- [115] S. J. Vannesjo, M. Haerberlin, L. Kasper, M. Pavan, B. J. Wilm, C. Barmet, and K. P. Pruessmann, "Gradient system characterization by impulse response measurements with a dynamic field camera", *Magn Reson Med*, vol. 69, no. 2, pp. 583–593, 2013. DOI: 10.1002/mrm.24263 (cit. on pp. 37, 84, 164).

## Bibliography

- [116] H. Liu and G. B. Matson, "Accurate measurement of magnetic resonance imaging gradient characteristics", *Materials*, vol. 7, no. 1, pp. 1–15, 2014, ISSN: 1996-1944. DOI: 10.3390/ma7010001. [Online]. Available: <http://www.mdpi.com/1996-1944/7/1/1> (cit. on p. 37).
- [117] F. Testud, "Dynamic magnetic field estimation for magnetic resonance imaging", PhD Dissertation, Albert-Ludwigs-Universität Freiburg im Breisgau, 2013 (cit. on p. 37).
- [118] S. Abo Seada, J. V. Hajnal, and S. J. Malik, "A simple optimisation approach to making time efficient verse-multiband pulses feasible on non-ideal gradients", in *Proc Intl Soc Mag Reson Med 25*, 2017, p. 5059 (cit. on pp. 37, 51, 164).
- [119] C. Aigner, A. Rund, S. Abo Seada, S. Malik, J. V. Hajnal, K. Kunisch, and R. Stollberger, "Time-optimal control based rf pulse design under gradient imperfections", in *Proc Intl Soc Mag Reson Med 26*, 2017, p. ... (Cit. on pp. 37, 77, 83–85).
- [120] S. Conolly, D. Nishimura, and A. Macovski, "Optimal control solutions to the magnetic resonance selective excitation problem", *IEEE Trans Med Imaging*, vol. MI-5, no. 2, pp. 106–115, 1986. DOI: 10.1109/TMI.1986.4307754 (cit. on pp. 39, 50, 59, 60, 94, 110).
- [121] C. H. Meyer, J. M. Pauly, A. Macovskiand, and D. G. Nishimura, "Simultaneous spatial and spectral selective excitation", *Magn Reson Med*, vol. 15, no. 2, pp. 287–304, 1990. DOI: 10.1002/mrm.1910150211 (cit. on p. 40).
- [122] C. H. Cunningham, D. B. Vigneron, A. P. Chen, D. Xu, R. E. Hurd, N. Sailasuta, and J. M. Pauly, "Design of symmetric-sweep spectral-spatial rf pulses for spectral editing", *Magn Reson Med*, vol. 52, no. 1, pp. 147–153, 2004. DOI: 10.1002/mrm.20116 (cit. on p. 40).
- [123] C. Yang, W. Deng, and V. A. Stenger, "Simple analytical dual-band spectral-spatial rf pulses for b<sub>1+</sub> and susceptibility artifact reduction in gradient echo mri", *Magn Reson Med*, vol. 65, no. 2, pp. 370–376, 2011. DOI: 10.1002/mrm.22725 (cit. on p. 40).
- [124] M. Shen, R. Roopchand, E. S. Mananga, J.-P. Amoureux, Q. Chen, G. S. Boutis, and B. Hu, "Revisiting nmr composite pulses for broadband 2h excitation", *Solid State Nucl Magn*, vol. 66-67, pp. 45–48, 2015. DOI: <https://doi.org/10.1016/j.ssnmr.2014.12.004> (cit. on p. 40).
- [125] A. Shaka, J. Keeler, T. Frenkiel, and R. Freeman, "An improved sequence for broadband decoupling: Waltz-16", *J Magn Reson*, vol. 52, no. 2, pp. 335–338, 1983. DOI: [https://doi.org/10.1016/0022-2364\(83\)90207-X](https://doi.org/10.1016/0022-2364(83)90207-X) (cit. on p. 40).
- [126] P. Hors, "A new method for water suppression in the proton nmr spectra of aqueous solutions", *J Magn Reson*, vol. 54, no. 3, pp. 539–542, 1983. DOI: [https://doi.org/10.1016/0022-2364\(83\)90335-9](https://doi.org/10.1016/0022-2364(83)90335-9) (cit. on p. 40).

## Bibliography

- [127] D. Atkinson, M. Brant-Zawadzki, G. Gillan, D. Purdy, and G. Laub, "Improved mr angiography: Magnetization transfer suppression with variable flip angle excitation and increased resolution.", *Radiology*, vol. 190, no. 3, pp. 890–894, 1994. DOI: 10.1148/radiology.190.3.8115646 (cit. on p. 40).
- [128] L. de Rochefort, X. Maître, J. Bittoun, and E. Durand, "Velocity-selective rf pulses in mri", *Magn Reson Med*, vol. 55, no. 1, pp. 171–176, 2006. DOI: 10.1002/mrm.20751 (cit. on pp. 40, 94).
- [129] L. Axel and L. Dougherty, "Mr imaging of motion with spatial modulation of magnetization.", *Radiology*, vol. 171, no. 3, pp. 841–845, 1989. DOI: 10.1148/radiology.171.3.2717762 (cit. on p. 40).
- [130] S. E. Fischer, G. C. McKinnon, S. E. Maier, and P. Boesiger, "Improved myocardial tagging contrast", *Magn Reson Med*, vol. 30, no. 2, pp. 191–200, 1993. DOI: 10.1002/mrm.1910300207 (cit. on p. 40).
- [131] D. G. Norris, P. J. Koopmans, R. Boyacıoğlu, and M. Barth, "Power independent of number of slices (PINS) radiofrequency pulses for low-power simultaneous multislice excitation", *Magn Reson Med*, vol. 66, no. 5, pp. 1234–1240, 2011. DOI: 10.1002/mrm.23152 (cit. on pp. 41, 56, 57, 75, 95, 118, 125, 129, 134, 146, 150, 152).
- [132] U. Katscher, P. Börnert, C. Leussler, and J. S. van den Brink, "Transmit sense", *Magn Reson Med*, vol. 49, no. 1, pp. 144–150, DOI: 10.1002/mrm.10353 (cit. on p. 41).
- [133] Y. Zhu, "Parallel excitation with an array of transmit coils", *Magn Reson Med*, vol. 51, no. 4, pp. 775–784, 2004. DOI: 10.1002/mrm.20011 (cit. on p. 41).
- [134] K. Setsompop, L. L. Wald, V. Alagappan, B. Gagoski, F. Hebrank, U. Fontius, F. Schmitt, and E. Adalsteinsson, "Parallel rf transmission with eight channels at 3 tesla", *Magn Reson Med*, vol. 56, no. 5, pp. 1163–1171, DOI: 10.1002/mrm.21042 (cit. on p. 41).
- [135] W. Grissom, C. Yip, Z. Zhang, V. A. Stenger, J. A. Fessler, and D. C. Noll, "Spatial domain method for the design of rf pulses in multicoil parallel excitation", *Magn Reson Med*, vol. 56, no. 3, pp. 620–629, DOI: 10.1002/mrm.20978 (cit. on p. 41).
- [136] A. Martin, E. Schiavi, Y. Eryaman, J. L. Herraiz, B. Gagoski, E. Adalsteinsson, L. L. Wald, and B. Guerin, "Parallel transmission pulse design with explicit control for the specific absorption rate in the presence of radiofrequency errors", *Magn Reson Med*, vol. 75, no. 6, pp. 2493–2504, DOI: 10.1002/mrm.25820 (cit. on p. 41).

## Bibliography

- [137] B. Guérin, M. Gebhardt, S. Cauley, E. Adalsteinsson, and L. L. Wald, "Local specific absorption rate (sar), global sar, transmitter power, and excitation accuracy trade offs in low flip angle parallel transmit pulse design", *Magn Reson Med*, vol. 71, no. 4, pp. 1446–1457, DOI: 10.1002/mrm.24800 (cit. on p. 41).
- [138] M. S. Vinding, B. Guérin, T. Vosegaard, and N. C. Nielsen, "Local sar, global sar, and power-constrained large flip angle pulses with optimal control and virtual observation points", *Magn Reson Med*, vol. 77, no. 1, pp. 374–384, DOI: 10.1002/mrm.26086 (cit. on p. 41).
- [139] A. Rund, C. Aigner, N. L., F.-K. R., L. E., K. Kunisch, and R. Stollberger, "Optimal control based design of parallel transmission rf pulses with minimum local sar", in *Proc Intl Soc Mag Reson Med 26*, 2017, p. ... (Cit. on pp. 41, 84, 86).
- [140] J. Moore, M. Jankiewicz, A. W. Anderson, and J. C. Gore, "Evaluation of non-selective refocusing pulses for 7t mri", *J Magn Reson*, vol. 214, pp. 212–220, 2012. DOI: <https://doi.org/10.1016/j.jmr.2011.11.010> (cit. on pp. 42, 50).
- [141] M. Shinnar, "Reduced power selective excitation radio frequency pulses", *Magn Reson Med*, vol. 32, no. 5, pp. 658–660, DOI: 10.1002/mrm.1910320516 (cit. on p. 44).
- [142] R. F. Schulte, J. Tsao, P. Boesiger, and K. P. Pruessmann, "Equi-ripple design of quadratic-phase rf pulses", *J Magn Reson*, vol. 166, no. 1, pp. 111–122, 2004. DOI: <https://doi.org/10.1016/j.jmr.2003.10.009> (cit. on p. 44).
- [143] T. Reese, O. Heid, R. Weisskoff, and V. Wedeen, "Reduction of eddy-current-induced distortion in diffusion MRI using a twice-refocused spin echo", *Magn Reson Med*, vol. 49, no. 1, pp. 177–182, 2003. DOI: 10.1002/mrm.10308 (cit. on pp. 44, 151).
- [144] H. Dyvorne, R. O'Halloran, and P. Balchandani, "Ultrahigh field single-refocused diffusion weighted imaging using a matched-phase adiabatic spin echo (mase)", *Magn Reson Med*, vol. 75, no. 5, pp. 1949–1957, 2016. DOI: 10.1002/mrm.25790 (cit. on p. 44).
- [145] M. H. Buonocore, "RF pulse design using the inverse scattering transform", *Magn Reson Med*, vol. 29, no. 4, pp. 470–477, 1993. DOI: 10.1002/mrm.1910290408 (cit. on pp. 50, 94).
- [146] J. Magland and C. L. Epstein, "Practical pulse synthesis via the discrete inverse scattering transform", *J Magn Reson*, vol. 172, no. 1, pp. 63–78, 2005, ISSN: 1090-7807. DOI: <https://doi.org/10.1016/j.jmr.2004.09.022> (cit. on p. 50).
- [147] J. Shen, "Delayed-focus pulses optimized using simulated annealing", *J Magn Reson*, vol. 149, no. 2, pp. 234–238, 2001. DOI: 10.1006/jmre.2001.2306 (cit. on pp. 50, 94).

## Bibliography

- [148] K. J. Lee, M. N. J. Paley, and J. M. Wild, "Combined simulated annealing and Shinnar–Le Roux pulse design of slice-multiplexed RF pulses for multi-slice imaging", *J Magn Reson*, vol. 182, no. 1, pp. 133–142, 2006. DOI: <http://dx.doi.org/10.1016/j.jmr.2006.06.019> (cit. on p. 50).
- [149] X.-L. Wu, P. Xu, and R. Freeman, "Delayed-focus pulses for magnetic resonance imaging: An evolutionary approach", *Magn Reson Med*, vol. 20, no. 1, pp. 165–170, 1991. DOI: [10.1002/mrm.1910200118](https://doi.org/10.1002/mrm.1910200118) (cit. on pp. 50, 94).
- [150] V. Manu and G. Veglia, "Genetic algorithm optimized triply compensated pulses in nmr spectroscopy", *J Magn Reson*, vol. 260, pp. 136–143, 2015, ISSN: 1090-7807. DOI: <https://doi.org/10.1016/j.jmr.2015.09.010> (cit. on p. 50).
- [151] J. D. Gezelter and R. Freeman, "Use of neural networks to design shaped radiofrequency pulses", *J Magn Reson*, vol. 90, no. 2, pp. 397–404, 1990. DOI: [10.1016/0022-2364\(90\)90149-4](https://doi.org/10.1016/0022-2364(90)90149-4) (cit. on pp. 50, 94).
- [152] M. Lapert, Y. Zhang, M. A. Janich, S. J. Glaser, and D. Sugny, "Exploring the physical limits of saturation contrast in magnetic resonance imaging", *Scientific Reports*, vol. 2, 2012. DOI: [10.1038/srep00589](https://doi.org/10.1038/srep00589) (cit. on pp. 50, 59, 94, 118).
- [153] M. S. Vinding, I. I. Maximov, Z. Tošner, and N. C. Nielsen, "Fast numerical design of spatial-selective RF pulses in MRI using Krotov and quasi-Newton based optimal control methods", *J Chem Phys*, vol. 137, no. 5, 2012. DOI: [10.1063/1.4739755](https://doi.org/10.1063/1.4739755) (cit. on pp. 50, 59, 94, 110, 118).
- [154] J. L. Ulloa, M. Guarini, A. Guesalaga, and P. Irarrazaval, "Chebyshev series for designing RF pulses employing an optimal control approach", *IEEE Trans Med Imaging*, vol. 23, no. 11, pp. 1445–1452, 2004. DOI: [10.1109/TMI.2004.835602](https://doi.org/10.1109/TMI.2004.835602) (cit. on pp. 50, 94).
- [155] B. Bonnard, M. Claeys, O. Cots, and P. Martinon, "Optimal control of coupled spin dynamics: Design of NMR pulse sequences by gradient ascent algorithms", *J Magn Reson*, vol. 172, no. 2, pp. 296–305, 2005. DOI: [10.1016/j.jmr.2004.11.004](https://doi.org/10.1016/j.jmr.2004.11.004) (cit. on pp. 50, 59, 94, 146).
- [156] T. E. Skinner, N. I. Gershenson, M. Nimbalkar, W. Bermel, B. Luy, and S. J. Glaser, "New strategies for designing robust universal rotation pulses: Application to broadband refocusing at low power", *J Magn Reson*, vol. 216, pp. 78–87, 2012. DOI: [10.1016/j.jmr.2012.01.005](https://doi.org/10.1016/j.jmr.2012.01.005) (cit. on pp. 50, 59, 94, 146).
- [157] C. K. Anand, A. D. Bain, A. T. Curtis, and Z. Nie, "Designing optimal universal pulses using second-order, large-scale, non-linear optimization", *J Magn Reson*, vol. 219, pp. 61–74, 2012. DOI: [doi:10.1016/j.jmr.2012.04.004](https://doi.org/10.1016/j.jmr.2012.04.004) (cit. on pp. 50, 94, 95, 146).

## Bibliography

- [158] G. Ciaramella and A. Borzi, "SKRYN: A fast semismooth-Krylov-Newton method for controlling Ising spin systems", *Comput Phys Commun*, vol. 190, pp. 213–223, 2015, ISSN: 0010-4655. DOI: <http://dx.doi.org/10.1016/j.cpc.2015.01.006> (cit. on pp. 50, 146).
- [159] M. Bödenler, C. S. Aigner, A. Rund, C. Clason, and R. Stollberger, "Fast optimization of RF excitation", in *Proc ESMRMB 29*, 2016, pp. 247–400 (cit. on pp. 51, 163).
- [160] S. Conolly, D. Nishimura, A. Macovski, and G. Glover, "Variable-rate selective excitation", *J Magn Reson*, vol. 78, no. 3, pp. 440–458, 1988 (cit. on pp. 51, 56, 95, 112, 125, 134, 146).
- [161] S. Souza, J. Szumowski, C. Dumoulin, D. Plewes, and G. Glover, "SIMA: Simultaneous multislice acquisition of MR images by Hadamard-encoded excitation", *J Comput Assist Tomogr*, vol. 12, no. 6, pp. 907–1093, 1988. DOI: 10.1097/00004728-198811000-00021 (cit. on pp. 52, 53).
- [162] S. Mueller, "Multifrequency selective RF pulses for multislice MR imaging", *Magn Reson Med*, vol. 6, no. 3, pp. 364–371, 1988. DOI: 10.1002/mrm.1910060315 (cit. on pp. 52, 53, 95, 125, 134, 146, 150).
- [163] D. J. Larkman, J. V. Hajnal, A. H. Herlihy, G. A. Coutts, I. R. Young, and G. Ehnholm, "Use of multicoil arrays for separation of signal from multiple slices simultaneously excited", *J Magn Reson Imaging*, vol. 13, no. 2, pp. 313–317, 2001. DOI: 10.1002/1522-2586(200102)13:2<313::AID-JMRI1045>3.0.CO;2-W (cit. on pp. 52, 94, 95, 112, 146).
- [164] R. Nunes, J. V. Hajnal, X. Golay, and D. J. Larkman, "Simultaneous slice excitation and reconstruction for single shot EPI", in *Proc Intl Soc Mag Reson Med 14*, 2006, p. 293 (cit. on pp. 52, 95, 112).
- [165] D. A. Feinberg and K. Setsompop, "Ultra-fast MRI of the human brain with simultaneous multi-slice imaging", *J Magn Reson*, vol. 229, pp. 90–100, 2013. DOI: 10.1016/j.jmr.2013.02.002 (cit. on pp. 52, 95, 112).
- [166] K. Uğurbil, J. Xu, E. J. Auerbach, S. Moeller, A. T. Vu, J. M. Duarte-Carvajalino, C. Lenglet, X. Wu, S. Schmitter, P. F. Van de Moortele, J. Strupp, G. Sapiro, F. De Martino, D. Wang, N. Harel, M. Garwood, L. Chen, D. A. Feinberg, S. M. Smith, K. L. Miller, S. N. Sotiropoulos, S. Jbabdi, J. L. R. Andersson, T. E. J. Behrens, M. F. Glasser, D. C. Van Essen, and E. Yacoub, "Pushing spatial and temporal resolution for functional and diffusion MRI in the human connectome project", *NeuroImage*, vol. 80, pp. 80–104, 2013. DOI: 10.1016/j.neuroimage.2013.05.012 (cit. on pp. 52, 94, 95, 102, 112).
- [167] P. B. Roemer, W. A. Edelstein, C. E. Hayes, S. P. Souza, and O. M. Mueller, "The nmr phased array", *Magn Reson Med*, vol. 16, no. 2, pp. 192–225, 1990. DOI: 10.1002/mrm.1910160203 (cit. on p. 53).

## Bibliography

- [168] K. P. Pruessmann, M. Weiger, M. B. Scheidegger, and P. Boesiger, "Sense: Sensitivity encoding for fast mri", *Magn Reson Med*, vol. 42, no. 5, pp. 952–962, 1999. DOI: 10.1002/(SICI)1522-2594(199911)42:5<952::AID-MRM16>3.0.CO;2-S (cit. on p. 53).
- [169] M. A. Griswold, P. M. Jakob, R. M. Heidemann, M. Nittka, V. Jellus, J. Wang, B. Kiefer, and A. Haase, "Generalized autocalibrating partially parallel acquisitions (grappa)", *Magn Reson Med*, vol. 47, no. 6, pp. 1202–1210, 2002. DOI: 10.1002/mrm.10171 (cit. on p. 53).
- [170] M. Blaimer, F. Breuer, M. Mueller, R. M. Heidemann, M. A. Griswold, and P. M. Jakob, "Smash, sense, pils, grappa: How to choose the optimal method", *Topics Magn Reson Imaging*, vol. 15, no. 4, 2004 (cit. on p. 53).
- [171] F. A. Breuer, M. Blaimer, M. F. Mueller, N. Seiberlich, R. M. Heidemann, M. A. Griswold, and P. M. Jakob, "Controlled aliasing in volumetric parallel imaging (2d caipirinha)", *Magn Reson Med*, vol. 55, no. 3, pp. 549–556, 2006. DOI: 10.1002/mrm.20787 (cit. on pp. 53, 69, 102).
- [172] K. Setsompop, B. A. Gagoski, J. R. Polimeni, T. Witzel, V. J. Wedeen, and L. L. Wald, "Blipped-controlled aliasing in parallel imaging for simultaneous multislice echo planar imaging with reduced g-factor penalty", *Magn Reson Med*, vol. 67, no. 5, pp. 1210–1224, 2012. DOI: 10.1002/mrm.23097 (cit. on pp. 53, 56, 69, 103, 146).
- [173] A. Sharma, M. Lustig, and W. A. Grissom, "Root-flipped multiband refocusing pulses", *Magn Reson Med*, vol. 75, no. 1, pp. 227–237, 2016. DOI: 10.1002/mrm.25629 (cit. on pp. 54, 56, 72, 96, 112, 118, 125, 128, 134, 146, 150, 163).
- [174] E. Wong, "Optimized phase schedules for minimizing peak RF power in simultaneous multi-slice RF excitation pulses", in *Proc. ISMRM 20*, 2012, p. 2209 (cit. on pp. 54, 96, 112, 118, 146, 150).
- [175] E. J. Auerbach, J. Xu, E. Yacoub, S. Moeller, and K. Ugurbil, "Multiband accelerated spin-echo echo planar imaging with reduced peak RF power using time-shifted RF pulses", *Magn Reson Med*, vol. 69, no. 5, pp. 1261–1267, 2013. DOI: 10.1002/mrm.24719 (cit. on pp. 55, 95, 112, 118, 146).
- [176] N. Kobayashi, K. Ugurbil, and X. Wu, "Shortening nonlinear phase multiband refocusing pulses with VERSE", in *Proc Intl Soc Mag Reson Med. 24*, 2016, p. 3253 (cit. on pp. 56, 118, 146).
- [177] S. Abo Seada, A. N. Price, T. Schneider, J. V. Hajnal, and S. J. Malik, "Multiband rf pulse design for realistic gradient performance", *Magn Reson Med*, n/a–n/a, DOI: n/a (cit. on p. 56).

## Bibliography

- [178] A. M. Huettner, N. J. Mickevicius, A. Ersoz, K. M. Koch, L. T. Muftuler, and A. S. Nencka, "Wavelet domain radiofrequency pulse design applied to magnetic resonance imaging", *PLOS ONE*, vol. 10, no. 10, pp. 1–17, 2015. DOI: 10.1371/journal.pone.0141151 (cit. on pp. 56, 146).
- [179] C. Eichner, L. L. Wald, and K. Setsompop, "A low power radiofrequency pulse for simultaneous multislice excitation and refocusing", *Magn Reson Med*, vol. 72, no. 4, pp. 949–958, 2014. DOI: 10.1002/mrm.25389 (cit. on pp. 56, 57, 95, 112, 118, 125, 134, 146, 150).
- [180] S. Williams, J. A. Fessler, and D. C. Noll, "Minimum out-of-slice error sms rf pulse design with direct peak, power, and in-slice error constraints", in *Proc ESMRMB 30*, 2017 (cit. on p. 56).
- [181] A. E. Bryson, "Optimal control-1950 to 1985", *IEEE Control Systems*, vol. 16, no. 3, pp. 26–33, 1996. DOI: 10.1109/37.506395 (cit. on p. 59).
- [182] B. Bonnard, M. Claeys, O. Cots, and P. Martinon, "Geometric and numerical methods in the contrast imaging problem in nuclear magnetic resonance", *Acta Appl Math*, vol. online first, 2014. DOI: 10.1007/s10440-014-9947-3 (cit. on pp. 59, 94).
- [183] F. Tröltzsch, *Optimal control of partial differential equations*. Amer Math Soc, 2004, ISBN: 978-0-8218-4904-0 (cit. on p. 59).
- [184] M. Vinding, I. Maximov, Z. Tošner, and N. Nielsen, "Fast numerical design of spatial-selective RF pulses in MRI using Krotov and quasi-Newton based optimal control methods", *J Chem Phys*, vol. 137, no. 5, 2012, ISSN: 00219606. DOI: 10.1063/1.4739755 (cit. on pp. 60, 146).
- [185] T. Steihaug, "The conjugate gradient method and trust regions in large scale optimization", *SIAM J Num Anal*, vol. 20, no. 3, pp. 626–637, 1983. DOI: 10.1137/0720042 (cit. on pp. 60, 62, 65, 72, 95, 99).
- [186] D. A. Knoll and D. E. Keyes, "Jacobian-free Newton–Krylov methods: A survey of approaches and applications", *J Comp Phys*, vol. 193, no. 2, pp. 357–397, 2004. DOI: 10.1016/j.jcp.2003.08.010 (cit. on pp. 61, 95, 98).
- [187] C. Aigner, C. Clason, A. Rund, and R. Stollberger, "Sar reduced excitation by joint design of rf pulse and slice selective gradient shape", in *Proc Intl Soc Mag Reson Med 23*, 2015, p. 915 (cit. on pp. 62, 63).
- [188] C. K. Anand, S. J. Stoyan, and T. Terlaky, "Optimizing the gVERSE RF pulse sequence: An evaluation of two competitive software algorithms", *Math Oper Res*, vol. 6, pp. 1–19, 2011 (cit. on p. 64).
- [189] C. Aigner, C. Clason, A. Rund, and R. Stollberger, "Low sar rf-pulse design by joint optimization of rf and gradient shape with physical constraints", in *Proc Intl Soc Mag Reson Med 24*, 2016, p. 1891 (cit. on pp. 65–67).

## Bibliography

- [190] M. Ulbrich, “Semismooth Newton methods for operator equations in function spaces”, *SIAM J Optim*, vol. 13, no. 3, pp. 805–841, 2003. DOI: 10.1137/S1052623400371569 (cit. on pp. 65, 72, 123).
- [191] K. Pieper, “Finite element discretization and efficient numerical solution of elliptic and parabolic sparse control problems”, PhD Dissertation, Technische Universität München, 2015 (cit. on pp. 65, 72, 124).
- [192] C. Aigner, C. Clason, A. Rund, and R. Stollberger, “Rf pulse design for simultaneous multislice excitation with highly reduced b<sub>1</sub> peak amplitude”, in *Proc Intl Soc Mag Reson Med* 23, 2015, p. 660 (cit. on p. 69).
- [193] C. Aigner, C. Clason, A. Rund, A. Petrovic, and R. Stollberger, “Design of complex rf pulse shapes for asymmetric excitation patterns via optimal control”, in *Proc BMT*, 2016, p. xx (cit. on p. 69).
- [194] C. Aigner, A. Rund, B. Bilgic, B. Gagoski, K. Setsompop, K. Kunisch, and R. Stollberger, “Application of time-optimal simultaneous multi-slice refocusing to tse/rare”, in *Proc Intl Soc Mag Reson Med* 25, 2017, p. 3843 (cit. on pp. 77, 79, 80).
- [195] B. A. Gagoski, B. Bilgic, C. Eichner, H. Bhat, P. E. Grant, L. L. Wald, and K. Setsompop, “RARE/turbo spin echo imaging with simultaneous multislice Wave-CAIPI”, *Magn Reson Med*, vol. 73, no. 3, pp. 929–938, 2015. DOI: 10.1002/mrm.25615 (cit. on pp. 79, 95, 112, 146).
- [196] H. C. Torrey, “Bloch equations with diffusion terms”, *Phys Rev*, vol. 104, pp. 563–565, 3 1956. DOI: 10.1103/PhysRev.104.563 (cit. on p. 84).
- [197] H. M. McConnell, “Reaction rates by nuclear magnetic resonance”, *J Chem Phys*, vol. 28, no. 3, pp. 430–431, 1958. DOI: 10.1063/1.1744152 (cit. on p. 84).
- [198] G. M. Bydder, G. D. Fullerton, and I. R. Young, *MRI of tissues with short T<sub>2</sub>s or T<sub>2</sub>\*s*. Wiley, 2012, vol. 1 (cit. on p. 94).
- [199] A. A. Khalifa, A.-B. M. Youssef, and Y. M. Kadah, “Optimal design of RF pulses with arbitrary profiles in magnetic resonance imaging”, in *Proc IEEE* 23, vol. 3, 2001, pp. 2296–2299. DOI: 10.1109/IEMBS.2001.1017234 (cit. on p. 94).
- [200] K. J. Lee, “General parameter relations for the Shinnar–Le Roux pulse design algorithm”, *J Magn Reson*, vol. 186, no. 2, pp. 252–258, 2007. DOI: 10.1016/j.jmr.2007.03.010 (cit. on pp. 94, 101).
- [201] P. Balchandani, J. Pauly, and D. Spielman, “Designing adiabatic radio frequency pulses using the Shinnar–Le Roux algorithm”, *Magn Reson Med*, vol. 64, no. 3, pp. 843–851, 2010. DOI: 10.1002/mrm.22473 (cit. on p. 94).
- [202] W. A. Grissom, G. C. McKinnon, and M. W. Vogel, “Nonuniform and multidimensional Shinnar–Le Roux RF pulse design method”, *Magn Reson Med*, vol. 68, no. 3, pp. 690–702, 2012. DOI: 10.1002/mrm.23269 (cit. on pp. 94, 118).

## Bibliography

- [203] C. Ma and Z.-P. Liang, “Design of multidimensional Shinnar–Le Roux radiofrequency pulses”, *Magn Reson Med*, 2014. DOI: 10.1002/mrm.25179 (cit. on p. 94).
- [204] P. de Fouquieres, S. Schirmer, S. Glaser, and I. Kuprov, “Second order gradient ascent pulse engineering”, *J Magn Reson*, vol. 212, no. 2, pp. 412–417, 2011. DOI: 10.1016/j.jmr.2011.07.023 (cit. on p. 95).
- [205] M. Hinze and K. Kunisch, “Second order methods for optimal control of time-dependent fluid flow”, *SIAM J Control Optim*, vol. 40, no. 3, pp. 925–946, 2001. DOI: 10.1137/S0363012999361810 (cit. on pp. 95, 99).
- [206] G. Ciaramella, A. Borzi, G. Dirr, and D. Wachsmuth, “Newton methods for the optimal control of closed quantum spin systems”, *SIAM J Scien Comp*, vol. 37, A319–A346, 2015. DOI: 10.1137/140966988 (cit. on p. 95).
- [207] G. Ciaramella and A. Borzi, “SKRYN: A fast semismooth-Krylov–Newton method for controlling Ising spin systems”, *Comput Phys Commun*, vol. 190, pp. 213–223, 2015. DOI: 10.1016/j.cpc.2015.01.006 (cit. on p. 95).
- [208] A. Sharma, R. O’Halloran, E. Aboussouan, A. Tu Van, J. Maclaren, M. Aksoy, V. A. Stenger, R. Bammer, and W. A. Grissom, “kT-PINS RF pulses for low-power field inhomogeneity-compensated multislice excitation”, in *Proc Intl Soc Mag Reson Med 21*, 2013, p. 44 (cit. on p. 95).
- [209] K. Setsompop, J. Cohen-Adad, B. A. Gagoski, T. Raij, A. Yendiki, B. Keil, V. J. Wedeen, and L. L. Wald, “Improving diffusion MRI using simultaneous multi-slice echo planar imaging”, *NeuroImage*, vol. 63, no. 1, pp. 569–580, 2012. DOI: 10.1016/j.neuroimage.2012.06.033 (cit. on pp. 95, 146).
- [210] K. Zhu, A. B. Kerr, and J. M. Pauly, “Nonlinear-phase multiband  $90^\circ$ – $180^\circ$  RF pair with reduced peak power”, in *Proc Intl Soc Mag Reson Med 22*, 2014, p. 1440 (cit. on pp. 96, 112).
- [211] U. Katscher, H. Eggers, I. Graesslin, G. Mens, and P. Boernert, “3D RF shimming using multi-frequency excitation”, in *Proc Intl Soc Mag Reson Med 16*, 2008, p. 1311 (cit. on pp. 96, 112).
- [212] X. Wu, S. Schmitter, E. J. Auerbach, S. Moeller, K. Uğurbil, and P.-F. Van de Moortele, “Simultaneous multislice multiband parallel radiofrequency excitation with independent slice-specific transmit B1 homogenization”, *Magn Reson Med*, vol. 70, no. 3, pp. 630–638, 2013. DOI: 10.1002/mrm.24828 (cit. on pp. 96, 112).
- [213] B. A. Poser, R. J. Anderson, B. Guérin, K. Setsompop, W. Deng, A. Mareyam, P. Serano, L. L. Wald, and V. A. Stenger, “Simultaneous multislice excitation by parallel transmission”, *Magn Reson Med*, vol. 71, no. 4, pp. 1416–1427, 2014. DOI: 10.1002/mrm.24791 (cit. on pp. 96, 112).

## Bibliography

- [214] B. Guérin, K. Setsompop, H. Ye, B. A. Poser, A. V. Stenger, and L. L. Wald, “Design of parallel transmission pulses for simultaneous multislice with explicit control for peak power and local specific absorption rate”, *Magn Reson Med*, vol. 73, no. 5, pp. 1946–1953, 2014. DOI: 10.1002/mrm.25325 (cit. on pp. 96, 112).
- [215] M. Hinze, R. Pinnau, M. Ulbrich, and S. Ulbrich, *Optimization with PDE constraints*, ser. Math Model Theory Appl. Springer, New York, 2009, vol. 23. DOI: 10.1007/978-1-4020-8839-1 (cit. on p. 99).
- [216] F. Santosa and W. W. Symes, “Computation of the Hessian for least-squares solutions of inverse problems of reflection seismology”, *Inverse Problems*, vol. 4, no. 1, p. 211, 1988. DOI: 10.1088/0266-5611/4/1/017 (cit. on p. 99).
- [217] Z. Wang, I. Navon, F. Le Dimet, and X. Zou, “The second order adjoint analysis: Theory and applications”, *Meteorol Atmos Phys*, vol. 50, no. 1–3, pp. 3–20, 1992. DOI: 10.1007/BF01025501 (cit. on p. 99).
- [218] R. Becker, D. Meidner, and B. Vexler, “Efficient numerical solution of parabolic optimization problems by finite element methods”, *Optim Method*, vol. 22, no. 5, pp. 813–833, 2007. DOI: 10.1080/10556780701228532 (cit. on p. 100).
- [219] S. F. Cauley, J. R. Polimeni, H. Bhat, L. L. Wald, and K. Setsompop, “Interslice leakage artifact reduction technique for simultaneous multislice acquisitions”, *Magn Reson Med*, vol. 72, no. 1, pp. 93–102, 2014. DOI: 10.1002/mrm.24898 (cit. on p. 103).
- [220] T. E. Skinner, N. I. Gershenzona, M. Nimbalkar, and S. J. Glaser, “Optimal control design of band-selective excitation pulses that accommodate relaxation and rf inhomogeneity”, *J Magn Reson*, vol. 217, pp. 53–60, 2012. DOI: 10.1016/j.jmr.2012.02.007 (cit. on p. 112).
- [221] S. Conolly, D. Nishimura, and A. Macovski, “Variable rate selective excitation”, *IEEE Trans Med Imaging*, vol. MI-5, p. 106, 1986 (cit. on p. 118).
- [222] M. Bergounioux, K. Ito, and K. Kunisch, “Primal-dual strategy for constrained optimal control problems”, *SIAM J Control Optim*, vol. 37, pp. 1176–1194, 1999. DOI: 10.1137/S0363012997328609 (cit. on p. 121).
- [223] M. Bergounioux, M. Haddou, M. Hintermüller, and K. Kunisch, “A comparison of a Moreau-Yosida based active set strategy and interior point methods for constrained optimal control problems”, *SIAM J Optim*, vol. 11, pp. 495–521, 2000. DOI: 10.1137/S1052623498343131 (cit. on p. 121).
- [224] M. Hintermüller, K. Ito, and K. Kunisch, “The primal-dual active set method as a semi-smooth Newton method”, *SIAM J Optim*, vol. 13, no. 3, pp. 865–888, 2003. DOI: 10.1137/S1052623401383558 (cit. on pp. 121, 123).

## Bibliography

- [225] M. Ulbrich, S. Ulbrich, and M. Heinkenschloss, "Global convergence of trust-region interior-point algorithms for infinite-dimensional nonconvex minimization subject to pointwise bounds", *SIAM J Control Optim*, vol. 37, no. 3, pp. 731–764, 1999. DOI: 10.1137/S0363012997325915 (cit. on p. 121).
- [226] M. Hintermüller and K. Kunisch, "Stationary optimal control problems with pointwise state constraints", in *Numerical PDE Constrained Optimization*, ser. Lecture Notes in Computational Science and Engineering, vol. 72, Berlin: Springer, 2009 (cit. on pp. 121, 149).
- [227] M. Ulbrich, *Semismooth Newton Methods for Variational Inequalities and Constrained Optimization Problems in Function Spaces*, ser. MOS-SIAM Series on Optimization. SIAM, 2011 (cit. on pp. 123, 124).
- [228] K. Ito and K. Kunisch, *Lagrange Multiplier Approach to Variational Problems and Applications*. SIAM, 2008 (cit. on p. 123).
- [229] W. Fischer and I. Lieb, *A Course in Complex Analysis*. Vieweg+Teubner Verlag, 2012. DOI: 10.1007/978-3-8348-8661-3 (cit. on pp. 123, 142).
- [230] T. Steihaug, "The conjugate gradient method and trust regions in large scale optimization", *SIAM J Num Anal*, vol. 20, pp. 626–637, 1983 (cit. on p. 124).
- [231] J. Nocedal and S. J. Wright, *Numerical Optimization*, 2nd, T. V. Mikosch, S. I. Resnick, and S. M. Robinson, Eds., ser. Springer Series in Operations Research and Financial Engineering. New York: Springer, 2006. DOI: 10.1007/978-0-387-40065-5 (cit. on p. 124).
- [232] R. H. Byrd, J. Nocedal, and R. B. Schnabel, "Representations of quasi-newton matrices and their use in limited memory methods", *Math Program*, vol. 63, no. 1, pp. 129–156, 1994. DOI: 10.1007/BF01582063 (cit. on p. 124).
- [233] B. Hargreaves, "Bloch equation simulation", 2003. [Online]. Available: <http://mrsrl.stanford.edu/~brian/blochsim/> (cit. on p. 139).
- [234] M. Çavuşoğlu, R. Mooiweer, K. P. Pruessmann, and S. J. Malik, "Verse-guided parallel rf excitations using dynamic field correction", *NMR Biomed*, vol. 30, no. 6, e3697–n/a, 2017, e3697 NBM-16-0080.R1. DOI: 10.1002/nbm.3697 (cit. on p. 140).
- [235] A. Rund, C. Aigner, K. Kunisch, and R. Stollberger, "Simultaneous multislice refocusing by time-optimal control", in *Proc Intl Soc Mag Reson Med 25*, 2017 (cit. on p. 141).
- [236] L. Chen, A. T. Vu, J. Xu, S. Moeller, K. Uğurbil, E. Yacoub, and D. Feinberg, "Evaluation of highly accelerated simultaneous multi-slice EPI for fMRI", *NeuroImage*, vol. 104, pp. 452–459, 2015. DOI: <http://dx.doi.org/10.1016/j.neuroimage.2014.10.027> (cit. on p. 146).

## Bibliography

- [237] B. Bilgic, B. Gagoski, S. Cauley, A. Fan, J. Polimeni, P. Grant, L. Wald, and K. Setsompop, "Wave-CAIPI for highly accelerated 3D imaging", *J Magn Reson*, vol. 73, no. 6, pp. 2152–2162, 2015. DOI: 10.1002/mrm.25347 (cit. on p. 146).
- [238] K. Setsompop, B. Bilgic, A. Nummenmaa, Q. Fan, S. F. Cauley, S. Huang, I. Chatnuntaweck, Y. Rathi, T. Witzel, and L. L. Wald, "Slice dithered enhanced resolution simultaneous multislice (SLIDER-SMS) for high resolution (700  $\mu\text{m}$ ) diffusion imaging of the human brain", in *Proc Intl Soc Mag Reson Med 23*, 2015, p. 0339 (cit. on p. 146).
- [239] J. P. Haldar, Q. Fan, and K. Setsompop, "Whole-brain quantitative diffusion MRI at 660  $\mu\text{m}$  resolution in 25 minutes using gSlider-SMS and SNR-enhancing joint reconstruction", in *Proc Intl Soc Mag Reson Med 24*, 2016, p. 0102 (cit. on p. 146).
- [240] S. Conolly, D. Nishimura, and A. Macovski, "Optimal control solutions to the magnetic resonance selective excitation problem", *IEEE Trans Med Imaging*, vol. MI-5, no. 2, pp. 106–115, 1986 (cit. on p. 146).
- [241] A. Rund, C. Aigner, K. Kunisch, and R. Stollberger, "Rf pulse design by optimal control with physical constraints", in *Proc Intl Soc Mag Reson Med 25*, 2017, p. 1324 (cit. on p. 147).
- [242] H. Hermes and J. P. Lasalle, *Functional Analysis and Time Optimal Control*, ser. Mathematics in Science and Engineering. New York: Academic Press, 1969. [Online]. Available: <http://books.google.at/books?id=U20pf6C83B8C> (cit. on pp. 147, 149).
- [243] K. Kunisch, K. Pieper, and A. Rund, "Time optimal control for a reaction diffusion system arising in cardiac electrophysiology – a monolithic approach", *ESAIM-Math Model Num*, vol. 50, no. 2, pp. 381–414, 2016. DOI: 10.1051/m2an/2015048 (cit. on p. 149).
- [244] H. Y. Carr and E. M. Purcell, "Effects of diffusion on free precession in nuclear magnetic resonance experiments", *Phys Rev*, vol. 94, pp. 630–638, 3 1954. DOI: 10.1103/PhysRev.94.630 (cit. on p. 163).
- [245] S. Meiboom and D. Gill, "Modified spin-echo method for measuring nuclear relaxation times", *Rev Sci Instrum*, vol. 29, no. 8, pp. 688–691, 1958. DOI: 10.1063/1.1716296 (cit. on p. 163).
- [246] W. A. Grissom, A. B. Kerr, P. Stang, G. C. Scott, and J. M. Pauly, "Minimum envelope roughness pulse design for reduced amplifier distortion in parallel excitation", *Magn Reson Med*, vol. 64, no. 5, pp. 1432–1439, 2010. DOI: 10.1002/mrm.22512 (cit. on p. 163).
- [247] M. A. Janich, R. F. Schulte, M. Schwaiger, and S. J. Glaser, "Robust slice-selective broadband refocusing pulses", *J Magn Reson*, vol. 213, no. 1, pp. 126–135, 2011. DOI: <http://doi.org/10.1016/j.jmr.2011.09.025> (cit. on p. 164).